

Yield and flow stress of steel in the austenitic state

van Liempt, Peter

DOI

[10.4233/uuid:92eb1908-8ac7-41ea-aa1e-09cbbdef4f55](https://doi.org/10.4233/uuid:92eb1908-8ac7-41ea-aa1e-09cbbdef4f55)

Publication date

2016

Document Version

Final published version

Citation (APA)

van Liempt, P. (2016). *Yield and flow stress of steel in the austenitic state*. [Dissertation (TU Delft), Delft University of Technology]. <https://doi.org/10.4233/uuid:92eb1908-8ac7-41ea-aa1e-09cbbdef4f55>

Important note

To cite this publication, please use the final published version (if applicable).
Please check the document version above.

Copyright

Other than for strictly personal use, it is not permitted to download, forward or distribute the text or part of it, without the consent of the author(s) and/or copyright holder(s), unless the work is under an open content license such as Creative Commons.

Takedown policy

Please contact us and provide details if you believe this document breaches copyrights.
We will remove access to the work immediately and investigate your claim.

Yield and flow stress of steel in the austenitic state

Peter van Liempt

The background of the illustration on the cover is a figure from a letter by Christiaan Huygens to Estienne, dated September 7th 1669. It shows a diagram of Huygens' pendulum clock that has its pendulum suspended between cycloidal cheeks, to ensure isochronism by forcing the pendulum bob to follow a cycloidal path. The equation describing anelastic dislocation strain in Chapter 5 is closely related to the cycloid equation, a peculiar coincidence.

Yield and flow stress of steel in the austenitic state

Proefschrift

ter verkrijging van de graad van doctor
aan de Technische Universiteit Delft
op gezag van de Rector Magnificus Prof. Ir.
K.Ch.A.M. Luyben, voorzitter van het
College voor Promoties,
in het openbaar te verdedigen op 29 november
2016 om 12:30 uur

door

Peter VAN LIEMPT

doctorandus Natuurkunde
Universiteit van Leiden, Nederland
geboren te Den Haag, Nederland

This dissertation has been approved by the promotor: Prof. dr. ir. J. Sietsma

Composition of the doctoral committee:

Rector Magnificus	chairman
Prof.dr.ir. J. Sietsma	Delft University of Technology, promotor

Independent members:

Prof.dr.ir. L.A.I. Kestens	Delft University of Technology
Prof.dr.-ing. W. Bleck	RWTH Aachen University
Prof.dr. K.O. Findley	Colorado School of Mines
Prof. dr.ir. M.G.D. Geers	Technische Universiteit Eindhoven
Prof.dr.ir. A.H. van den Boogaard	University of Twente
Dr. P.J.J. Kok	Tata Steel Research and Development

Reserve member:

Prof.dr. I. M. Richardson	Delft University of Technology
---------------------------	--------------------------------

This research was funded by Tata Steel Research and Development and carried out under project no.MC10.07297 in the framework of the Research Program of the Materials innovation institute(M2i).

Contents

Chapter 1.	Introduction.....	5
1.1	Steel.....	5
1.1.1	Industrial issues	6
1.1.2	Theoretical issues	7
1.2	Outline of the thesis	8
Chapter 2.	Background: the Flow Stress of polycrystalline metals.....	10
2.1	Introduction.....	10
2.1.1	Flow stress phenomenology.....	10
2.2	Mechanisms of plastic deformation.....	14
2.2.1	Deformation mechanism maps	17
2.2.2	Long and short range stress fields.....	19
2.3	The yield stress and pre-yield phenomena	21
2.3.1	Pre-yield phenomena	22
2.4	Resistance due to thermally activated dislocation glide.....	27
2.5	Work hardening.....	32
2.5.1	The Bergström model.....	35
2.5.2	The Kocks- Mecking model.....	44
2.6	Other Bergström/Kocks-Mecking like models.....	46
2.7	Dynamic strain ageing	47
2.8	Scientific questions.....	55
Chapter 3.	Experimental methods & techniques.....	63
3.1	Introduction.....	63
3.2	Comparison of some testing techniques.....	63
3.2.1	Plane strain compression	64
3.2.2	Axisymmetric compression	70
3.2.3	Torsion.....	72
3.3	Tensile test	72
3.4	Hot tensile testing techniques.....	74

3.4.1	General description of the Gleeble system	74
3.4.2	A tensile specimen design to minimise the temperature gradient 76	
3.4.3	Video equipment	82
3.4.4	Contactless temperature measurement	82
3.4.5	Contactless strain measurement.....	84
3.5	Special deformation techniques.....	88
3.5.1	Ausforming: deformation of metastable austenite	89
3.5.2	Strain rate jump tests	90
3.5.3	Stress cycling	92
3.6	Data assessment.....	94
3.6.1	Kocks-Mecking diagram.....	94
3.7	Instrumental issues	98
3.7.1	Machine stiffness	98
3.7.2	Signal noise of the Gleeble force and elongation channels	103
3.7.3	Conclusion	106
Chapter 4.	A Revised Criterion for the Portevin–Le Châtelier Effect Based on the Strain-rate Sensitivity of the Work Hardening Rate.....	110
4.1	Introduction.....	111
4.2	Background.....	112
4.3	Stability criterion	116
4.4	Discussion	118
4.5	Conclusion	123
Chapter 5.	A physically based yield criterion I	127
5.1	Introduction.....	127
5.2	Pre-yield behaviour	129
5.3	Experimental details.....	134
5.4	Results and discussion.....	134
5.4.1	Pre-yield behaviour	134
5.4.2	Reversibility of pre-yield strain.....	137
5.5	The extended Kocks-Mecking plot	140

5.6	Conclusion	143
Chapter 6.	A physically based yield criterion II.	150
6.1	Introduction.....	150
6.2	Grain boundary strain incompatibility	151
6.2.1	The grain boundary stress	152
6.2.2	The Hall-Petch relation	155
6.3	Experimental	157
6.3.1	Hall-Petch analysis.....	158
6.3.2	The yield stress as a function of temperature and strain rate.	159
6.4	Discussion.	164
6.5	Conclusions.....	166
Chapter 7.	Work hardening.....	170
7.1	Introduction.....	170
7.2	Experimental	171
7.3	Analysis of strain rate jump tests	174
7.3.1	Dislocation glide resistance as a function of strain	177
7.3.2	State variable for work hardening.....	178
7.4	Constant temperature / strain rate tests	180
7.4.1	Occurrence of dynamic strain ageing behaviour.....	180
7.4.2	Dislocation storage and recovery rates.....	182
7.4.3	Hall-Petch effect on post-yield behaviour.....	184
7.5	Selection of sub-models	187
7.5.1	Thermally activated effects on the hardening rate.....	187
7.5.2	Immobilisation rate	189
7.5.3	The sub-model for the dislocation mean free path	191
7.5.4	Dynamic recovery.....	192
7.6	Model Fit	194
7.6.1	Dislocation mean free path	199
7.7	Discussion	200
7.7.1	Post-yield flow stress and yield stress.....	200
7.7.2	The Taylor relation and the proposed yield stress theory	203

7.8	Conclusions.....	206
-----	------------------	-----

Chapter 1. Introduction

Duct tape is like the force. It has a light side, a dark side, and it holds the universe together....

Carl Zwanzig

1.1 Steel

Steel may very well be characterised as the most versatile technical material. Its use is manifold: in transportation, building, construction, warfare, ... The quote above this chapter therefore applies equally well to steel. The history of steelmaking stretches over four millennia [1]. With the exception of wood and stone, steel has a longer history than any other technical material. Up to one century ago, the manufacture and application of steel and steel products was a matter of skill. Nevertheless that practice has led in the past to the development of steel grades of exceptional quality and properties, like the (in)famous (true) Damascus steel [2]. The secret to its manufacture has however been lost, which is possibly the inevitable fate of skills that are transferred by an oral tradition. It certainly needs to be known how steel "works" internally in order to be able to work with it. During the last century steelmaking and application of steel therefore has become increasingly a matter of science and scientific engineering.

With the advance of computational power, we now have entered an era in which successful manufacture and application of steel relies heavily on the application of physical-mathematical models that can explain and predict the mechanical behaviour of steel in manufacture and application. Physical-mathematical modelling is increasingly crucial since there is a strong trend of the industry to produce more advanced high strength steels that have a more complex relation between microstructure and composition than plain carbon steel grades.

A commonly used quantification for "mechanical behaviour" is flow stress. Flow stress –or deformation resistance- is the stress that has to be applied to plastically deform the material at the desired strain rate and at a given temperature. Metals deform by propagation of lattice defects known as dislocations through the crystal lattice. In Figure 1-1 a schematic cross section of a cubic crystal containing an edge dislocation is shown.

The flow stress is the applied stress that is necessary to make the dislocations propagate at a sufficiently high velocity to cause deformation to proceed at the

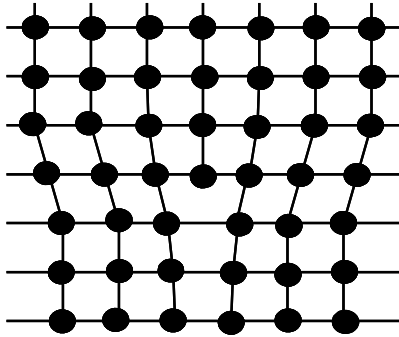


Figure 1-1. An edge dislocation.
Circles denote atoms.

desired strain rate. Mobile dislocations are eventually stored in the lattice, while new dislocations are generated during deformation. The increase of dislocation density causes an increase of the flow stress, which is called work hardening. The flow stress is thus the sum of a yield stress that is necessary to make deformation possible, a stress contribution that is necessary for dislocation propagation at the

desired velocity and a work hardening contribution. The subject of this thesis is to investigate the flow stress of steel for the range of temperatures and strain rates of the hot rolling process.

1.1.1 Industrial issues

Tata Steel IJmuiden is a manufacturer of sheet metal for the packaging and automotive industry and for industries producing commodities such as bathtubs, refrigerators, washing machines and such. Steel sheet is produced from continuously cast slabs, which after reheating are either hot rolled and sold as such or hot rolled and subsequently cold rolled, annealed, temper rolled and either are coated or left uncoated. The full range of Tata Steel products can be found at www.tatasteeleurope.com.

After the hot rolling process, the material undergoes a controlled transformation on the runout table, where the optimal (either for hot rolled qualities or for subsequent cold rolling) microstructure and properties are acquired. A modern alternative for the conventional casting/reheating/hot rolling process is the direct sheet process, where a strip rather than a slab is cast, heated, hot rolled and transformed in one integrated plant.

The target process for the research in this thesis is the hot rolling process, which involves a roughing mill phase, in which the material is reverse rolled for a number of passes, and a final rolling phase, in which seven consecutive passes in the finishing rolling mill train. A schematic of the conventional reheating/hot rolling/transformation plant is shown in Figure 1-2.

As indicated in the figure, any precipitates that have formed in the prior casting process are dissolved in the reheating step. In the roughing mill new precipitates form by segregation of precipitating elements to the dislocations that are “stored” in the material during deformation. Both in the roughing mill section and in the finishing mill the material recrystallizes, either statically between the deformation steps or dynamically during the deformation steps. These two processes are influenced by the deformation energy that is stored in the dislocation structures that are formed during the deformation process. This is also the case for the subsequent transformation process. At present, a project to establish a through process model with which the evolution of the microstructure and the properties of the material during the hot rolling and

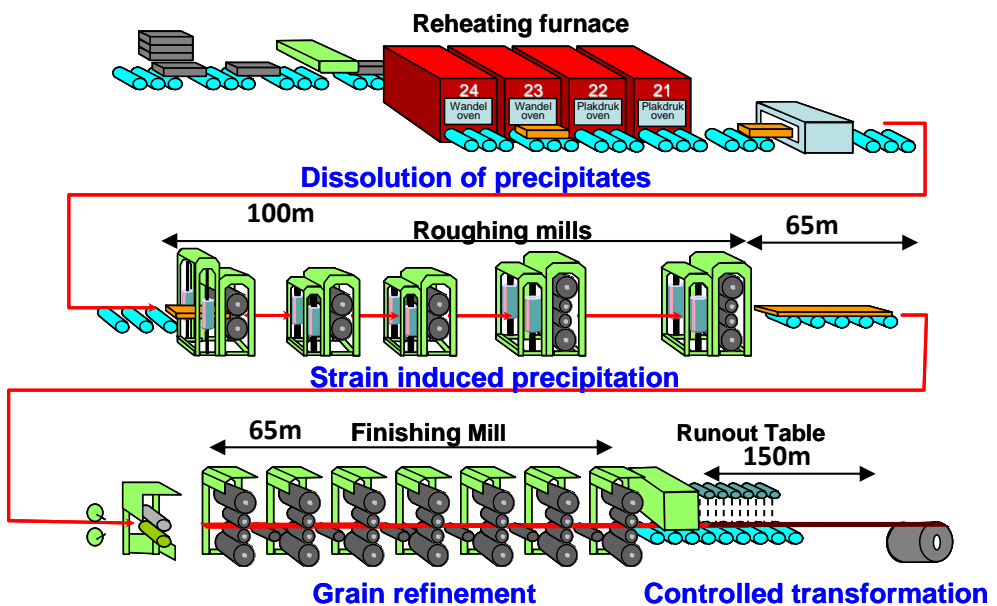


Figure 1-2. Schematic of Hot Rolling Mill 2 at IJmuiden. Strip width 2 m.

transformation process is currently carried out in Tata Steel IJmuiden R&D. A physical understanding of the work hardening process is now crucial in through process modelling of the evolution of the microstructure in the hot rolling process.

1.1.2 Theoretical issues

In addition to the aspiration of developing a physical model for the flow stress of steel at elevated temperatures that is to be used in computational simulations of the hot rolling process, there are equally important matters to be dealt with that are in the realm of physical understanding of the involved

mechanisms. It is the purpose of this study to address both: a viable flow stress model will be developed, while some issues of a more philosophical character, i.e. concerning the physical explanation of the expressions applied in the model, will be addressed.

1.2 Outline of the thesis

In Chapter 2 the literature pertaining to the dislocation theory of the flow stress of polycrystalline metals is reviewed. This is introduced by a qualitative overview of formulating constitutive equations. This is followed by a discussion on thermally activated dislocation glide, work hardening and dynamic strain ageing.

In Chapter 3 the experimental methods and techniques used in this study are discussed. The choice for executing tensile tests rather than compression testing is explained and the advantages/disadvantages of the Gleeble thermomechanical testing system discussed. Some techniques to remedy these disadvantages are introduced, followed by a discussion of some special test techniques (other than at constant strain rate and temperature) and post processing methods that are helpful as a diagnostic tool for determining the nature of the plastic flow process. The chapter is concluded with a section pertaining to instrumental issues like machine stiffness corrections and suppression of disturbances in the measured signals.

Chapter 4 is a theoretical exercise in which the relation between the onset of Portevin- le Châtelier instabilities (which are associated with dynamic strain ageing) and the strain rate sensitivity of the flow stress is discussed.

In Chapter 5 a physically based yield stress criterion based on Kocks-Mecking analysis of the flow stress is proposed. The pre-yield theory based on reversible dislocation glide that is developed in this chapter is further developed in chapter 6 by incorporation of the effects of grain size hardening, and dislocation glide resistance. The resulting yield stress theory is then fitted to a comprehensive set of tensile test results.

In Chapter 7 the work hardening behaviour, obtained by subtraction of the yield stress from the flow stress data, is first examined qualitatively. On the basis of the results from that analysis, a suitable work hardening equation is proposed and fitted to the experimental data. The last section contains a discussion of theoretical character, in which the alternative explanation of the Taylor relation between work hardening and dislocation density and the consistency between the interpretation of the yield stress and work hardening models are discussed. The chapter is concluded with the main conclusions and recommendations that have been found in this study.

References

- [1] Akanuma, H. (2008). The Significance of Early Bronze Age Iron Objects from Kaman-Kalehöyük, Turkey. *Anatolian Archaeological studies*. 313-200.
- [2] Verhoeven, J. D. and Peterson, D. T. (1992). What is a Damascus steel? *Materials characterization*, 1992, 29.4.: 335-341.

Chapter 2. Background: the Flow Stress of polycrystalline metals

Nothing is as practical as good theory.

Kurt Lewin

2.1 Introduction

The objective of this study is to formulate a constitutive model for the flow stress of Steel grades in the temperature range where it is in the austenitic state. This model will be applied as a sub-model in hot rolling models that aim to predict the influence of hot rolling parameters on the resulting microstructure.

In this chapter the theory of flow stress is reviewed. First the limits that define which mechanisms of plastic deformation of polycrystalline metals fall within the scope of this study are outlined. After having identified dislocation glide and multiplication as the mechanisms of interest, the choice for continuum mean field modelling rather than more detailed descriptions is substantiated. In the sections 2.2 to 2.4 the theories of plastic yielding and dislocation glide resistance are reviewed, followed by a critical review of the Bergström and Kocks-Mecking theories of work hardening and dynamic recovery.

2.1.1 Flow stress phenomenology

Before reviewing the physical theories of plastic flow and flow resistance, we will introduce the main basic phenomena.

Plastic deformation of crystalline solids is caused by propagation of crystal defects known as dislocations through the crystal lattice. After the passing of a dislocation, the crystal volume on one side of the plane in which the dislocation has propagated (the glide plane) is displaced by one lattice constant relative to the volume on the other side. Many dislocations must traverse the crystal to result in macroscopically significant amounts of deformation. Dislocations can therefore be regarded as the elementary carriers of plastic deformation.

Dislocation propagation is impeded by several kinds of obstacles that exert a stress on the dislocations which must be overcome by the externally applied stress. Some of these interactions between dislocations and obstacles are of long range character, i.e. they act over distances that are large in relation to the

dislocation size. The applied stress must be larger than the maximum long range stress to make dislocation propagation possible. The other class of obstacles are local obstacles, which have a stress field that acts over a short range. The short range stresses are superposed on the long range stresses (section 2.2). These local obstacles can be passed by thermal activation, i.e. occurring when the mechanical work that is needed to pass the obstacle can be provided by thermal fluctuations of the dislocation's energy. Since thermal activation involves a waiting time for passing the obstacle, the applied stress must be higher than the long range stress in order to make dislocation propagation possible such that deformation proceeds *at the desired strain rate*.

A common phenomenon of plastic deformation of metals is work hardening. This is caused by dislocation multiplication. The dislocations that are created in the multiplication process are initially mobile. After having propagated over some free path, they are eventually stored as immobile dislocations when they encounter an unsurpassable obstacle. During plastic deformation the immobile dislocations cause an increasing long range stress field. The stored immobile dislocations are associated with an increase in internal energy, which constitute a "driving force" for processes like recrystallisation, grain growth and transformation. They are stored in a substructure in the form of a tangled network after small plastic strain, which evolves into a cell like substructure for larger strains. This rearrangement of the stored dislocation substructure is influenced by diffusion processes, and that it thus causes work hardening to be dependent on strain rate and temperature as well as on strain. Work hardening must now be described by an evolution equation that predicts the dislocation density as a function of strain. This will be discussed in more detail in section 2.5.

Work hardening is of long range character and therefore inherently athermal, which means that it cannot be overcome by thermal activation, its strength is nevertheless is dependent on strain rate and temperature. This relationship is however based on strain rate and temperature *history* rather than on their instantaneous values. The work hardening contribution to the flow stress does therefore not vanish immediately at zero strain rate as the glide resistance does. It can only vanish due to static recovery, recrystallisation, grain growth and phase transformation.

The flow stress σ_f is thus seen to be the sum of a yield stress σ_y , a work hardening contribution $\sigma_w(\varepsilon, \dot{\varepsilon}, T)$ and a resistance due to thermally activated glide $\sigma^*(\dot{\varepsilon}, T)$. In the equivalent stress notation¹:

$$\sigma_f = \sigma_y + \sigma_w(\varepsilon, \dot{\varepsilon}, T) + \sigma^*(\dot{\varepsilon}, T), \quad (2.1)$$

where it is indicated that the work hardening contribution, which as discussed in itself has a long range character, is nevertheless dependent on strain rate $\dot{\varepsilon}$ and temperature T . This type of strain-rate/temperature behaviour is caused by the evolution of dislocation density. After an increase of strain rate, the effect on the work hardening contribution becomes noticeable only after an increment of strain. It is described by the evolution equation, not in the flow stress equation itself.

In contrast to this behaviour, the strain-rate/temperature influence that is caused by the effective stress is instantaneous: if the strain rate is increased, the stress must directly increase in order to accelerate the thermally activated passing of obstacles.

There exist therefore two types of strain rate sensitivities of the flow stress: a direct strain rate sensitivity (DSRS) Ψ_D

$$\Psi_d = \frac{d\sigma}{d\dot{\varepsilon}} \quad (2.2)$$

that pertains to thermally activated glide mechanism and an indirect strain rate sensitivity (ISRS) Ψ_I ,

$$\Psi_I = \frac{d}{d\dot{\varepsilon}} \left(\frac{d\sigma}{d\varepsilon} \right) \quad (2.3)$$

that pertains to the work hardening rate [1], [2]. Experimentally, these two strain rate sensitivities -and consequently the work hardening and effective stress- cannot be separated by performing deformation experiments at constant strain rate and temperature. They can be distinguished only by manipulation of the strain rate history. The most rigorous -and sensitive- method is imposing a constant strain rate followed by an instantaneous

¹ In this thesis, shear stress and strain notation will be used when discussing mechanisms on the dislocation scale, and equivalent stress and strain notation when formulating equations that are to be used in an experimental context.

increase or decrease of $\dot{\varepsilon}$: the strain rate jump test. In analogy to Ψ_D and Ψ_I , similar temperature sensitivities can be defined, but these are of little practical interest since it is virtually impossible to impose instantaneous temperature changes experimentally. The strain rate and temperature sensitivities are normally of positive respectively negative sign: higher temperature results in lower stress. Only in the special case where Dynamic Strain Ageing occurs, they may be of negative respectively positive sign. This will be discussed in Chapter 4.

It must be noted that all contributions to the flow stress are proportional to the elastic shear modulus G of the material, which is temperature dependent [3]. This is due to the fact that both long and short range interactions are transmitted by stress fields that cause elastic distortions of the crystal lattice. It is good practice to remove this trivial temperature influence from experimental data by scaling stress values with $\frac{G(T_0)}{G(T)}$, where T_0 is an arbitrary reference

temperature, in order to have a clearer view on temperature effects that pertain to dislocation glide and multiplication.

For steel in the temperature range where it is in the austenitic phase, we will use the following empirical equation [3]

$$G(T) = 92.648 \cdot \left[\begin{array}{l} 1 - 7.9921 \cdot 10^{-7} \text{K}^{-2} T^2 \\ + 3.3171 \cdot 10^{-10} \text{K}^{-3} T^3 \end{array} \right] \text{GPa}, \quad (2.4)$$

where T is expressed in Kelvin.

The modelling approach of formulating constitutive equations obviously strives to formulate models in the form of analytical functions. This style of modelling has been called continuum or mean field modelling, as some a priori averaging method is necessary. This averaging is often done tacitly, by formulating models in terms of e.g. average dislocation densities, segment lengths, screw or line character, of average grain sizes and so on. An important example is the a priori averaging over all glide systems, which is a common feature of most mean field hardening theories outside the field of crystal plasticity.

In the past two decades the methods of 3D discrete dislocation plasticity [4], [5], [6], phase field plasticity [7], [8] and molecular dynamics [9], [10] have been developed to a stage where the mechanisms of interest can in be simulated in detail. These methods do not however, yield analytical equations that describe bulk behaviour in the fashion of mean field continuum modelling. Analytical expressions on the basis of these methods can only be derived by a posteriori averaging of the results. Such an averaging procedure necessitates a

choice of an analytical expression to execute the averaging procedure, much like the situation when dealing with experimental data. Another class of models aims to describe the material behaviour at the mesoscale of e.g. the grain structure. Models in this class are for instance cellular automata and Finite Element Modelling Crystal Plasticity [4], [11], [12]. In these methods, the collective behaviour at a smaller scale than the mesoscale level is again modelled by continuum theories.

The important difference between these two approaches is that in mean field modelling the averaging is done a priori when formulating the model equations, and in discrete modelling averaging must be performed a posteriori. If it is now assumed that averaging and computation are commutative, the choice for mean field modelling -which we make here- simply implies that some variables like dislocation segment length and density have to be interpreted as being effective, a priori averaged parameters.

The choice for mean field continuum modelling that we have made also serves a practical goal: the model equations are to be implemented in a model suite that describes the evolution of microstructure in the hot rolling process. To achieve that by using data generated by 3D discrete dislocation plasticity, phase field and molecular dynamics will either throw us back in empiricism (albeit that we have total control over the experiment), or a mean field model must be used to perform the averaging. The challenge of mean field modelling lies in the formulation of concise mathematical formulations that nevertheless capture the collective behaviour of the complex interplay between -in the field of dislocation plasticity- dislocations and obstacles. 3D discrete dislocation plasticity, phase field and molecular dynamics can play an important role by corroborating the assumptions made in that process.

2.2 Mechanisms of plastic deformation

Plastic deformation is generally understood as an irreversible change of shape of a solid material in response to mechanical loading. In general this is accompanied by a change of state of the material. Macroscopic shape is not a physically acceptable state variable. Before discussing the constitutive models that describe plasticity as occurring in the target process -viz. hot rolling of steel- we must identify the relevant physical mechanisms and state variables.

A phenomenon that is typical for the case of plastic deformation of metals is that they appear to show a yield stress. This is commonly understood as a threshold stress below which no irreversible (plastic) deformation occurs. It is often assumed that reversible deformation below the yield stress is linear elastic deformation (in the sense of proportional to stress) of the crystal lattice. It is an established fact that the strain increments as a function of stress

increments below the yield stress are small relative to those above the yield stress. The yield stress is an important parameter since it defines a restriction to the stress range where constitutive models for irreversible plastic deformation can be applied. The mechanical behaviour of a deformable material can formally be described by a set of constitutive equations that consists of a rate equation that couples strain rate $\dot{\varepsilon}$ to stress σ , stress rate $\dot{\sigma}$ and temperature T and a number of evolution equations that describe the change of the state of the material as a function of time [13], [14], [15]. The response of the material to an external mechanical load depends on its state, which enters in the constitutive equations through a number of state variables $\mathbf{S}_i = \mathbf{S}_1, \mathbf{S}_2, \dots, \mathbf{S}_n$, which describe the microstructure.

A century after the pioneering work of Prandtl, developed further by Burgers, Taylor and many others [16], [17], it is an established fact that plastic deformation of mono- and polycrystalline metals is brought about by the propagation of line defects called dislocations. It is indeed the combination of a crystal structure, which is the cause of their strength, with the propensity to form dislocations, which cause formability, which is responsible for the unique place that metals have in engineering. In the field of constitutive modelling of plastic deformation of polycrystalline metal alloys, the obvious state variables are then grain size, dislocation density, dislocation segment length, solute atom density, etc. The evolution of these microstructural variables depends on physical parameters $\mathbf{C}_j = \mathbf{C}_1, \mathbf{C}_2, \dots, \mathbf{C}_m$ which are diffusion constants, activation energies, etc. This can be represented formally as

$$\begin{aligned}\dot{\varepsilon} &= f(\sigma, \dot{\sigma}, T, \mathbf{S}_i, \mathbf{C}_j) \\ \dot{\mathbf{S}}_i &= \mathbf{g}_i(\sigma, \dot{\sigma}, T, \mathbf{S}_i, \mathbf{C}_j) .\end{aligned}\tag{2.5}$$

Strictly speaking, the strain and stress tensor components should appear in these equations. We have chosen to use equivalent plastic strain ε and stress σ instead, which are defined in terms of the Euclidean norm of their associated tensors [18], [19], [20]:

$$\begin{aligned}\sigma &= \sqrt{\frac{3}{2} \mathbf{S}_{ij} \mathbf{S}_{ji}} \\ \varepsilon &= \sqrt{\frac{2}{3} \varepsilon_{ij} \varepsilon_{ji}},\end{aligned}\tag{2.6}$$

where $\mathbf{S}_{ij} = \sigma_{ij} - \frac{\sigma_{kk}}{3} \tilde{\mathbf{I}}$ is the deviatoric stress tensor with $\tilde{\mathbf{I}}$ the unit tensor.

Equivalent stress and strain are by definition positive definite variables. During deformation, equivalent strain is a monotonously non-decreasing function of time, which is an expression of the fact that the plastic deformation process is essentially irreversible. Since in this study we are interested in the response of the material and the evolution of the microstructural parameters during the deformation process, this has the advantage that the constitutive equations can be formulated with strain rather than time as an independent variable, as is customary in the dislocation theory of plastic deformation.

Equivalent stress and strain are concepts from the field of continuum mechanics. Since the constitutive equations that are subject of this study will be implemented in process models that are formulated according to that paradigm, they must eventually be formulated in terms of equivalent stress and strain.

Dislocation theory is however formulated in terms of shear strain γ that is caused by the propagation of dislocations under influence of shear stress τ that acts along the glide plane of those dislocations. The deformation of crystalline material is caused by dislocation glide on one or more glide systems. In a polycrystal, the glide systems of each crystallite are differently oriented. The reformulation of expressions from dislocation theory to continuum mechanics therefore requires an averaging over all orientations of the individual crystallites and the glide systems inside the crystallites. An elementary expression for the averaging of shear stress to equivalent stress developed in the field of crystal plasticity is [21]

$$\sigma = \bar{M}\tau, \quad (2.7)$$

where \bar{M} is the Taylor factor, which expresses the equivalent stress in terms of the directional average of the resolved shear stresses on all active glide systems and crystallite orientations. The corresponding equation for the relation between shear strain and equivalent strain is then found by application of the virtual work principle [22], which is formulated as

$$\tau d\gamma = \sigma d\varepsilon, \quad (2.8)$$

then follows the relation

$$\dot{\varepsilon} = \frac{1}{\bar{M}} \dot{\gamma}. \quad (2.9)$$

The constitutive rate equation (2.5) is written in the form of strain rate as a function of the stress rate, or stress and time. From a physical point of view, this is the correct description. Macroscopically however, it presumes a stress controlled process, like e.g. creep testing. Many -if not most- macroscopic

deformation processes are however strain controlled (e.g. tensile and compression testing, rolling processes etc.) and a formulation of stress as a function of strain is then more suitable from an engineering point of view. A more physical argument has been formulated by Kocks [23], [24]. His argument relates to the distinction between static and dynamic recovery. The former pertains to softening of work hardened material as a function of time for unloaded material and the latter to the decrease of hardening during deformation (hence *dynamic* recovery). He noted that static recovery does not produce a similar degree of softening as dynamic recovery during plastic deformation during an equal time interval, and consequently that strain is the more logical choice for the independent variable during deformation

2.2.1 Deformation mechanism maps

Frost and Ashby conceived the concept of deformation mechanism (DM) maps [25], [26] which, however simplified as in some aspects they are, can guide us to identify the physical processes that are relevant in industrial hot deformation processes. A typical DM Map is shown in Figure 2-1. It must be borne in mind that these deformation maps are calculated from simplified expressions that describe steady state flow, i.e. at constant flow stress. In other words work hardening and dynamic recovery are supposed to be balanced and mutually cancelled. This is an obvious disadvantage for the low-temperature plasticity region, where steady state flow does not occur in reality. At elevated temperatures, steady state does not occur before appreciable hardening has occurred.

They recognize five mechanisms of plastic flow of polycrystalline materials:

1. Elastic collapse at a stress equal to the ideal strength
2. Low-temperature plasticity by dislocation glide
3. Low-temperature plasticity by twinning
4. Power-law creep by dislocation glide, or glide-plus-climb
5. Diffusional flow

Of these, elastic collapse is an idealisation that pertains to defect-free crystals. It is of little importance to the study of materials commonly used in engineering. The other four mechanisms generally occur at a much lower stress than the ideal strength, and since the material of interest in this study is far from defect-free, elastic collapse can be ignored. Likewise, twinning can be

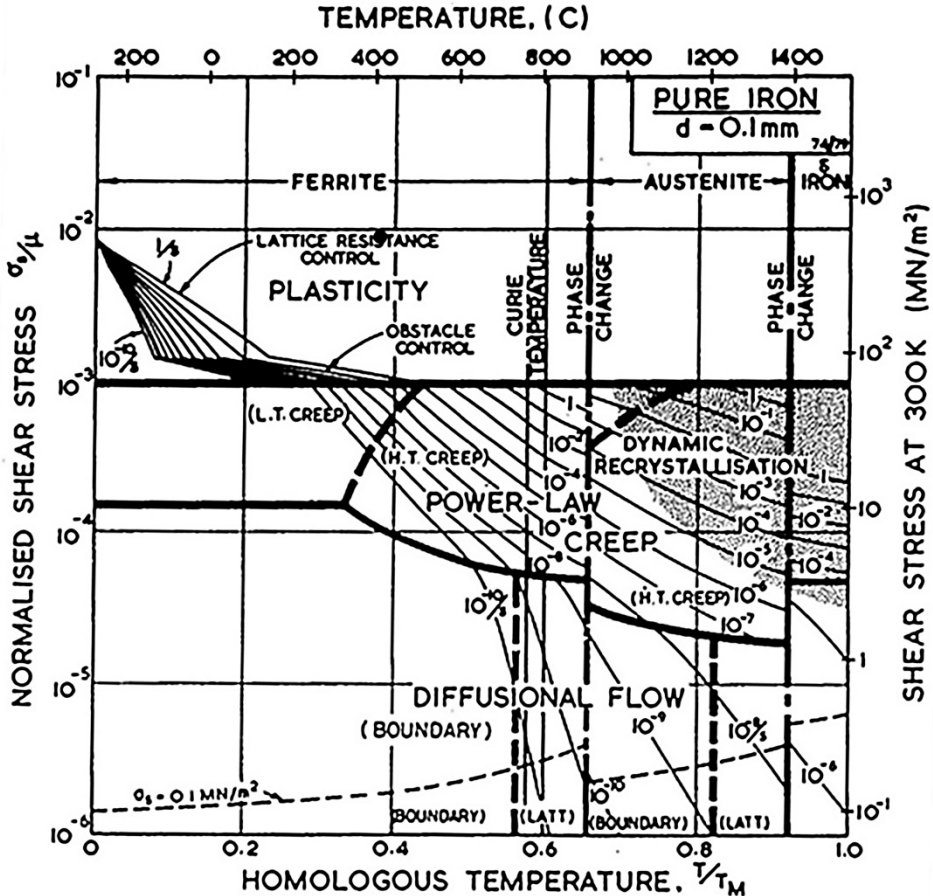


Figure 2-1. DM map for pure iron of grain size 100 μm [26].

ignored since it generally occurs at low stresses and low temperatures, and causes only a limited degree of deformation [25]. TWIP alloys are an exception to this rule, but the TWIP mechanism falls outside the scope of this study. Diffusional creep, which may be bulk/lattice diffusion or grain boundary diffusion, occurs only at very low strain rates even at high temperature, and is therefore of no interest in the context of the hot rolling process. The remaining

two mechanisms are both dependent on dislocation glide. The plastic deformation mechanism of polycrystalline materials at strain rates and temperatures that are relevant for industrial manufacturing processes therefore occurs almost exclusively by dislocation glide, as is widely recognized in literature [13].

Plastic deformation of crystalline solids is caused by propagation of crystal defects known as dislocations through the crystal lattice. Many dislocations must traverse the crystal to result in macroscopically significant deformation. Dislocations can therefore be regarded as the elementary carriers of plastic deformation, and physical models of plastic deformation must involve some kind of a priori /posteriori averaging over the individual glide events.

The flow stress can be interpreted as the stress that is required to make dislocations propagate through the material at a sufficient velocity to attain the externally imposed strain rate. It is generally accepted that the resistance that mobile dislocations are subjected to is the sum of long and short range internal stress fields according to a simple superposition principle [13], [23], [27], [28], [29], [30], [31]. The terminology long respectively short range literally pertains to the extensiveness of the stress fields relative to the size of the dislocation's core which is of the order of the lattice constant. A more practical distinction can be made by the quality of the obstacle with respect to the question whether it can be passed by thermal activation or only by raising the applied stress to a level larger than the strength of the stress field. Thermally activated passing of an obstacle that exerts a stress larger than the applied stress on the dislocation is possible if the thermal fluctuations of the dislocation segment's energy are large enough to provide the mechanical work that is involved. This will be discussed in detail in section 2.4. In the deformation mechanism map shown in Figure 2-1, thermally activated passing is labelled as "obstacle controlled". Note that it is absent in the austenitic temperature range according to the DM map. In chapter 5 and 6 we will however find that it is far from negligible for that condition.

2.2.2 Long and short range stress fields

In Figure 2-2 a stress field $\tau(x)$ that is a superposition of an internal stress that is independent of position, a stress field that varies slowly as a function of position and the field due to a number of localized obstacles is schematically visualized as a function of position x in the crystal. These stress fields can be respectively categorized as long range, medium range and short range.

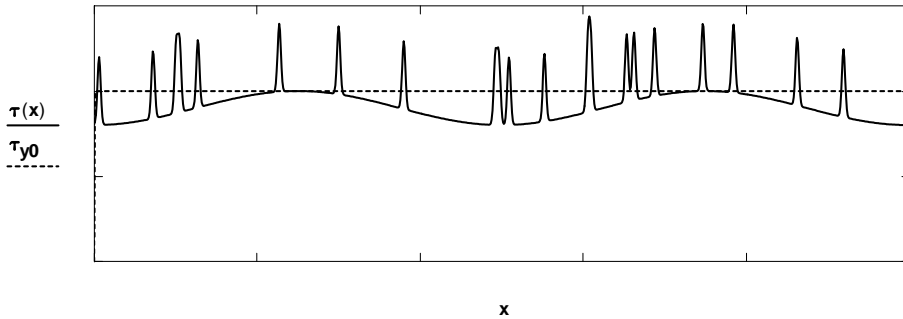


Figure 2-2. Superposition of long and short range stress fields (schematic).

Stress fields of different range can be caused by several types of microstructural elements, viz. grain boundaries, other dislocations, precipitates and solute atoms. Grain boundary stress fields are exceptionally pervasive, since they are the result of the collective of grain boundaries and act over distances that are large compared to the glide paths of dislocations which are restricted to propagate within the individual grains at maximum. In the Hall-Petch theory presented in Chapter 6, grain boundary stresses are considered as constant over the dislocation glide path.

Stress fields of intermediate range are commonly associated with the cell walls of the dislocation cell-like substructure that forms by the storage of immobile dislocations during plastic deformation [32], [33], [34]. That interpretation presumes that the dislocation walls defining the substructure are always of low angle grain boundary character. There is no consensus on this matter: other authors advance the idea that the structure of the dislocation walls is such that there is “...mutual stress screening among near neighbour dislocations” [35], according to which point of view the stress fields caused by the dislocation substructure are small. This issue is of primary importance in the scope of this study, since it pertains to the relation between the density of (stored) dislocations and the associated work hardening (i.e. the long range stress due to stored dislocations that has to be overcome by the externally applied stress). We will return to this issue in section 7.4.

As noted above, a stress field caused by a microstructural feature can be considered as short range if the stresses exerted by the obstacle on an approaching dislocation are sufficiently localized for thermally activated passing of the obstacle by the dislocation to be possible. More precisely, the energy needed to overcome such obstacles must be small enough to be provided by thermal fluctuations of the energy of the atoms in the dislocation segment that is involved in passing the obstacle.

A long range stress field can only be overcome if the applied stress exceeds the critical value of the internal stress associated with that field [13]. Below this threshold, dislocations will not propagate over appreciable distances. The long range stress fields can thus be interpreted as associated with a stress threshold τ_{y0} , that has to be overcome by the applied stress to make macroscopic plastic deformation possible, albeit at infinitesimally low deformation rates. This threshold τ_{y0} can therefore be interpreted as the proper yield stress. In Figure 2-2 this threshold is shown as a dotted line. For applied stresses higher than τ_{y0} the dislocations will propagate over large distances at a velocity which is determined by the “effective” stress $\tau^* = \tau_f - \tau_{y0}$, where τ_f is the flow stress (applied stress) at a finite strain rate. τ^* is then the portion of the applied stress that is in equilibrium with the sum of

1. the resistance due to the localized stress fields
2. the resistance due to drag mechanisms between the dislocations and the crystal lattice.

For maintaining a finite strain rate therefore application of an external stress larger than τ_{y0} is necessary. A more practical definition of the yield stress is therefore obtained by taking it equal to the flow stress at zero strain and a finite strain rate.

Note that this interpretation of the yield stress allows a degree of local, contained plastic deformation at stresses below the yield stress (within the “valleys” of the long range stress field), and that it is interpreted as athermal, i.e. independent of strain rate and temperature.

During plastic deformation mobile dislocations will propagate at a velocity that is dependent on the effective stress and temperature. For deformation at an imposed strain rate, the effective stress is therefore dependent on strain rate and temperature. A more descriptive name for the effective stress is “resistance associated with thermally activated dislocation glide”. In the literature it is often referred to as “thermal stress” (which is a confusing nomenclature since in engineering this pertains to stresses caused by temperature gradients). Thermally activated dislocation glide will be discussed in more detail in section 2.4.

2.3 The yield stress and pre-yield phenomena

Strictly speaking, any internal stress field that fluctuates as a function of position can be passed by thermal activation at temperatures above absolute

zero temperature, even if the degree of localization of those stress fields is small, e.g. long range stress fields that vary in strength over distances that are large with respect to the dislocation size. Frost and Ashby [26] express this as *“Although it is often convenient to think of a polycrystalline solid as having a well-defined yield strength, below which it does not flow and above which flow is rapid, this is true only at absolute zero”*. Nevertheless, a large portion of a typical deformation mechanism map shows virtually zero strain rates, and an even larger area where the strain rate is negligibly low with respect to the target process. Some authors label that region as elastic [36], as Ashby did in his original publication [25]. In [13], the yield stress at absolute zero temperature is called the mechanical threshold, above which no equilibrium of a dislocation’s position is possible at $T=0$, but below which thermally activated glide is possible at higher temperatures. The problem is that Frost and Ashby’s strict definition of yield only recognizes thermally activated mechanisms, some of which are infinitesimally slow at low stresses and which hardly contribute to the large degree of deformation that we are interested in. The fundamental point of critique is that they assume that no athermal contributions to the yield stress exist, which is contradicted by the existence of a grain size (Hall-Petch) contribution to the yield stress. The Hall-Petch effect cannot be interpreted otherwise than being athermal, since its cause is purely geometrical. The definition of the yield stress given in section 2.2.2 better suits our purpose, since it has the advantage that it discriminates between mechanisms that cause storage of dislocations with the associated increase of long range stress fields and mechanisms that do not. In practice, it also separates mechanisms that are only of interest during long service periods of constructive elements at severe circumstances, e.g. creep, from those that pertain to fast plastic deformation processes.

2.3.1 Pre-yield phenomena

The existence of a threshold yield stress below which no plastic deformation occurs does not imply that below the yield stress the material behaviour is purely elastic in the sense of linear elasticity of the crystal lattice. Non-linearly elastic reversible strains are frequently observed below the yield stress. The term anelasticity was introduced by Zener [37] to denote non-linear reversible deformation effects below the yield stress. One particular mechanism is the reversible bowing out of initially present dislocation segments under a stress smaller than the yield stress [38], [39]. Dislocation anelasticity causes a decrease of the pre-yield modulus since the shear produced by dislocation glide is additional to the elastic shear of the crystal lattice. The original authors of this theory [40], [41], [42], derived expressions for the degradation of the pre-yield modulus at zero stress only, in which it is tacitly assumed that the

dislocation segments in case are elements of a uniform dislocation network. In Chapter 6 an expression that is valid up to the yield stress will be derived. The pre-existing dislocation segments that are the cause of this effect are potential Frank-Read (FR) sources [43] that cause dislocation multiplication once the yield stress is exceeded.

The FR mechanism, which is the mechanism of dislocation multiplication as well as of pre-yield anelastic strain, is depicted schematically in Figure 2-3. Consider a dislocation segment BC that bows out under the action of the resolved shear stress τ in its glide plane. The end points B and C of the segment are defined by the pinning by other crystal defects, like solute atoms, precipitates or other dislocations. Another possibility is that the segment is part of a prismatic dislocation loop. Let the applied shear stress increase from zero. The segment will then bow out to a curvature $\frac{1}{r}$ for which the segment's line stress is in

equilibrium with τ . The line stress of the segment is given by

$$\tau_{line} = \frac{Gb}{2r}, \tag{2.10}$$

where b is the magnitude of the Burgers vector and G the elastic shear modulus of the crystal lattice.

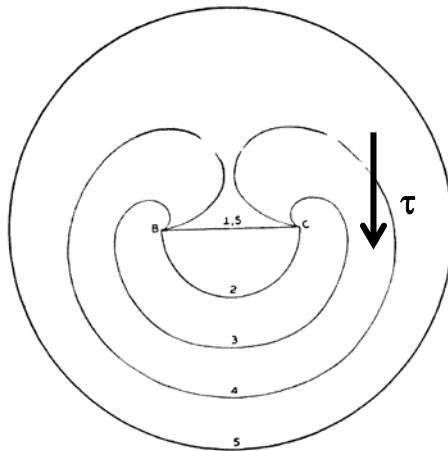


Figure 2-3. The Frank-Read mechanism [43]. The sequence of configurations labelled 1...5 is explained in the text.

Up to configuration 2 in Figure 2-3. **The Frank-Read mechanism [43]**. the process is reversible, as the dislocation will relax to its initial configuration under the action of its line stress if the applied stress is removed. The local glide that the crystal has undergone in the area bound by B, C and the stressed dislocation segment (configuration 2), is then undone. This is the basic mechanism of dislocation anelasticity, which is to be identified as reversible dislocation glide. The reversible shear due to the dislocation's glide over the area between configuration 1 and 2 in Figure 2-3 is large compared to the elastic shear of the crystal lattice. It will effectively resolve the pre-yield stiffness of the material. This is the topic of Chapter 5 and 6.

If the stress is now increased above the line stress in configuration 2, the curvature of the dislocation must decrease, and the line stress of the dislocation will become lower than the applied stress. The equilibrium between the applied stress and the line stress is then lost, and the segment bows out in an unstable manner. The dislocation then bows around the original position of the segment (configuration 3 and 4) where both branches re-join and split into a copy of the original segment and an expanding loop.

The line stress at the instant of incipient instability is the critical Frank-Read shear stress τ_{FR} , which is given by

$$\tau_{FR} = \frac{Gb}{L}, \quad (2.11)$$

where L is the length of the segment (the distance B-C in Figure 2-3). If no other resistance to the motion (bowing out) of the dislocation would exist, τ_{FR} would be the yield stress, since it indicates the onset of irreversible dislocation propagation. In reality, there do however exist additional resistances, like the resistance due to thermally activated dislocation glide and the Hall-Petch stress.

Note that the contribution described by eq. (2.11) to the yield stress is athermal. This is a second argument against Frost and Ashby's characterisation of the yield stress being exclusively due to thermally activated mechanisms.

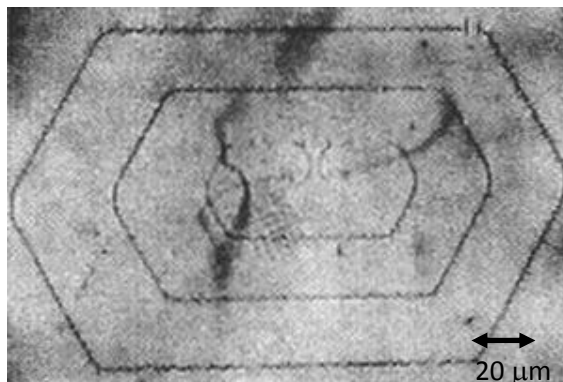


Figure 2-4. A Frank-Read source in Si [44].

When the stress is increased above τ_{FR} the dislocation bows out further to configuration 3. Since the end points B and C are pinned, it must curve backwards around the pinning points. When it has reached configuration 4, two branches of screw character and opposite sign meet, and the contacting part is annihilated. In configuration 5 the dislocation has dissociated into a loop which expands in an unstable manner and a segment between the pinning points. The latter is a recovered copy of the original segment (configuration 1 = configuration 5), and therefore as long as the applied resolved shear stress is larger than the critical stress for reaching the unstable configuration 2, this process will repeat itself. The loop will expand since its line stress decreases further below τ_{FR} and will eventually be immobilized by impenetrable obstacles.

The critical Frank-Read stress (eq. (2.11)) is therefore the actual yield stress, since it is the external stress above which irreversible dislocation multiplication and propagation occurs. A classic physical example of the FR multiplication process is shown in Figure 2-4. Recently the multiplication process has been recorded by in situ TEM video technique by Louchet [45]².

Note that the contribution described by eq. (2.11) to the yield stress is athermal. This is a second argument against Frost and Ashby's characterisation of the yield stress being exclusively due to thermally activated mechanisms.

This elementary theory of the yield stress recognises the dislocation structure only. It does not quantitatively explain the influences of grain size, strain rate, solute and precipitation hardening on the observed yield stress. It is one of the objectives of this study to develop a comprehensive model that incorporates these effects, which is developed in Chapters 5 and 6.

² A visit to his website is highly recommended

The Frank-Read mechanism is now seen to be associated with pre-yield anelastic strain, which is a natural precursor of yield. The magnitude of the dislocation anelasticity effect is dependent on the density and distribution of segment lengths of the initially present dislocation segments. Since the crystal structure deforms elastically under stress, the pre-yield strain ε^{PY} is the sum of crystal elasticity and dislocation anelasticity

$$\varepsilon^{PY} = \frac{\sigma}{E} + \varepsilon^{AE}, \quad (2.12)$$

where E is Young's modulus, $\sigma \leq \sigma_y$ the applied stress with σ_y the yield stress and ε^{AE} the dislocation anelastic strain which is a non-linear function of stress. An expression for ε^{AE} will be developed in Chapter 6.

From eqn. (2.12), the apparent pre-yield modulus is

$$\Theta_{PY} = \left(\frac{d\varepsilon^{PY}}{d\sigma} \right)^{-1} = \frac{E\Theta_{AE}}{E + \Theta_{AE}}, \quad (2.13)$$

$$\text{where } \Theta_{AE} = \left(\frac{d\varepsilon^{AE}}{d\sigma} \right)^{-1}$$

The apparent -or technical- elastic modulus as measured in a tensile test can therefore be appreciably lower than the value of Young's modulus of the crystal lattice. For steel at temperatures below $T=300-500$ °C, the dislocations are pinned by C atoms. The stiffness Θ_{AE} pertaining to dislocation anelasticity then becomes very large and the apparent pre yield stiffness approaches theoretical value of E [46]. At higher temperatures, anelastic pre-yield phenomena can be expected to occur. The initially present dislocations that are responsible for the pre yield deformation must be subject to a resistance due to thermally activated glide. This is the reason why the elastic moduli of the crystal lattice must be determined by high frequency acoustic techniques [47], rather than by a macroscopic deformation process like a tensile test. In chapter 5 of this thesis a model for anelasticity due to reversible dislocation glide will be developed.

Plastic yield will occur when the "softest members" of the initial dislocation distribution, i.e. those that have the longest segment length, will become unstable and emit dislocation loops according to the Frank-Read mechanism. The yield stress is thus the applied stress for which the resolved shear stress in the glide plane of the longest segments exceeds the critical Frank-Read stress τ_{FR} (eq. (2.11)).

It is a well-known fact that the yield stress is also dependent on the grain size. This was first recognized by Hall and Petch [48], [49], who found that the yield (and fracture) stress are in part proportional to the inverse of the square root of the grain size:

$$\sigma_y = \sigma_0 + K_y \frac{1}{\sqrt{D}} \quad (2.14)$$

where D is the grain size, K_y the Hall-Petch coefficient and σ_0 the limiting yield stress for $D \rightarrow \infty$. A number of models have been proposed to explain this behaviour [50], [51], [52], [53], [54], [55], [56], none of which address the problem that the yield stress is dependent on both the grain size and the size of the Frank-Read sources. This is the subject of Chapter 6, where a model is proposed that is a synthesis of the Frank-Read mechanism and dislocation anelasticity with a mechanism of generation of long range stresses by grain boundaries. This model forms a viable explanation of the Hall-Petch relation.

The stress at which dislocation propagation after prior plastic deformation and work hardening is resumed can also be called a yield stress. In order to avoid confusion with the yield stress of the undeformed material we will adopt the term deformation resistance τ_d (or σ_f) [13], [38], [15] for the yield stress after (or during) prior work hardening.

2.4 Resistance due to thermally activated dislocation glide

When the long range stresses -i.e. the yield stress- have been exceeded by the applied stress, the relation between dislocation velocity v_m , shear strain rate $\dot{\gamma}$ and density of mobile dislocations ρ_m is expressed by the Orowan equation [57]:

$$\dot{\gamma} = \rho_m b v_m \quad (2.15)$$

The velocity of the mobile dislocations is controlled by dislocation glide resistance mechanisms. Possible mechanisms are resistance caused by the crystal lattice or by discrete localized obstacles.

The fundamentals of resistance due to thermally activated dislocation glide can be understood by an elementary one-dimensional representation of the process [58] as shown in Figure 2-5. Consider a dislocation segment that propagates through the crystal under the influence of an applied shear stress τ_f , which exceeds the deformation resistance τ_d . The difference $\tau^* = \tau_f - \tau_d$

is commonly called the effective stress since this is the stress responsible for the velocity of the dislocations. Consider a back stress $\tau_o(X)$ exerted by some discrete obstacle at position x_{obs} that is superposed on the long range internal stress τ_d , as depicted in Figure 2-5. The dislocation will come to rest at a stable equilibrium position x_s that is dependent on τ^* .

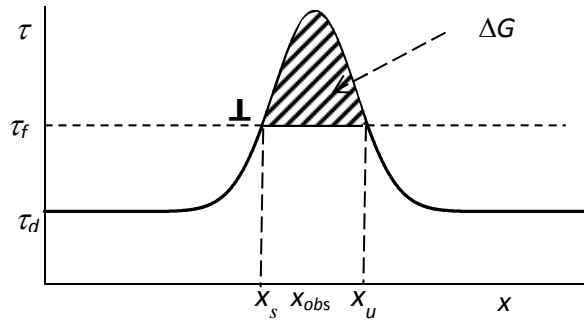


Figure 2-5. Thermally activated passing of a local obstacle. Resistive stress as a function of the position of the dislocation. Solid line: local resistance $\tau_d + \tau_o$, the dashed region is the Gibbs free energy ΔG .

The local stress barrier can be overcome by thermal fluctuations in the energy of the atoms in the vicinity of the dislocation. The Gibbs free energy ΔG is given by [59]

$$\Delta G = bl_a \int_{x_s}^{x_u} (\tau - \tau_d) dx - bl_a (x_u - x_s) (\tau - \tau_d), \quad (2.16)$$

where l_a is the length of the dislocation segment involved in passing the obstacle and x_u the unstable activated equilibrium position (see Figure 2-5). The first term at the right hand side is the change in free energy during passing of the obstacle, the second is the work done by the applied stress during the activation event [59].

After a successful activation event the dislocation moves toward the next local obstacle at a velocity dependent on the resistance mechanism caused by the interaction between the dislocation and the crystal lattice. The resistance mechanisms due to the lattice are due to phonon drag. In the case where the

average dislocation velocity is obstacle controlled, the velocity of a dislocation between obstacles is much higher than the average velocity. The dislocations then move in a jerky fashion [13] and their average velocity is governed by the waiting time for thermal activation at localized obstacles.

Since the positions x_s and x_u are functions of the effective stress τ^* , this is also the case for the activation energy ΔG .

The obstacle will be overcome after a waiting time t_w has passed which is the product of the inverse of an attempt frequency ν_a and the rate of success given by the Boltzmann factor that gives the probability of an energy fluctuation of amount $\Delta G(\tau^*)$

$$t_w = \frac{1}{\nu_a} \exp\left(\frac{\Delta G}{k_b T}\right), \quad (2.17)$$

where k_b is Boltzmann's constant and T the temperature. The attempt frequency is associated with the thermal lattice vibrations that occur for $T > 0$ K. At temperatures above the Debye temperature Θ_D all possible vibrational states are occupied, the shortest phonon wavelength is then equal to the lattice constant. The vibration of a dislocation can be described as that of a vibrating string [60], [61], the ground frequency ν_l of which is given by

$$\nu_l = \frac{\nu_D b}{l_a}, \quad (2.18)$$

where ν_D is the Debye frequency. The attempt frequency is often given as $\frac{\nu_D b}{2l_a}$

[62], where it is assumed that the obstacle to be passed lies midway between the pinning points [63]. A dislocation vibrates with a spectrum of simultaneous harmonic modes having frequencies between the ground frequency (eq. (2.18)) and ν_D . For a dislocation passing the obstacle, it is sufficient that a sub segment that has a length of the order of the size of the local stress field performs the passing event.

The relevant attempt frequency then pertains to a wavelength λ_a which is of the order of the size $X_u - X_s$ of the local stress field of the obstacle that is being passed [64]:

$$\nu_a = \frac{\nu_D b}{\lambda_a} \quad (2.19)$$

For steel in the austenitic phase, $v_D = 2 \times 10^{12} \text{ s}^{-1}$ [65] and $\Theta_D = 335 \text{ K}$ [66], and consequently we can assume v_a to be a material constant in the temperature regime of interest. After passing an obstacle, the dislocation glides over an area A until it is stopped by the next local obstacle, producing a shear increment $\Delta\gamma$ that is equal to $\Delta\gamma = bA$. The area A depends on the dislocation segment length and the spatial distribution of the obstacles.

The number of dislocation segments per unit volume N_m that are simultaneously operative is given by

$$N_m = \frac{\rho_m}{l}, \quad (2.20)$$

where ρ_m is the density of mobile dislocations. Combining eqs. (2.17)..(2.20), the macroscopic shear rate of the population of mobile dislocations is now

$$\dot{\gamma} = \frac{\rho_m}{l} bA \frac{v_D b}{\lambda_a} \exp\left[-\frac{\Delta G}{k_b T}\right]. \quad (2.21)$$

The final step is now to formulate the relation between ΔG and τ^* . This function is specific for different types of obstacles. These can for instance be forest dislocations, solute atoms and small shearable precipitates which are fixed obstacles to the dislocations, jogs and the Peierls mechanism [67], [68], [69]. The latter two are obstacles associated with the dislocation itself (or rather its interaction with the crystal lattice). $\Delta G(\tau^*)$ should therefore in principle be formulated as a sum of different mechanisms. Such an approach is however not suitable in an experimental context like here, where the aim is to develop a practical model of flow stress as a function of strain, strain rate and temperature, and not to study the fundamentals of each contributing mechanism. For that reason the following semi-empirical relation –“ empirical” in the sense that the interaction between dislocation and obstacles is described phenomenologically, “semi ” because it is formulated in accord with the physical theory of thermally activated processes- is often used [13],[70], [71], [72]

$$\Delta G = \Delta G_0 \left[1 - \left(\frac{\tau^*}{\tau_0^*} \right)^p \right]^q, \quad (2.22)$$

where ΔG_0 is the activation energy at $T=0$ and τ_0^* the maximal strength of (resistance due to) the obstacle. The parameters p ($0 < p \leq 1$) and q

($1 \leq q \leq 2$) are phenomenological parameters that define the shape of the $\tau^*(x)$ profile of the obstacle. Solving eq. (2.22) for τ^* yields:

$$\tau^* = \tau_0^* \left[1 - \left(\frac{\Delta G}{\Delta G_0} \right)^{1/q} \right]^{1/p}. \quad (2.23)$$

From eq. (2.21) the activation energy ΔG can be written as

$$\Delta G(\dot{\gamma}) = -k_b T \ln \left(\frac{\dot{\gamma}}{\dot{\gamma}_0} \right), \quad (2.24)$$

where $\dot{\gamma}_0 = \frac{\rho_m}{l} b A \frac{v_D}{\lambda_a}$. Substituting eq. (2.24) in eq. (2.23) yields

$$\tau^* = \tau_0^* \Delta G \left[1 + \left(\frac{k_b T}{\Delta G_0} \ln \left[\frac{\dot{\gamma}}{\dot{\gamma}_0} \right] \right)^{1/q} \right]^{1/p}. \quad (2.25)$$

Equation (2.25) has been formulated in terms of a shear strain and shear stress in the glide plane of a dislocation. It can be converted to the experimentally more practical variables equivalent stress σ^* and equivalent strain rate $\dot{\epsilon}$ by using the relations eq. (2.7) and (2.9), resulting in

$$\sigma^* = \sigma_0^* \left[1 + \left(\frac{k_b T}{\Delta G_0} \ln \left[\frac{\dot{\epsilon}}{\dot{\epsilon}_0} \right] \right)^{1/q} \right]^{1/p}, \quad (2.26)$$

where $\dot{\epsilon}_0 = \frac{1}{M} \frac{\rho_m}{l} b A \frac{v_D}{\lambda_a}$.

Note that by the definition in eq. (2.24), ΔG can be regarded as a strain rate-compensated temperature, a term often used for the Zener-Hollomon parameter Z [73], and $\dot{\epsilon}_0$ as its scaling parameter. If a single value of $\dot{\epsilon}_0$ scales all $\sigma^*(\dot{\epsilon}, T)$ data to a single valued function $\sigma^*(\Delta G)$ for the complete range of stresses (which must be made as large as possible by choosing a wide $\dot{\epsilon}, T$ window), it may be concluded that a single mechanism is dominant. This scaling method is employed in Chapter 6 section 6.3.2. figs, 6.5 and 6.6.

Of the possible mechanisms associated with thermally activated dislocation glide, the Peierls mechanism is special in that it is localized, but the position along the dislocation segment where it occurs is not predetermined. This is due to the fact that the Peierls activation energy is the formation energy of a kink pair [74], [1] in the dislocation segment, which occurs at a random position along the dislocation segment. A Peierls barrier must be overcome every time the dislocation propagates to the next crystal plane. The Peierls glide resistance therefore has the quality of a crystallographic drag resistance: it causes jerky glide, but over very small displacement increments. The sheared area for a dislocation segment of length l between activation events is then $A=la$ (where a is the lattice constant), which is relatively small. The Peierls energy of FCC materials is also rather small ($\Delta G = 0.2 \text{ eV}$) [72], and the glide resistance due to this effect is expected to be negligible, even at room temperature.

Resistance associated with thermally activated passing of local obstacles is often ignored in constitutive models for deformation at high temperatures, with some exceptions [70], [71], [72]. This is probably due to the notion of an athermal limit, i.e. the temperature where thermally activated glide ceases to give an appreciable contribution to the flow stress (for a given strain rate) [75]. In Chapter 6 we will find that the resistance due to thermally activated glide is far from negligible in the austenitic temperature region.

2.5 Work hardening

Since Ludwik [76] published the first equation for the description of hardening due to cold work as a function of strain, a plethora of empirical stress-strain equations have been proposed, some of which include dependencies on strain rate and temperature [27]. Modelling of work hardening on a physical basis has become possible after it was found that the structures that are responsible for plastic deformation are dislocations by Dehlinger [77], Orowan, Polanyi and Taylor [78] and Burgers [79]. A formulation that describes work hardening σ_w as a function of dislocation density ρ was proposed by Taylor [80]:

$$\sigma_w = \alpha \bar{M} G b \sqrt{\rho} . \quad (2.27)$$

Taylor derived this equation for the case of regularly distributed, infinitely long, straight and parallel edge dislocations on the same glide plane. The proportionality constant α denotes an average over the actual distribution of dislocations which are not straight, of infinite length, have different orientations and directions and are of mixed screw/edge character and have

different glide planes. The averaging over glide systems is taken care of in eq. (2.27) by the Taylor factor \bar{M} .

Extensive experimental research on the relation between dislocation density and flow stress [81], [82], has shown that eq. (2.27) is not very sensitive to the spatial distribution of the dislocations [24]. As noted before in section 2.2.2, the explanation of the resistance to the propagation of mobile dislocations by immobile dislocations is subject to debate. It is one of the more theoretical objectives of this study to comment on this further.

Since work hardening obviously is a function of strain, an evolution equation for the dislocation density must be formulated. In eq. (2.1) it is anticipated that work hardening is also dependent on strain rate and temperature.

The mobile dislocations that are created by e.g. the Frank-Read mechanism can be annihilated e.g. at the grain boundaries or due to interactions between dislocations of opposite sign. Alternatively, they can be immobilized or stored by encountering insurmountable obstacles, or by forming intangible structures with other dislocations, which is called immobilisation. Bergström [83] has introduced the possibility of remobilisation of stored dislocations. The work hardening rate ("rate" to be understood as pertaining to strain rather than time), and therefore the net dislocation storage rate are decreasing functions of strain, the explanation of which must be sought in the change of the balance between creation-immobilisation-annihilation/immobilisation rates.

The net dislocation storage rate $\frac{d\rho}{d\varepsilon}$, which is the increment $d\rho$ of dislocation density that remains in the system per increment $d\varepsilon$ of strain, is the difference between the creation rate $\frac{d\rho^+}{d\varepsilon}$ and the annihilation/remobilisation rate

$$\frac{d\rho}{d\varepsilon} = \frac{d\rho^+}{d\varepsilon} - \frac{d\rho^-}{d\varepsilon} \quad (2.28)$$

which is the starting point of most work hardening theories. The hardening rate

$$\theta = \frac{d\sigma}{d\varepsilon} = \frac{d\sigma_w}{d\varepsilon} \quad (2.29)$$

is related to the dislocation storage rate eq. (2.28) by eq. (2.27).

The property that the hardening rate decreases as a function of strain implies that either $\frac{d\rho^+}{d\varepsilon}$ must be a decreasing function of strain, and/or $\frac{d\rho^-}{d\varepsilon}$ must be an increasing function of strain.

Alternatively, the rates $\frac{d\rho^+}{d\varepsilon}$ and $\frac{d\rho^-}{d\varepsilon}$ are often interpreted as dislocation storage and –dynamic- recovery rates rather than creation and annihilation rates. We will return to this issue in the section on Kocks-Mecking and Bergström theories.

From TEM studies on plastically deformed single and polycrystals it is known, that dislocations are stored in the form of a dislocation microstructure of immobile dislocations. At strains larger than a few percent the spatial distribution of these dislocations is a cellular network of dislocations, consisting of walls having a high dislocation density with virtually empty interiors, an example of which is shown in Figure 2-6.

Staker and Holt [84] found that the dislocation cell size d_c is proportional to the average dislocation spacing $\frac{1}{\sqrt{\rho}}$ according to

$$d_c = \frac{K_{sh}}{\sqrt{\rho}}, \quad (2.30)$$

where $K_{SH} \approx 10-15$ is a proportionality constant. Holt [85] theoretically rationalized this equation by modelling the decomposition of a uniform one-dimensional array of dislocations in analogy to spinodal decomposition.

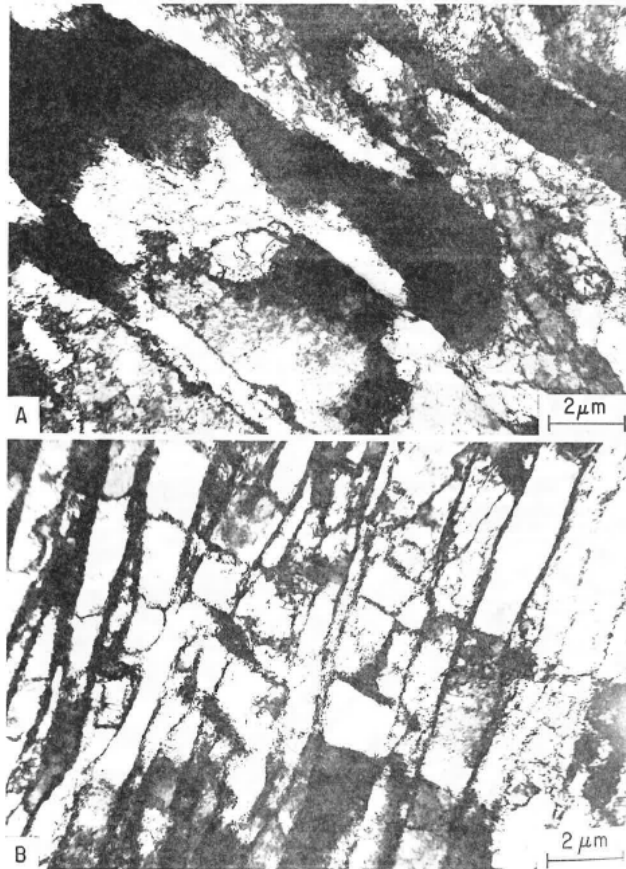


Figure 2-6. Dislocation substructure after wire drawing to $\varepsilon = 0.2$ at room temperature. A: transverse, B: longitudinal cross section [86].

Staker and Holt showed that this relation holds over two decades of dislocation density, which according to eq. (2.27) is equivalent with one decade of stress. This work also showed that there is a strong tendency for the formation of dislocation cells at high temperatures for Cu, which, like steel in the austenitic phase, has a low stacking fault energy.

2.5.1 The Bergström model

Bergström developed his work hardening model [83] on the basis of a balance equation of dislocation creation, immobilisation and annihilation rates. Bergström considered in his model development that the total dislocation

density ρ is the sum of the density of mobile dislocations ρ_m and the density of immobile dislocations ρ_i . He assumed that the density of mobile dislocations is constant, arguing that the resistance due to thermally activated dislocation glide -which depends on the density of mobile dislocations by eq. (2.26)- is virtually independent of strain. This will be shown to be a reasonable assumption in section 7.1.1. Bergström further introduced the concept of remobilisation, which is conceived as the release of immobile dislocations from the immobile dislocation substructure, enabling them to become mobile.

After it has become possible to observe dislocation motion in real time by in-situ TEM techniques [87], some video footage of dislocation multiplication and other mechanisms has become accessible. An example of dislocation immobilisation and remobilisation in Ge is shown in Figure 2-7, which shows two stills from a clip where incoming mobile dislocations (A) can be seen to be immobilized (B) at the tail of an immobile pile-up (C).

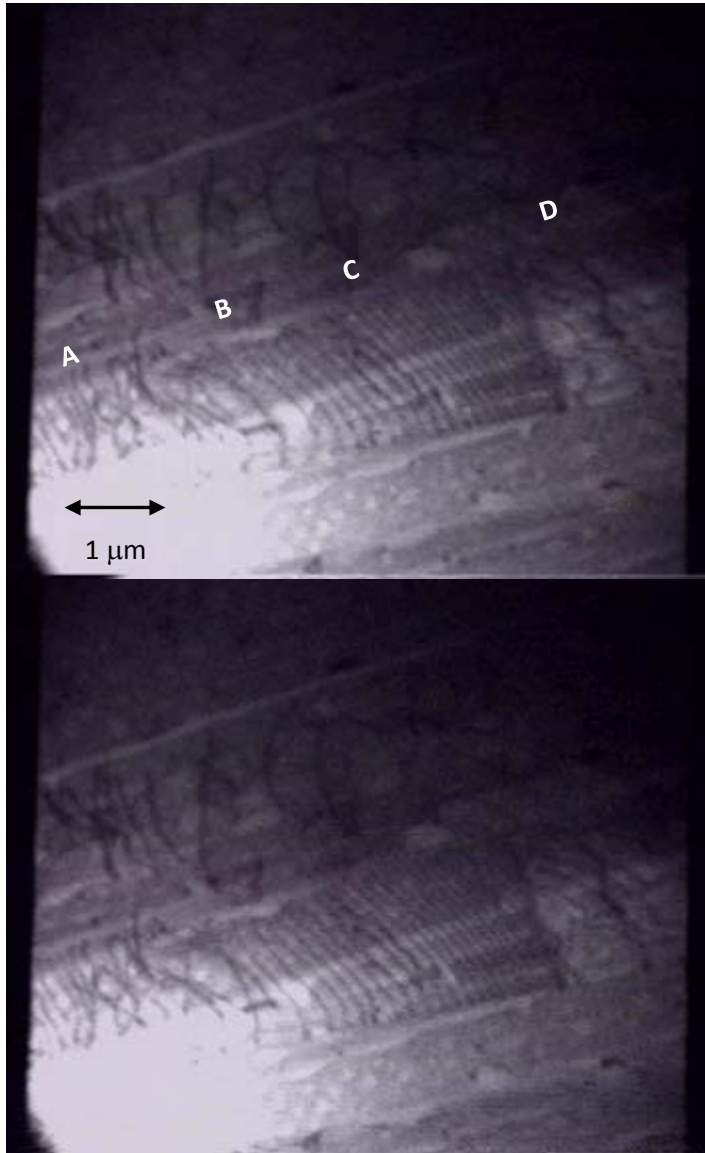


Figure 2-7. Two consecutive frames of in-situ observation of immobilisation-remobilisation events [88]. The dislocations move from left to right.

At the head of the pile up, dislocations are remobilized (D). This is probably an early stage of cell wall formation. An example of remobilisation of dislocations from fully developed cell walls is shown in Figure 2-8.

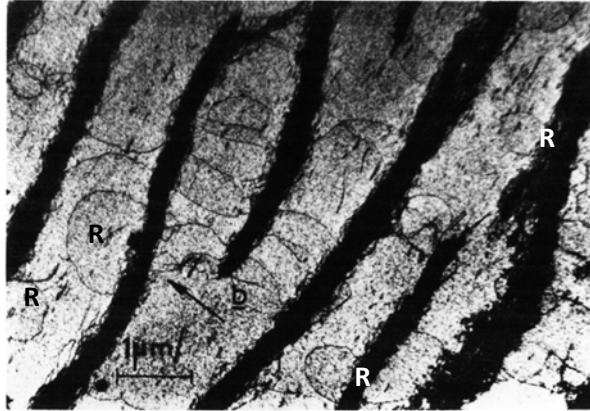


Figure 2-8. Remobilisation events (marked R) from dense dislocation walls [89].

The dislocation loops that are seen to be emerging from the cell walls in Figure 2-8 cannot be interpreted as loops that have been emitted by a continuously operating Frank-Read source, since the restoration of the source segment after emission of a loop like shown in Figure 2-3, from configuration 2 to 5 is obstructed by the cell wall. A more probable explanation is that these are occurrences of the remobilisation, or the regeneration of a segment by a dislocation stored earlier in the wall structure, which is a single rather than a recursive event. Such an event might be triggered by the changing local stress field in the wall due to the arrival and immobilisation of mobile dislocations at the wall, like in Figure 2-7.

The basic principle of the model is the creation-annihilation balance, eq. (2.28)

$$\frac{d\rho_i}{d\varepsilon} = \frac{d\rho_m}{d\varepsilon} \Big|_c - \frac{d\rho}{d\varepsilon} \Big|_a, \quad (2.31)$$

where the subscripts c and a denote the creation respectively the annihilation rate. The creation term on the right hand side pertains to mobile dislocations since a newly created dislocation is by definition mobile. The annihilation term is the sum of the annihilation rates of mobile and immobile dislocations.

For the mobile dislocation density to remain constant, the immobilisation rate of mobile dislocations

$$U = \frac{d\rho_m}{d\varepsilon} \Big|_i, \quad (2.32)$$

where the subscript i denotes immobilisation, is the sum of the rate at which mobile dislocations are created and immobile dislocations are remobilized:

$$U = \left. \frac{d\rho_m}{d\varepsilon} \right|_c + \left. \frac{d\rho_i}{d\varepsilon} \right|_r, \quad (2.33)$$

where the subscript r stands for remobilisation. From eqs. (2.31) and (2.33) follows:

$$\left. \frac{d\rho}{d\varepsilon} \right|_a = U - \left. \frac{d\rho_m}{d\varepsilon} \right|_r - \left. \frac{d\rho}{d\varepsilon} \right|_a \quad (2.34)$$

At this stage, the model expresses the equivalence of the creation-annihilation and storage-recovery interpretations of eq. (2.28) mathematically. A schematic rendition of the dislocation evolution balance by Bergström is shown in Figure 2-9.

The time rate with of immobilisation of mobile dislocations is proportional to their velocity v , to their density and to the inverse of the dislocation mean free path λ :

$$\left. \frac{d\rho_m}{dt} \right|_i = \frac{v\rho_m}{\lambda} \quad (2.35)$$

The immobilisation rate U , which is a rate with respect to strain is then

$$U = \left. \frac{d\rho_m}{d\varepsilon} \right|_i = \frac{1}{\dot{\varepsilon}} \left. \frac{d\rho_m}{dt} \right|_i \quad (2.36)$$

Substituting for the strain rate $\dot{\varepsilon}$ from the Orowan equation (2.15) expressed in equivalent strain using eq. (2.9), U can be expressed as:

$$U = \frac{\bar{M}}{b\lambda} \quad (2.37)$$

Dynamic recovery is interpreted as the sum of remobilisation and annihilation in the model. Remobilisation pertains to immobile dislocations only, and is assumed to follow first order kinetics, so the remobilisation rate is proportional to the density of immobile dislocations:

$$\left. \frac{d\rho_i}{d\varepsilon} \right|_r = \theta_1 \rho_i \quad (2.38)$$

where θ_1 is a constant.

Likewise, the annihilation rate of mobile dislocations at annihilation centres of combined density N_a , like voids, grain boundaries and the surface is

proportional to the density of mobile dislocations, and the annihilation rate due to reactions between pairs of mobile dislocations is proportional to the square of the density of mobile dislocations. Finally the annihilation rate due to reactions between mobile and immobile dislocations is proportional to the product of the density of both types:

$$\left. \frac{d\rho}{d\varepsilon} \right|_a = \lambda_1 \rho_m^2 + \lambda_2 \rho_m \rho_i + \theta_2 N_a \rho_m \quad (2.39)$$

where λ_1 , λ_2 and θ_2 are constants.

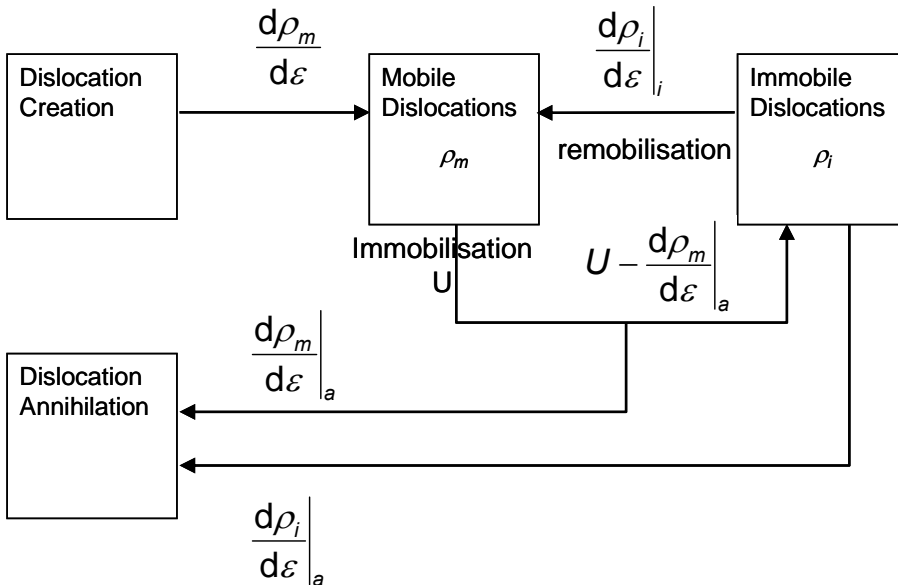


Figure 2-9. Flow diagram of the dislocation balance. The subscript m stands for mobile, the subscript i for immobile dislocations after Bergström [83].

Since the density of mobile dislocations is constant, the rate of increase of mobile dislocations vanishes, and

$$\frac{d\rho}{d\varepsilon} = \frac{d\rho_i}{d\varepsilon} + \frac{d\rho_m}{d\varepsilon} = \frac{d\rho_i}{d\varepsilon} \quad (2.40)$$

So that with eqs. (2.34), (2.38), (2.39) and substituting $\rho_i = \rho - \rho_m$ follows:

$$\frac{d\rho}{d\varepsilon} = U - \theta_1(\rho - \rho_m) - \lambda_1 \rho_m^2 - \lambda_2 \rho_m (\rho - \rho_m) - \theta_2 N_a \rho_m \quad (2.41)$$

Now define

$$\Omega = \theta_1 + \lambda_2 \rho_m$$

and

$$A_m = (\lambda_1 - \lambda_2) \rho_m^2 + (\theta_2 N_a - \theta_1) \rho_m, \quad (2.42)$$

where Ω is a probability factor that pertains to the combined remobilisation of immobile dislocations with annihilation through reactions between mobile and immobile dislocations. The parameter A_m pertains to the annihilation of mobile dislocations due to mutual dislocation reactions and at intrinsic annihilation sites.

Substituting Ω and A_m in eq. (2.41) then yields the expression

$$\frac{d\rho_i}{d\varepsilon} = U - \Omega \rho_i - A \quad (2.43)$$

In a series of subsequent papers [90], [91], [92], it was found from experiments on dynamic strain ageing that the contribution of annihilation is negligible. In Chapter 7 section 7.1 it will be demonstrated that this holds true for non-ageing material at elevated temperatures. Kocks and Mecking also found that the dynamic recovery rate is much larger than the -time dependent- static recovery rate, which is associated with dislocation annihilation processes [24]. Neglecting annihilation leads to the final form of Bergström's evolution equation of the dislocation density:

$$\frac{d\rho_i}{d\varepsilon} = U - \Omega \rho_i \quad (2.44)$$

This equation has the required property that the rate of increase of the dislocation density is smaller at higher dislocation densities, that is for increasing strain. This is in agreement with the experimental observation of a decreasing work hardening rate.

Although Bergström -correctly- identified λ with the diameter of the cells of the dislocation substructure in which the immobile dislocations are stored, he assumed λ , and consequently U , to be constant.

This issue was addressed by Vetter and van den Beukel [93], who described the strain dependence of λ by the relation for dislocation cell size d_c as a function of dislocation density by Staker and Holt eq. (2.30) [84]

$$\lambda = f d_c = f \frac{K_{sh}}{\sqrt{\rho}}, \quad (2.45)$$

where f is a constant of the order 1 and K_{SH} is Staker and Holt's constant which has a value of approximately $K_{SH} = 10 \dots 15$. Vetter and van den Beukel's modified Bergström dislocation density evolution equation reads

$$\frac{d\rho_i}{d\varepsilon} = \frac{\bar{M}\sqrt{\rho_i}}{bfK_{SH}} - \Omega\rho_i \quad (2.46)$$

which is mathematically identical to the equation proposed by Kocks and Mecking [23].

With eq. (2.27) the corresponding expression for the hardening rate as a function of stress reads:

$$\Theta = \frac{\bar{M}}{2bfK_{SH}} - \frac{\Omega}{2\alpha\bar{M}Gb} \sigma_w \quad (2.47)$$

The hardening rate according to the Bergström/Vetter-van den Beukel theory is proportional to stress. This property forms the basis of Kocks and Mecking's method of analysing work hardening behaviour by means of a plot of the hardening rate vs. stress, which will be discussed in section 2.5.2.

Dynamic recovery

In a subsequent paper [94], Bergström found that the dynamic recovery parameter is strain rate and temperature dependent.

Assuming that dislocation climb induced by vacancy diffusion is responsible for the increase of the remobilisation factor Ω , he arrived at

$$\Omega = \Omega_o + \left(kn_v \sqrt{2D_o} \right)^{2/3} \exp\left(-\frac{Q_m}{3k_b T} \right) \dot{\varepsilon}^{-1/3}, \quad (2.48)$$

where D_o and Q_m are a pre factor and activation energy pertaining to vacancy diffusion, n_v the vacancy density and k a proportionality constant (that has the dimension of volume) that pertains to the success of the vacancies to reach the cell walls. A vital step in the development of eq. (2.48) is that it is recognized that the vacancy diffusion -which is essentially a time dependent process- must

be coupled to an equation with strain as the independent variable. This is not a trivial matter: as Kocks noted, dynamic recovery is a process that proceeds at the rate of strain, not as a function of time [23]. This problem is solved in the following way. According to Bergström's theory, since the dynamic recovery parameter expresses the probability of remobilisation of an immobilized dislocation segment. The time rate at which dislocations are remobilized is

$$\left. \frac{d\rho}{dt} \right|_r = \left. \frac{d\rho}{d\varepsilon} \right|_r \frac{d\varepsilon}{dt} = -\Omega \dot{\varepsilon} \rho, \quad (2.49)$$

where the subscript r denotes remobilisation. Integration of this expression yields

$$\rho = \rho_0 \exp(-\Omega \dot{\varepsilon} t), \quad (2.50)$$

where ρ_0 is an initial dislocation density. The mean time t_R that elapses before a remobilisation event takes place is now

$$t_R = \frac{\int_0^\infty t \rho dt}{\int_0^\infty \rho dt} = \frac{1}{\Omega_v \dot{\varepsilon}}, \quad (2.51)$$

where Ω_v is the contribution due to vacancy capture to the remobilisation rate Ω and Ω_0 is neglected.

This derivation is not dependent on a particular interpretation of the nature of the remobilisation process. Bergström's idea of dislocations being fully remobilized could well be replaced by a picture where immobile dislocations can act as one-off or recurrent sources of new dislocations due to the constantly changing configuration of dislocations and local stress fields inside the dislocation walls. Such an interpretation still renders the derivation of t_R fully valid. The possibility to incorporate time dependent interactions between dislocations and other crystal defects in the inherently strain dependent dislocation density evolution equation is an invaluable feature of the Bergström theory.

In deriving eq. (2.48), Bergström assumed that vacancy diffusion is controlled by the Einstein relationship [95]

$$l_v = (2D_b t)^{1/2}, \quad (2.52)$$

where l_v is the distance covered by a vacancy in time t and D_b the diffusivity, i.e. Bergström assumed bulk diffusion through a crystal lattice that is not disturbed by other defects, like in the Cottrell-Bilby theory for diffusion of point defects

influenced by the stress field of a dislocation [96]. The number of vacancies per unit area that arrive at the cell walls during the time interval t_R is then

$$N = 2n_v (2D_b t_R)^{1/2} \quad (2.53)$$

Substituting for t_R from eq. (2.51) yields:

$$N = 2n_v \left(\frac{2D_b}{\Omega_v \dot{\epsilon}} \right)^{1/2} \quad (2.54)$$

Assuming that the partial probability of remobilisation events due to dislocation climb Ω_v is proportional to N , Ω_v is given by

$$\Omega_v = \left(kn_v \sqrt{2D_0} \right)^{2/3} \exp\left(-\frac{Q_m}{3k_b T} \right) \dot{\epsilon}^{-1/3} \quad (2.55)$$

which is the second term in eq. (2.48).

2.5.2 The Kocks- Mecking model

The Kocks-Mecking equation [97], [23], [98], which is a much cited single state variable hardening model, was formulated as a synthesis of work hardening with dislocation recovery creep phenomena. By careful analysis of experimental stress-strain experiments on several pure metals and alloys, they proposed a differential equation for the evolution of dislocation density as a function of strain, which can be regarded as a rationalisation of the Voce equation for work hardening.

The Voce equation reads:

$$\sigma = \sigma_s - (\sigma_s - \sigma_y) \exp(-n\epsilon), \quad (2.56)$$

where n is a hardening parameter and σ_s the saturation stress, which is the flow stress at the limit at high strains. Eq. (2.56) can be written in a differential form as

$$\Theta = \frac{d\sigma}{d\epsilon} = \Theta_0 \left(1 - \frac{\sigma}{\sigma_s} \right), \quad (2.57)$$

where $\Theta_0 = n\sigma_s$ is the work hardening rate at yield ($\epsilon = 0$). According to eq. (2.57), the work hardening decreases linearly as a function of stress from the

initial hardening rate Θ_0 to zero at the saturation stress. This kind of behaviour is indeed often observed in hardening rate vs. stress graphs for many pure metals and alloys. Kocks and Mecking made most of their analysis of work hardening behaviour by plotting the hardening rate vs. flow stress, which now often is referred to as a Kocks-Mecking plot in literature.

By analysing the dependence of the saturation stress as a function of stress and strain rate, Kocks arrived at a variant of the Voce equation that includes strain rate and temperature:

$$\Theta = \Theta_0 \left(1 - \frac{\sigma}{\sigma_{s0}} \left(\frac{\dot{\epsilon}_r}{\dot{\epsilon}} \right)^{-\frac{k_b T}{Q_K}} \right), \quad (2.58)$$

where σ_{s0} is the saturation stress at $T = 0$ K, $\dot{\epsilon}_r$ a reference strain rate and Q_K an empirical constant that has the dimension of energy.

Starting from the storage-recovery interpretation of eq. (2.28), Kocks arrived at an expression for the increase of dislocation density as a function of strain only, which reads in the shear stress/strain notation as

$$\frac{d\rho}{d\gamma} = \frac{\sqrt{\rho}}{2\beta} - \frac{L_r}{2b} \rho \quad (2.59)$$

Note that this equation is mathematically identical to Vetter's version of Bergström's equation (2.46), where annihilation is neglected. The notion that first term at the right hand side pertains to the dislocation mean free path λ was arrived at by similar arguments as Bergström's, and further by taking λ proportional to the average spacing between -stored- dislocations according to

$\lambda = \frac{\beta_{km}}{\sqrt{\rho}}$, where β_{km} is a proportionality constant. The second term was

formulated from the assumptions that it is due some "...recovery or rearrangement process...", and that an average length L_R of dislocation gets annihilated or become ineffective at each potential recovery site, the density of which was taken proportional to the dislocation density. Substituting shear stress for dislocation density from the Taylor relation (eq. (2.27)) which in shear stress/strain notation reads $\tau = \alpha G b \sqrt{\rho}$, they showed that eq. (2.59) is mathematically to the Voce equation eq. (2.57) in differential form:

$$\Theta_\tau = \frac{d\tau}{d\gamma} = \frac{\alpha G}{2\beta} - \frac{L_R}{2b} \tau \quad (2.60)$$

If we now compare this result to eq. (2.58) it follows that L_R must be

proportional to $\left(\frac{\dot{\varepsilon}_r}{\dot{\varepsilon}}\right)^{-\frac{k_b T}{Q_k}}$. This observation does not seem to be justified by

the assumptions that have been made in the derivation of eq. (2.59), namely that L_R is basically a structural athermal variable. For this reason, for the possibility to incorporate time dependent mechanisms, and since the basic principle of the KM model is identical to Bergström's dislocation balance equation (2.34), we prefer Bergström's approach over that of Kocks and Mecking.

2.6 Other Bergström/Kocks-Mecking like models

Some authors recognize additional impenetrable obstacles besides the dislocation cell walls that may restrict the dislocation mean free path [99], [100]. Obvious candidates are grain boundaries and precipitates. Since the smallest distances between the obstacles will define the actual free path λ , this is then taken as the harmonic mean of the individual contributions, which are respectively equal to that pertaining to the dislocation cell size λ_d (eq. (2.45)), the grain size $\lambda_g = D$ and the distance between precipitates $\lambda_p = d_p$:

$$\begin{aligned} \frac{1}{\lambda} &= \frac{1}{\lambda_s} + \frac{1}{\lambda_g} + \frac{1}{\lambda_p} \\ &= \frac{K_{SH}}{\sqrt{\rho}} + \frac{1}{D} + \frac{1}{d_p} \end{aligned} \quad (2.61)$$

The dislocation evolution equation then reads:

$$\frac{d\rho_i}{d\varepsilon} = \frac{\bar{M}}{b} \left(\frac{1}{D} + \frac{1}{d_p} \right) + \frac{\bar{M}\sqrt{\rho_i}}{bfK_{SH}} - \Omega\rho_i \quad (2.62)$$

and with eq. (2.27) the corresponding expression for the hardening rate reads

$$\Theta = \frac{\alpha\bar{M}^2 G}{2} \left[\left(\frac{1}{D} + \frac{1}{d_p} \right) \frac{\alpha\bar{M}Gb}{\sigma_w} + \frac{1}{fK_{SH}} \right] U + \frac{\Omega}{2} \sigma_w \quad (2.63)$$

Note that the $\left(\frac{1}{D} + \frac{1}{d_p}\right)$ term causes the model to predict an infinite hardening rate at zero work hardening. This problem will be addressed in Chapter 7.

2.7 Dynamic strain ageing

Static strain ageing at room temperature is a time dependent process in which an upper yield stress and the associated Lüders instability -which are characteristic features of annealed material at room temperature- return after these phenomena have been removed by cold work [101], [102]. It is explained by the diffusion of free interstitial solute atoms -notably C and N in steel- that segregate to the dislocations [96]. By this process, the dislocations acquire an atmosphere of N and/or C atoms. This causes the dislocations to be pinned, with the consequence that potentially mobile dislocations are no longer mobile, and immobile dislocations will be harder to remobilize.

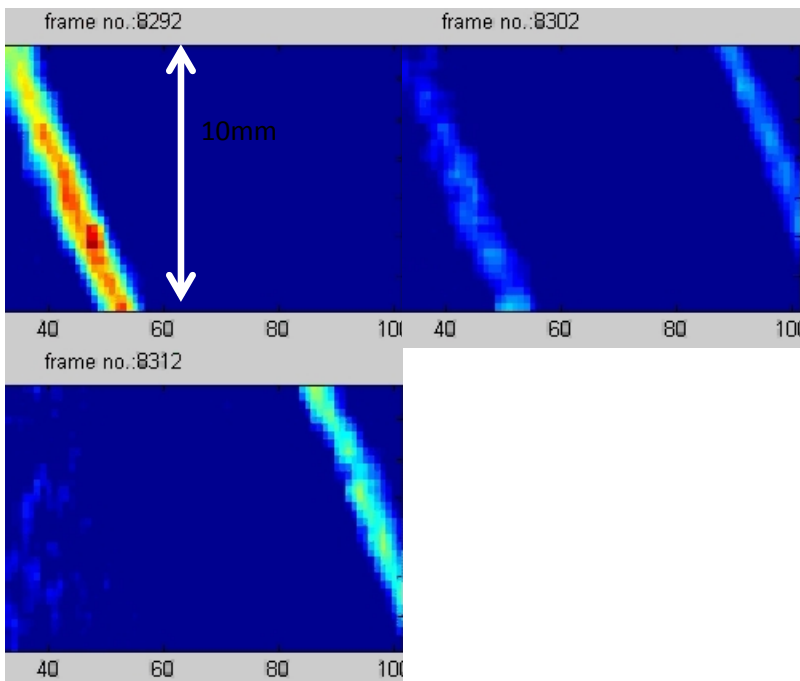


Figure 2-10. Repetitive propagation of DSA bands. Propagation direction is from right to left. $T = 250\text{ }^{\circ}\text{C}$, time interval = 0.333 s. Steel composition (wt%): 0.039 C, 0.207 Mn, 0.025 Al, 0.038 N, 0.012 P.

Dynamic strain ageing (DSA) is basically the same mechanism, but occurring during deformation. The magnitude of DSA phenomena is dependent on the strain rate. This is a natural consequence of the fact that the time available for C and N segregation is shorter at a higher strain rate. Since solute diffusion is a thermally activated process, the observable occurrence of the DSA phenomenon shifts to higher temperatures for increasing strain rates. The most conspicuous feature of DSA is associated with the occurrence of plastic instabilities known as Portevin–Le Châtelier bands [103]. These have the appearance of propagative deformation bands, much like the Lüders bands that form during deformation of statically aged or annealed steel, but with the difference that Lüders bands traverse the volume only once, whereas the DSA bands are repetitive [104], [105].

An example of DSA bands that repetitively traverse a tensile sample is shown in Figure 2-10. The bands are recorded by infrared thermography. In the figure the local strain rate is shown, which was obtained from the IR footage by application of a digital filtering technique based on the heat transport equation [107].

These instabilities show as serrations in the stress-strain curves, a typical example of which is shown in Figure 2-11.

After Penning [108] explained the DSA plastic instability by the condition of the

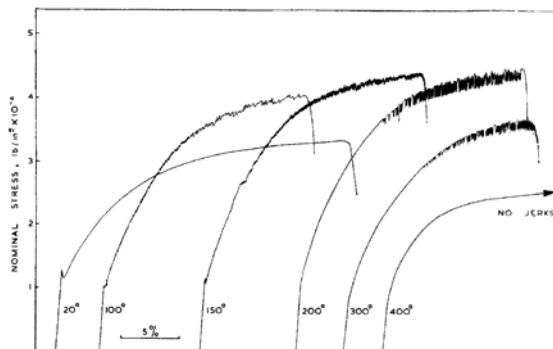


Figure 2-11. Typical serrations by DSA [106]. (A weak Lüders phenomenon is seen at $T < 200$ °C.)

strain rate sensitivity being negative, a large body of models have appeared in literature, all of which are based on the assumption that the direct strain rate sensitivity is negative, which is a simplification made for reasons of mathematical simplicity and clarity by Penning.

These theories therefore attribute the DSA effect to the dislocation glide resistance (eq. (2.26)). The effect is then explained by intermittent locking by solute atoms and unlocking due to the increased applied stress that is required

to maintain the strain rate by propagation of the decreased (due to locking) density of mobile dislocations.

According to these theories, this intermittent decrease/increase of the mobile dislocation density and the increase/decrease of the glide resistance eq. (2.26) is the cause of the stress serrations.

Another obvious feature of DSA that can be seen in Figure 2-11 is that the work hardening rate for increasing temperature first increases as a function of temperature, before it decreases at higher temperatures. The indirect temperature sensitivity is thus positive for $T < 200$ °C. This implies that the indirect strain rate sensitivity is negative in that region. It has been shown in a paper that is included in this thesis as chapter 4, that a negative indirect strain rate sensitivity can also lead to plastic instabilities of DSA type. The occurrence of such anomalous hardening rates cannot be explained by a theory that relies on the dislocation glide resistance alone.

An important additional characteristic of DSA effect is thus an anomalously high work hardening rate in a temperature regime that depends on the strain rate [109], [110], [111] [112], [113]. Qualitatively, this can be explained by the pinning of immobile dislocations by solute atoms. A pinned dislocation cannot be easily remobilized, and can be categorized as locked. From Bergström's equation (2.46) it now follows that for a decreased remobilisation rate $\frac{d\rho}{d\varepsilon}$

increases, the consequence of which is an increased hardening rate.

The decrease of the hardening rate at higher temperatures can be explained as follows. At high temperatures, the interstitials segregate onto the dislocations at a very high rate. Since the density of interstitials is finite, the interstitial reservoir will be depleted at an increasingly lower strain at increasing temperatures. The vacancy density however remains constant, and dynamic recovery -which causes a decrease of hardening rate with temperature-, will eventually remain as the only mechanism that causes an indirect strain rate sensitivity.

Additionally, a competition between segregation of interstitials and of vacancies to dislocations will exist. A dislocation can therefore be remobilized before it is completely locked. The balance between locking and remobilisation will depend on the ratio of the diffusivities of vacancy and solute diffusion, which depends on temperature.

Locking of immobile dislocations is obviously more likely than that of mobile dislocations. At higher strain rates, the velocity of mobile dislocations increases proportionally to the strain rate. Since the diffusion rate of solute atoms is independent of strain rate, this implies that the probability of locking of mobile dislocations decreases linearly with increasing strain rate, since the locking rate will be proportional to the inverse of dislocation velocity.

The remobilisation rate of immobile dislocations on the other hand increases with increasing strain rate as $\dot{\epsilon}^{-1/3}$ due to vacancy-assisted climb according to eq. (2.48). This is counteracted by the decrease of the probability of solute atoms to arrive at the immobile dislocations. Consequently, the probability of locking of immobile dislocations will not be very sensitive to the strain rate since they are stored in relatively permanent structures and their velocity is zero.

A simple calculation shows that the likelihood of solute C atoms segregating to mobile dislocations is negligibly small:

Assuming that the density of mobile dislocations is $\rho_m = 1.10^{12} \text{ m}^{-2}$, then from

eq. (2.15) and $b = 2.58 \cdot 10^{-10} \text{ m}$ their velocity for $\dot{\epsilon} = 1 \text{ s}^{-1}$ is $v = 4 \cdot 10^{-3} \text{ ms}^{-1}$. The diffusion coefficient of carbon in α -Fe at $T = 300 \text{ }^\circ\text{C}$ is $D = 10^{-12} \text{ m}^2\text{s}^{-1}$ [15]. At

$\dot{\epsilon} = 1 \text{ s}^{-1}$, the time of the deformation process is of the order of 1 s, so that from eq. (2.52) it follows that the diffusion velocity of carbon is $v_c = 1.4 \times 10^{-6} \text{ ms}^{-1}$.

This is more than two orders of magnitude slower than the velocity of mobile dislocations. Additionally, the absence of an appreciable upper yield stress at this temperature, as seen in Figure 2-11, indicates that the locking stress exerted by solute atoms on dislocations is negligible. That implies that solute drag by solute atoms on mobile dislocations also is improbable. DSA and the associated plastic instabilities are therefore most probably caused by a negative strain rate sensitivity of the work hardening rate due to the segregation of solute atoms to immobile dislocations. In Chapter 4 it will be shown that a negative strain rate sensitivity of the work hardening rate can explain DSA instabilities.

Virtually all studies of DSA pertain to Fe in the ferritic phase. Stewart and Jonas have found for an austenitic stainless steel that DSA also occurs in the FCC phase [114]. They claim to have found evidence of DSA effects at temperatures around $T = 950^\circ\text{C}$ by strain rate sensitivity analysis. They did not distinguish between direct strain rate sensitivity and indirect strain rate sensitivity, but

computed the nominal strain rate sensitivity defined as $m = \frac{d \ln(\sigma_f)}{d \ln(\dot{\epsilon})}$. This

quantity did not attain negative values, but showed a decreasing trend between $T = 800$ and $950 \text{ }^\circ\text{C}$. Actually, the nominal strain rate sensitivity is a compound quantity, since from eq. (2.1) and the definition of the work hardening rate θ follows :

$$\begin{aligned}
\sigma_f &= \sigma_y + \sigma_w(\varepsilon, \dot{\varepsilon}, T) + \sigma^*(\dot{\varepsilon}, T) \\
&= \sigma_y + \int_0^\varepsilon \Theta(\varepsilon, \dot{\varepsilon}, T) d\varepsilon' + \sigma^*(\dot{\varepsilon}, T)
\end{aligned}
\tag{2.64}$$

This implies for the nominal strain rate sensitivity

$$\begin{aligned}
m &= \frac{\dot{\varepsilon}}{\sigma_f} \frac{d\sigma_f}{d\dot{\varepsilon}} \\
&= \frac{\dot{\varepsilon}}{\sigma_f} \left(\int_0^\varepsilon \frac{d\Theta}{d\dot{\varepsilon}} d\varepsilon + \frac{d\sigma^*}{d\dot{\varepsilon}} \right)
\end{aligned}
\tag{2.65}$$

The nominal strain rate sensitivity is therefore a summation of the indirect and the direct strain rate sensitivities. In two earlier papers Barnett and Jonas **[115]**, **[116]** reported the strain rate sensitivity m of low carbon steel up to $T = 1250$ °C. A similar decrease of m as in **[114]** was found in the intercritical temperature range, which appears to indicate that DSA does not occur in austenitic low carbon steel.

The possibility of anomalous work hardening due to DSA in low and medium carbon steels in the austenitic temperature range can nevertheless not be ruled out, and indeed is of some interest in the scope of this thesis.

In an earlier publication **[117]** a further development of the Bergström model including additional evolution equations that describe dislocation locking and its effect on the work hardening rate has been described, which will now be reviewed. The model is based on ideas on dislocation locking that were published in a paper by Bergström **[90]** in which he analysed DSA by fitting $U(T)$ and $\Omega(T)$ to his model *sans* DSA in the ferritic temperature regime.

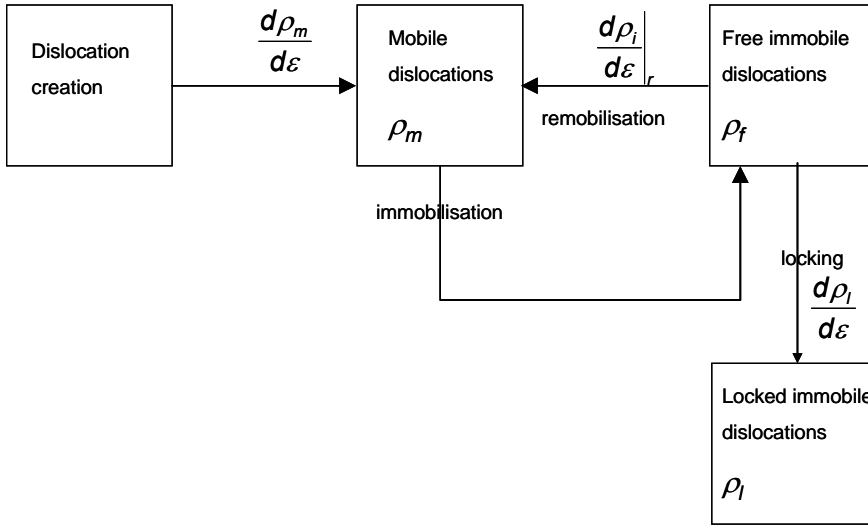


Figure 2-12. Dislocation balance for strain ageing material according to the Beraström model (sans annihilation)

The dislocation balance must now be extended with respect to the original theory by making a distinction between locked and free immobile dislocations and a locking rate, as depicted in Figure 2-12, where immobile dislocations become locked by the formation of a Cottrell atmosphere of solute atoms that have segregated to immobile dislocations, concurrently with the remobilisation process due to vacancy assisted climb of immobile dislocations.

Let ρ_f be the density of free immobile dislocations (i.e. free to be remobilized) and ρ_l the density of locked dislocations

$$\rho_f = \rho - \rho_l \quad (2.66)$$

Depending on the number of solute atoms that have segregated to the dislocations per unit of dislocation line length, there must exist a degree of locking, i.e. the remobilisation probability will gradually decrease to zero when this number increases. The model however only recognizes totally free or locked dislocations. Further, dislocations that are created or remobilized are free dislocations. The dislocation evolution equation is now from eq. (2.46)

$$\frac{d\rho_f}{d\varepsilon} = \frac{\bar{M}\sqrt{\rho}}{bfK_{sh}} - \Omega(\rho - \rho_l), \quad (2.67)$$

where the mean free path is assumed to obey Staker and Holt's relation (eq. (2.45)), expressed in terms of the *total* dislocation density.

There will be a competition between remobilisation due to vacancy induced dislocation climb and dislocation locking by solute atoms. Not all free dislocations will be locked, since some are remobilised before locking is complete. From eq. (2.51) follows, that the strain increment $\delta\varepsilon$ during which free dislocations remain immobile and are susceptible to locking is:

$$\delta\varepsilon = \frac{1}{\Omega} \quad (2.68)$$

Two additional differential equations are now required, respectively for the description of the change of ρ_l and for the density N_{sf} of interstitial solute atoms that have not been segregated onto dislocations (free solute atoms) and which are still available for the locking process.

Since the locking rate will be proportional to N_{sf} , the number N_s of solute atoms per unit of dislocation line length that arrive at free dislocations during $\delta\varepsilon$ is similar to eq. (2.54)

$$N_s = z_l N_{sf} \left(\frac{2D_s}{\Omega \dot{\varepsilon}} \right)^{1/2}, \quad (2.69)$$

where z_l is a proportionality constant pertaining to the affinity between

dislocations and solute atoms, $D_s = D_{s0} \exp\left(-\frac{Q_s}{k_b T}\right)$ is the solute diffusivity

with D_{s0} the pre factor and Q_s the activation energy for solute atom diffusion. In [117] Cottrell diffusion kinetics [96] was assumed, which describes diffusion under the influence of the gradient of the stress field of an isolated dislocation. Our present view is that Einstein diffusion kinetics, which is assumed here, is more appropriate, since the gradient of the stress field of a dislocation wall is less steep than that of a single dislocation.

The density of free dislocations that are susceptible to locking ρ_f^l is then

$$\rho_f^l = \frac{\rho_f}{\Omega(\dot{\varepsilon}, T)} \quad (2.70)$$

Assuming first order kinetics with respect to the density of free dislocations the locking rate will now be proportional to the product of the density of free dislocations ρ_f^l , the strain interval during which they can be locked before remobilisation takes place, $\delta\varepsilon$ (eq. (2.68)), and N_s (eq. (2.69)):

$$\frac{d\rho_l}{d\varepsilon} = z_l N_{sf} \frac{\rho_f}{\Omega} \left(\frac{2D_s}{\Omega \dot{\varepsilon}} \right)^{1/2} \quad (2.71)$$

Finally, the third differential equation for the rate at which the free solute atoms segregate out of solution is necessary, since N_{sf} decreases due to the locking process. This rate will be proportional to the sum of the density of free solute atoms and -since solute atoms will still segregate to locked dislocations-

the total dislocation density and the rate factor $\left(\frac{2D_s}{\Omega \dot{\varepsilon}} \right)^{1/2}$ from eq. (2.69):

$$\frac{dN_{sf}}{d\varepsilon} = z_l N_{sf} \left[\rho_l + \frac{\rho_f}{\Omega} \right] \left(\frac{2D_s}{\Omega \dot{\varepsilon}} \right)^{1/2} \quad (2.72)$$

This set of three simultaneous evolution eqs. (2.67), (2.71) and (2.72) can only be solved numerically. The resulting total dislocation density can then be substituted in the Taylor relation(2.27) to compute work hardening as a function of strain. An example result of the model is shown in Figure 2-13.

The DSA model that we now have formulated describes the temperature and strain rate dependence of work hardening, taking dynamic recovery and dynamic strain ageing into account. The model has three state variables, namely free dislocation density, locked dislocation density and solute density, the last of which only appears in the evolution equations.

According to the model, the DSA effect manifests itself as an anomalously high hardening rate at an intermediate temperature range as shown in Figure 2-13. The work hardening peak decreases and shifts to higher T at increasing strain rates. This is in agreement with the behaviour that is schematically depicted in [115] and [116]. Negative DSRS values occur at temperature ranges where the flow stress of a low strain rate curve exceeds that of one at higher strain rate.

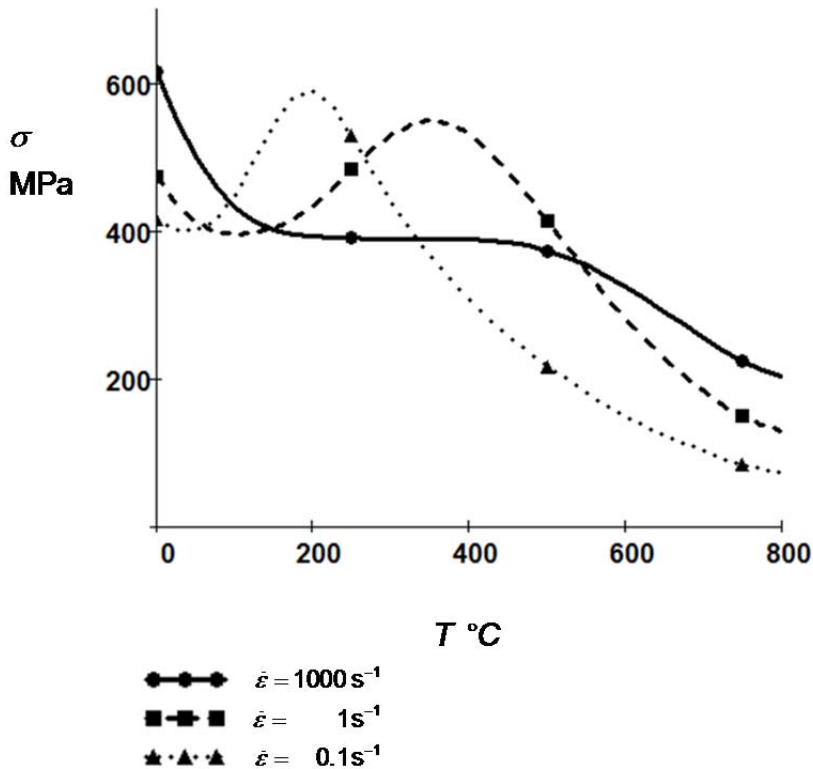


Figure 2-13. Computed strain ageing work hardening peak ($\epsilon = 0.4$) for three strain rates (BCC Fe).

This model has been fitted to work hardening data obtained by axisymmetric compression testing for several steel grades [117]. The success of that fit may only yield circumstantial evidence of dynamic strain ageing in the austenite temperature range, since the model did not incorporate a glide resistance equation for that temperature range, and no proper assessment of DSA from the raw data was conducted. This problem will be revisited in Chapter 7.

2.8 Scientific questions

The following scientific subjects of inquiry may now be formulated

- How does the anomalous work hardening rate that is associated with DSA contribute to the onset of Portevin-le Châtelier plastic instabilities?

- Which mechanism causes the yield stress to depend on both the initially present dislocation structure and the grain size?
- How are strain rate and temperature sensitivity of the flow stress dependent on work hardening and glide resistance?
- Can the disagreement between the Bergström and Kocks-Mecking interpretations of the dislocation density evolution equation be resolved?
- Does dynamic strain ageing occur in the austenitic temperature range?
- Why is the Taylor relation that describes work hardening as a function of dislocation density not very sensitive to the spatial distribution of the dislocations?

The first question is the subject of Chapter 4. In Chapters 5 and 6 a pre-yield/yield stress model is developed. In Chapter 7 the relative strengths of the glide resistance and work hardening contributions to the flow stress are evaluated and the occurrence of DSA in the austenitic temperature range is discussed. In that chapter a contribution to the Kocks-Mecking vs. Bergström discourse is presented, and some thought given to answering the question concerning the Taylor relation.

References

- [1] Klepaczko, J. R., & Chiem, C. Y. (1986). On rate sensitivity of fcc metals, instantaneous rate sensitivity and rate sensitivity of strain hardening. *Journal of the Mechanics and Physics of Solids*, 34(1), 29-54.
- [2] van Liempt, P., & Sietsma, J. (2011). A revised criterion for the Portevin–Le Châtelier effect based on the strain-rate sensitivity of the work-hardening rate. *Metallurgical and Materials transactions A*, 42(13), 4008-4014.
- [3] Ghosh, G., & Olson, G. B. (2002). The isotropic shear modulus of multicomponent Fe-base solid solutions. *Acta materialia*, 50(10), 2655-2675.
- [4] D. Raabe. *The simulation of materials microstructures and properties. Computational Materials Science. Wiley-VCH. 1998*
- [5] Rhee, M., Zbib, H. M., Hirth, J. P., Huang, H., & De la Rubia, T. (1998). Models for long-/short-range interactions and cross slip in 3D dislocation simulation of BCC single crystals. *Modelling and Simulation in Materials Science and Engineering*, 6(4), 467.
- [6] Lalli, L. A. (1998). Multiscale modeling for light metals alloy development. *Current Opinion in Solid State and Materials Science*, 3(3), 283-287.
- [7] Wang, Y. U., Jin, Y. M., Cuitino, A. M., & Khachatryan, A. G. (2001). Phase field microelasticity theory and modeling of multiple dislocation dynamics. *Applied Physics Letters*, 78(16), 2324-2326.

-
- [8] Chen, L. Q. (2002). Phase-field models for microstructure evolution. *Annual review of materials research*, 32(1), 113-140.
- [9] Buehler, M. J., Hartmaier, A., Gao, H., Duchaineau, M. A., & Abraham, F. F. (2005). The dynamical complexity of work-hardening: a large-scale molecular dynamics simulation. *Acta Mechanica Sinica*, 21(2), 103-111.
- [10] Proville, L., Rodney, D., & Marinica, M. C. (2012). Quantum effect on thermally activated glide of dislocations. *Nature materials*, 11(10), 845-849..
- [11] Janssens, K. G. F. "An introductory review of cellular automata modeling of moving grain boundaries in polycrystalline materials." *Mathematics and Computers in Simulation* 80.7 (2010): 1361-1381.
- [12] Roters, F., Eisenlohr, P., Hantcherli, L., Tjahjanto, D. D., Bieler, T. R., & Raabe, D. (2010). Overview of constitutive laws, kinematics, homogenization and multiscale methods in crystal plasticity finite-element modeling: Theory, experiments, applications. *Acta Materialia*, 58(4), 1152-1211.
- [13] Kocks, U. F., Argon, A. S., & Ashby, M. F. (1975). Thermodynamics and Kinetics of Slip, Volume 19 in *Progress in Materials Science*, B. Chalmers, JW Christian and TB Massalski, Eds. *Materials Science* vol. 19 p 1-291 (1975)
- [14] Cabrera, J. M., Al Omar, A., Prado, J. M., & Jonas, J. J. (1997). Modeling the flow behavior of a medium carbon microalloyed steel under hot working conditions. *Metallurgical and Materials Transactions A*, 28(11), 2233-2244.
- [15] Brown, S. B., Kim, K. H., & Anand, L. (1989). An internal variable constitutive model for hot working of metals. *International journal of plasticity*, 5(2), 95-130. 1989
- [16] Seeger, A. K. (1980). Early work on imperfections in crystals, and forerunners of dislocation theory. *Proceedings of the Royal Society of London. Series A, Mathematical and Physical Sciences*, 371(1744), 173-177.
- [17] Nabarro, F. R. N. (1952). Mathematical theory of stationary dislocations. *Advances in Physics*, 1(3), 269-394.
- [18] Mendelson, A. (1973). *Plasticity: theory and application*, 1968. New York: The Macmillan Company.
- [19] Backofen, W. A. (1972). *Deformation processing*. Addison-Wesley Pub. Co..
- [20] Anand, L., Zavaliangos, A., & von Turkovich, B. F. (1990). Hot working—constitutive equations and computational procedures. *CIRP Annals-Manufacturing Technology*, 39(1), 235-238.
- [21] Bishop, J. F. W., & Hill, R. (1951). XLVI. A theory of the plastic distortion of a polycrystalline aggregate under combined stresses. *The London, Edinburgh, and Dublin Philosophical Magazine and Journal of Science*, 42(327), 414-427.
- [22] Przybyla, C. P., Adams, B. L., & Miles, M. P. (2007). Methodology for determining the variance of the Taylor factor: application in Fe-3% Si. *Journal of Engineering Materials and Technology*, 129(1), 82-93.
- [23] Kocks, U. F. (1976). Laws for work-hardening and low-temperature creep. *Journal of engineering materials and technology*, 98(1), 76-85.
- [24] Kocks, U. F., & Mecking, H. (2003). Physics and phenomenology of strain hardening: the FCC case. *Progress in materials science*, 48(3), 171-273.

-
- [25] Ashby, M. F. (1972). A first report on deformation-mechanism maps. *Acta Metallurgica*, 20(7), 887-897.
- [26] Ashby, M. F., & Frost, H. J. (1982). *Deformation-mechanism maps* (pp. 44-45). Oxford: Pergamon Press.
- [27] Schulze, V., & Vöhringer, O. (2001). Plastic deformation: constitutive description. *Encyclopedia of materials: science and technology*, 7, 7050-7064.
- [28] Mughrabi, H. (1983). Dislocation wall and cell structures and long-range internal stresses in deformed metal crystals. *Acta metallurgica*, 31(9), 1367-1379.
- [29] Hirth, J. P., & Lothe, J. (1982). *Theory of Dislocations*, 2nd. Ed.: John Wiley & Sons.
- [30] Cottrell, A. H., & Dexter, D. L. (1954). Dislocations and Plastic flow in Crystals. *American Journal of Physics*, 22(4), 242-243.
- [31] Friedel, J. (2013). *Dislocations: International Series of Monographs on Solid State Physics* (Vol. 3). Elsevier.
- [32] Gibeling, J. G., & Nix, W. D. (1980). A numerical study of long range internal stresses associated with subgrain boundaries. *Acta Metallurgica*, 28(12), 1743-1752.
- [33] Sedláček, R., & Blum, W. (1998). Internal stresses in dislocation subgrain structures. *Computational materials science*, 13(1), 148-153.
- [34] Mughrabi, H. (2001). The effect of geometrically necessary dislocations on the flow stress of deformed crystals containing a heterogeneous dislocation distribution. *Materials Science and Engineering: A*, 319, 139-143.
- [35] Kuhlmann-Wilsdorf, D. (2001). Q: Dislocations structures—how far from equilibrium? A: Very close indeed. *Materials Science and Engineering: A*, 315(1), 211-216.
- [36] Gottstein, G. (2013). *Physical foundations of materials science*. Springer Science & Business Media.
- [37] Zener, C., & Hollomon, J. H. (1946). Problems in Non-Elastic Deformation of Metals. *Journal of Applied Physics*, 17(2), 69-82.
- [38] Ghosh, A. K. (1980). A physically-based constitutive model for metal deformation. *Acta Metallurgica*, 28(11), 1443-1465.
- [39] Kuhlmann-Wilsdorf, D. (1999). The theory of dislocation-based crystal plasticity. *Philosophical Magazine A*, 79(4), 955-1008.
- [40] Mott, N. F. (1952). CXVII. A theory of work-hardening of metal crystals. *The London, Edinburgh, and Dublin Philosophical Magazine and Journal of Science*, 43(346), 1151-1178.
- [41] Friedel, J. (1953). XLVI. Anomaly in the rigidity modulus of copper alloys for small concentrations. *The London, Edinburgh, and Dublin Philosophical Magazine and Journal of Science*, 44(351), 444-448.
- [42] Schoek, G. (1956). Dislocation theory of plasticity of metals. *Advances in applied mechanics*, 4, 229-279.
- [43] Frank, F. C., & Read Jr, W. T. (1950). Multiplication processes for slow moving dislocations. *Physical Review*, 79(4), 722.
- [44] Kittel, C. (2004). *Wiley: Introduction to Solid State Physics*. 8th ed. ISBN 0-471-41526-X
- [45] F. Louchet 2003. http://www.numodis.fr/tridis/TEM/recordings/FR_loin_53.mpg

-
- [46] Peil, U., & Wichers, M. (2004). Schweißen unter Betriebsbeanspruchung–Werkstoffkennwerte für einen S 355 J2G3 unter Temperaturen bis 1200 C. *Stahlbau*, 73(6), 400-415.
- [47] Scruby, C. B., & Moss, B. C. (1993). Non-contact ultrasonic measurements on steel at elevated temperatures. *NDT & E International*, 26(4), 177-188.
- [48] Hall, E. O. (1951). The deformation and ageing of mild steel: III discussion of results. *Proceedings of the Physical Society. Section B*, 64(9), 747.
- [49] Petch, N. J. (1953). The cleavage strength of polycrystals. *J. Iron Steel Inst.*, 174, 25-28.
- [50] Li, J. C. (1963). Petch relation and grain boundary sources. *Transactions of the Metallurgical Society of AIME*, 227(1), 239.
- [51] Li, J. C. M., & Chou, Y. T. (1970). The role of dislocations in the flow stress grain size relationships. *Metallurgical and Materials Transactions*, 1(5), 1145-1159.
- [52] Sinclair, C. W., Poole, W. J., & Bréchet, Y. (2006). A model for the grain size dependent work hardening of copper. *Scripta Materialia*, 55(8), 739-742.
- [53] Delincé, M., Bréchet, Y., Embury, J. D., Geers, M. G. D., Jacques, P. J., & Pardoën, T. (2007). Structure–property optimization of ultrafine-grained dual-phase steels using a microstructure-based strain hardening model. *Acta Materialia*, 55(7), 2337-2350.
- [54] Meyers, M. A., & Ashworth, E. (1982). A model for the effect of grain size on the yield stress of metals. *Philosophical Magazine A*, 46(5), 737-759.
- [55] Fu, H. H., Benson, D. J., & Meyers, M. A. (2001). Analytical and computational description of effect of grain size on yield stress of metals. *Acta Materialia*, 49(13), 2567-2582.
- [56] Bata, V., & Pereloma, E. V. (2004). An alternative physical explanation of the Hall–Petch relation. *Acta Materialia*, 52(3), 657-665.
- [57] Orowan, E. (1940). Problems of plastic gliding. *Proceedings of the Physical Society*, 52(1), 8.
- [58] Gibbs, G. B. (1965). The Thermodynamics of Thermally-Activated Dislocation Glide. *physica status solidi (b)*, 10(2), 507-512.
- [59] Surek, T., Luton, M. J., & Jonas, J. J. (1973). Dislocation glide controlled by linear elastic obstacles: a thermodynamic analysis. *Philosophical Magazine*, 27(2), 425-440.
- [60] Granato, A. V., Lücker, K., Schlipf, J., & Teutonico, L. J. (1964). Entropy factors for thermally activated unpinning of dislocations. *Journal of Applied Physics*, 35(9), 2732-2745.
- [61] Jonas, J. J., & Luton, M. J. (1970). The relation between theoretical and experimental activation areas in high temperature deformation. *Philosophical Magazine*, 21(174), 1283-1289.
- [62] Gibbs, G. B. (1967). The activation parameters for dislocation glide. *Philosophical Magazine*, 16(139), 97-102.
- [63] Kocks, U.F., *Plastic Deformation: Thermal Activation Approach*, *Encyclopedia of Materials: science and technology (Second Edition)*, Elsevier, Oxford, 2001, Pages 7084-7088
- [64] Suzuki, H. in: *Rate Processes in Plastic Deformation of Materials*, J.C. M. Li and A. K. Mukherjee (eds.), ASM, Metals Park, OH (1975) 47.

-
- [65] Zurob, H. S., Hutchinson, C. R., Brechet, Y., & Purdy, G. (2002). Modeling recrystallization of microalloyed austenite: effect of coupling recovery, precipitation and recrystallization. *Acta materialia*, 50(12), 3077-3094.
- [66] Van Dijk, N. H., Butt, A. M., Zhao, L., Sietsma, J., Offerman, S. E., Wright, J. P., & Van der Zwaag, S. (2005). Thermal stability of retained austenite in TRIP steels studied by synchrotron X-ray diffraction during cooling. *Acta Materialia*, 53(20), 5439-5447.
- [67] Peierls, R. (1940). The size of a dislocation. *Proceedings of the Physical Society*, 52(1), 34.
- [68] Seeger, A. (1956). LXV. On the theory of the low-temperature internal friction peak observed in metals. *Philosophical Magazine*, 1(7), 651-662.
- [69] Lothe, J., & Hirth, J. P. (1959). Dislocation dynamics at low temperatures. *Physical Review*, 115(3), 543.
- [70] Sarkar, S., & Militzer, M. (2009). Microstructure evolution model for hot strip rolling of Nb–Mo microalloyed complex phase steel. *Materials Science and Technology*, 25(9), 1134-1146.
- [71] K. Domkin. Thesis, Luleå University of Technology. 2005
- [72] Nemat-Nasser, S., & Li, Y. (1998). Flow stress of fcc polycrystals with application to OFHC Cu. *Acta Materialia*, 46(2), 565-577.
- [73] Nabarro, F. R. N. (1989). Work hardening and dynamical recovery of FCC metals in multiple glide. *Acta metallurgica*, 37(6), 1521-1546.
- [74] Koizumi, H., Kirchner, H. O. K., & Suzuki, T. (1993). Kink pair nucleation and critical shear stress. *Acta metallurgica et materialia*, 41(12), 3483-3493.
- [75] Rusinek, A., Zaera, R., & Klepaczko, J. R. (2007). Constitutive relations in 3-D for a wide range of strain rates and temperatures—application to mild steels. *International Journal of Solids and Structures*, 44(17), 5611-5634.
- [76] P. Ludwik. *Elemente der technologischen Mechanik*. J. Springer, 1909.
- [77] Dehlinger, U. (1929). Zur theorie der rekristallisation reiner metalle. *Annalen der Physik*, 394(7), 749-793.
- [78] Nabarro, F. R. N. (1952). Mathematical theory of stationary dislocations. *Advances in Physics*, 1(3), 269-394.
- [79] Burgers, J. M. (1940). Geometrical considerations concerning the structural irregularities to be assumed in a crystal. *Proceedings of the Physical Society*, 52(1), 23.
- [80] Taylor, G. I. (1934). The mechanism of plastic deformation of crystals. Part I. Theoretical. *Proceedings of the Royal Society of London. Series A, Containing Papers of a Mathematical and Physical Character*, 145(855), 362-387.
- [81] Dingley, D. J., & McLean, D. (1967). Components of the flow stress of iron. *Acta metallurgica*, 15(5), 885-901.
- [82] François, D., Pineau, A., & Zaoui, A. (1998). *Mechanical behaviour of materials*. Dordrecht: Kluwer academic publishers.
- [83] Bergström, Y. (1970). A dislocation model for the stress-strain behaviour of polycrystalline α -Fe with special emphasis on the variation of the densities of mobile and immobile dislocations. *Materials Science and Engineering*, 5(4), 193-200.

-
- [84] Staker, M. R., & Holt, D. L. (1972). The dislocation cell size and dislocation density in copper deformed at temperatures between 25 and 700 C. *Acta Metallurgica*, 20(4), 569-579.
- [85] Holt, D. L. (1970). Dislocation cell formation in metals. *Journal of Applied Physics*, 41(8), 3197-3201.
- [86] Langford, G., & Cohen, M. (1969). Strain hardening of iron by severe plastic deformation. *ASM Trans Quart*, 62(3), 623-638.
- [87] Louchet, F., Cochet Muchy, D., Brechet, Y., & Pelissier, J. (1988). Investigation of dislocation mobilities in germanium in the low-temperature range by in situ straining experiments. *Philosophical Magazine A*, 57(2), 327-335.
- [88] Louchet, F., <http://www.numodis.fr/tridis/TEM/index.html>
- [89] Mughrabi, H. (1983). Dislocation wall and cell structures and long-range internal stresses in deformed metal crystals. *Acta metallurgica*, 31(9), 1367-1379.
- [90] Y. Bergström and W. Roberts, *Acta Met.*, 19 (1971) 815.
- [91] Y. Bergström, *Mater. Sci. Eng.*, 9 (1972) 101.
- [92] W. Roberts et al, *Mat. Sci. Eng.*, 11 (1973) 247-254
- [93] R. Vetter and A. van den Beukel *Scripta Met.* Vol. II, pp. 143-146, 1977]
- [94] Y. Bergström and H. Hallen, *Mat. Sci. Eng.*, 55 (1982) 49 - 61
- [95] A. Einstein, *Ann. Phys* (1905) Vol. 322 -8, pp 549 - 560
- [96] A. H. Cottrell and B. A. Bilby, *Proc. Phys.Soc.. A*, 1949, 62.1: 49.
- [97] H. Mecking, Argonne National Lab., Ill.(USA), 1975. Conference on radiation damage in metals, Cincinnati, Ohio, USA, 9 Nov 1975
- [98] Mecking, H., U.F. Kocks, and H. Fischer. 4. International Conference On Strength Of Metals and alloys, Nancy, France, 30 Aug 1976. 1976.
- [99] G. Engberg and L Lissel. *Steel Res Int* 79.1 (2008): 47-58.
- [100] Hansson, Sofia, and Konstantin Domkin. "Physically based material model in finite element simulation of extrusion of stainless steel tubes." 8th International Conference on Technology of Plasticity (ICTP), Verona, Italy, 9-13 oktober 2005, 2005. 2005.
- [101] J. D. Baird, *Iron and steel*, 1963, 36.5: 186-192.
- [102] W. C Leslie and E. Hornbogen, (1994). *Physical Metallurgy*, ed. by RW Cahn and P. Haasen.
- [103] Penning, P. (1972). Mathematics of the Portevin-Le Chatelier effect. *Acta Metallurgica*, 20(10), 1169-1175.
- [104] Kang, J., Wilkinson, D. S., Jain, M., Embury, J. D., Beaudoin, A. J., Kim, S.,... & Sachdev, A. K. (2006). On the sequence of inhomogeneous deformation processes occurring during tensile deformation of strip cast AA5754. *Acta Materialia*, 54(1), 209-218.
- [105] Ait-Amokhtar, H., Fressengeas, C., & Boudrahem, S. (2008). The dynamics of Portevin–Le Chatelier bands in an Al–Mg alloy from infrared thermography. *Materials Science and Engineering: A*, 488(1), 540-546.
- [106] Brindley, B. J., & Barnby, J. T. (1966). Dynamic strain ageing in mild steel. *Acta Metallurgica*, 14(12), 1765-1780.

-
- [107] Wullink, J., van den Berg, F., van Liempt, P., & de Haas, M. (2008). Thermography applied to the evaluation of non-uniform deformation heat of metals. *Quantitative InfraRed Thermography Journal*, 5(1), 69-80.
- [108] P. Penning. *Acta Met.* Vol. 20, 1169- 1175 (1972)
- [109] C. G. Schmid, A. K. Miller. *Acta Met.* 30 615-635 (1982)
- [110] J. Cheng, S. Nemat-Nasser. *Acta Mater.* 48 3131-3144 (2000)
- [111] K. Dehghani , J.J. Jonas. *Met. Mat. Trans. A Volume31 A*, 1375 -1384 (2000)
- [112] K. Dehghani, Thesis. McGill Univerity Montreal Canada (1999)
- [113] G.A. Henshall & A.K. Miller. *Acta Met.* Vol. 37. No. 10. 2693-2704. (1989)
- [114] Stewart, G. R., and J. J. Jonas. Static and dynamic strain aging at high temperatures in 304 stainless steel. *ISIJ international* 44.7 (2004): 1263-1272.
- [115] Barnett, M. R., & Jonas, J. J. (1999). Distinctive aspects of the physical metallurgy of warm rolling. *ISIJ international*, 39(9), 856-873.
- [116] Barnett, M. R., & Jonas, J. J. (1997). Influence of ferrite rolling temperature on microstructure and texture in deformed low C and IF steels. *ISIJ international*, 37(7), 697-705.
- [117] P. van Liempt , M. Onink, A. Bodin. *Adv. Eng. Mat.* 4 No 4 225-232 (2002)

Chapter 3. Experimental methods & techniques

Door meten tot weten, zou ik gaarne als zinspreuk boven elk physisch laboratorium willen schrijven.

H. Kamerlingh Onnes

3.1 Introduction

In this chapter a review of different mechanical tests that are commonly used for obtaining stress-strain data is presented. The choice for the tensile test to conduct this research is based on a strength/weakness analysis of the different tests in section 3.2. The details of the experimental equipment are summarized in section 3.4, and some innovative methods that were developed to improve on the weaknesses of the tensile test and to optimize the reliability of the obtained data are described. Some special experimental techniques that are helpful in recognizing different contributions to the flow stress and some issues regarding the fitting of constitutive equations to the data are discussed in section 3.5. The chapter closes with some sections that pertain to instrumental effects.

3.2 Comparison of some testing techniques

The main challenges in the field of fitting constitutive equations to experimental data are firstly that all sources of systematic errors in the experiments must be identified and where possible, avoided. Secondly, if the resulting model equations are to be used in the analysis and setup of an industrial process, care must be taken that the parameter values are valid within the process window. For plastic deformation processes the process window can be characterized by the variables strain, strain rate and temperature, of which in industrial processes the former two are either outside the range that is accessible with laboratory equipment, or can only be accessed with methods that compromise the requirements of minimal systematic error. In the following subsections some commonly used techniques will be discussed with respect to these issues and our choice of a suitable experimental method for obtaining work hardening data will be substantiated.

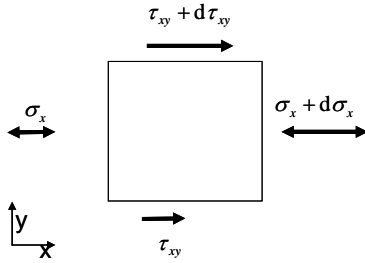
3.2.1 Plane strain compression

In order to obtain stress-strain data at high temperatures, compression testing and tensile testing are equally popular. Compression tests do not exhibit obvious plastic instabilities like the necking phenomenon, which limits the maximal accessible strain in the tensile test. The accessible strain rates are commonly an order of magnitude higher than those that can be reached with tensile testing, due to the more advantageous ratio between sample size and deformation velocity.

On the other hand, friction is inevitable in compression testing, which is the cause of an increase of the measured compression force relative to the ideal value for zero friction and causes strain inhomogeneity. This effect becomes more pronounced as the compression progresses, as a consequence of the equilibrium between shear and normal stress, which will be explained in section 0

The effect of friction during compression testing

Consider a plane strain compression process. In two dimensions for a rectangular coordinate system (see Figure 3-1) the equilibrium equation reads



$$\frac{\partial \sigma_x}{\partial x} + \frac{\partial \tau_{xy}}{\partial y} = 0, \quad (3.1)$$

Figure 3-1. Equilibrium of stresses: horizontal gradient of σ_x caused by a vertical gradient of τ_{xy}

where σ_x and τ_{xy} are respectively the normal and shear stress and x and y the horizontal and vertical coordinates. At $y = 0$ (mid-thickness of the specimen), the shear stress is zero for reasons of symmetry, since the shear forces at the top and bottom of the specimen have the same and the corresponding surface normals have opposite directions.

Approximating the vertical shear stress gradient $\frac{\partial \tau_{xy}}{\partial y}$ by $\frac{\Delta \tau_{xy}}{\Delta y}$ taking $\Delta y = \frac{t}{2}$

and $\Delta \tau = \tau_{xy} \left(y = \frac{t}{2} \right) - \tau_{xy} (y = 0) = \tau$, yields

$$\frac{\partial \tau_{xy}}{\partial y} \approx \frac{\Delta \tau_{xy}}{\Delta y} = \frac{2\tau}{t}, \quad (3.2)$$

where τ is the shear stress at the surface of the specimen and t its thickness It is obvious that the shear stress gradient, and therefore the gradient of the horizontal stress component becomes larger for decreasing values of t , since from eqs.(3.1) and (3.2) the horizontal stress gradient reads

$$\frac{\partial \sigma_x}{\partial x} = -\frac{2\tau}{t} \quad (3.3)$$

The horizontal stress can now be computed by integration along the width of the contact area w $-\frac{w}{2} \leq x \leq \frac{w}{2}$. The boundary conditions are

$$\sigma_x(x = w/2, -w/2) = 0 \text{ for the horizontal stress and } \begin{cases} \tau(-w/2 \leq x \leq 0) = \tau_f \\ \tau(0 \leq x \leq w/2) = -\tau_f \end{cases} \text{ for}$$

the shear stress, the value of which for simplicity is taken constant here:

$$\left| \tau_{xy} \left(x, y = \frac{1}{2} \right) \right| = \tau_f.$$

The horizontal stress function then reads:

$$\sigma_x = \text{sgn}(x) \frac{2\tau_f}{t} x - \frac{\tau_f}{t} w \quad (3.4)$$

The vertical stress component follows from the horizontal stress component and the flow stress by application of the von Mises expression for equivalent stress:

$$\sigma_e = \frac{1}{\sqrt{2}} \left\{ (\sigma_x - \sigma_y)^2 + (\sigma_y - \sigma_z)^2 + (\sigma_z - \sigma_x)^2 + 6\tau_{xy}^2 \right\}^{1/2} \quad (3.5)$$

In the case of plane strain deformation,

$$\sigma_z = \frac{\sigma_x - \sigma_y}{2} \quad (3.6)$$

which when substituted in eq. (3.5), yields

$$\sigma_e = \frac{\sqrt{3}}{2} \left\{ (\sigma_x - \sigma_y)^2 + 4\tau_{xy}^2 \right\}^{1/2}. \quad (3.7)$$

By substitution of eq. (3.4) into eq. (3.5) and integrating over the width of the deformation zone, an equation for the mean vertical stress as a function of friction shear stress, sample width and thickness can be derived as:

$$\bar{\sigma}_y = 2 \left(\frac{\sqrt{3} \sqrt{\sigma_f^2 - \tau_f^2}}{3} + \frac{\tau_f W}{4t} \right), \quad (3.8)$$

where σ_f is the flow stress, which is equal to the equivalent stress during plastic deformation. Eq. (3.8) can be regarded as an elementary constant friction plane strain compression model. The assumption of constant friction, which simplifies the mathematics considerably, yields a more conservative estimation of the effects of friction and thickness to width ratio on the compressive stress than the assumption of Coulomb friction.

Introducing a friction factor¹ $\mu_{VM} = \frac{\tau_f}{\sigma_f}$ and the thickness to width ratio

$r_{tw} = \frac{t}{W}$, the ratio R of the mean stress to the flow stress reads

$$R = \frac{3\mu_{VM} + 4\sqrt{3}r_{tw}\sqrt{1-3\mu_{VM}^2}}{6r_{tw}}. \quad (3.9)$$

For the variable range $0 \leq \mu_{VM} < 0.3$ and $0.2 \leq r_{tw} < 1$, this function is plotted in Figure 3-2. For moderate to high values of m , this shows that R differs considerably from $R=1$, and increases as a function of the thickness to width ratio. The correction factor to compute true stress from the compression force thus increases during compression

¹ μ_{VM} is a "constant friction" factor, where it is assumed that the shear stress is proportional to the flow stress. It must not be confused with Coulomb's coefficient of friction.

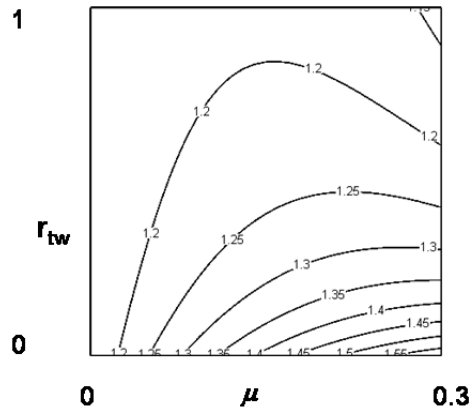


Figure 3-2. Compressive to yield stress ratio R as a function of μ_{VM} and r_{tw}

This problem is aggravated by the complex nature of the friction process, which cannot adequately be described by simple relationships like Coulomb's or constant friction equations [1], [2].

A second effect of friction is that it causes deformation gradients, since according to the Lévy-von Mises flow rule the strain rate tensor is proportional to the deviatoric stress tensor \tilde{S}

$$\tilde{\epsilon} = \Delta\lambda \cdot \tilde{S}, \tag{3.10}$$

where $\Delta\lambda = \frac{3}{2} \frac{\dot{\epsilon}_e}{\sigma_e}$ and the stress tensor \tilde{S} are not constant in the deforming

volume by virtue of eq. (3.1). Hence the equivalent strain will not be homogeneous, and this inhomogeneity will increase during the test. In the next section a second type of inhomogeneity of strain (and consequently of stress), that occurs due to the two dimensional nature of deformation in the plane strain process, will be discussed.

Slip-line field-like inhomogeneity in the compression test

In the analysis of force displacement measurement obtained by compression testing, in particular for the calculation of true stress and strain curves, it is often assumed that the strain distribution is continuous (like in the previous section) or even homogeneous. The opposite assumption, namely that the distribution of strain is discontinuous, forms the basis of (discrete) slip-line field analysis. In this approach, the strain distribution of the plane strain compression test is described as a collection of infinitely narrow slip planes that

separate blocks of material that do not plastically deform. The slip-line field theory can only be formulated for two dimensional deformation processes, like rolling, sheet drawing and the plane strain compression test. In the absence of friction the shear planes are flat; if friction is taken into account they are curved. The slip planes are chosen so as to meet the kinematic boundary conditions. During deformation, the pattern obviously has to change to maintain the boundary conditions. The optimal slip-line field as a function of the thickness to length ratio Δ according to this theory is found by a principle of minimum energy dissipation.

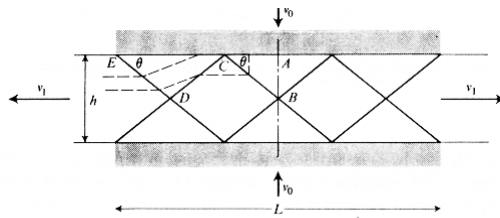


Figure 3-3. Slip-line field for frictionless plane strain compression [3].

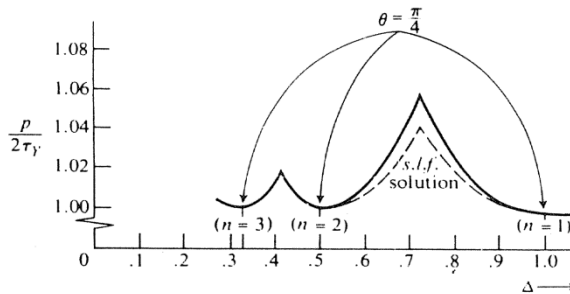


Figure 3-4. Tool pressure p normalized by yield stress in shear τ_y as a function of Δ [3].

For the plane strain compression problem of Figure 3-3 this is shown in Figure 3-4, where the normalized tool pressure which is proportional to the energy dissipation rate is plotted for three slip-line configurations. In this figure, n is the number of slip-line pairs in the solution. (For each possible field only the part of the curve that is lower than any of the others is plotted.) Note that for

integer values of $\frac{1}{\Delta}$ the energy dissipation is minimal, and the orientation of the slip-lines to the horizontal is $\Theta = \frac{\pi}{4}$.



*Figure 3-5. Discontinuous strain distribution in plane strain compression. FEM simulation.
From Gelin et al. [4].*

The slip-line field theory, which assumes rigid-ideally plastic (zero work hardening) behaviour, has become quite obsolete in practice, as FEM simulations are able to describe any stress and strain gradient and pose no restrictions to the constitutive behaviour. Surprisingly, the assumption of a discontinuous strain distribution appears to be valid to a certain degree [4] as shown in Figure 3-5 Figure 3-6, where the strain gradients appear to be quite localized and resemble a mildly smoothed slip-line field picture.

In the latter it is seen that the pattern of shear planes adapts to the changing kinematic boundary conditions during the test, not unlike what is predicted by slip-line field theory. The FEM and experimental results suggest that a localized strain distribution is energetically favourable to an –as usually assumed– continuous strain gradient or homogeneous strain distribution. This was also concluded by Kudo [5], who calculated the internal energy dissipation rates for continuous and discontinuous velocity fields in plane strain extrusion.

Backofen [3] noted that eventually the pattern has to spread out from the slip-lines due to work hardening. From results of hardness tests on deformed material he however concluded that even for work hardening material, there is evidence of a deformation pattern resembling a more discrete slip-line field. The consequence of this behaviour is that the local strains and strain rates are larger than their nominal values, and that a temperature gradient will develop. At large strains, this becomes less severe due to the refinement of the deformation pattern, which smooths out the deformation gradients. This implies that the measured stress- strain curve in a plane-strain compression

test is a weighted average of a distribution of stress-strain curves over a range of strain, strain rate and temperature.

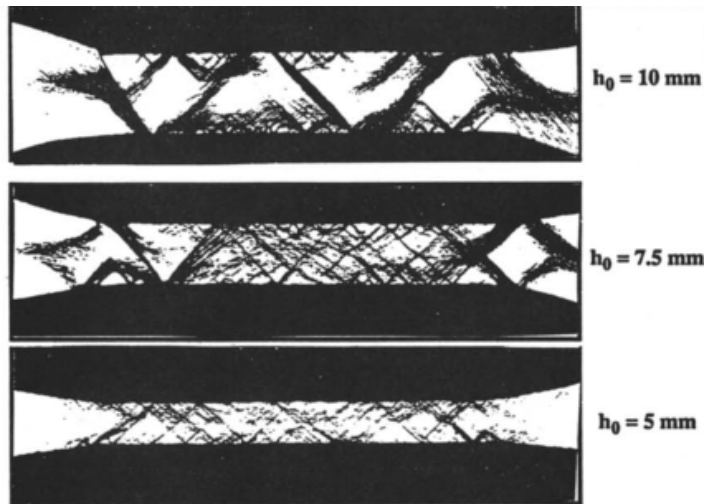


Figure 3-6. Discontinuous strain distribution in plane strain compression of Al. From Gelin [4]

To address this problem, the analysis of compression test results is now sometimes done with the aid of inverse FEM methods in order to identify the parameters that can be related to a constitutive model [6], [7].

Conclusion

From the discussion in the previous two sections it follows that the effect of friction on process force increases with strain, but that the slip-line field like gradients are becoming less pronounced at increasing strains.

3.2.2 Axisymmetric compression

The situation in axisymmetric compression has many similarities to that of plane strain compression, and we will not discuss it here in the same detail. There are however a few important differences.

A discontinuous gradient like that of the slip-line field of the plane strain test is not likely to occur, since the plastic flow is three dimensional. Any continuous strain gradients associated with friction will be observable to a certain extent as an increasingly barrel like shape of the outer surface. In many cases the strain gradients can be considerably more complex as the outer shape suggests, as can be seen in Figure 3-7, where the segregation bands were originally parallel. FEM

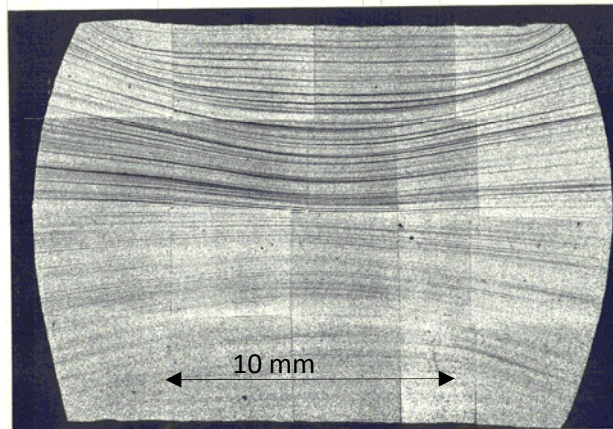


Figure 3-7. Barrelled uniaxial compression sample.

simulations of an axisymmetric compression test [8] also show large strain gradients, see Figure 3-8.

The effect of friction on the stress and strain state will be much larger in axisymmetric compression than in in plane strain compression, since the contact area increases during deformation (whereas that in plane strain compression is constant), so that the equivalent of the integration in eq. (3.3) leads to much higher compressive stresses.

The conclusion is that the correction for friction for axisymmetric compression

testing is probably more problematic than that for plane strain compression. Another adverse effect of friction is that the stress gradients cause yielding not to take place in the complete volume at the same stress, but that it gradually

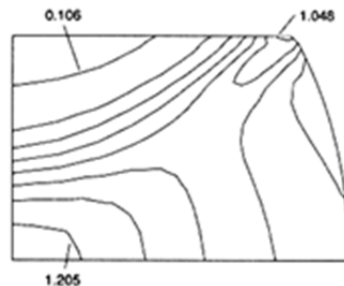


Figure 3-8. FEM simulation of an axisymmetric compression test. Local strain contours (top right hand quarter), nominal strain $\epsilon_e = 0.69$. From [8].

spreads from the position where the equivalent stress is maximal. The result is that the apparent stiffness gradually decreases, and that the yield point is poorly defined.

3.2.3 Torsion

The torsion test is free from friction and its associated stress and strain gradients.

On the other hand, the torsion test exhibits a pronounced strain gradient in the radial direction, which is however of geometrical origin, and can therefore quite reliably be taken into consideration.

The usual algorithm [9] for reducing torque vs. torsion curves to true stress and true strain relies on the assumption of constant work hardening behaviour as a function of radial position of the considered material elements. This is not an unrealistic assumption in the case of slow torsion tests at room temperature, but will be unrealistic at higher temperatures, where the mechanical behaviour is strongly dependent on strain rate and temperature. High torsion rates will worsen the situation, as they will cause temperature gradients due to the strain rate gradient in the radial direction.

A workaround is to perform the torsion test with hollow samples, which will however become prone to buckling for thin walled samples (which are desirable for reducing radial strain rate and temperature gradients). Another approach is differential torsion [9], [10] the principle of which is to repeat each torsion test with one where the specimen has a slightly different diameter. Subtracting the torsion signals of the two tests will yield the torsion value for a (virtual) hollow sample. The buckling problem is effectively circumvented by this method.

3.3 Tensile test

Like the torsion test, the tensile test is free from friction. Provided that the length to width region of the tensile sample is large enough, the stress state is one of uniaxial stress and is constant in the gauge section. Consequently, the strain tensor will have a zero gradient in that region.

An important advantage of the lack of stress gradients is that the observability of the yield stress is optimal. This will be further discussed in the section on the yield criterion. It is assumed that the sample is free from residual stresses, which may also have a negative effect on the observability of the yield stress. Since our experiments are conducted at elevated temperatures, and after a phase transformation, it is safe to assume that residual stresses will be absent.

A disadvantage of the tensile test is the development of a plastic instability as soon as the work hardening rate of the material becomes smaller than the

geometrical softening rate due to the decreasing cross section. This is the necking phenomenon, which is essentially the development of a strain gradient (and to a lesser degree a stress gradient) after an initially uniform elongation range of strain. The onset of necking can be predicted by the well-known Considère criterion

$$\left. \frac{d\sigma}{d\varepsilon} \right|_{\text{onset of necking}} = \sigma \quad (3.11)$$

This condition is equivalent to that of maximal force in the tensile test, which condition is met when the work hardening rate becomes smaller in magnitude than the geometrical softening rate. In eq. (3.11), σ and ε have the meaning of equivalent stress and strain. In the tensile test σ and ε are equal to the longitudinal stress and strain, which in that case are by definition equal to the equivalent stress and strain.

The onset of necking is readily observable from the raw data, as the engineering stress reaches its maximum at that instant. In the case of deformation in the austenitic temperature range, the uniform elongation is typically a few tens of percent, which is much smaller than the thickness reduction of the material in a Hot Rolling mill stand.

The necking phenomenon thus limits the range of strains that are accessible in a tensile test. Without special measures only the data obtained in the uniform strain range can be used to be converted to true stress vs. strain curves, for example by a post-mortem analysis of the depth of the neck, which after interpolation of necking between onset of necking and failure can be used to compute true stress vs. strain curves that extend into the post uniform strain range by the application of a Bridgman correction [11]. Another option is to measure local strains during necking with a contacting [12] or non-contacting device. In the case of flat specimens, all relevant stress and strain gradients are observable. In this study a non-contacting method applying simple means will be developed, which will be described in section 3.4.5.

The disadvantage of a limited useful strain range in the tensile test can now be overcome by straightforward methods, and values of true stress and strain can be obtained up to the strain at which local necking sets in. Combined with the absence of intrinsic deformation and stress gradients this has been decisive for our choice to apply tensile test as standard method to obtain stress-strain data. The other disadvantage, i.e. the limited strain rates, will be discussed in section 3.5.1 on ausforming.

In the following sections we will show how the advantage of the tensile test with regard to observing deformation gradients can be put into practice by the employment of imaging techniques.

3.4 Hot tensile testing techniques

Several methods for conducting tensile tests at elevated temperature have been developed. Some of these apply an external heating source, like a radiation furnace. Another is by heating of the specimen by means of an electrical current, which allows superior control of temperature and heating/cooling rates. This is implemented in the DSI Gleeble system, which will be used in this study.

3.4.1 General description of the Gleeble system

The tensile testing machine used in our research project is a Gleeble 3800 thermomechanical simulator. The Gleeble system excels in fast and accurate temperature control. In the Gleeble system, the sample is heated by an electric current, which results in a quite direct temperature control.

The specifications of the Gleeble can be summarized as

- Displacement rate up to 2000 mm/s (depending on load)
- Maximum stroke distance 150 mm (depending on sample length)
- Maximum force/load: in tension 98 kN, in compression 196 kN
- Heating rate up to 10.000 °C/s (for welding simulations, depending on sample size)
- Steady state equilibrium temperatures within +/- 1 °C
- Cooling rate: up to 250 °C/s (depending on material and sample size, quench media)
- Atmospheric conditions: rough/high vacuum, protective gasses (argon, nitrogen)
- Sample sizes and shapes: round, hollow and square shapes, maximum cross-section area 250 mm²
- maximum length 250 m
- Measured parameters: displacement, dilatation, temperature (4 couples of any kind + 1 infrared pyrometer) , force,
- Other devices: Hot zone LVDT, Dilatometer LVDT, spot welder for attaching thermal couples
- Digitally controlled force or displacement system
- Maximum sample rate 20.000 Hz

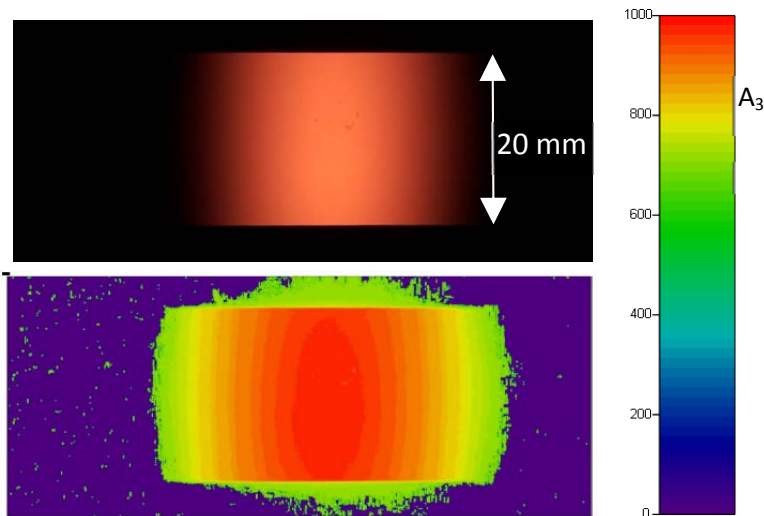


Figure 3-9. Temperature map Gleeble specimen (below) obtained by thermal imaging (above),

A disadvantage of the Gleeble tensile system is that no heated grips are available. Consequently, a large temperature gradient will develop in the sample. The temperature difference between the centre and ends of the gauge section can become in excess of 200 °C as shown in Figure 3-9, which was produced by visible light imaging and thermography. This will contribute to the necking phenomenon: a neck which is not due to plastic instability in the sense discussed in section 3.3 will be initiated at the very start of the test, because the centre of the gauge section is softer than its extremities.

At nominal temperatures close to the γ - α transformation temperature this can lead to a situation where the centre of the sample is in the austenitic phase, while close to the shoulders it will still be in the ferritic state. Since the yield and flow stresses of ferrite at temperatures just below the transformation temperature are lower than that of austenite just above that temperature [13], the sample will then deform more easily in the ferrite regions, as shown in Figure 3-10.

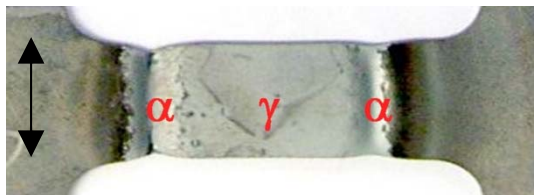


Figure 3-10. Sample that has transformed to ferrite at the shoulders.

From the thermal image shown in Figure 3-9, it is obvious that the image contrast between the shoulders and the background is lost due to the temperature gradient. Since we -as will be discussed in a subsequent section- will make use of an edge detection technique to measure local deformation during necking, this is a second disadvantage of the heating system. In order to minimize the thermal gradients and their associated negative effects, a new type of sample was developed.

3.4.2 A tensile specimen design to minimise the temperature gradient

Aims

The aim of the development of a low T-gradient sample combined with a method to measure local strains is to arrive at a situation where the temperature at any point of the gauge section is as close as possible to the nominal temperature, and to extend the useful strain range beyond the uniform strain. These requirements can be stated more precisely as follows.

A major goal of the development is to measure local strains, so that true stress and strains can be computed in the post-uniform strain range of the test. We will restrict the application of the correction for local strains of the stress-strain curve to the diffuse necking phase of the post uniform strain range. In that range it may be assumed that the strain gradient in the width direction is negligible. It is therefore sufficient to measure the total strain in the width direction (and for non-isotropic materials in the thickness direction). We have chosen to achieve that by recording the sample shape during deformation by a video device. To obtain the width (and thickness) strain from the video stream an edge detection technique is applied to the resulting images, as will be described in section 3.4.5. This also requires a constant contrast between the sample surface and the background. It is therefore of importance to avoid temperature gradients in the gauge section, as the intensity of radiation of the surface is a strong function of temperature at the target test temperatures.

The video stream can at the same time be utilized for pyrometry, so that the temperatures at the specimen surface can be recorded as a function of time and position. This is applied in setting up the sample for achieving a minimal temperature gradient.

Design considerations

The temperature gradient in a conventional tensile sample that is heated by an electrical current is caused by the heat flow from the heated gauge section to the cooled grips of the tensile machine. In addition, the current density in the wider shoulders of the specimen is lower than that in the gauge section, by a factor equal to the ratio of the gauge cross section to the shoulder cross section. Consequently, there is a substantial heat flow from the gauge to the shoulders. By virtue of Fourier’s law of heat

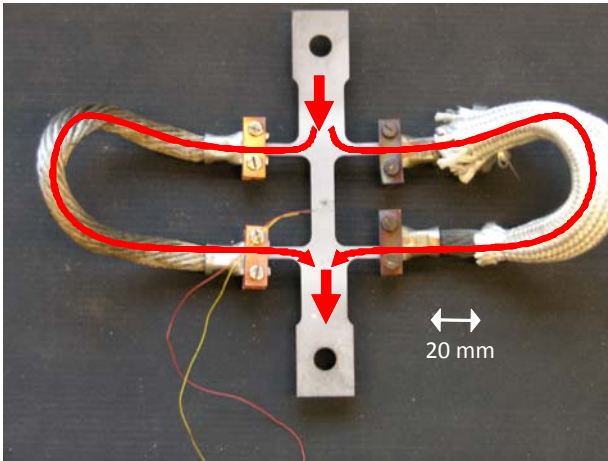


Figure 3-11. The low T gradient design sample.

condition this heat flow is associated with a temperature gradient in the direction of the heat flow. Compensation of this heat flow and the associated temperature gradient requires an additional heat source between the gauge section and the grips. Ideally, if two regions on the sample can be controlled to have the same temperature, no heat will flow between them and no temperature gradient will develop. This however requires two power sources (for the gauge respectively the shoulder regions) that can be separately controlled.

Therefore a simplified approach was chosen, where the electrical current density in the shoulders is made equal to that in the gauge section. If the distance between the grips and the shoulder to the gauge section is large enough, this will lead to an equal heating

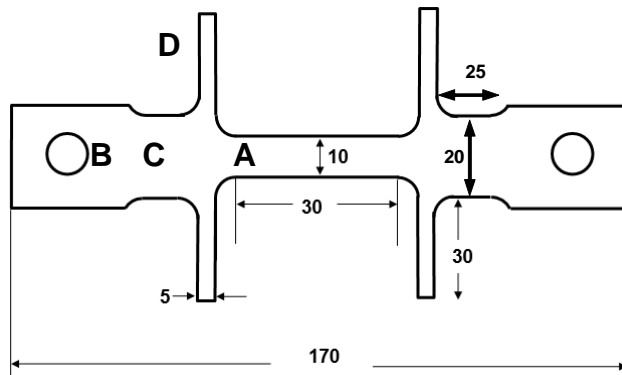


Figure 3-12. Low temperature gradient specimen design (dimensions in mm).

rate and eventually equal temperatures of in the shoulder and gauge section. Consequently, no temperature gradient will develop.

This can be achieved by shunting a part of the electrical current between the

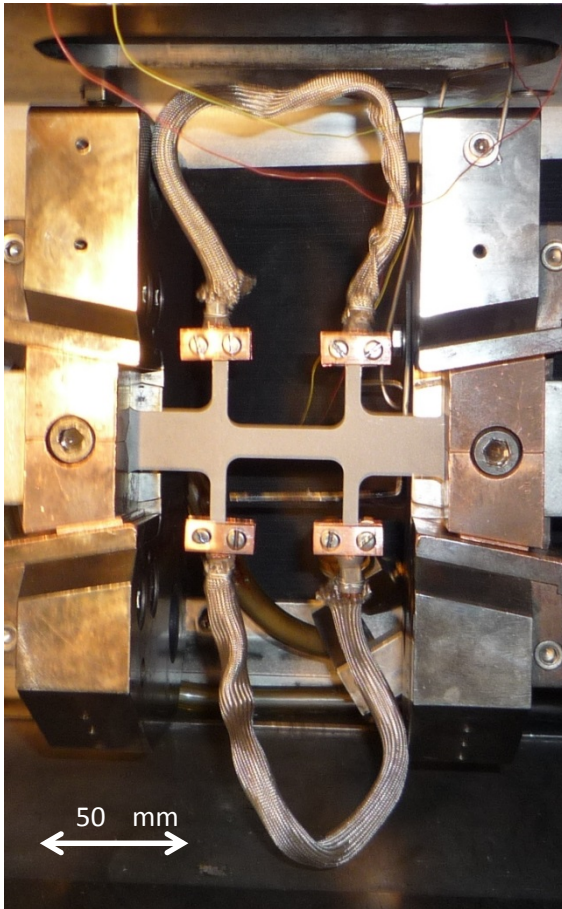


Figure 3-13. Fully rigged sample mounted in Gleeble tensile machine.

grips past the gauge section as shown in Figure 3-11. The shunt resistance is implemented by the legs that protrude in the transverse direction between the gauge region and the shoulders, which are connected by a flexible braided copper cable. The shunt resistance is adjustable by the positioning of copper clamps with which the cables are bolted to the shunt legs, as shown in Figure 3-11 and Figure 3-13. The position of the clamps should be chosen such that the electrical current densities in the gauge, shoulder and shunt sections are equal.

The heating rates will then be equal and consequently the temperatures in these sections will eventually become equal to the gauge temperature that is controlled by the heating system. The temperature gradient

in the gauge section will become minimal. An optimal adjustment can be achieved by monitoring the temperature in these three parts of the sample with the pyrometric technique that will be described in section 3.4.4. Additionally, as the shoulders now have a higher temperature, additional shoulders wider than the existing ones will have to be added, to avoid deformation of the sample close to the grips.

The new tensile specimen design, the dimensions of which are shown in Figure 3-12, has an additional section **C** of intermediate width between the gauge section **A** and the shoulders **B**. As customary in tensile sample design, the width

w_C of section **C** taken $w_C = 2w_A$, where w_A is the width of the gauge section. This is in order to avoid plastic deformation in the C section, which cannot occur before the engineering stress in the gauge section A has increased to twice the value of the yield stress.

The shunt resistance consists of strips of metal **D** projecting perpendicularly from the joint between the gauge and auxiliary sections. Two of these sets of

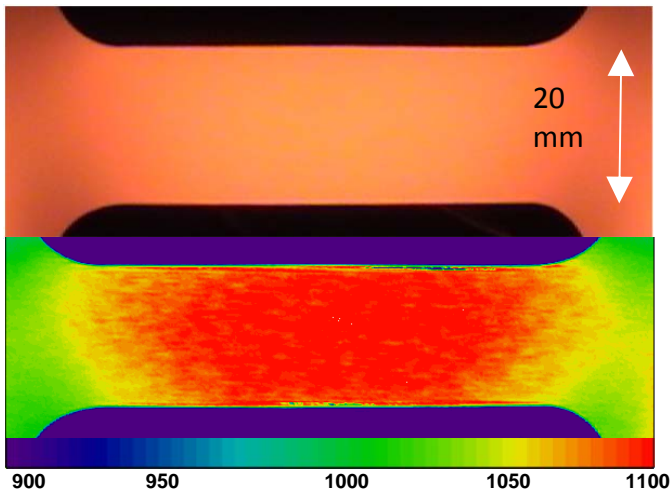


Figure 3-14. Temperature distribution in the low T gradient design sample.

shunt strips are implemented on each side of the specimen, in order to maintain symmetry of electrical currents and heating rates in the width direction. The width w_D of the shunt strips is taken as $w_C = \frac{1}{2}w_A$.

To ensure that the current densities in the sections **A**, **C** and **D** are equal,

the widths should be chosen according to the rule: $w_A + 2w_D = w_C$. Equal current densities are equivalent to equal heating rates and eventually to equal temperatures in the three sections. That ensures that no heat flows into or out of the gauge section. The joints between sections **C** and **D**, respectively **A** and **D**, are rounded to avoid both electrical current and stress concentrations.

The performance of this setup is quite satisfactory, as shown in Figure 3-14 and Figure 3-15. The temperatures in these figures were determined by the method described in section 3.4.4. The temperature differences within the gauge section of the improved sample are smaller than 5 °C. This has recently been corroborated by a FEM simulation of the system [14]. The temperature in the joining areas between sections **A**, **C** and **D** is 50-100 °C below the nominal temperature. This is caused by the inevitable locally lower electric current density in this region because of the larger local width. During deformation, especially after the onset of necking, the temperature gradient will deteriorate somewhat, which is caused by the non-uniform cross section of the gauge section and the consequently higher current density and heating rate in the necking region.

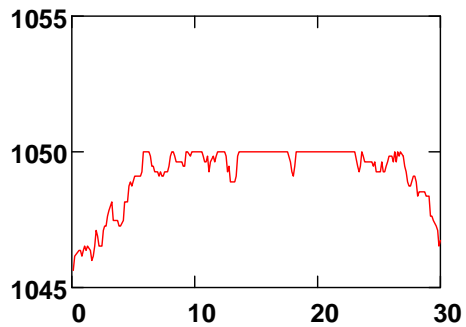


Figure 3-15. Example of the temperature gradient in the gauge section. T vs. position in the gauge section.

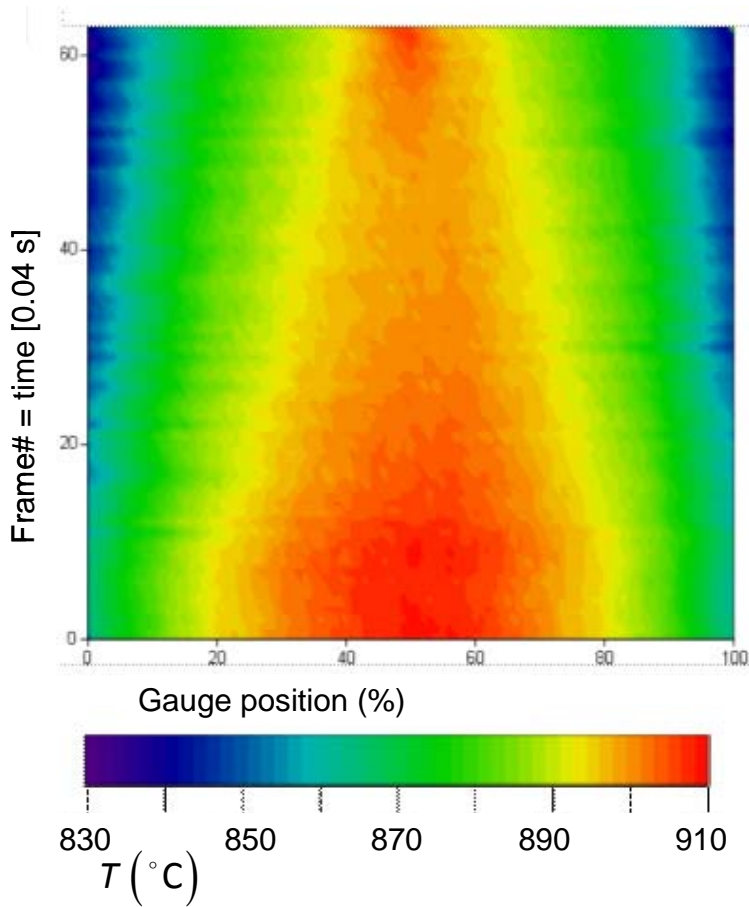


Figure 3-16. Temperature along the gauge during deformation.

$$T = 910 \text{ } ^\circ\text{C} \quad \dot{\epsilon} = 0.2 \text{ s}^{-1}.$$

In the tests at strain rates higher than $\dot{\epsilon} = 0.02 \text{ s}^{-1}$ the heating has been switched off during deformation. This proved to be possible since the resulting cooling rate is small, and the temperature drop during deformation is negligible ($< 5 \text{ } ^\circ\text{C}$). This is beneficial for the noise in the force and elongation signals caused by the heating system that is discussed in section 3.7.2. During necking, the temperature will rise again slightly in the necking region as a consequence of the higher local strain rate in the neck region. The performance of the system with regard to temperature distribution during deformation is shown in Figure 3-16. The remaining temperature gradient poses no problems in fitting stress strain data to a model equation, since we will measure strain rate and temperature locally in the middle of the sample where necking occurs and the strain becomes maximal.

3.4.3 Video equipment

All deformation experiments are routinely recorded with a digital video camera, which enables to quantify any visually observable phenomena like strain and temperature gradients². For experiments at strain rates $\dot{\epsilon} \leq 0.2 \text{ s}^{-1}$ a standard commercial digital HD camcorder was used, the resolution and frame rate of which are 1920X1080 pixels and 25 fps. For higher strain rates, a Phantom V5.0 by Vision Research was used. The frame rate of this camera is dependent on the resolution. We have chosen for a resolution of 1024X512 pixels, which yields optimal image definition. The maximal frame rate for this setting is 2100 frames.s⁻¹. At the maximal applied strain rate $\dot{\epsilon} = 15 \text{ s}^{-1}$, 40 frames can be recorded at an estimated total strain range $\epsilon = .3$ which is considered to be adequate. The video streams of either camera can be read by the open source image processing application ImageJ [15], which is implemented in the Java programming language. With this application all final image processing and conversion of video data to ASCII data files was performed.

3.4.4 Contactless temperature measurement

Due to the necking phenomenon a temperature gradient will develop in the neck (Figure 3-16), as the deformation rate inside the neck increases relative to the more slowly deforming sections. More deformation energy will therefore be dissipated in the neck. Additionally, the electrical current density will become non uniform and be maximal in the neck. The latter situation can be avoided for fast ($\dot{\epsilon} > 0.1 \text{ s}^{-1}$) deformation tests by switching the heating off during deformation.

It is therefore desirable to quantify the temperature field in the sample during the tests. As the tests on steel in the austenitic phase are executed at temperatures where the emitted radiation by the specimen is in the visible part of the spectrum, we have chosen for visible light pyrometry.

² The idea to measure temperatures visually was inspired by the blacksmith's traditional skill of judging temperature.

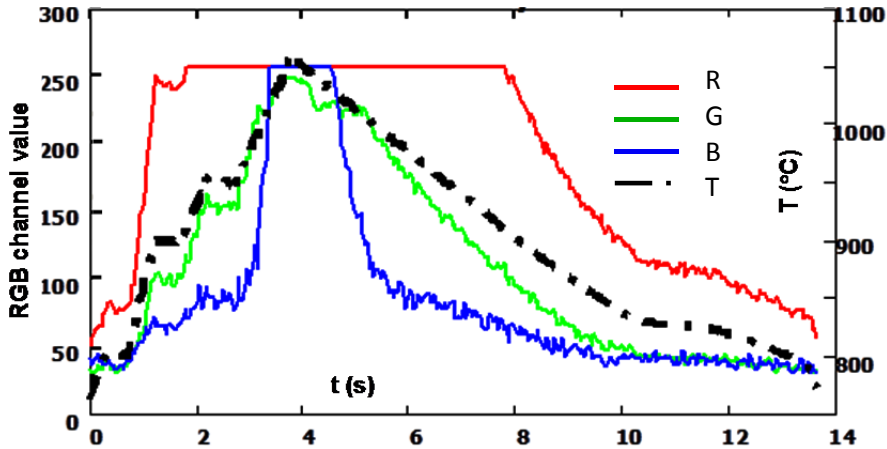


Figure 3-17. RGB intensities HD camera during a heat cycle. R, G, B channels and thermocouple temperature are shown.

The measurement of temperatures as a function of time and position is carried out by extracting the RGB intensities from the video stream as a function of time and position from a video stream using ImageJ. For calibrating the recorded intensities to actual temperatures, a series of heat cycles was programmed. The camera recording is started by a Gleeble system relay at a programmed instant. A sample of the recorded RGB intensities and the thermocouple readout are shown in Figure 3-17. Note that particularly the red channel tends to saturate at the chosen exposure setting. This could be avoided by choosing a less sensitive exposure, which however proved to be detrimental for the signal to noise ratio. Therefore, and since the high-speed equipment records in B&W, the actual calibration is carried out by fitting the thermocouple temperature during the heating cycle as a function of luminosity L , defined as

$$L = \frac{R + G + B}{3},$$

where R , G and B are respectively the 8-bit pixel intensity values of the red, green and blue channels of a pixel at the position of the thermocouple. Fitting was done by a simple polynomial. This was carried out for the range of exposure settings of the camera used for the range of temperatures covered in the experiments.

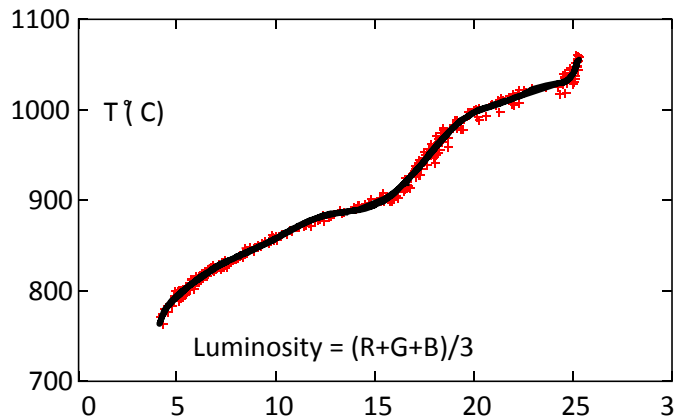


Figure 3-18. Fit of temperature to intensity signal.

This procedure, of which a result is shown in Figure 3-18, yields an accuracy of 5 degrees, which was considered to be adequate for our purpose.

We conclude that in the austenitic temperature range visible light pyrometry using a commercial HD video system is an adequate method for measuring temperature.

3.4.5 Contactless strain measurement

A major disadvantage of the tensile test is that a spontaneous strain gradient evolves once the work hardening rate drops below the flow stress (necking). In Figure 3-19 a sample in an advanced stage of necking is shown.

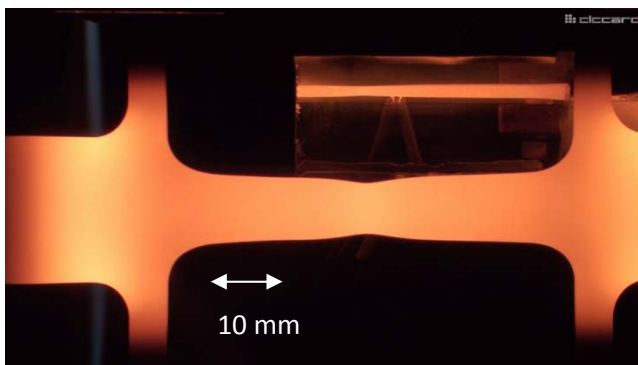


Figure 3-19. Video frame of a deforming sample. Note the mirror for thickness measurements that is mounted above the sample at 45°.

Beyond the onset of diffuse necking, the calculation of true stress and strain data is no longer straightforward: a method of observing the strain gradient is necessary to find the value of the local true strain in the neck. Commonly, only data from the uniform strain range is used in the calculation of true stress and strain.

In a tensile sample designed to deform in uniaxial tension, the strain distribution across the width of the specimen remains fairly uniform during necking [16]. This is confirmed by the results of a tensile experiment that was recorded with the Aramis digital image correlation system present at Tata Steel, an example of which is shown in Figure 3-20, where it is compared with the strain measured with the system developed here. Even at the fairly advanced

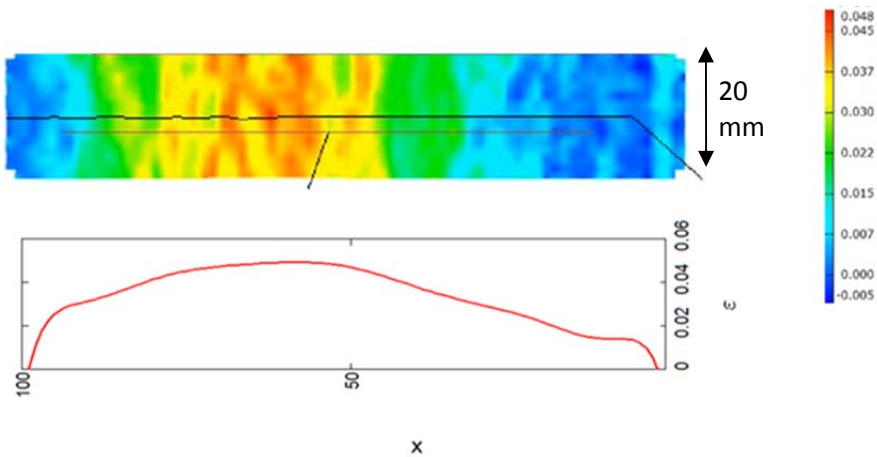


Figure 3-20. Strain distribution recorded with Aramis (above) and the system developed here (below).

stage of necking shown, the transverse strain gradient is negligible. The strain distribution calculated with the system developed here compares favourably with the Aramis graph.

This implies that full knowledge of the two dimensional strain gradient, as can be obtained for example by digital image correlation is not strictly necessary for evaluation of the test results in the post uniform strain region. It is sufficient to compute the local transverse stresses from the local displacements of the sample edges.

We record the shape of the specimen by a digital video camera for low deformation rates or by a High speed camera for strain rates larger than 0.2 s^{-1} . A sample of a frame of a typical video stream is shown in Figure 3-19.

The edge coordinates of the sample as a function of time are determined by application of an edge detection filter technique [17]. For the edge filter, an implementation of the Canny-Deriché filter was chosen, which is available in the public domain as a plug-in for the ImageJ package [18]. This filter produces the detected edges in the form of a video stream. Prior to application of the edge filter, the video stream is convoluted by a Gauss blur filter, in order to avoid the necessity to clean up the edge video stream for artefacts and spatial noise. It was found that application of a Gauss filter with a radius of 4 pixels does not have an effect on the detected edge positions. Finally, the grey scale edge video stream is thresholded and the edge position data written to an ASCII file.

The detected edge shown in corresponds to the frame shown in Figure 3-19. A requirement for success of this technique is that the image contrast between the edge and the background is of a good and constant quality. The improved sample design provides just that, which is a second advantage of the newly designed specimen.

In order to identify the region of interest (ROI, which here is the gauge section) of the edge detected video stream, the centres of the quarter circle fillets of the specimen shoulders between the gauge section and the auxiliary heating sections C of the sample are detected by a Hough transform technique from the edge detected stream. The Hough transform is a feature extraction technique used in image analysis, computer vision and digital image processing [19], which is used extensively in EBSD devices to detect the individual lines of Kikuchi patterns. The technique is applicable for detection of any general shape that can be parameterized, including circles and ellipses.

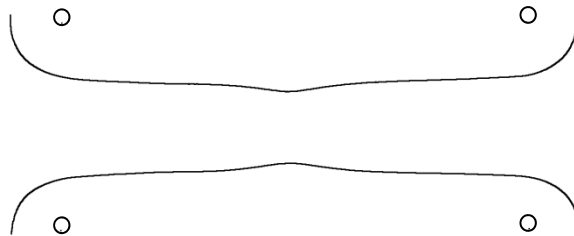


Figure 3-21. Output of the edge detection and Hough transform.

For our requirements a Hough Circle ImageJ plug-in [20] was slightly adapted. The measured coordinates of the extremities of the gauge section serve a secondary purpose as a virtual or contactless clip on gauge. Both the shoulder fillet centre coordinates and the coordinates of the specimen edges are written to files, from which then the local transverse strain $\varepsilon_y(x,t)$ as a function of time and position along the gauge section is computed. An example of a map of the true strain is shown in Figure 3-22 where the locus of maximal strain, which eventually becomes the position of the deformation neck, is shown.

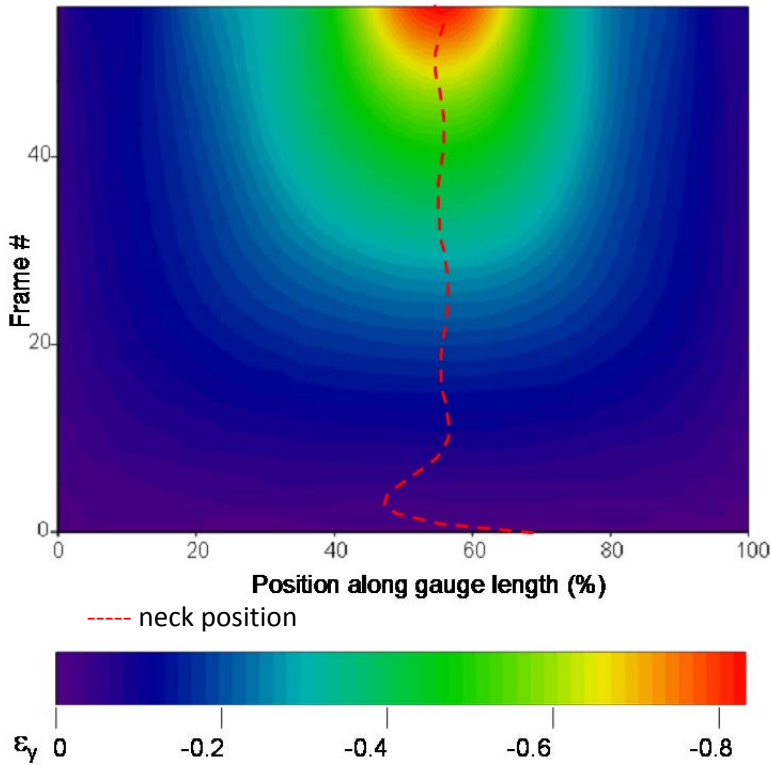


Figure 3-22. Map of the computed longitudinal strain in a tensile test. $T = 950 \text{ }^\circ\text{C}$ $\dot{\varepsilon} = 0.2 \text{ s}^{-1}$

By definition, the true strain ε_e is defined as the logarithmic longitudinal strain ε_x in the tensile test. The transverse strain values must therefore be converted to longitudinal strains. If the material is plastically isotropic, this poses no problem, because then the transverse and thickness strains are equal, and both equal to minus $\frac{1}{2}$ times the longitudinal strain: result from $\varepsilon_x = -2\varepsilon_y = -2\varepsilon_z$. For anisotropic materials, the ratio of transverse to thickness strain is expressed

by Lankford's r -value, in which case $\varepsilon_x = -\frac{1+r}{r}\varepsilon_y$. In our research project, most experiments are carried out on steel in the austenitic phase, which is expected to be nearly isotropic. In order to check this, a mirror is mounted above the specimen at a 45° angle to the horizontal, so that the thickness change during deformation can be observed during the test. The mirror is visible above the gauge section in Figure 3-19.

The image in the mirror is post processed by the same steps (except the Hough transform) as that of the gauge section, leading to a map of the thickness strain as a function of time and position, an example of which is shown in Figure 3-23. Note that an increasing part of the sample disappears out of view due to the limited size of the mirror, and that some artefacts appear at large strains. Therefore, after selection of an area where the measurement is considered reliable, an average of Lankford's r_L value is computed, which is used to convert the transverse strains to longitudinal and equivalent strain. The computed r_L values on average have a value $r_L = 1.0 \pm 0.1$ for all experiments, so that the material behaviour can be considered to be isotropic.

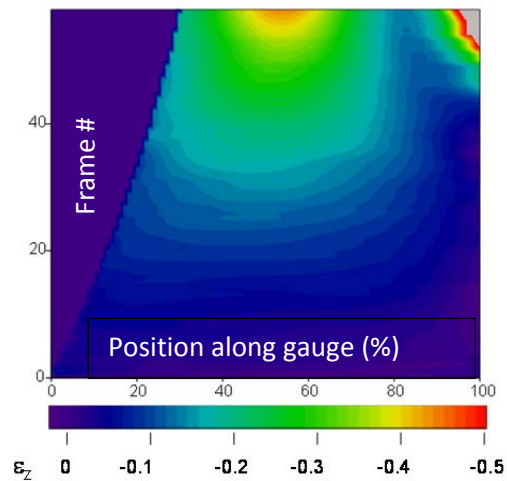


Figure 3-23. Thickness strain map

$T = 950^\circ\text{C}$ $\dot{\varepsilon} = 0.2\text{ s}^{-1}$.

From the strain map, the deformation history, which can be defined as the equivalent strain and strain rate of any material point can be calculated. Although this can be done for any arbitrary point, we have chosen to consider only the neck locus, because that yields the maximum range of strains.

3.5 Special deformation techniques

In this section some techniques will be discussed that are either necessary to circumvent limitations of the experimental equipment, or that are helpful in determining the relative importance of different contributions to the flow stress.

3.5.1 Ausforming: deformation of metastable austenite

The strain rates that can be attained with our sample size on the Gleeble Tensile Test rig are $\dot{\epsilon} = 20 \text{ s}^{-1}$ at maximum. This is one order of magnitude lower than the strain rates in the hot rolling process.

In general, the flow stress σ_f is the sum of a yield stress σ_y , a resistance due to work hardening that is associated with dislocation multiplication σ_w and a resistance associated with thermally activated dislocation glide σ^* . As is discussed in Chapter 2, the latter two are a function of strain rate and temperature:

$$\sigma_f = \sigma_y + \sigma_w(\dot{\epsilon}, T) + \sigma^*(\dot{\epsilon}, T) \quad (3.12)$$

The strain rate and temperature sensitivities of work hardening and dislocation glide resistance are in general -except when dynamic strain aging occurs- such that the flow stress increases for increasing strain rate and decreasing temperature. This behaviour can now be put to advantage to compensate for the limited experimental strain rate by executing hardening tests at temperatures lower than that of the hot rolling process: a lower temperature

will increase the flow stress, as will a higher strain rate.

The temperature range of the target Hot Rolling process extends downwards to the A3 temperature at which austenite starts to transform to ferrite. Considering the Iron-Carbon diagram only, it would seem that trading high strain rate for lower temperature is not feasible since the material will transform to ferrite below the A3 temperature.

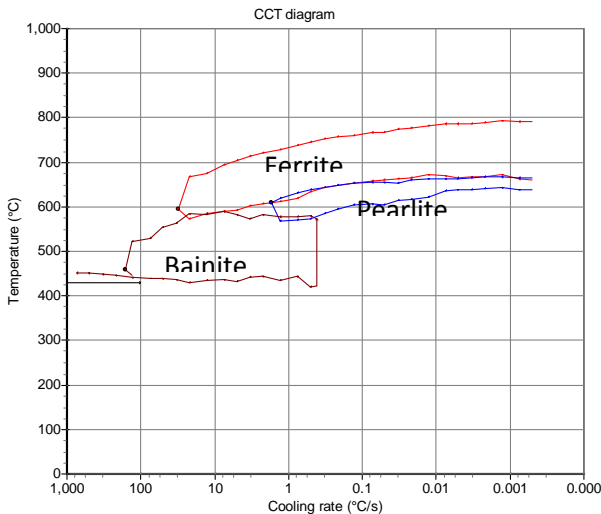


Figure 3-24. Calculated CCT diagram of investigated steel grade.

This may be the case for plain low carbon steel grades, for which the transformation rate is high. However, the steel grade that is investigated in this

study, an Fe-C-Mn alloy of composition 0.09 wt.% C, 1.63 wt.% Mn, 0.25 wt.% Si and 0.55 wt.% Cr, transforms rather slowly, as is shown in Figure 3-24. This CCT diagram was calculated with a model available at TUDelft and Tata Steel [21].

By quenching with Ar, a quenching rate $\frac{dT}{dt} = -60 \text{ }^\circ\text{C s}^{-1}$ can be achieved. This leaves 2.5 s before transformation sets in, which is ample time to perform a tensile test after quenching to temperatures as low as $T = 600 \text{ }^\circ\text{C}$, except for tests at strain rates below $\dot{\epsilon} = 0.2 \text{ s}^{-1}$. It is therefore possible to quench the steel rapidly after austenitisation to a temperature below A3, and perform a tensile test on the metastable austenite before transformation starts. This technique is similar to the ausforming process described by Mukherjee [22] and to Hot Forming [23] of car body parts.

3.5.2 Strain rate jump tests

The flow stress of steel (or any other metal) is a sum of several contributions, like lattice resistance, solute and precipitation hardening, the grain size dependent Hall Petch effect, work hardening and dislocation glide resistance. Of these, the strain dependent work hardening and the dislocation glide resistance are functions of strain rate and temperature due to the underlying thermally activated mechanisms. As discussed in Chapter 2, the flow stress σ_f can be written as

$$\sigma_f = \sigma_o + \frac{K_y}{\sqrt{D_g}} + \sigma_w + \sigma^*, \quad (3.13)$$

where σ_o is the sum of lattice resistance, solute and precipitation hardening, K_y the Hall-Petch coefficient, D_g the grain size, σ_w is work hardening and σ^* the dislocation glide resistance. The sensitivity to strain rate (and temperature) of σ^* is direct because the velocity of dislocations will change immediately when the strain rate (or temperature) is changed. This is not the case for work hardening, as it is the hardening rate $\Theta = \frac{d\sigma}{d\epsilon}$ which depends on strain rate

and temperature. The effect of a change in strain rate (or temperature) is therefore only reflected by a change in work hardening after an increment of strain. For this reason, the strain rate sensitivities of dislocation glide resistance and work hardening have been termed direct respectively indirect strain rate sensitivity (DSRS and ISRS) by the author [24], (Chapter 4).

For this reason –viz. the difference between indirect and direct strain rate sensitivity- the strain rate jump test is a tool that has been used by some authors [25], [26], [27], [28], [29], to distinguish between the work hardening and dislocation glide resistance contributions to the flow stress, something that is impossible with constant temperature – strain rate testing. An alternative name for this technique is “constant structure test” [30], [31]. This name emphasizes that the internal (dislocation sub-) structure does not change appreciably during the strain rate jump. An example is shown in Figure 3-25, where two tests at a constant strain rate $\dot{\epsilon} = 0.01$ respectively 0.1s^{-1} are compared to tests where the strain rate is abruptly changed at $\epsilon = 0.08$ from the higher to the lower rate and vice versa. Note that the DSRS is clearly observable as an abrupt change of the flow stress.

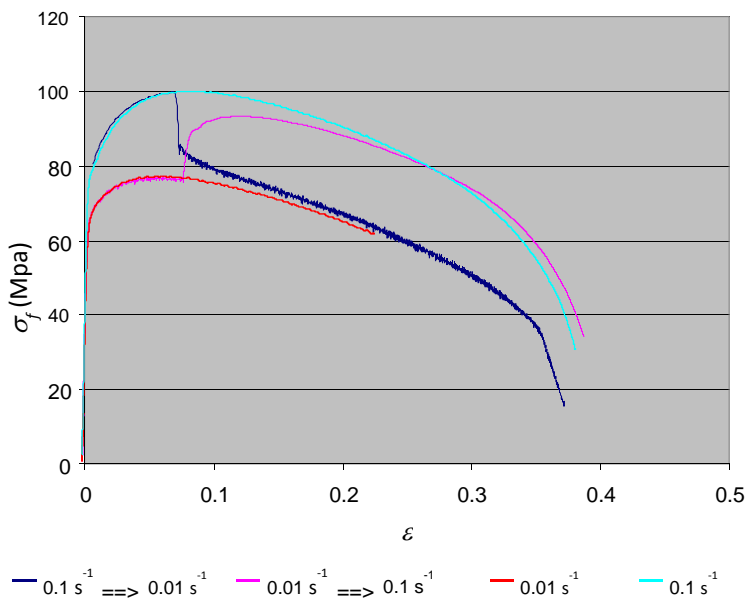


Figure 3-25. Strain rate jump tests at 950 °C. Engineering stress vs. strain.

Another use of this test is to detect any differences between the transient hardening after the jump for jumps from low to high strain rate respectively in the reverse direction. This might reveal different dynamic recovery kinetics in the case of an excess respectively a shortage of dislocation density between these cases. These results will be analysed in more detail in Chapter 7 on work hardening. Repeated strain rate changes during the course of the deformation experiment will reveal whether the glide resistance is a function of strain or remains constant. If the latter proves to be the case, it is also an argument that

corroborates Bergström's assumption [32] that the mobile dislocation density ρ_m is constant, since the glide resistance parameter $\dot{\epsilon}_0$ is proportional to ρ_m .

3.5.3 Stress cycling

Stress cycling is a technique that can provide information with respect to the question whether deformation is reversible or irreversible. Stress cycling at stress amplitudes that remain below the yield stress as depicted Figure 3-26 [33] generally shows the following behaviour:

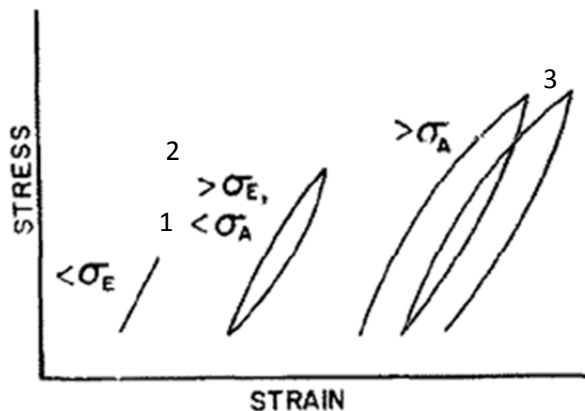


Figure 3-26. Stress cycling behavior below the yield stress. Linear elastic (1), anelastic (2) and microplastic (3) behaviour [33].

1. Reversible linear elasticity at low stresses. The modulus of the stress is equal to the elastic modulus of the crystal lattice.
2. At stresses above the elastic limit σ_E the stress becomes a nonlinear function of strain, and generally shows hysteresis between the loading and unloading legs of the cycle. This indicates that other processes than elastic deformation of the crystal lattice occur, and that energy is dissipated during the cycle. This behaviour is conventionally called anelasticity.
3. At stresses above the anelastic limit σ_A the loops are not closed and the behaviour is called microplastic.

Anelasticity is modelled in chapter 6 and 7 as reversible dislocation glide associated with bowing out of dislocation segments under stress. That implies that the linear elastic strain below the elastic limit can only occur if the dislocations are pinned –probably by solute atoms- and therefore unable to move. The elastic limit must then be interpreted as the stress at which dislocations break free of their solute atmosphere. According to this interpretation, the elastic limit is not unlike the upper yield stress that is observed for statically aged material, the main difference being that the upper yield stress is higher than the yield stress. Since the unlocking process of dislocation segments from a solute atmosphere is a thermally activated process, σ_E is expected to approach zero at elevated temperatures.

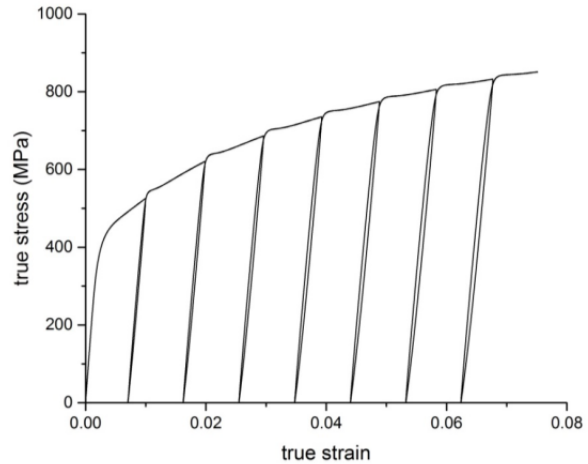


Figure 3-27. Unloading/reloading in the post yield regime at room temperature [34].

The nonlinear anelastic behaviour for stresses above σ_E is explained in

chapter 6 as being a natural consequence of bowing out of a dislocation segment under stress. The hysteresis can be explained by the resistance due to dislocation glide associated with thermally activated passing of local obstacles by the moving dislocations. The hysteresis is then a consequence of the fact that forward glide during loading is easier to be activated than backward glide during unloading. Finally, microplasticity can be explained by trapping of dislocations during unloading behind obstacles that were easy to be passed during loading.

That implies that microplasticity is a natural phenomenon associated with relaxation of previously stressed dislocations towards an equilibrium position during unloading. The same phenomenon is known to occur after much larger strain amplitudes than those in the pre-yield regime [35], [36], as shown in Figure 3-27. Although stress cycling can provide clues about the degree of reversibility of strain in the pre-yield regime, it cannot provide information on the question if deformation is in the pre or post yield regime. That problem can only be resolved by a proper method to determine the yield stress, which will be developed in section 3.6.1 and chapter 6. In that chapter stress cycling is utilized in interpreting and modelling pre yield behaviour.

3.6 Data assessment

3.6.1 Kocks-Mecking diagram

The Kocks-Mecking (KM) diagram is a valuable tool in the estimation of work hardening parameters. A KM plot is basically a plot of the work hardening rate $\Theta = \frac{d\sigma}{d\varepsilon}$ versus stress σ . The KM plot, an example of which taken from [37] is shown in 3-28, is mainly used in the analysis of work hardening behaviour.

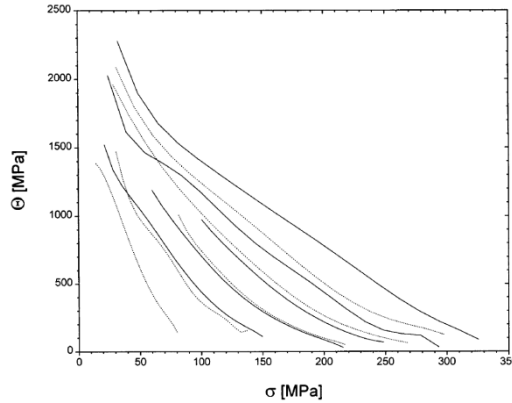


Figure 3-28. A Kocks Mecking plot of Cu [37].

$\dot{\varepsilon} = 10^{-1} \text{ s}^{-1}$ (solid lines) and 10^{-4} s^{-1} (dashed).

The principle of KM analysis can be explained from elementary work hardening theory:

The flow stress σ_f can be written as

$T = 100 \dots 400 \text{ }^\circ\text{C}$.

$$\sigma_f = \sigma_y + \alpha \bar{M} G b \sqrt{\rho}, \quad (3.14)$$

where σ_y is the yield stress. α is a crystallographic constant, \bar{M} the Taylor factor, G the shear modulus and b the magnitude of the Burgers vector. The second term in eq. (3.14) is the Taylor relation [38]. The dislocation density ρ is a function of strain ε , which can be approximated for low and medium strains by the elementary work hardening equation

$$\frac{d\rho}{d\varepsilon} = U\sqrt{\rho} - \Omega\rho \quad (3.15)$$

which here is presented in the Bergström notation where U is a hardening parameter and Ω is the dynamic recovery parameter. The Bergström model is mathematically identical to the Kocks-Mecking model [39]. These models describe elementary stage III hardening behaviour.

From eqs.(3.14) and (3.15) follows for the work hardening rate:

$$\Theta = \frac{1}{2}(\alpha GbU - \Omega\sigma_w) \quad (3.16)$$

This shows that approximate values of U and Ω can be obtained from the initial value $\Theta(\sigma_w = 0)$ and of the slope of a KM plot. The factor $\frac{\alpha GbU}{2}$ is the athermal hardening rate at the yield point, and the intercept must be evaluated at the yield stress $\sigma_f = \sigma_y$.

In practice, this requires an estimate of σ_y , and Θ is usually plotted vs. $\sigma_w = \sigma_f - \sigma_y$. The conventional KM plot does not provide information on the value of σ_y . The common method to evaluate σ_y is by the 0.2% offset yield stress $R_{p0.2}$ that is computed by most tensile machine process computer programs. This definition of the yield stress lacks a physical basis and its use is commonly justified by the fact that metals often “...do not show a clearly defined yield point in the tensile curve...” [40], [41], [42].

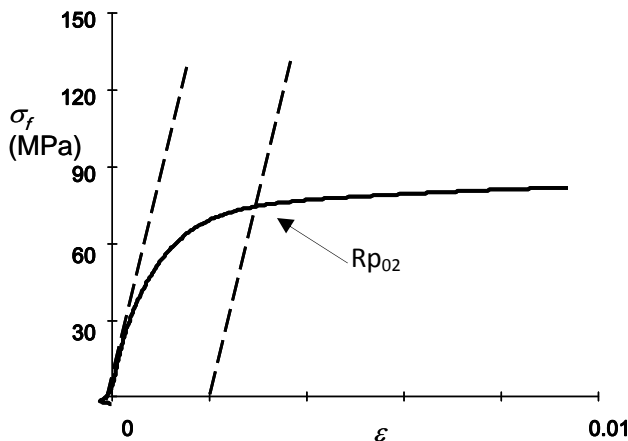


Figure 3-29. Initial part of the flow stress curve of the Fe C Mn steel. $R_{p0.2}$ construction shown (dotted lines)

$T = 910 \text{ }^\circ\text{C}$, $\dot{\epsilon} = 0.1 \text{ s}^{-1}$

The $R_{p0.2}$ algorithm requires that a reliable estimate of the elastic modulus can be extracted from the tensile curve. This frequently presents problems in hot tensile tests that are due to temperature gradients in the sample or to pronounced nonlinearity of the pre-yield modulus, which actually is the cause of

the difficulty to observe the yield stress in the stress strain curve. Temperature gradients in particular may be the cause of a gradual transition from elastic to fully plastic deformation of the gauge section. In compression experiments that situation is aggravated by strain gradients that are caused by friction.

The new sample design described in section 3.4.2 ensures that temperature gradients are minimized, thereby creating optimal circumstances for the observation of the yield stress. Nevertheless, no clear yield point is observable in the stress strain curve, as shown in Figure 3-3, which shows only the initial part of the hardening curve. The $R_{p0.2}$ construction shown in this figure does not seem to indicate a point of particular interest.

A technique to improve the observability of the yield stress is to construct an extended KM plot, i.e. to extend it to zero stress. Where in the case of linear elasticity in the pre-yield range a constant value $\Theta = E$ and a shear drop to a lower value at the yield point is expected (in which case the yield point should be clearly observable in a $\sigma(\varepsilon)$ plot), this is in practice only the case for aged materials at room temperature.

In Figure 3-30 the extended KM plot corresponding to the flow stress curve of Figure 3-29 is shown for the total range of stresses up to localized necking. Two distinct branches at low respectively high stress are observable, that are distinguishable by a clear transition in $\Theta(\sigma)$ behaviour.

We propose that this transition is the proper yield stress, which will be substantiated in chapter 6. The yield stress can be found by intersection of two linear functions to the distinctive branches, as shown in Figure 3-30. We conclude that the extended KM plot is a valuable

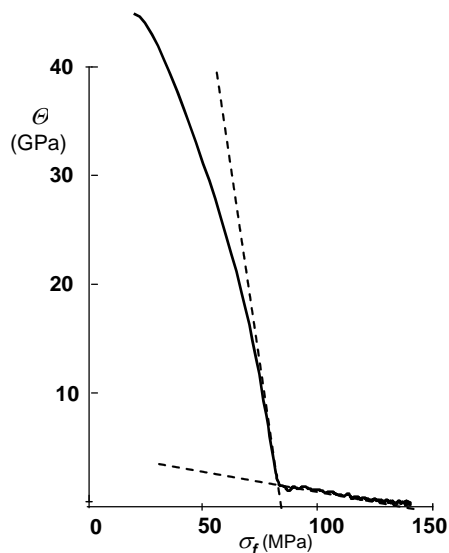


Figure 3-30. Extended Km plot of the Fe C Mn steel. $T = 910 \text{ }^\circ\text{C}$, $\dot{\varepsilon} = 0.1 \text{ s}^{-1}$. Yield stress construction shown (dotted lines).

tool in determining the yield stress, and does not rely on arbitrary definitions. In chapter 5 and 6, this claim will be substantiated by theoretical arguments and experimental evidence.

The new tensile sample design ensures that temperature gradients are minimized, thereby creating optimal circumstances for the observation of the yield stress.

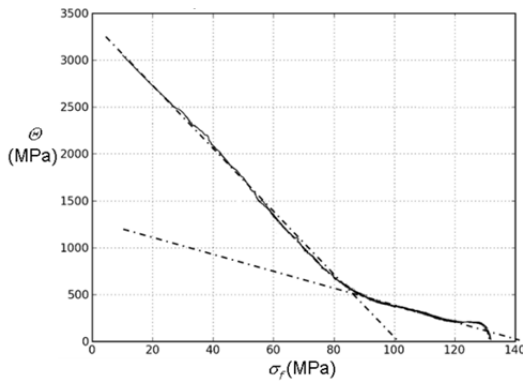


Figure 3-31. KM plot of an axisymmetric compression test, $T = 950\text{ }^{\circ}\text{C}$, $\dot{\epsilon} = 1.0\text{ s}^{-1}$.
Dotted lines: Yield point construction.

The extended Km plot is also a valuable tool in assessing the quality of a deformation test. In Figure 3-31 it is applied to an axisymmetric compression test at elevated temperature of a material of composition C= 0.09 Mn= 1.688 Si= 0.264 Al=.014 wt. %. If we compare this to Figure 3-30, it is seen that although the yield stresses are of similar value, the apparent pre yield stiffness is an order of magnitude lower in the compression

test than in the tensile test, and that the uncertainty in the yield point is much larger, since the lines fitted to the pre- and post-yield branches do not differ much in slope.

For the uniform strain range of the hardening curve obtained by tensile testing, the KM plot is also helpful in deciding whether a model for simple Stage III hardening behaviour according to Bergström-Vetter/ Kocks-Mecking [43], [39] applies. For a standard tensile test the uniform strain range is limited by the onset of diffuse necking. In our case, since local strains can be determined, the useful strain range is extended to the onset of localized necking.

The onset of diffuse and localized necking in a tensile test, which occurs at

$\Theta = \sigma$ respectively $\Theta = \frac{\sigma}{2}$ [3], the latter of which is the limit at which the

calculated equivalent strain and stress is correct, can be readily determined from the KM diagram. Any non-linear decrease of the $\Theta(\sigma)$ curve at lower

stresses than for which $\Theta = \frac{\sigma}{2}$ indicates the onset of a structural weakness or

stress recovery mechanism like recrystallisation or phase transformation of the material. This is for example the case at $\sigma \approx 125\text{ MPa}$ in Figure 3-31. KM plot of an axisymmetric compression

3.7 Instrumental issues

3.7.1 Machine stiffness

The technique of non-contacting strain measurement does not allow the application of a clip-on strain gauge, since this would obstruct the view. While this is not a problem for the measurement of large strains, any observations in the lower strain range, particularly of pre-yield phenomena, must now be made by the stroke/ crosshead displacement signal. For the study of pre-yield phenomena the sensitivity of the local contactless strain measurement method described in section 3.4.5 is not adequate.

Obtaining the gauge strain from the crosshead displacement requires knowledge of the machine stiffness. The machine stiffness is usually measured by comparison of the crosshead displacement signal to the clip-on gauge signal. In our case this requires a dedicated test run.

The usual assumption is that any deformation outside the strain gauge span is a machine effect. This implies that the machine stiffness is partly affected by the compliance of a part of the tensile specimen. Strictly, this requires that the machine stiffness should be determined for each specimen thickness and at elevated temperatures for each temperature if the usual procedure is followed. For the new sample design described in section 3.4.2 this is a particularly important issue, since the out of gauge parts are rather large. It may be assumed that strain gradients in the shoulders are negligible, since they are not loaded to stresses above the yield stress.

Since the shoulders are maintained at the same temperature as the gauge, both are subject to the same pre yield phenomena. The machine elongation $\Delta X_m(F)$ is a function of the tension force F only, since the clamps are maintained at room temperature. The stress in the shoulders is $\frac{1}{2}$ times that in the gauge, since the shoulder width $w_C = 2w_A$ with w_A the width of the gauge section. This makes it possible to separate the part of the out of gauge strains in the shoulders from that of the tensile machine. In the case where the pre-yield behaviour of the material is linearly elastic, the strain in the shoulders ε_{sh} in relation to the gauge strain ε_g is given by

$$\varepsilon_{sh} = \varepsilon \left(\frac{\sigma}{2} \right) = \frac{\sigma}{2} \frac{1}{E} = \frac{1}{2} \varepsilon_g, \quad (3.17)$$

where E is Young's modulus at the experimental temperature and $\sigma = \frac{F}{A}$ is the nominal stress with A the cross section of the gauge section of the sample.

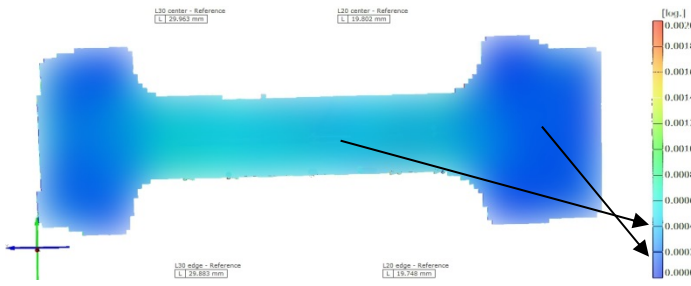


Figure 3-32. Local pre-yield strain in the sample, room temperature.

The validity of eq. (3.17) was corroborated by a tensile test at room temperature where local strains were measured with the Aramis digital image correlation system available at Tata Steel laboratories IJmuiden. In Figure 3-32 the

result at a stress $\sigma \approx \frac{1}{2} \sigma_y$ is shown. The local strain in the gauge region appears to be twice as large as that in the shoulder within experimental error.

The total elongation Δx_t is the sum of the machine deformation Δx_m and that of the gauge and shoulder sections Δx_g and Δx_{sh} :

$$\Delta x_t = \Delta x_g + 2\Delta x_{sh} \quad (3.18)$$

Since the elongation $\Delta x = l \varepsilon$, where l is the length of the section, and the length of the shoulders l_{sh} including that of the gauge section l_g in our design (see Figure 3-12) is

$$\begin{aligned} \Delta x_t &= \Delta x_m + l_g \frac{\sigma}{E} + 2l_{sh} \frac{\sigma}{2E} \\ &= \Delta x_m + 2l_g \frac{\sigma}{E} \\ &= \Delta x_m + 2\Delta x_g \quad \Rightarrow \\ \Delta x_m &= \Delta x_t - 2\Delta x_g \end{aligned} \quad (3.19)$$

The machine elongation as a function of tensile force was determined by a testing at room temperature, on a sample that showed linear elastic behaviour in the pre-yield regime. This ensures that the assumptions made in deriving eq.

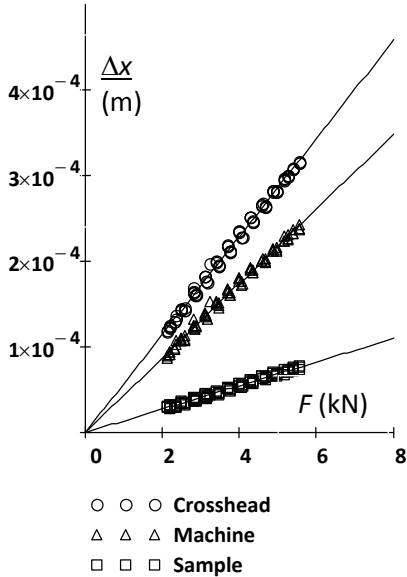


Figure 3-33. Correction of the crosshead elongation for sample strain.

(3.19) are valid. Another advantage is that the range of force is large, since the yield stress at room temperature is high. Testing was done by cycling the force F in the range $2 < F < 6$ (kN).

In Figure 3-33 the result of the machine stiffness test is shown. The measured total (crosshead) elongation, that of the sample which was computed from the measured strain gauge elongation and the resulting machine elongation are plotted vs. the tensile force. Note that all elongations are linear functions of the tensile force. The linearity of the strain gauge elongation indicates that the material behaviour is indeed linearly elastic.

With the machine elongation $\Delta x_m(F)$ known, the procedure for correction for out of gauge deformation is now

$$\Delta x_g = \frac{1}{2} \{ \Delta x_t - \Delta x_m(F) \} \quad (3.20)$$

In practice, the pre-yield behaviour –especially at high temperatures- is seldom purely elastic. In chapter 6 and 7 it will be shown that at elevated temperatures the pre yield stiffness is degraded by anelasticity and becomes a non-linear function of stress. In the next section it will be shown that the correction developed above is still adequate under those conditions.

Sample stiffness at elevated temperature

A simulation with the anelastic model developed in chapter 6 and shown in Figure 3-34 yields the result that the average ratio of the gauge stiffness to that

of the total sample is approximately $\frac{\Theta_{gauge}}{\Theta_{sample}} = 2$.

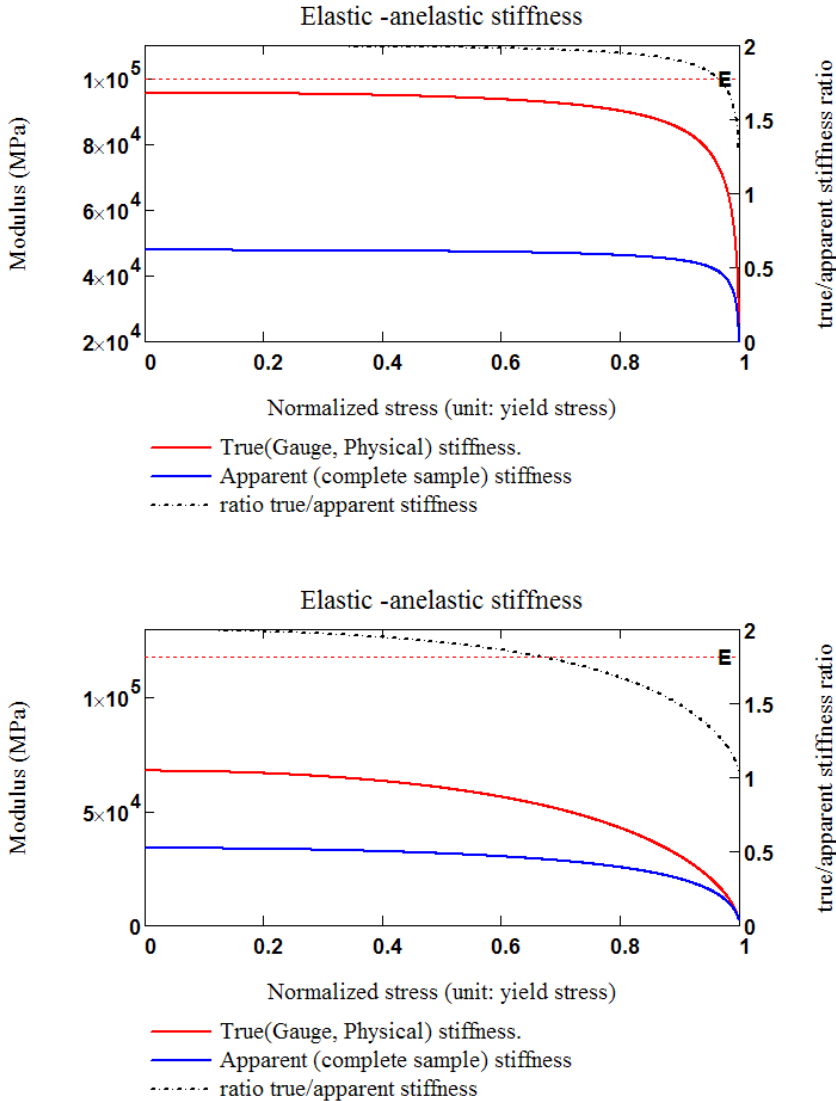


Figure 3-34. Sample and physical stiffness for moderate ($\rho L^2 = 1$, top) and strong anelasticity ($\rho L^2 = 16$, bottom) $T = 800$ °C, austenitic phase. Represented as stiffness as a function of stress (KM plot).

It may seem that the $\frac{\Theta_{gauge}}{\Theta_{sample}} = 2$ approximation is rather crude for stresses

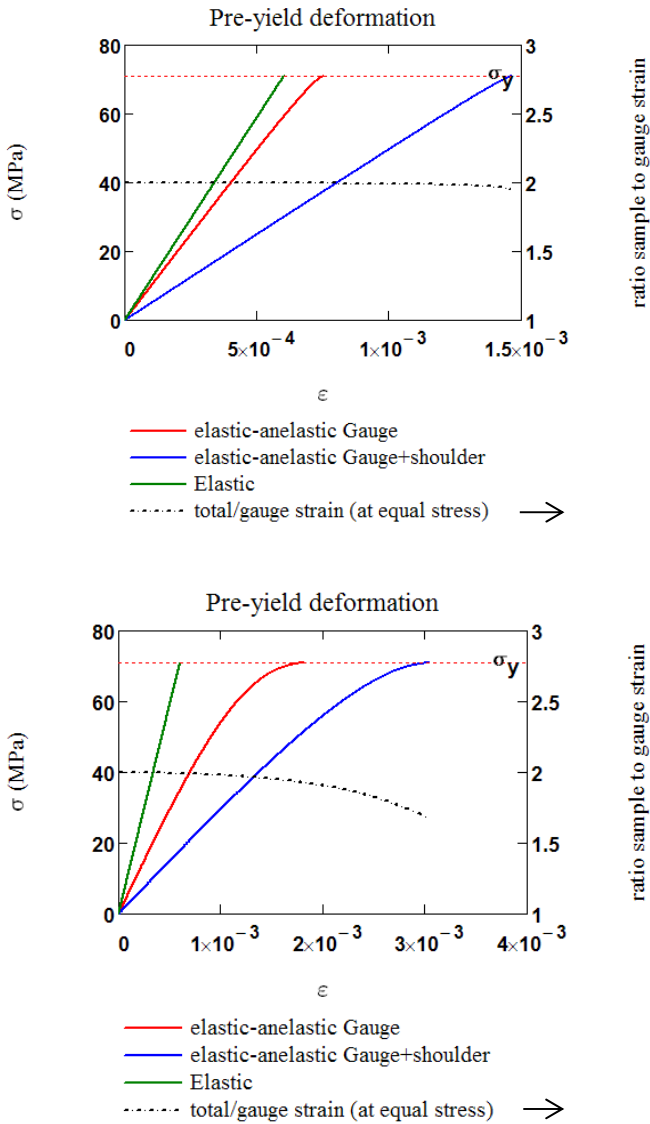


Figure 3-35. Sample and gauge strain for moderate ($\rho L^2 = 1$, top) and strong anelasticity ($\rho L^2 = 16$, bottom) $T = 800^\circ\text{C}$, austenitic phase.

larger than $\frac{1}{2}\sigma_y$, especially for strong anelasticity. The KM representation is however quite sensitive to differences in stiffness. The equivalent approximation $\frac{\epsilon_{gauge}}{\epsilon_{sample}} = 2$ is shown to be adequate (within 2-10%) even for strong anelasticity in the more conventional stress vs strain representation in Figure 3-35.

3.7.2 Signal noise of the Gleeble force and elongation channels

Now that all possible sources of systematical error in our test have been identified, we must turn our attention to instrumental sources of experimental noise in order to improve the accuracy of the results. It may be argued that a valid model is the best noise filter, but since we will have to differentiate the stress strain curves for the construction of KM plots, application of noise filtering techniques is inevitable. Furthermore, we will find that the noise in this case is dominated by a deterministic disturbance, rather than being a random error of measurement.

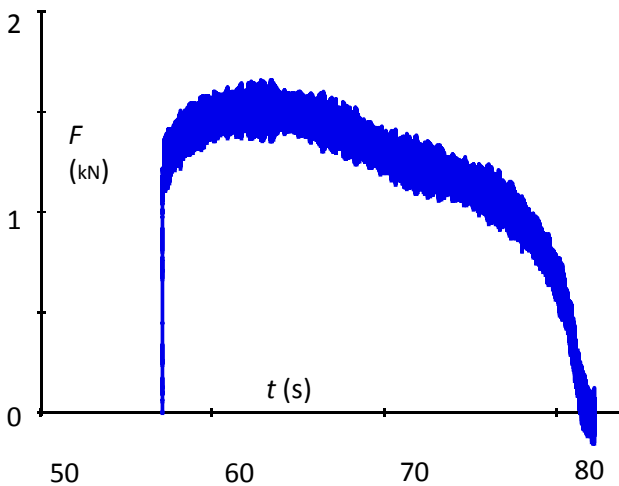


Figure 3-36. Typical Noisy $F(t)$ signal.

$$T = 910 \text{ }^\circ\text{C} \quad \dot{\epsilon} = 0.02 \text{ s}^{-1}.$$

A major source of experimental noise in the Gleeble system is due to the choice of heating by an AC electrical current. The current is controlled by a phase fired thyristor control circuit. This type of control conducts the AC current during a part of each phase. The resulting output contains strong higher harmonics in its power spectrum, which cause disturbances in the force and displacement transducer signals. This is especially

problematic at high temperatures, where the force signal is low. A typical load vs. time signal is shown in Figure 3-36, an enlarged detail of which is shown in

Figure 3-37. The high harmonic content of both is clearly visible. This type of noise can effectively be attenuated by a low pass filter.

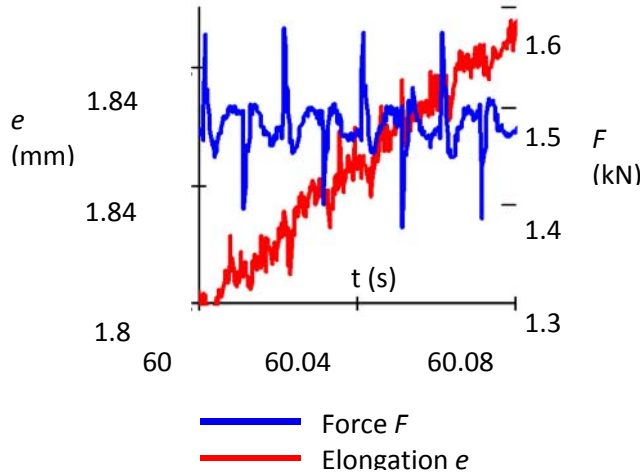


Figure 3-37. Detail of Figure 3-36 with displacement signal e also shown.

We have chosen to apply a type II Chebychev filter [44] in the frequency domain, as the setting of the filter can then be conveniently chosen on the basis of the Fourier power spectrum

$$F_{ChII}(\omega, \omega_c) = 1 + \frac{1}{\sqrt{1 + \varepsilon_a^2 p_{Ch}^2\left(n, \frac{\omega_c}{\omega}\right)}}, \quad (3.21)$$

where $p_{Ch}\left(n, \frac{\omega_c}{\omega}\right)$ is a Chebychev polynomial with ω the Fourier frequency of the signal, ω_c the cut-off frequency of the filter and n a non-negative integer. ε_a is an attenuation parameter.

Type II Chebychev filters have no ripple in the passband gain. It is of importance to check the low strain region of the filtered signal, to make sure that no artefacts in the pre-yield region and around the yield point are produced. The power spectrum and filter response of the force signal of the hardening curve shown in Figure 3-36 are shown in Figure 3-38. The power spectrum is quite smooth below 50 Hz. The attenuation of the disturbances is 8 orders of magnitude.

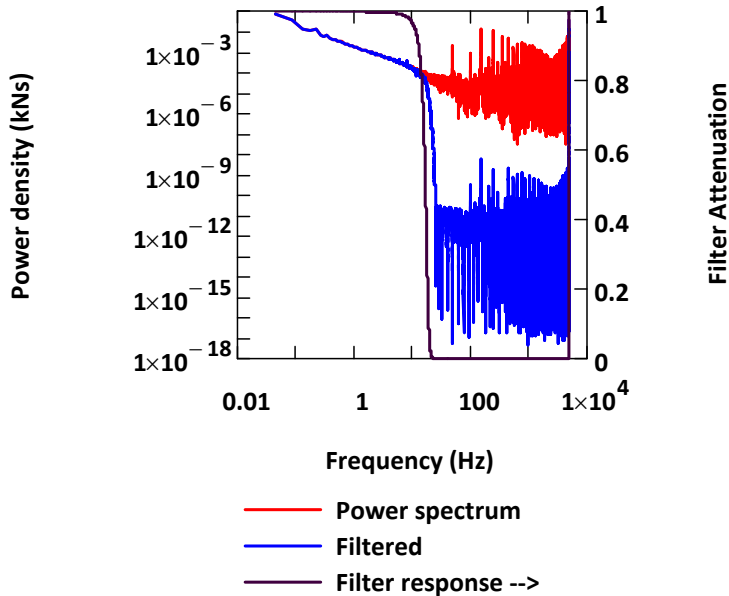


Figure 3-38. Power spectrum and filter response.

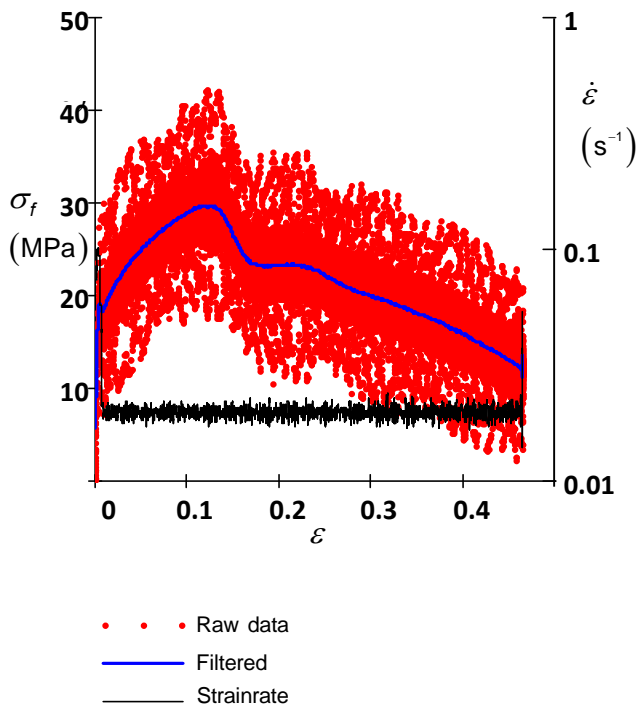


Figure 3-39. Filtering an extremely noisy signal.

$$T = 1200 \text{ }^\circ\text{C} \quad \dot{\epsilon} = 0.02 \text{ s}^{-1}$$

of experiments. The flow stress and signal to noise ratio are consequently minimal.

This technique has proven to be crucial in producing noise-free KM diagrams.

3.7.3 Conclusion

In this chapter, a number of experimental methods were developed aimed at improvement of the accuracy of the tensile test at elevated temperatures on the Gleeble system as well as to aid in post processing and interpretation of the obtained stress-strain data. These methods will be employed in Chapter 5-7 for obtaining experimental data and post processing.

To show the full potential of this technique, it is applied to the test shown in Figure 3-39 that has an extremely low signal to noise ratio.

The upper yield point-like detail at yield is an artefact caused by an overshoot in the strain rate. While this must be remedied by better settings of the PID velocity control, it shows what level of detail can be obtained from the rather noisy raw signal by this technique. The example shown is the worst case, the temperature and strain rate are the maximal respectively lowest values in the set

References

- [1] Beynon, J. H. (1998). Tribology of hot metal forming. *Tribology International*, 31(1), 73-77.
- [2] Y.H. Li et al. *Acta. Met. Sin.* 2000 Vol13 No. 1 p359-368
- [3] Backofen, W. A. (1972). *Deformation processing*. Addison-Wesley Pub. Co..
- [4] Gelin, J. C., Ghouati, O., & Shahani, R. (1994). Modelling the plane strain compression test to obtain constitutive equations of aluminium alloys. *International journal of mechanical sciences*, 36(9), 773-796.
- [5] Kudo, H. (1960). An upper-bound approach to plane-strain forging and extrusion—I. *International Journal of Mechanical Sciences*, 1(1), 57-83.
- [6] Gelin, J. C., & Ghouati, O. (1995). The inverse approach for the determination of constitutive equations in metal forming. *CIRP Annals-Manufacturing Technology*, 44(1), 189-192.
- [7] Cooreman, S., Lecompte, D., Sol, H., Vantomme, J., & Debruyne, D. (2007). Elasto-plastic material parameter identification by inverse methods: Calculation of the sensitivity matrix. *International journal of solids and structures*, 44(13), 4329-4341.
- [8] Rietman, A. D., Liempt, V. P., & Huetink, H. (1997). The modeling of compression tests with a physically based material model using finite elements.
- [9] Fields, D. S., & Backofen, W. A. (1957). Determination of strain hardening characteristics by torsion testing. In *Proc. ASTM* (Vol. 57, pp. 1259-1272).
- [10] Sillekens, W. H., Dautzenberg, J. H., & Kals, J. A. G. (1991). Strain path dependence of flow curves. *CIRP Annals-Manufacturing Technology*, 40(1), 255-258.
- [11] Bridgman, P. W. (1952). *Studies in large plastic flow and fracture* (Vol. 177). New York: McGraw-Hill.
- [12] Fang, X. F., & Dahl, W. (1995). Strain hardening of steels at large strain deformation. Part I: Relationship between strain hardening and microstructures of bcc steels. *Materials Science and Engineering: A*, 203(1), 14-25.
- [13] Barnett, M. R., & Jonas, J. J. (1999). Distinctive Aspects of the Physical Metallurgy of Warm Rolling. *ISIJ international*, 39(9), 856-873.
- [14] Ganapathy, M., Li, N., Lin, J., Abspoel, M., Guido, H., & Bhattacharjee, D. (2015). Analysis of new Gleeble tensile specimen design for hot stamping application. In *MATEC Web of Conferences* (Vol. 21, p. 05013). EDP Sciences.
- [15] ImageJ website.<http://rsb.info.nih.gov/ij/>
- [16] Ghosh, A. K. (1974). Strain localization in the diffuse neck in sheet metal. *Metallurgical Transactions*, 5(7), 1607-1616.
- [17] Bovik, A. *Handbook of Digital Image & Video Processing*. Elsevier Academic Press. ISBN 0-12-119792-1.
- [18] Boudier, T. Edge Detection By Canny-Deriche filtering.
http://imagejdocu.tudor.lu/doku.php?id=plugin:filter:edge_detection:start
- [19] http://en.wikipedia.org/wiki/Hough_transform
- [20] Pistori, H and Rocha Costa, E. *Hough_Circles.java*.
<http://rsb.info.nih.gov/ij/plugins/hough-circles.html>

-
- [21] van der Wolk, P. J. (2001). Modelling CCT-Diagrams for Engineering Steels using Neural Networks. TU Delft, Delft University of Technology.
- [22] Mukherjee, J K (1966) Thermomechanical ausforming technique for producing substitute ultra high strength steels. In: Symposium on Metallurgy of Substitute Ferrous & Non-Ferrous Alloys, 27-30 April, NML, Jamshedpur.
- [23] Abspoel, M., Neelis, B. M., & van Liempt, P. (2016). Constitutive behaviour under hot stamping conditions. *Journal of Materials Processing Technology*, 228, 34-42.
- [24] van Liempt, P., & Sietsma, J. (2011). A revised criterion for the Portevin–Le Châtelier effect based on the strain-rate sensitivity of the work-hardening rate. *Metallurgical and Materials transactions A*, 42(13), 4008-4014.
- [25] Dorn, J. E., Goldberg, A., & Tietz, T. E. (1949). The effect of thermal-mechanical history on the strain hardening of metals. *TRANSACTIONS OF THE AMERICAN INSTITUTE OF MINING AND METALLURGICAL ENGINEERS*, 180, 205-224.
- [26] Immarigeon, J. A., & Jonas, J. J. (1971). Flow stress and substructural change during the transient deformation of armco iron and silicon steel. *Acta Metallurgica*, 19(10), 1053-1061.
- [27] Follansbee, P. S., & Kocks, U. F. (1988). A constitutive description of the deformation of copper based on the use of the mechanical threshold stress as an internal state variable. *Acta Metallurgica*, 36(1), 81-93.
- [28] Klepaczko, J. R. (1991). Physical-state variables—the key to constitutive modeling in dynamic plasticity. *Nuclear engineering and design*, 127(1), 103-115.
- [29] Brown, S. B., Kim, K. H., & Anand, L. (1989). An internal variable constitutive model for hot working of metals. *International journal of plasticity*, 5(2), 95-130.
- [30] Klepaczko, J. R., & Chiem, C. Y. (1986). On rate sensitivity of fcc metals, instantaneous rate sensitivity and rate sensitivity of strain hardening. *Journal of the Mechanics and Physics of Solids*, 34(1), 29-54.
- [31] Dave, V. R., & Brown, S. B. (1994). Critical experiments used to determine flow relations for rate-dependent metal deformation. *International journal of plasticity*, 10(3), 237-262.
- [32] Bergström, Y. (1970). A dislocation model for the stress-strain behaviour of polycrystalline α -Fe with special emphasis on the variation of the densities of mobile and immobile dislocations. *Materials Science and Engineering*, 5(4), 193-200.
- [33] Brown, N. Microplasticity, in *Advances in Materials Research*, Vol 11. Ed. by CJ McMahon, Jr. (1968): 45.
- [34] Torkabadi, A., Van Liempt, P., Meinders, V. T., & Van den Boogaard, A. H. (2015). A constitutive model for the anelastic behavior of Advanced High Strength Steels. In *COMPLAS XIII: proceedings of the XIII International Conference on Computational Plasticity: fundamentals and applications* (pp. 378-385). CIMNE.
- [35] Sritharan, T., & Chandel, R. S. (1997). Phenomena in interrupted tensile tests of heat treated aluminium alloy 6061. *Acta materialia*, 45(8), 3155-3161.
- [36] Sun, L., & Wagoner, R. H. (2011). Complex unloading behavior: Nature of the deformation and its consistent constitutive representation. *International Journal of Plasticity*, 27(7), 1126-1144.

-
- [37]** Kocks, U. F. (2001). Realistic constitutive relations for metal plasticity. *Materials Science and Engineering: A*, 317(1), 181-187.
- [38]** Taylor, G. I. (1934). The mechanism of plastic deformation of crystals. Part I. Theoretical. *Proceedings of the Royal Society of London. Series A, Containing Papers of a Mathematical and Physical Character*, 145(855), 362-387.
- [39]** Kocks, U. F. (1976). Laws for work-hardening and low-temperature creep. *Journal of engineering materials and technology*, 98(1), 76-85.
- [40] Tamarin, Y. (2002). *Atlas of stress-strain curves*. 2nd ed., 2002, ASM International, ISBN 0-87170-739-X
- [41]** Smolik, G. R., & Chen, C. W. (1970). Radiation hardening in vanadium. *Journal of Nuclear Materials*, 35(1), 94-101.
- [42]** Gedge, G. (2008). Structural uses of stainless steel—buildings and civil engineering. *Journal of constructional steel research*, 64(11), 1194-1198.
- [43]** Vetter, R., & Van Den Beukel, A. (1977). Dislocation production in cold worked copper. *Scripta Metallurgica*, 11(2), 143-146.
- [44]** Wikipedia lemma. http://en.wikipedia.org/wiki/Chebyshev_filter

Chapter 4. A Revised Criterion for the Portevin–Le Châtelier Effect Based on the Strain-rate Sensitivity of the Work Hardening Rate¹

Merlin, explaining his inverse sense of time to the Wart:

You see, one gets confused with Time, when it is like that. All one's tenses get muddled, for one thing. If you know what is going to happen to people, and not what has happened to them. It makes it difficult to prevent it happening, if you don't want it to have happened, if you see what I mean? Like drawing in a mirror.

T.H. White: The Once and Future King.

Abstract

An improved analysis is presented of the stability of plastic deformation under conditions where dynamic strain ageing (DSA) occurs, which leads to instabilities known as the Portevin-Le Châtelier (PLC) effect. It is shown that PLC instabilities can occur for conditions that are not covered by the currently prevailing criterion [Y. Estrin and L. P. Kubin., *Mat. Sci. Eng., A* 137 (1991) 125-134], which focuses on a negative strain-rate sensitivity of the flow stress, caused by interactions of solute atoms with thermally activated glide of mobile dislocations. The present analysis recognizes that the strain-rate sensitivity of the flow stress consists of two contributions, one associated with glide of mobile dislocations, the second with work hardening, related to storage of immobile dislocations. In the present paper, an instability criterion is proposed that takes into account the possibility of a negative strain-rate sensitivity of the work hardening rate, which is caused by diffusion of solute atoms to immobile dislocations. The latter contribution leads to an extended instability criterion. This criterion also provides an explanation for the existence of a critical strain above which instabilities occur. In this paper previously published tensile test data are used to show that a negative strain-rate sensitivity of the work

¹ Published as: van Liempt, P., & Sietsma, J. (2011). A revised criterion for the Portevin–Le Châtelier effect based on the strain-rate sensitivity of the work-hardening rate. *Metallurgical and Materials transactions A*, 42(13), 4008-4014.

hardening rate, which significantly influences the occurrence of the PLC-effect, can indeed occur under DSA conditions.

4.1 Introduction

The Dynamic Strain Ageing (DSA) phenomenon, also commonly referred to as the Portevin-Le Châtelier (PLC) effect, is an anomaly of the mechanical properties of many metals and alloys. DSA manifests itself in the form of instabilities in the flow-stress curve during plastic deformation in a certain range of temperatures and strain-rates. The instabilities are associated with repetitive stationary or propagating bands of localized deformation. Physically, DSA is related to static strain ageing, which occurs after deformation, and is the cause of yield phenomena (Lüders effect). Lüders instabilities are also propagating deformation bands, but in contrast to PLC-instabilities, they are not repetitive.

In industrial processes like deep drawing, both types of instability are the cause of surface defects, and are therefore undesirable. The Lüders phenomenon can be suppressed by temper rolling prior to the sheet-forming process. For instabilities due to DSA an easily applicable countermeasure is not readily available, since DSA occurs when ageing conditions are met during deformation, and can only be avoided by a careful choice of the temperature and strain-rate for the sheet-forming process. A reliable instability criterion is an important prerequisite for making that choice.

The presently prevailing criterion, proposed by Estrin and Kubin, recognizes that DSA is caused by the diffusion of solute atoms to dislocations [1], [2], [3], [4]. The dislocations eventually become locked by the acquired solute atmosphere, which affects the flow stress, in particular its dependence on strain-rate and temperature. Commonly, PLC-instabilities due to DSA are explained by assuming that the strain-rate sensitivity of the flow stress becomes negative due to dislocation locking.

Negative strain-rate sensitivity is generally accepted as a cause of plastic instability, but the effect of negative strain-rate on the work-hardening rate has so far not been analyzed in the literature. In the present paper, we analyze the general case in which both the flow stress and the work hardening rate are functions of strain-rate. This results in a new formulation of the criterion for flow instability, in which the strain-rate sensitivity of both the flow stress and the work-hardening rate are taken into account. Its validity will be discussed on the basis of previously published experimental data.

4.2 Background

In the literature, modeling of the dynamic features of the PLC-effect (stress drops and PLC-band nucleation and propagation) has received wide attention. Physically, the PLC-effect is commonly explained [1], [2], [5] by a dynamic interaction between mobile dislocations and diffusing solute atoms. Mobile dislocations that are temporarily arrested at local obstacles (which is the origin of the thermal flow-stress contribution), will become pinned by solute atmospheres that form while the dislocation is immobilized. This causes an increase of the thermal flow-stress contribution. At low strain-rates the waiting time increases, and consequently the pinning becomes more prominent and the flow stress increases. At high rates the diffusion rate of the solute atoms is too low to cause pinning, and the thermal flow-stress contribution is then an increasing function of the strain-rate, as is normal for thermally-activated dislocation propagation. In the majority of these models the hypothesis of negative strain-rate sensitivity is the central element. This concept was introduced by Penning [3], based on the assumption that the constitutive equation can be separated in the variables ϵ and $\dot{\epsilon}$, where ϵ is the plastic strain and $\dot{\epsilon}$ the strain-rate. The described mechanism leads to a range of strain-rates for which the strain-rate sensitivity of the flow stress is negative. In practice, this range of strain-rates is unattainable by the process. This is schematically shown in Figure 4-1. If the nominal strain-rate is increased to the lower limit of the region of negative slope, the stress is sufficient for the strain-rate to jump to a value beyond the upper limit of the unstable range. The strain will then become localized in order to maintain the nominal strain-rate.

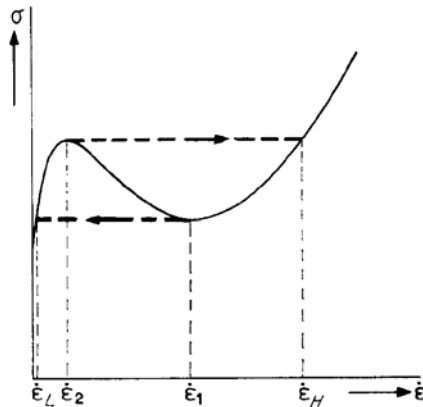


Figure 4-1. Flow stress as a function of strain-rate. strain-rates between $\dot{\epsilon}_1$ and $\dot{\epsilon}_2$ are inaccessible [3].

The occurrence of a negative strain-rate sensitivity has recently been the subject of debate, after Korbel [6] dismissed the idea of the occurrence of

negative strain-rate sensitivity as an artifact, arguing that the PLC bands are localized plastic instabilities having at least three degrees of freedom that can be responsible for the stress drop following an increase in cross head velocity [7], [8], [9].

Penning's theory of DSA [3] and most subsequent work on the subject treat the strain-rate sensitivity as an instantaneous increase or decrease of the flow stress after a change in strain-rate. This is the normal case for steel at room temperature, where the strain-rate sensitivity is related to thermally activated glide of dislocations.

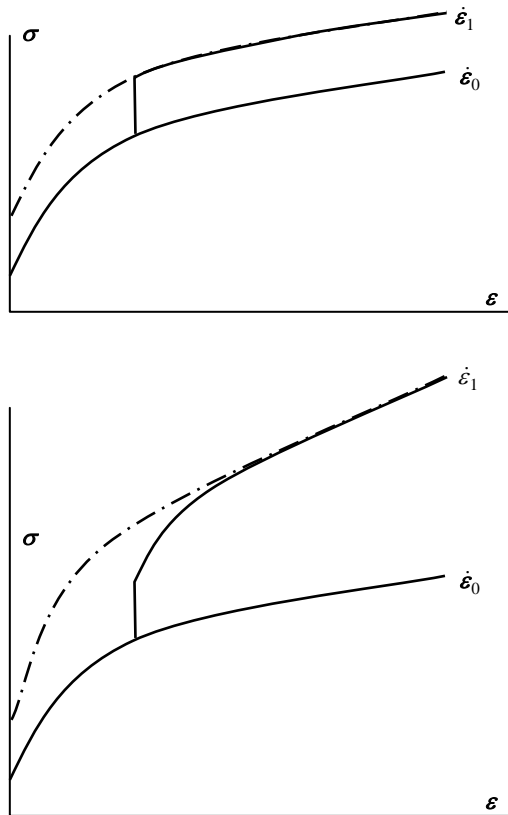


Figure 4-2. Stress response to a strain-rate jump in the case of DSRS only (above) and both ISRS and DSRS (below).

It is widely recognized that at elevated temperatures, including the range in which DSA occurs, the work-hardening rate $\Theta = \frac{\partial \sigma_f}{\partial \epsilon}$, where σ_f is the flow

stress, which is also a function of temperature T and strain-rate $\dot{\epsilon}$. Obviously, the strain-rate influence on θ will not cause an immediate change in flow stress when the strain-rate changes: the effect will become significant on continued straining. Some authors therefore use the terminology “*instantaneous strain-rate sensitivity*” for the strain-rate sensitivity associated with thermally activated glide and “*strain-rate sensitivity of work hardening*” for the strain-rate sensitivity of the athermal stress [10]. Also, “*explicit*” respectively “*hidden*” strain-rate and temperature sensitivity is used [11]. We will use the terminology “*direct strain-rate sensitivity (DSRS)*” and “*indirect strain-rate sensitivity (ISRS)*” for strain-rate sensitivity of the flow stress and the work-hardening rate, respectively. The difference between these two is illustrated qualitatively in Figure 4-2.

Figure 4-2a shows the behaviour of a material exhibiting athermal work hardening and thermally activated dislocation glide. The stress response to the strain-rate jump is then instantaneous. Figure 4-2b shows the response of a material exhibiting thermally activated effects on the work hardening rate, in addition to thermally activated dislocation glide. The response then shows an instantaneous change followed by a transient in stress. Similar behaviour is expected for temperature changes. In general, the work hardening of BCC metals, like α -Fe, is athermal at low temperatures, whereas the thermally activated dislocation glide resistance is large at those temperatures. At higher temperatures, where the glide resistance becomes negligible, the work hardening of Fe is dependent on temperature and strain-rate due to interactions between dislocations and diffusing point defects. For FCC materials like Al, the thermal effects on the work hardening dominate the thermally activated glide resistance effects at room temperature [12].

Physically, the existence of ISRS can be explained as follows. The contributions to the flow stress σ_f can be written as

$$\sigma_f = \sigma_0 + \alpha Gb\sqrt{\rho} + \sigma^*, \quad (4.1)$$

where σ_0 is the sum of lattice resistance, solute hardening, precipitation hardening and Hall-Petch hardening. The second term is due to the work hardening and the third to the contribution σ^* of thermally assisted dislocation glide, which is associated with short range interactions between dislocations or between dislocations and the crystal lattice. The parameter α is a crystallographic constant, G the shear modulus, which is temperature dependent, and b the magnitude of the Burgers vector. The variable ρ denotes the dislocation density, which in general increases with increasing strain ϵ . The thermal stress σ^* , which is the stress contribution associated with thermally-

activated passing of local obstacles by mobile dislocations, is only non-zero during deformation and is the cause of the direct strain-rate sensitivity [13].

Work hardening is a contribution to the flow stress that is not thermally activated since it is caused by the long range stresses generated by the dislocation substructure resulting from the net storage rate associated with dislocation generation and recovery processes. However, for homologous temperatures above $T_h = 0.2 / 0.3$, diffusing solute atoms and vacancies interact with the recovery mechanism, which causes the work hardening rate to become a function of strain-rate and temperature. In that case, the work hardening term in eq. (4.1) becomes a function of strain-rate and temperature in addition of being dependent of strain. Note the interesting feature that work hardening which is associated with the essentially athermal process of dislocation storage, is nevertheless a function of strain-rate and temperature. This is directly associated with the existence of the indirect strain-rate sensitivity, which is explained as follows.

The increase of the dislocation density during deformation follows an evolution law that can be formally written as [14]

$$\frac{d\rho}{d\varepsilon} = H - R(\dot{\varepsilon}, T), \quad (4.2)$$

where H is the dislocation storage rate and R the recovery rate. In the Bergström model [15], U is interpreted as the rate of immobilization of mobile dislocations by trapping in the dislocation substructure, and R as the probability of remobilization and annihilation of immobile dislocations.

By eq. (4.1) and (4.2), any change due to strain-rate changes in flow stress that can be attributed to the work hardening contribution is transient in nature. The strain-rate sensitivity that is associated with work hardening is therefore indirect. The activation energy of the work hardening term is associated with recovery due to dislocation climb caused by vacancy diffusion [16], [17], while the dislocation glide resistance is related to dislocation kink pair formation or forest dislocation cutting in the case of BCC respectively FCC metals [18].

Many authors have found that a distinguishing feature of DSA is the increased work-hardening rate [19], [20], [21] [22], [23]. The effect has been proposed as an alternative hardening mechanism to work hardening at room temperature by some investigators [24], [25], or as an increased bake-hardening effect [21]. Brindley [26] reported measurements of increased dislocation densities after deformation at temperatures up to 700 K. Static strain ageing is also known to cause an increase of the work-hardening rate [27], [28]. It can therefore be

concluded that strain ageing and therefore the strain-rate does affect the work-hardening rate. An adequate stability criterion for the occurrence of Portevin – Le Châtelier instabilities should therefore take the strain-rate sensitivity of the work-hardening rate into account.

4.3 Stability criterion

Estrin and Kubin [4] [5] analysed the stability of a strain and strain-rate sensitive material subjected to a local disturbance in plastic strain. For purposes of stability analysis, the constitutive equation describing the flow stress as a function of strain and strain-rate is linearized around a working point $\sigma_f(\varepsilon, \dot{\varepsilon}) = \sigma_f(\varepsilon_0, \dot{\varepsilon}_0)$, according to

$$\sigma_f(\varepsilon, \dot{\varepsilon}) = \sigma_f(\varepsilon_0, \dot{\varepsilon}_0) + \Theta(\varepsilon - \varepsilon_0) + S \cdot \left(\ln \left(\frac{\dot{\varepsilon}}{\dot{\varepsilon}_0} \right) \right), \quad (4.3)$$

where $\Theta = \left. \frac{\partial \sigma_f}{\partial \varepsilon} \right|_{\dot{\varepsilon}}$ is the work-hardening rate at constant strain-rate, and

$S = \left. \frac{\partial \sigma_f}{\partial \ln(\dot{\varepsilon})} \right|_{\varepsilon}$ is the strain-rate sensitivity at constant strain. The variation of

stress $\delta\sigma$ caused by fluctuations $\delta\varepsilon$ in strain and $\delta\dot{\varepsilon}$ in strain-rate then reads:

$$\delta\sigma = \Theta \delta\varepsilon + S \frac{\delta\dot{\varepsilon}}{\dot{\varepsilon}} \quad (4.4)$$

This equation was originally proposed by Penning [3] in a slightly different form, under the simplifying assumption that $\sigma_f(\varepsilon, \dot{\varepsilon})$ is separable in the variables ε and $\dot{\varepsilon}$. Noting that from stress equilibrium and plastic incompressibility it follows that

$$\delta\sigma = \sigma \delta\varepsilon. \quad (4.5)$$

The analysis proposed in [4] and [5] continues by introducing a disturbance in plastic strain in the mathematical form

$$\delta\varepsilon = (\delta\varepsilon)_0 \exp(\lambda t), \quad (4.6)$$

where $(\delta\varepsilon)_0$ is the magnitude of the disturbance at $t = 0$ and λ is a growth parameter. A negative value for λ implies that fluctuations fade with a time constant $1/\lambda$, while positive values of λ mean that the disturbance will grow into an instability. The value of λ is a consequence of the deformation behaviour, notably Θ , S and σ . The eqs.(4.4) to (4.6) lead to an expression for λ in terms of the deformation characteristics given by

$$\lambda = \frac{-(\Theta - \sigma_f)}{S} \dot{\varepsilon}. \quad (4.7)$$

In obtaining this result the relation $\delta\dot{\varepsilon} = \lambda(\delta\varepsilon)_0 \exp(\lambda\varepsilon) = \lambda\delta\varepsilon$, which follows directly from eq. (4.6), was used. In the case $\Theta > \sigma_f$, where the tensile test is intrinsically stable, i.e. before necking, noting that the equivalent strain-rate $\dot{\varepsilon}$ is positive and considering that $\lambda > 0$ leads to instabilities, Estrin and Kubin's instability criterion reads

$$S < 0 \quad (4.8)$$

So, within this framework, negative strain-rate sensitivity is a necessary and sufficient requirement for PLC instabilities to occur. Eq. (4.8) forms the basis of many subsequent analyses in literature [110], [29], [30], [31], [32]. Zbib et al. [33], working from the same assumptions as used in [4], arrived at eq. (4.8) by means of a non-linear instability analysis using strain gradient plasticity.

The strain-rate sensitivity parameter S in eq. (4.4) can be identified as pertaining to the stress contribution caused by thermally activated dislocation glide. This is however not the only strain-rate dependent factor in the constitutive equation, and consequently eq. (4.4) is not the total differential with respect to the strain-rate.

A more comprehensive formulation takes into account also the strain-rate sensitivity of the work-hardening rate (ISRS), leading to

$$\delta\sigma = \Theta \delta\varepsilon + \varepsilon \frac{\partial\Theta}{\partial\dot{\varepsilon}} \delta\dot{\varepsilon} + \frac{S}{\dot{\varepsilon}} \delta\dot{\varepsilon}. \quad (4.9)$$

Estrin and Kubin [4] assumed the term due to the strain-rate dependence of the work-hardening rate to be zero. As discussed in section 4.2, there is

evidence that $\frac{\partial\Theta}{\partial\dot{\varepsilon}}$ is not negligible, and that the extra term in eq. (4.9) can

therefore have a significant effect. This leads to a revised expression for λ , derived from eq. (4.9) in the same way as eq. (4.7) follows from eq. (4.4), and which is written as

$$\lambda = \frac{-(\Theta - \sigma)}{\varepsilon\psi + S} \dot{\varepsilon}, \quad (4.10)$$

where $\Psi = \frac{\partial \Theta}{\partial \ln(\dot{\varepsilon})}$. An alternative criterion for PLC-instability can now be

formulated:

$$\frac{(\Theta - \sigma)}{\varepsilon\Psi + S} < 0 \quad (4.11)$$

For the strain range where $\Theta > \sigma$, the conclusion is that instability will occur if

$$\varepsilon\Psi + S < 0, \quad (4.12)$$

which is the extended stability criterion.

In the case where Ψ is negative and S is positive, the appearance of the strain ε in eq. (4.12) predicts that instability will start when a critical strain ε_c is exceeded, which is given by

$$\varepsilon_c = -\frac{S}{\Psi}. \quad (4.13)$$

Eq. (4.13) implies that $\varepsilon_c < 0$ if S and Ψ are both negative, in which case instabilities will occur from the start of the deformation process. For positive values of S and negative Ψ , sudden stress drops are not expected to occur, since those must be associated with a negative value of S which describes direct response on a strain-rate jump. The indirect strain-rate sensitivity Ψ , which is associated with work hardening, can only cause transient stress changes. Most probably the deformation bands will propagate steadily in this case, with gentle undulations of the flow-stress curve. Within the scope of this paper we will not consider further analysis and modelling of the dynamics of the PLC instabilities as in [29...32].

4.4 Discussion

The conventional explanation of the PLC effect is based on the concept of negative direct strain-rate sensitivity. Published theoretical models focus on ageing effects acting on the mobile dislocations, and only address possible

changes of the thermal stress that are associated with thermally activated glide of mobile dislocations. Although some recent publications [34], [35] criticize the proposed physical mechanisms in earlier publications, the models those authors proposed again are restricted to a description of DSA effects pertaining to mobile dislocations. The assumed mechanism in these theories is solute drag on mobile dislocations by interstitial solute atoms that have segregated to the dislocations forming a Cottrell atmosphere [36], [37].

Experimental evidence has to be treated with caution, firstly because during PLC instabilities the local strain-rate inside the deformation bands will be higher than the nominal strain-rate, and secondly because the range of strain-rates where DSRS is negative, is experimentally inaccessible, see Figure 4-1. Practically, the feature of the theory pertaining to negative values of DSRS is particularly awkward, as it precludes a meaningful confrontation of the theory with the experiment. On the other hand, the work-hardening rate and its strain-rate sensitivity are observable quantities, and it is worthwhile to analyze experimental data and relate observed strain-rate sensitivities to the occurrence of the PLC -instabilities.

Not much attention has been paid in literature to the strain-rate sensitivity of the work-hardening rate associated with DSA and to the problem whether it exhibits negative values. Keh et al. [38] reported *“an inverse strain-rate dependence of the flow stresses... [that] shifted to higher strain-rates at still higher temperatures”*. Kocks et al [39] observe that *“It is evident that the lower strain-rate causes more hardening”*. This influence of DSA on the work-hardening rate is not surprising, as obviously the ageing time, which can be defined as the time available for a sufficient number of solute atoms to diffuse to a dislocation segment to produce locking, is larger for immobile dislocations than for mobile dislocations. The ageing time can be identified with the resting time of immobile dislocations between a storage event and a remobilization/annihilation event in the Bergström model [40]. The immobile dislocations therefore have a greater probability than mobile dislocations to acquire a Cottrell atmosphere, and be locked or pinned by it. This will in turn decrease the (dynamic) recovery rate, which leads to an increased work-hardening rate. At high strain-rates, the ratio of the locking rate to the rate of dislocation storage will decrease, which explains the negative value of the work-hardening rate.

Referring to ageing of mobile dislocations only, Soare and Curtin [35] observed that *“bulk diffusion of Mg in Al at room temperature is far too slow, by a factor of 10^6 , to account for the dynamic strain-aging effects observed”*, and that *“pipe diffusion is also inadequate for accelerating the accumulation of solute atoms in the dislocation core”*. This suggests that the mechanism of pinning of mobile

dislocations, which is associated with DSRS, is insufficient to explain Portevin - Le Châtelier instabilities. Therefore, in addition to negative direct strain-rate sensitivity, an additional effect is influencing the mechanical behavior. We will now show using published experimental data that ISRS is negative in the range of temperatures and strain-rates where Portevin-Le Châtelier instabilities occur.

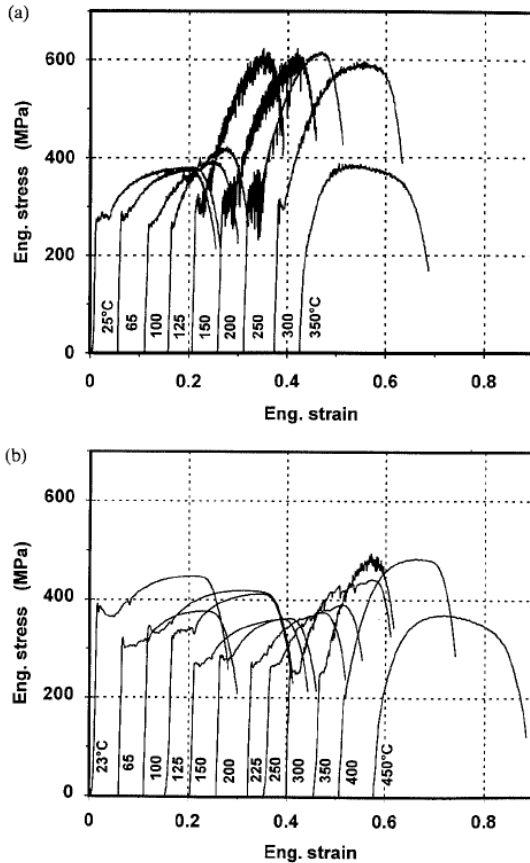


Figure 4-3. Stress vs. strain curves for specimens tensile tested at various temperatures and a strain-rate of: (a) $\dot{\epsilon} = 10^{-4} s^{-1}$ (b) $\dot{\epsilon} = 10^{-1} s^{-1}$. (composition (in wt%): 0.07 C, 0.46 Mn, 0.04 Si, 0.006 P, 0.012 S, 0.04 Cu, 0.07 Ni, 0.05 Cr, 0.001 V, 0.03 Co, 0.0032 N) [41].

(Figure 4-3b) shows that the work-hardening rates at both strain-rates do not significantly differ (the curves have the same shape). Therefore, the strain-rate sensitivity in these experiments should be classified as direct, and it is positive for this temperature.

Karimi Taheri et. al. [41] published a series of tensile curves of low carbon steel that quite clearly show the anomaly in hardening rate and its dependence of temperature and strain-rate, which are reproduced in Figure 4-3. Additionally they published the flow stress at a number of constant strain values as a function of temperature for a wide range of strain-rates. Because of the completeness of these data in combination to the prominent anomalous hardening peak, we chose this study as the basis for the following quantitative analysis. Similar, but less comprehensive data or results from experiments on alloys showing a less prominent effect can be found in [21], [22], [24], [26], [38] and [42].

Comparison of the mechanical behaviour for $T \leq 100$ °C for low strain-rate (Figure 4-3a) to that for high strain-rate (Figure 4-3b) shows that the work-hardening rates at both strain-rates do not significantly differ (the curves have the same shape). Therefore, the strain-rate sensitivity in these experiments should be classified as direct, and it is positive for this temperature.

At temperatures above 100°C the shape of the hardening curve changes conspicuously, and the work-hardening behaviour becomes sensitive to the strain-rate. This can be classified as indirect strain-rate sensitivity. Since the work hardening is clearly stronger in Figure 4-3a than in Figure 4-3b, ISRS is negative for 100 °C < T < 350 °C. The flow-stress curves are jerky in this range, so that we may conclude that both the PLC-instabilities and negative ISRS are caused by DSA.

At temperatures above 350 °C, the DSA-effect decreases, and will eventually be superseded by dynamic recovery, because of which ISRS becomes positive.

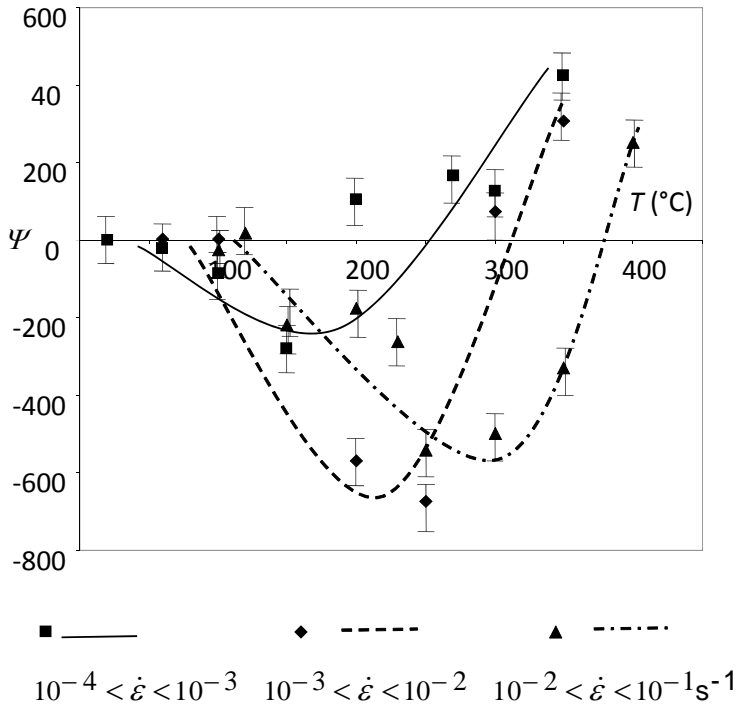


Figure 4-4. Strain-rate sensitivity Ψ of the work hardening rate. Computed from [41]. Errors estimated from PLC fluctuations in Figure 4-3.

From the flow stress vs. temperature and strain-rate data [41] an estimate of the strain-rate sensitivity of the work-hardening rate $\Psi = \frac{\partial \Theta}{\partial \ln(\dot{\epsilon})}$ as a function of temperature for different strain-rate intervals was made (Figure 4-4). From these results it is seen that ISRS becomes negative in the temperature ranges where instabilities occur. Figure 4-3 shows that the

instabilities vanish at temperatures above 250 °C and 350 °C for strain-rates of 10^{-4} s^{-1} and 10^{-1} s^{-1} , respectively, which is in agreement with the crossover of Ψ to positive values shown in Figure 4-4. The position of the minimum in Ψ shifts to higher temperatures if the strain-rate is increased. The magnitude of

$\left| \frac{\partial \Theta}{\partial \ln(\dot{\epsilon})} \right|$ is 400–700 MPa. It must be stressed that these are nominal values.

Because of the strain localization during the PLC-instabilities, the local strain-rate will be larger than the nominal strain-rate. The physically correct value of Ψ (which has to be computed from *local* strain-rates) will differ from the nominal value in cases where PLC-instability occurs.

Values of S for LC steels used in early work on negative DSRs values are in the range $S = 1\text{-}2 \text{ MPa}$ [43]. The term Ψ in eq. (4.11) will therefore exceed S at

quite small values of strain (less than 0.5% with $\left| \frac{\partial \Theta}{\partial \ln(\dot{\epsilon})} \right|$ being 400–700 MPa),

and cannot be neglected in the analysis of PLC instabilities and in models that aim to predict the dynamics of PLC band nucleation and propagation.

The remaining question to be answered lies in the physical explanation of the negative strain-rate sensitivity of the work-hardening rate. In contrast to the state of affairs regarding modelling the dynamic aspects of DSA, models of the increased work-hardening rate during DSA are few in number. The Bergström model [15], [40] has been developed to describe the increase of work-hardening rate in the case of Fe containing free interstitial solute atoms [44]. The Bergström model is mathematically equivalent to the Kocks- Mecking model, but differs in the interpretation of the recovery term. In the Bergström theory, remobilization of immobile dislocations is a secondary source of mobile dislocations in addition to dislocation creation. At higher temperatures, the remobilization process is enhanced by dislocation climb due to vacancy diffusion, which lowers the work-hardening rate. At increasing strain-rates this effect decreases, so that the strain-rate sensitivity of the work-hardening rate (ISRS) due to this effect is positive. The remobilization concept is similar to that of dynamic recovery, albeit that in the prevailing KM interpretation recovery is interpreted as an annihilation mechanism. Neither the Bergström nor the Kocks- Mecking model offer a viable explanation for the increased work hardening rate for conditions where DSA occurs.

In the extended Bergström model [44], the increased rate of work hardening is explained by locking of immobile dislocations by diffusing solute atoms, which renders them ineffective for remobilization. This interaction leads to an opposite effect as in the case of dislocation-vacancy interaction: the strain-rate

sensitivity of the work-hardening rate will be negative. Consequently, the creation rate of mobile dislocations will increase, to fulfill the requirement that the mobile dislocation density remain constant. The model recognizes locked and free immobile dislocations with respect to their ability to remobilize. Formally, a locking rate term is added in this model to the dislocation evolution equation (4.2), which then reads

$$\frac{d\rho}{d\varepsilon} = H - R(\dot{\varepsilon}, T) + L(\dot{\varepsilon}, T) \quad (4.14)$$

A more detailed description of this model can be found in [44]. The model was used to describe experimental data in the stable austenite temperature range, which led to the conclusion that DSA occurs in austenite as well as in ferrite. The model predicts that ISRS is negative for temperatures where DSA occurs. This can be understood as follows: DSA increases the work hardening rate by locking/pinning immobile dislocations. At high deformation rates, the remobilization rate increases, and the probability of locking will decrease. The increase in work hardening rate due to DSA will then be lower than for a low strain-rate. In other words, during DSA the hardening rate decreases with increasing strain-rate.

4.5 Conclusion

In this paper an extended criterion for the onset of Portevin - Le Châtelier instabilities is presented. The proposed criterion is an extension of the Kubin - Estrin criterion by including the indirect strain-rate sensitivity. The criterion indicates that plastic deformation will become unstable at a critical strain if the direct strain-rate sensitivity or the indirect strain-rate sensitivity (or both, in which case the critical strain is zero) becomes negative.

Experimental evidence is presented that shows ISRS to be negative in the range where DSA/PLC instabilities occur. Analysis of literature data showed the contribution of ISRS to stress variations to be of the same order of magnitude or even larger than the DSRS-contribution. Consequently, the strain-rate sensitivity of the work-hardening rate should be taken into account in dynamical models of PLC instabilities.

The occurrence of negative ISRS-values can be explained by the extended Bergström model. If this model is used to describe a comprehensive set of tensile data, it can in conjunction to the derived stability criterion be employed to map the strain-rate / temperature regime where instabilities will occur.

References

- [1] Mulford, R. A., & Kocks, U. F. (1979). New observations on the mechanisms of dynamic strain aging and of jerky flow. *Acta Metallurgica*, 27(7), 1125-1134.
- [2] Schwink, C., & Nortmann, A. (1997). The present experimental knowledge of dynamic strain ageing in binary fcc solid solutions. *Materials Science and Engineering: A*, 234, 1-7.
- [3] Penning, P. (1972). Mathematics of the Portevin-le Chatelier effect. *Acta Metallurgica*, 20(10), 1169-1175.
- [4] Estrin, Y., & Kubin, L. P. (1991). Plastic instabilities: phenomenology and theory. *Materials Science and Engineering: A*, 137, 125-134.
- [5] Kubin, L. P., & Estrin, Y. (1985). The Portevin-Le Chatelier effect in deformation with constant stress rate. *Acta Metallurgica*, 33(3), 397-407.
- [6] Korbel, A., & Dybiec, H. (1981). The problem of the negative strain-rate sensitivity of metals under the portevin-lechatelier deformation conditions. *Acta Metallurgica*, 29(1), 89-93.
- [7] Dybiec, H. (1988). The strain-rate sensitivity during serrated yielding. *Scripta metallurgica*, 22(5), 595-599.
- [8] Kubin, L. P., & Estrin, Y. (1989). Comment on "the strain-rate sensitivity during serrated yielding". *Scripta Metallurgica*, 23(5), 815-817.
- [9] Dybiec, H. (1989). Reply to comment on "the strain-rate sensitivity during serrated yielding". *Scripta metallurgica*, 23(11), 1997-1999.
- [10] Klepaczko, J. R., & Chiem, C. Y. (1986). On rate sensitivity of fcc metals, instantaneous rate sensitivity and rate sensitivity of strain hardening. *Journal of the Mechanics and Physics of Solids*, 34(1), 29-54.
- [11] K. Domkin. Thesis, Luleå University of Technology, 2005.
- [12] Zerilli, F. J. (2004). Dislocation mechanics-based constitutive equations. *Metallurgical and Materials Transactions A*, 35(9), 2547-2555.
- [13] Kocks, U. F., & Mecking, H. (2003). Physics and phenomenology of strain hardening: the FCC case. *Progress in materials science*, 48(3), 171-273.
- [14] Mecking, H., & Kocks, U. F. (1981). Kinetics of flow and strain-hardening. *Acta Metallurgica*, 29(11), 1865-1875.
- [15] Bergström, Y. (1970). A dislocation model for the stress-strain behaviour of polycrystalline α -Fe with special emphasis on the variation of the densities of mobile and immobile dislocations. *Materials Science and Engineering*, 5(4), 193-200.
- [16] Nes, E., Marthinsen, K., & Brechet, Y. (2002). On the mechanisms of dynamic recovery. *Scripta Materialia*, 47(9), 607-611.
- [17] Stüwe, H. P. (1965). Dynamische erholung bei der warmverformung. *Acta Metallurgica*, 13(12), 1337-1342.
- [18] Gao, C. Y., & Zhang, L. C. (2010). A constitutive model for dynamic plasticity of FCC metals. *Materials Science and Engineering: A*, 527(13), 3138-3143.

-
- [19] Schmid, C. G., & Miller, A. K. (1982). Overview 16: The effect of solutes on the strength and strain hardening behaviour of alloys. *Acta Metall*, 30, 615-625.
- [20] Cheng, J., & Nemat-Nasser, S. (2000). A model for experimentally-observed high-strain-rate dynamic strain aging in titanium. *Acta materialia*, 48(12), 3131-3144.
- [21] Dehghani, K., & Jonas, J. J. (2000). Dynamic bake hardening of interstitial-free steels. *Metallurgical and Materials Transactions A*, 31(5), 1375-1384.
- [22] K. Dehghani, Thesis. McGill University Montreal Canada (1999)
- [23] Henshall, G. A., & Miller, A. K. (1989). The influence of solutes on flow stress plateaus, with emphasis on back stresses and the development of unified constitutive equations. *Acta Metallurgica*, 37(10), 2693-2704.
- [24] Lloyd, D. J., & Tangri, K. (1972). Dynamic strain ageing as a strengthening mechanism. *Materials Science and Engineering*, 10, 75-80.
- [25] Spitzig, W. A., & Sober, R. J. (1975). Dynamic strain aging as a strengthening mechanism in iron and iron-phosphorus alloys. *Materials Science and Engineering*, 20, 179-184.
- [26] Brindley, B. J., & Barnby, J. T. (1966). Dynamic strain ageing in mild steel. *Acta Metallurgica*, 14(12), 1765-1780.
- [27] Wilson, D. V., & Russell, B. (1960). The contribution of atmosphere locking to the strain-ageing of low carbon steels. *Acta metallurgica*, 8(1), 36-45.
- [28] Leslie, W. C. *The Physical Metallurgy of Steels*, 1981. McGraw HillBook Company, New York.
- [29] Rajesh, S., & Ananthakrishna, G. (2000). Relaxation oscillations and negative strain-rate sensitivity in the Portevin–Le Chatelier effect. *Physical Review E*, 61(4), 3664- 3674.
- [30] Fressengeas, C., Beaudoin, A. J., Lebyodkin, M., Kubin, L. P., & Estrin, Y. (2005). Dynamic strain aging: a coupled dislocation—solute dynamic model. *Materials Science and Engineering: A*, 400, 226-230.
- [31] Ananthakrishna, G., & Bharathi, M. S. (2004). Dynamical approach to the spatiotemporal aspects of the Portevin–Le Chatelier effect: chaos, turbulence, and band propagation. *Physical Review E*, 70(2), 026111.-15.
- [32] Ait-Amokhtar, H., Fressengeas, C., & Boudrahem, S. (2008). The dynamics of Portevin–Le Chatelier bands in an Al–Mg alloy from infrared thermography. *Materials Science and Engineering: A*, 488(1), 540-546.
- [33] Zbib, H. M., & Aifantis, E. C. (1988). A gradient-dependent model for the Portevin-Le Chatelier effect. *Scripta Metallurgica*, 22(8), 1331-1336.
- [34] Hähner, P. (1996). On the physics of the Portevin-Le Châtelier effect part 1: The statistics of dynamic strain ageing. *Materials Science and Engineering: A*, 207(2), 208-215.
- [35] Soare, M. A., & Curtin, W. A. (2008). Solute strengthening of both mobile and forest dislocations: The origin of dynamic strain aging in fcc metals. *Acta Materialia*, 56(15), 4046-4061.
- [36] Cottrell, A. H., & Bilby, B. A. (1949). Dislocation theory of yielding and strain ageing of iron. *Proceedings of the Physical Society. Section A*, 62(1), 49-62.

-
- [37] Zhao, J. Z., De, A. K., & De Cooman, B. C. (2001). Formation of the Cottrell atmosphere during strain aging of bake-hardenable steels. *Metallurgical and Materials Transactions A*, 32(2), 417-423.
- [38] Keh, A. S., Nakada, Y., & Leslie, W. C. (1968). *Dislocation Dynamics*, ed. by AR Rosenfield, GT Hahn, AL Bement, Jr. and RI Jaffee, 381-408.
- [39] Kocks, U. F., Cook, R. E., & Mulford, R. A. (1985). Strain aging and strain hardening in Ni- C alloys. *Acta Metallurgica*, 33(4), 623-638.
- [40] Bergström, Y. (1983). The Plastic Deformation of Metals--a Dislocation Model and Its Applicability. *Rev. Powder Metall. Phys. Ceram.*, 2(2), 79-265.)
- [41] Taheri, A. K., Maccagno, T. M., & Jonas, J. J. (1995). Dynamic strain aging and the wire drawing of low carbon steel rods. *ISIJ international*, 35(12), 1532-1540.
- [42] Gilat, A., & Wu, X. (1997). Plastic deformation of 1020 steel over a wide range of strain-rates and temperatures. *International journal of plasticity*, 13(6), 611-632.
- [43] McCormick, P. G. (1988). Theory of flow localisation due to dynamic strain ageing. *Acta Metallurgica*, 36(12), 3061-3067.
- [44] van Liempt, P., Onink, M., & Bodin, A. (2002). Modelling the influence of dynamic strain ageing on deformation behaviour. *Advanced Engineering Materials*, 4(4), 225-232.

Chapter 5. A physically based yield criterion I¹

Determination of the yield stress based on analysis of pre-yield dislocation behaviour

Can you see anything?"... "Yes, wonderful things

G.E.S.M.H. Carnarvon & H. Carter

Abstract

In this paper a physically based method to determine the yield stress of metals from tensile curves is proposed. The criterion is based on the identification of the transition in dislocation behaviour from limited reversible glide in the pre-yield stage, without essential changes in the dislocation structure, to dislocation multiplication in the post-yield stage. This transition point is a clearly distinguishable feature in a plot of the hardening rate vs. the flow stress (a Kocks-Mecking plot). Literature shows that this is a common feature shared by metallic alloys under different circumstances. The present paper shows, on the basis of stress-cycling experiments, that the pre-yield behaviour, *i.e.* at stresses below the observed transition point, is explained by reversible dislocation behaviour. Schoeck's classical theory of this anelastic deformation is extended to give a quantitative description of dislocation behaviour in the pre-yield stage. The extended theory provides a very accurate description of pre-yield deformation and can be used to determine structural parameters that characterise the initial dislocation structure.

5.1 Introduction

The yield stress is by far the most widely used parameter to define the strength of metallic alloys. The yield stress is normally determined from a stress-strain curve resulting from a tensile test, but these curves seldom show a clear transition between (an)elastic and plastic deformation. For this reason, the practical concept of the 0.2% off-set is used to determine the yield stress. Apart from the value of 0.2% strain being rather arbitrary, the method does not rely on a physical basis that is related to the actual onset of plastic yielding. It is obvious that it would be of great scientific and industrial interest to have an

¹ Published as: van Liempt, P., & Sietsma, J. (2016). A physically based yield criterion I. Determination of the yield stress based on analysis of pre-yield dislocation behaviour. *Materials Science and Engineering: A*, 662, 80-87.

adequate criterion to actually determine the stress value at which plastic deformation starts.

In many fields of engineering, from structural engineering [1] to that of surgical tools [2], knowledge of the yield stress of the applied materials is of great importance, as it defines the limits of structural integrity of constructional elements. In the field of process engineering of manufacturing steel and other metals the yield stress also plays a crucial role. The successful manufacture of advanced high-strength steels calls for physically based constitutive models. A trend is emerging for through-process modelling of the hot-rolling process, from reheating furnace to hot coiling. Reliable rolling models play an essential part in this development, since during roughing and finishing deformation processes the final precipitate and grain structures form. The models for these processes must be able to predict the flow stress during hot rolling for the purpose of Hot Mill Process control as well as to predict the microstructure at the moment that the material enters the run-out table. In this stage of the process the evolution of the microstructure, which can be defined as the phases present, grain size and dislocation structure, depends on dynamic and static recrystallization, influenced by Zener pinning by precipitates or solute drag, and on the thermodynamic driving force that can be identified with the stored energy, which in turn is constituted by the dislocation density formed during work hardening.

The understanding and quantification of strength and stored energy relies on a robust definition of the yield stress, which is supposed to be the stress at the onset of plastic deformation. The commonly used 0.2% offset yield stress lacks a physical basis and its use is commonly justified by the fact that metals often “...do not show a clearly defined yield point in the tensile curve...” [3], [4], [5]. In the present paper the stress-strain curve from a tensile test will be interpreted in terms of dislocation behaviour in the stress regime before yielding (pre-yield) and after yielding (post-yield). In the pre-yield regime it is widely accepted that dislocations show reversible bowing due to the relatively low applied stress (anelastic deformation), the post-yield regime is defined by Frank-Read sources being active and dislocation multiplication taking place (plastic deformation). It will be shown that the transition between these regimes can be clearly identified in a graph of the hardening rate as a function of the flow stress, which provides a well-defined and physically based yield criterion.

Related fundamental questions that will be addressed in this paper pertain to the nature of pre-yield behaviour. Pre-yield behaviour is not strictly linearly elastic up to the yield point, with Young's modulus as the proportionality constant between stress and strain. Distinct non-linearity occurs in the pre-yield regime, which is related to reversible behaviour of dislocations. The

relation between the non-linear pre-yield behaviour and the motion of dislocations will be investigated. It will be experimentally shown and theoretically discussed that the pre-yield behaviour is largely determined by dislocation glide that is mainly reversible and does not involve changes in the dislocation structure. This enables a characterisation of the dislocation structure in the metal from the pre-yield tensile curve.

5.2 Pre-yield behaviour

The yield stress σ_y is commonly defined as the value of equivalent von Mises stress above which irreversible, plastic strain occurs. This definition implies that for stresses below the yield stress, the strain is reversible. Note that this definition only involves macroscopic observations and does not relate to the microscopic mechanisms at the level of dislocation motion. Nevertheless, it is widely accepted that plastic deformation is accompanied by massive multiplication of dislocations acting as Frank-Read sources and consequently significant changes in the dislocation structure and density. An appropriate physical definition of the yield stress at the microscopic level is therefore the stress at which Frank-Read sources become activated and the dislocation structure starts to change.

The standard procedure for determining the yield stress [6], [7] consists of constructing the tangent to the stress-strain curve in the pre-yield regime and determining the intersection of that tangent with the measured stress strain curve after applying a strain offset of 0.2%. The resulting yield stress is often indicated as the $R_{p0.2}$ -value. Although the chosen magnitude of 0.2% strain is arbitrary, this method is widely accepted due to the difficulty in most cases to identify the yield transition. However, this yield criterion is not directly related to the physical transition from pre-yield to post-yield behaviour of the material. In other words, there is no physical reason to assume that the $R_{p0.2}$ -value represents the actual onset of plastic deformation.

In order to analyse the strain behaviour in the pre- and post-yield regimes, the total strain ε is taken equal to the pre-yield strain ε^{pre} for stresses lower than the yield stress σ_y , and equal to the sum of ε^{pre} and the post-yield strain ε^{post} for higher stresses, which can be expressed as

$$\varepsilon = \varepsilon^{pre} + \varepsilon^{post}, \text{ with } \varepsilon^{post} = 0 \text{ for } \sigma < \sigma_y. \quad (5.1)$$

The stress-strain relation for deformation below the yield stress is basically not linear; it depends on two contributions: (i) linear elastic behaviour according to

Hooke's law; (ii) bowing out of dislocation segments under a relatively low stress, i.e. a stress below the critical stress for Frank-Read sources. On the other hand, the relation between stress and plastic strain above the yield stress is determined by the dislocation multiplication process and interactions between dislocations and the various microstructural obstacles that restrict their propagation. Note that the non-linear stress-strain behaviour in the pre-yield regime compromises the accuracy of the $R_{p0.2}$ determination.

An alternative view on the tensile curve is provided by the so-called Kocks-

Mecking plot, a graph of the work-hardening rate $\Theta = \frac{d\sigma_f}{d\varepsilon}$ versus the flow

stress σ_f at constant strain rate and temperature. This plot is based on the Kocks-Mecking model [8], [9], [10], or alternatively the Bergström model [11], [12], [13], which describes the increase of dislocation density ρ in the post-yield regime as a function of strain, combined with the Taylor relation [14] between ρ and the work-hardening contribution σ_w to the flow stress. The relation between flow stress, yield stress and work-hardening contribution is by definition $\sigma_f = \sigma_y + \sigma_w$. The dislocation theory leads to a linear relation between Θ and σ_w in the so-called Stage-III regime that can be expressed as

$$\Theta^{post} = \frac{1}{2}(\alpha \bar{M} G b U - \Omega \sigma_w), \quad (5.2)$$

where U and Ω are parameters describing the dislocation storage rate and the dynamic recovery rate, respectively, in Bergström's notation. G is the elastic shear modulus, which is a function of temperature [15], [16], \bar{M} is the Taylor factor and α is a material parameter that pertains to the dislocation density and distribution. For the non-textured -as found in additional measurements- austenite that was used $\alpha = 0.15$ and $\bar{M} = 3.06$ [17], [18], [19]. Dynamic recovery is associated with thermally activated dislocation climb, and consequently the recovery parameter Ω is a function of the strain rate $\dot{\varepsilon}$ and the temperature T . The parameters Ω and U can respectively be determined from the slope of the Kocks-Mecking curve in Stage III and from the value of Θ at $\sigma = \sigma_y$ ($\sigma_w = 0$). Values of Θ during Stage-III work hardening, including that at the yield stress, are typically two orders of magnitude smaller than the theoretical Young's modulus [10].

In the literature, the Kocks-Mecking (KM) plot is usually given as a function of the work-hardening contribution σ_w , i.e. after subtraction of the yield stress from the flow stress, as shown in the recent example of Figure 5-1, where Θ is linear for $\sigma_w > 0$ (or $\sigma > \sigma_y$) on the basis of eq. (5.2). However, it can be interesting to consider the slope Θ of the tensile curve also in the pre-yield region, as will be done in the present paper.

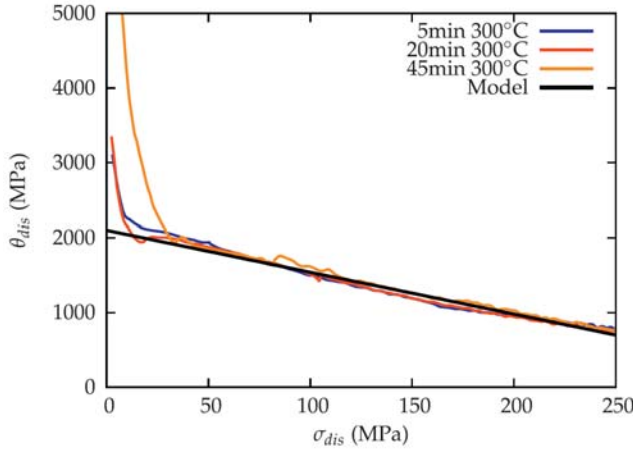


Figure 5-1. Kocks-Mecking plot of an Al–Mg–Sc alloy tested at $T = 77$ K after different ageing treatments [20]. The model that is indicated by the black solid line is a model for plastic deformation.

In view of the non-linearity of the stress-strain curve in the pre-yield region, the term “anelasticity” was coined by Zener [21] to denote the deviating behaviour of metals for small strain, where “strain is not a linear single-valued function of stress alone, but yet where no permanent plastic deformation takes place” [22]. This anelastic behaviour is based on limited, predominantly reversible dislocation motion. The pre-yield strain is thus the sum of the linear elastic strain and the non-linear anelastic strain ε^{AE} , according to

$$\varepsilon^{pre} = \frac{\sigma}{E} + \varepsilon^{AE} \quad (5.3)$$

where σ is the equivalent stress, which is equal to the applied stress in a tensile test, and E is Young’s modulus. From eq. (5.3), the pre-yield slope Θ^{pre} of the tensile curve is derived as

$$\begin{aligned} \Theta^{pre} &= \frac{d\sigma}{d\varepsilon^{pre}} = \left(\frac{d\varepsilon^{pre}}{d\sigma} \right)^{-1} \Rightarrow \\ \Theta^{pre^{-1}} &= \frac{d\varepsilon^{pre}}{d\sigma} = \frac{1}{E} + \frac{d\varepsilon^{AE}}{d\sigma} = \frac{1}{E} + \frac{1}{\Theta^{AE}} \Rightarrow \\ \Theta^{pre} &= \frac{E\Theta^{AE}}{E + \Theta^{AE}}, \end{aligned} \quad (5.4)$$

$$\text{with } \Theta^{AE} = \frac{d\sigma}{d\varepsilon^{AE}}.$$

The anelastic contribution to the pre-yield deformation behaviour, quantified by θ^a , is determined by the dislocation structure and behaviour. Dislocation segments bow out under the influence of the applied stress before reaching the yield stress, which is the stress at which Frank-Read sources are activated.

The anelastic behaviour of dislocations can schematically be described by the configuration sketched in Figure 5-2. Here, it is shown that, when a shear stress

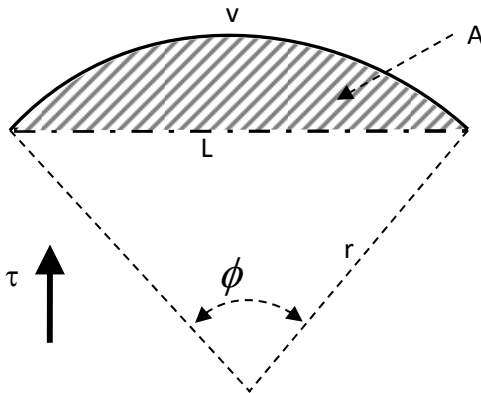


Figure 5-2. Dislocation segment with length L (dash-dot line) bows out under an applied stress τ to the solid line: part of a circle with radius r , causing a shear strain that is proportional to the dashed area A . v is the vertex position of the bowed-out segment.

τ is applied, a dislocation segment of length L bows out, thus causing a shear strain that is proportional to the area A swept by the dislocation. This area can be calculated by

$$A = \frac{1}{2}r^2(\phi - \sin(\phi)). \quad (5.5)$$

The relation between A and the total shear strain γ is

$$\gamma = \frac{\rho b A}{L}. \quad (5.6)$$

At equilibrium, the line stress caused by the radius of curvature r (Figure 5-2) counteracts the applied stress τ . Thus, the stress τ needed to bend a dislocation to a radius r is given by

$$\tau = \frac{Gb}{2r} \quad (5.7)$$

For the determination of the area A , Schoeck [23] assumed that all segments are of equal size and made the approximation $\phi = L/r$ for small angles, which results in $A = \frac{L^3}{12r}$ and eventually in

$$\Theta^{AE} = \frac{3\bar{M}^2 E}{\rho L^2 (1 + \nu)}, \quad (5.8)$$

in which ν is the Poisson ratio. However, Schoeck's approximation is not valid for larger values of ϕ , and eq. (5.8) can therefore not be applied for stresses that approach the yield stress. When instead the exact expression of eq. (5.5) is used, the mathematical derivation presented in the Appendix leads to the relation between the normalised applied stress $s = \sigma/\sigma_c$ and the anelastic slope Θ^p given by

$$\Theta^{AE} = \frac{\bar{M}^2 E s^3 \sqrt{1 - s^2}}{\rho L^2 (1 + \nu) \left(s - \sqrt{1 - s^2} \arcsin(s) \right)} \quad (5.9)$$

and Θ^{pre} , with eq. (5.4), by

$$\Theta^{pre} = \frac{\bar{M}^2 E s^3 \sqrt{1 - s^2}}{\bar{M}^2 s^3 \sqrt{1 - s^2} + \rho L^2 (1 + \nu) \left(s - \sqrt{1 - s^2} \arcsin(s) \right)} \quad (5.10)$$

The critical stress σ_c is defined as the stress at which a dislocation segment of length L yields and starts acting like a Frank-Read source, given by

$$\sigma_c = \frac{\bar{M}Gb}{L} = \frac{\bar{M}Eb}{2(1 + \nu)L} \quad (5.11)$$

Note that eqs. (9) and (10) are applicable for entire range $0 < \phi < \pi$, and can therefore be used for stresses up to the critical stress ($s = 1$).

At the critical stress σ_c a transition to the Stage-III behaviour described by eq. (5.2) is expected. Figure 5-1 shows that indeed distinct deviations from the Stage-III behaviour of plastic deformation occur at low stress. This deviating behaviour can be identified as pre-yield behaviour, and the transition between these regimes as the yield stress, as will be shown in the present paper.

5.3 Experimental details

The alloy used for the experimental research is an Advanced High Strength steel grade of the nominal composition 0.09 wt% C, 1.63 wt% Mn, 0.25 wt% Si and 0.55 wt% Cr. No precipitates are present in the microstructure. The steel is industrially hot rolled to a thickness of 2.0 mm. The material is tested at 910°C, at which temperature it is completely austenitic.

Tensile tests were performed in a Gleeble 3800 thermo-mechanical simulator. This system can perform uniaxial tensile tests under controlled thermal conditions, during which heating is by electric current. Samples can be quenched by a gas/mist nozzle system. The system is mounted inside a vacuum chamber, in order to minimize oxidation and decarburisation of the sample.

In the Gleeble tensile test module, the specimen is held by grips that are kept at room temperature. For standard specimens this causes a large temperature gradient, with temperature variations of typically 200°C over the gauge length. In order to reduce temperature gradients, a tensile specimen of a special design is employed [24]. The temperatures achieved with this technique are uniform within 5–10°C.

Elongation was measured by the cross-head extensometer. The tests have been routinely recorded with a CCD camera to measure local temperatures and transverse/thickness strain. The machine stiffness was determined by a series of stress-cycling tests in the stress regime below the yield stress and corrected for. In these tests a clip-on strain gauge was used to compare crosshead elongation to the elongation of the gauge section.

For the calculation of the stress derivative, an adequate noise filtering procedure is required. The experimental noise in the Gleeble system is mainly due to interference of the electrical AC heating current in the stress and strain measurement system. The observed noise contains 50 Hz and harmonic components, due to the method of control of the electric current. The data have been filtered by processing with a FFT Chebychev low pass filter.

5.4 Results and discussion

5.4.1 Pre-yield behaviour

In Figure 5-3a the low-strain part of a tensile curve of austenite at $T = 910^\circ\text{C}$ recorded at a strain rate of 0.11 s^{-1} is shown. The procedure to determine the $R_{p0.2}$ -value is indicated in the figure. The enlargement of the low-strain data shows that the yield stress, in its physical meaning of the stress at which Frank-Read sources are activated, cannot be determined unambiguously.

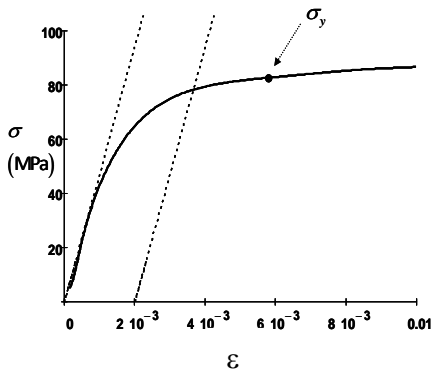
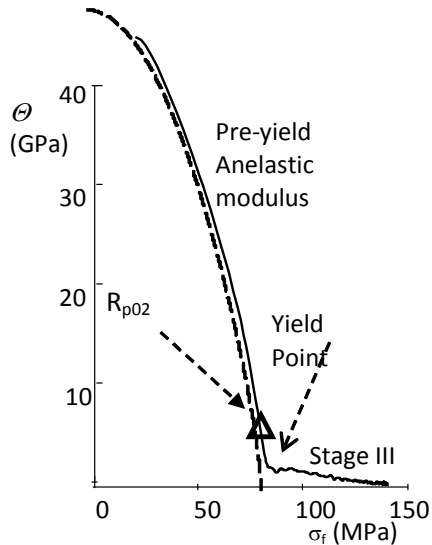


Figure 5-3 (a) Yield regime of a tensile test, showing R_{p02} construction and the yield stress determined from Figure 5-3b. The test is performed on austenite at $T = 910^\circ\text{C}$ and $\dot{\epsilon} = 0.11 \text{ s}^{-1}$.



(b) Extended Kocks-Mecking plot of the data in Figure 5-3a showing a well-defined yield point. The solid line represents experimental data, the dashed line the model description of the pre-yield behaviour with eq. (5.10).

In Figure 5-3b the Kocks-Mecking plot of the same data as in Figure 5-3a is shown, for which we have extended the Kocks-Mecking plot to $\sigma = 0$. The curve shows the same behaviour as in Figure 5-1: two branches of different slope, with a quite sharp transition point between the two. As stated before, the linear high-stress part of the KM-plot describes the plastic behaviour of the material (eq. (5.2)). The low-stress branch, on the other hand, provides information on the pre-yield behaviour of the material, and thus on the dislocation structure in the material. Note that the Young's modulus of the steel at 910°C is 130 GPa [15].

If the pre-yield behaviour would consist solely of linear elastic deformation, the extended KM-plot of Figure 5-3b would be $\Theta^{\text{pre}} = 130 \text{ GPa}$ for $\sigma < \sigma_y$, with a sharp drop to the typical value of Θ at the yield stress, on the order of two orders of magnitude smaller than E [10]. Instead, the initial part of the plot is gradually decreasing, with a slope that is much higher than that of Stage III. The initial value (*i.e.* for $\sigma = 0$) is approximately $\Theta^{\text{pre}} = 47 \text{ GPa}$, which is considerably

lower than the Young's modulus of 130 GPa. This deviation is the result of anelastic strain caused by dislocations, implying that \mathcal{O}^{pre} at zero stress is 35 GPa (eq. (5.4)). At these low stress values Schoeck's approximation (eq. (5.8)) should be valid. Using a value $\nu = 0.3$ for the Poisson ratio, the dislocation structure is quantified by the value $\rho L^2 = 80$, which appears to be a relatively high value. It should be noted that this value is not based on the presently proposed model, but follows directly from the application of Schoeck's classical approximation to the initial value of \mathcal{O}^{pre} . Interpreting the transition point to Stage-III behaviour, which occurs at a stress of 82 MPa, as the critical stress σ_c , eq. (5.11) yields a value $L = 470$ nm and subsequently $\rho = 3.6 \times 10^{14} \text{ m}^{-2}$. Although these are physically realistic values, it should be borne in mind that the measurements have been performed at elevated temperature, and thermally activated dislocation glide, as well as the Hall Petch contribution to the glide resistance, will affect the yield stress. The derived segment length is therefore underestimating the actual value. In a subsequent paper [25], the elementary pre-yield model presented here, will be extended by taking the influence of thermally activated glide and the Hall-Petch resistance into account.

During stress increase from $\sigma = 0$ the dislocation structure (and therefore also the dislocation density and the segment length) remains essentially unaltered as long as the onset of Stage-III plastic deformation is not reached. In Schoeck's approximation (eq. (8)) this would mean that \mathcal{O}^{pre} would remain constant with increasing stress at its initial value of 47 GPa. When the exact solution for the situation of Figure 5-2 eq. (5.10) is applied with the pre-determined parameters $\rho = 3.6 \times 10^{14} \text{ m}^{-2}$ and $L = 470$ nm, the model curve in Figure 5-3b results. Without additional fitting parameters a very accurate reproduction of \mathcal{O}^{pre} as a function of σ is obtained. When σ approaches σ_c , the angle ϕ approaches the value π (cf. Figure 5-2) and dislocation segments are being activated as Frank-Read sources. This implies that the pre-yield behaviour of eq. (5.10) changes into the plastic Stage-III behaviour of eq. (5.2). This transition, very clearly present in the extended Kocks-Mecking plot, is the physical definition of the yield stress σ_y . Exactly how sharp this transition is depends on the dislocation structure in the material, particularly on the distribution of segment lengths. The segment length L in eq. (5.10) should be regarded as the effective segment length of the distribution.

The appearance in eq. (5.10) of the two parameters ρ and L , which characterize the dislocation structure in the material, makes it possible to quantify the initial dislocation structure from stress-strain data in the pre-yield stage. Quantitative determination of these two parameters is possible since not only the product ρL^2 appears in eq. (5.10)), but the effective segment length also appears in the stress parameter s (through eq. (5.11)). An accurate measurement of the pre-

yield stage of a tensile curve is therefore an effective tool for the quantification of the dislocation structure, not only in terms of the dislocation density, but also the effective segment length. In the present case the Hall-Petch contribution to the yield stress has been neglected.

Tiryakioğlu and Alexopoulos [26] observed similar behaviour for the aluminium alloy Al A537 (Al-7%Si-0.5%Mg), which is a dispersion-hardened cast alloy. The material was prepared in different states of precipitation and tested at room temperature. These authors define a transition work-hardening rate $\dot{\sigma}^{\dagger}$ and transition stress σ^{\dagger} closely resembling the yield point according to the criterion proposed in the present paper, but classify the steep branch of the KM-curve as Stage-II work hardening. It is however argued in the literature [10] that Stage-II plastic deformation is only observed in single crystals, and degenerates to a single point at the yield stress for polycrystalline material.

5.4.2 Reversibility of pre-yield strain

As discussed in section 4.1, the pre-yield branch of the extended Kocks-Mecking plot can be adequately explained and quantitatively described by assuming that limited dislocation glide, essentially without changes in the dislocation structure, occurs at stresses below the yield stress.

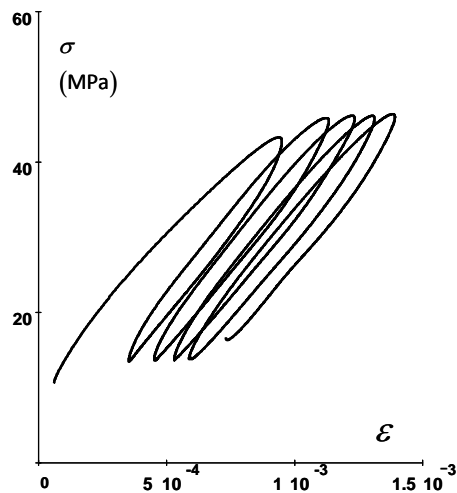


Figure 5-4. Stress-strain behaviour of austenite during a stress-cycling test. The stress rate is 20 MPa s^{-1} , the temperature is $910 \text{ }^{\circ}\text{C}$.

The proposed mechanism, see Figure 5-2, implies that this behaviour should be reversible as long as the stress is below the yield stress. Therefore, stress-

cycling tests at low stresses were performed, and an example of the results obtained is shown in Figure 5-4.

These experiments were carried out on the Gleeble 3800 system at $T = 910^{\circ}\text{C}$. The maximum stress was chosen to be well below the yield stress of 82 MPa, and the minimum stress to be slightly above zero, to ensure adequate grip on the specimen. The stress rate was $\dot{\sigma} = 20 \text{ MPa/s}$ and the resulting strain rate of the order $\dot{\epsilon} = 10^{-3} \text{ s}^{-1}$. It is seen in Figure 5-4 that the strain is largely reversible, with an average slope of 21 GPa, which is significantly lower than the Young's modulus of 130 GPa, but in the range that was described by eq. (5.8) for the normal tensile curve of Figure 5-3. It can be concluded that dislocation motion is the basis for this reversible behaviour, since the slope is much lower than the Young's modulus. However, the strain is not completely reversible. Two additional features are observed: a small strain increment in each cycle (microplasticity [27], [28]) and stress-strain hysteresis. These occur only during cyclic straining, and are of no consequence for the events during monotonous loading. Nevertheless, they indicate the role of dislocations in the pre-yield range, as will be discussed in the next paragraph.

In order to understand these features, we consider an individual dislocation segment, which bows out under the influence of an applied stress that is increasing with time. The line tension of the segment increases when the dislocation bows out from its initial state. In the case that no other sources of stress are present, the position v of the vertex of the segment (see Figure 5-2) is determined by the equilibrium of the dislocation line tension and the applied stress. The line tension increases with increasing distance from the rest position (depicted by the solid line in Figure 5-5, derived from Figure 5-2). The equilibrium position of the dislocation for an applied stress σ_a given by the dotted line in Figure 5-5, is then in point A. In that case the dislocation motion will be completely reversed when the stress is decreased, and the strain associated with this dislocation glide will be reversible. However, in the case of the presence of an obstacle (solute atoms or other dislocations for the material used in this paper), an additional stress component occurs, namely the stress that the obstacle exerts on the dislocation. When the dislocation is on the left-hand side of the obstacle in Figure 5-5, the repulsive stress of the obstacle acts in the same direction as the dislocation line stress. Therefore the dashed line in Figure 5-5 gives the total stress counteracting the applied stress. The equilibrium position of the dislocation segment is now such that the applied stress is in equilibrium with the sum of line tension of the bowed dislocation and the back stress caused by the obstacle, which is position B in Figure 5-5. In this case the dislocation will not pass the obstacle, and the behaviour will be reversible. However, if in a cycling experiment the applied stress is large enough for the dislocation to pass the obstacle (indicated by the upper dash-

dotted line in Figure 5-5); the dislocation will pass the obstacle and proceed to position C. Once the dislocation is on the right-hand side of the obstacle, the obstacle stress acts opposite to the line tension. Therefore the dashed line is below the solid line on the right-hand side of the obstacle. When the stress decreases in the cycle experiment, the dislocation will be trapped behind the obstacle, at position D when the stress reaches the value given by σ_a . Only when the stress level is decreased to the lower dash-dotted line will the dislocation pass the obstacle again. This is the origin of the hysteresis that is observed: the strain is recovered, but at a lower stress level. However, some obstacles will not be passed in the decreasing branch. The behaviour is then not completely reversible and microplasticity will occur. This type of microplasticity will largely be exhausted in the first stress cycle, and explains the conspicuous difference between the first and subsequent cycles.

At elevated temperature ($T = 910^\circ\text{C}$ in the present experiment) localized obstacles can also be passed by means of thermal activation. The probability for a dislocation to pass the obstacle is determined by the activation energy ΔG and the temperature in a Boltzmann factor [29]. The precise profile is a characteristic of the interaction between the dislocation segment and the obstacle. This thermally activated passing of obstacles will take place only for a certain fraction of the obstacles during stress increase, and therefore the consequent microplasticity takes place during the subsequent cycles. Thermally activated passing of obstacles during stress decrease is also possible, but less likely because of the larger activation energy.

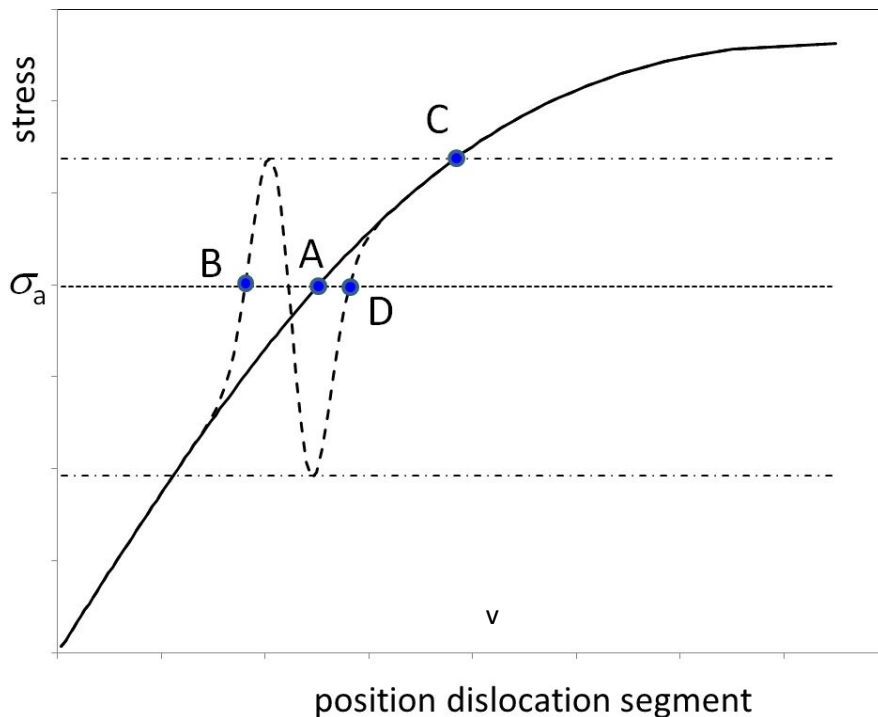


Figure 5-5. Stress on a bowing dislocation segment in the presence of an obstacle. The dislocation is viewed in the line direction. The dislocation line stress (the solid line) is related to the position v of the vertex of the segment according to Figure 5-2, the applied stress is given by the horizontal dotted line. The dashed line applies in the presence of an obstacle.

5.5 The extended Kocks-Mecking plot

It is shown in this study that the transition point that can be observed in an extended Kocks-Mecking plot marks the transition between reversible dislocation glide for low values of stress and the occurrence of dislocation multiplication and irreversible strain at higher stress. The anelastic process in the pre-yielding stage pertains to the movement of dislocation segments in an essentially constant dislocation structure, while the post-yield or plastic branch is associated with irreversible changes in the dislocation distribution. The yield stress can therefore be determined from an extended Kocks-Mecking plot by describing the appropriate branches of the graph by reversible dislocation motion (eq. (5.10) and Stage-III work hardening by eq. (5.2), respectively. The intersection between the two lines gives the yield stress.

The occurrence of anelastic pre-yield behaviour and the distinct transition to plastic post-yield behaviour can be expected for all metals. In the literature Kocks-Mecking plots are commonly shown only for stresses above the yield stress. Kocks-Mecking plots including the low-stress range have been published by Brown and Anand [27] for ferritic Fe-2%Si at elevated temperatures (Figure 5-6a) and by Mecking [28] for the case of polycrystalline Cu (Figure 5-6b) and Au single crystals at room temperature and cryogenic temperatures, and more recently by De Vaucorbeil et al. [20] for an aged Al-Mg-Sc alloy (Figure 5-1). All these plots show similar features as presented in the present paper, namely a steep descent followed by a more gradual one, distinguished by a clear transition point.

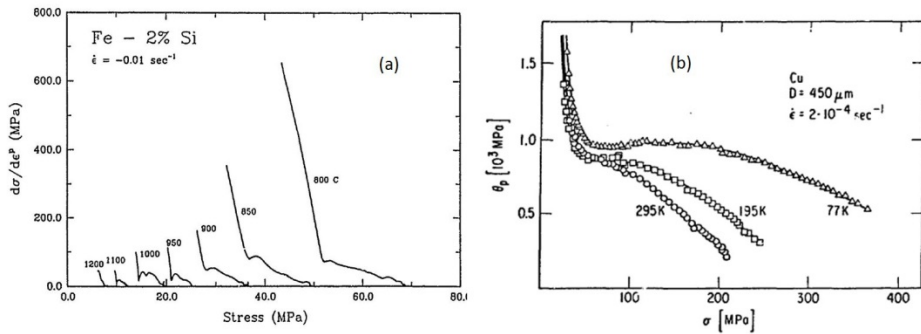


Figure 5-6. Kocks-Mecking plots for (a) ferritic Fe-2%Si [30], (b) polycrystalline Cu [31].

The physical description of the pre-yield behaviour does not only yield a method for an unambiguous determination of the yield stress, but also provides a tool for the characterisation of the dislocation structure of the material, as mentioned in section 4.1. Since the pre-yield behaviour depends on the dislocation structure, an accurate measurement of the pre-yield behaviour provides information on the dislocation structure of the material on which the tensile test is performed. In order to show the sensitivity of the method, in Figure 5-7 a series of curves is shown, which were calculated from eq. (5.10), with the dislocation density ρ and the effective segment length L as variable parameters. Figure 5-7a shows the extended Kocks-Mecking plots for stresses below the yield stress, Figure 5-7b the standard tensile curves $\sigma(\varepsilon)$. The dislocation density was varied between 10^{13} m^{-2} and 10^{15} m^{-2} for $L = 140 \text{ nm}$ (solid lines) and the segment length was varied between 100 nm and 200 nm for $\rho = 10^{14} \text{ m}^{-2}$ (dashed lines). The thin lines in Figure 5-7a and b indicate the

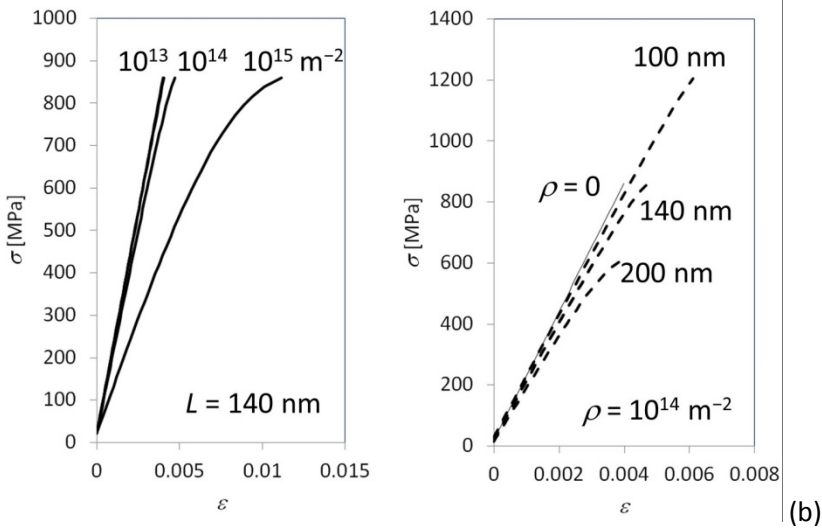
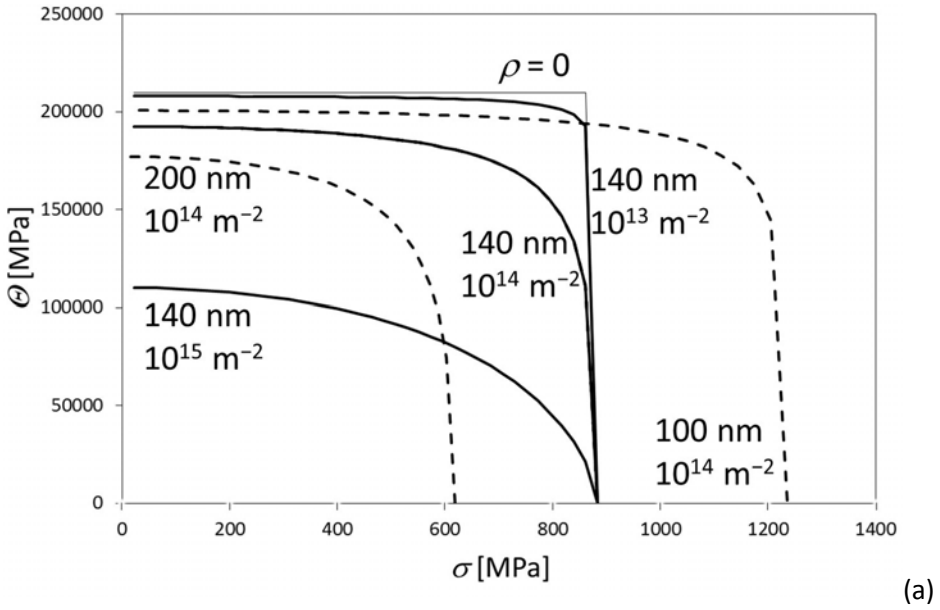


Figure 5-7. (a) Extended Kocks-Mecking plots calculated (γ -Fe) with eq. (5.10), for $L = 140$ nm with $\rho = 10^{13} \text{ m}^{-2}$, 10^{14} m^{-2} , 10^{15} m^{-2} (solid lines) and for $\rho = 10^{14} \text{ m}^{-2}$ with $L = 100$ nm, 140 nm, 200 nm (dashed lines). The thin line indicates the pre-yield behaviour without dislocations. (b) Pre-yield range of tensile curves calculated by numerical integration of eq. (5.10), for the same values as Figure 5-7a. Again, the thin line indicates the pre-yield behaviour without dislocations.

pre-yield behaviour without dislocations, *i.e.* linearly elastic behaviour with $\theta = E$. Figure 5-7 shows that the effect of bowing dislocations is very distinct for medium to high dislocation densities, *e.g.* for $\rho > 10^{14} \text{ m}^{-2}$, and not too short segment lengths. The figure also shows that significant effects of the dislocation structure can be observed and quantified in terms of the two parameters ρ and L at such sufficiently high values of ρ and L .

5.6 Conclusion

A criterion for the determination of the yield stress is proposed that is based on the actual meaning of the yield stress, namely the transition from pre-yield behaviour, with an essentially unchanged dislocation structure, to post-yield behaviour, where dislocation multiplication occurs. This transition can be made clearly visible in an extended Kocks-Mecking plot for the stress range from zero to well into the plastic range of a tensile experiment. It is shown by stress-cycle testing experiments below the yield stress that the pre-yield behaviour indeed involves reversible motion of dislocations. Schoeck's theory of anelasticity has been extended to make it valid for stresses up to the yield stress. The model equations provide a means to derive the effective dislocation segment length and the dislocation density from tensile-test data.

The main conclusions from this study are:

- Anelastic pre-yield behaviour is caused by limited dislocation glide, without changes to the dislocation structure.
- A mathematical extension of Schoeck's classical concept of bowing dislocation segments at low stress provides a very accurate description of the pre-yield behaviour, which is dependent on the dislocation density and the effective segment length.
- The transition point that can be identified in an extended Kocks-Mecking plot is a physically adequate measure for the yield stress, since it marks the transition from the anelastic pre-yield behaviour to plastic deformation causing changes in the dislocation structure.
- Accurate measurement of the pre-yield range in a tensile test can provide quantitative information on the dislocation structure in terms of two parameters: the dislocation density and the effective length of dislocation segments.

Acknowledgements

This research was carried out under project no. MC10.07297 in the framework of the Research Program of the Materials innovation institute (M2i) (www.m2i.nl). The support of M2i and Tata Steel Europe is gratefully acknowledged. The authors wish to thank ir. Heleen Schnitger for fruitful discussions on the pre-yield slope of the Kocks-Mecking plot and dr. Zalao Aretxabaleta for critically reading the manuscript.

References

- [1] Sen, M. (2006). Basic Mechanical Engineering. Firewall Media.
- [2] Reiss et al., United States Patent [19], US005916166 A[iii] Patent Number: [45], 5, 916,166, June 29, 1999
- [3] Moosbrugger, C. (2002). Atlas of stress-strain curves. ASM international, Ohio, 299. ISBN 0-87170-739-X
- [4] Smolik, G. R., & Chen, C. W. (1970). Radiation hardening in vanadium. Journal of Nuclear Materials, 35(1), 94-101.
- [5] Gedge, G. (2008). Structural uses of stainless steel—buildings and civil engineering. Journal of constructional steel research, 64(11), 1194-1198.
- [6] ASTM A370 – 11 Standard Test Methods and Definitions for Mechanical Testing of Steel Products.
- [7] NEN-EN-ISO 6892-1 (en) Metallic materials - Tensile testing, Part 1: Method of test at room temperature (ISO 6892-1:2009, IDT).
- [8] Kocks, U. F. (1976). Laws for work-hardening and low-temperature creep. Journal of engineering materials and technology, 98(1), 76-85.
- [9] Mecking, H. (2001). Work hardening of single-phase polycrystals, Encyclopedia of Materials: Science and Technology.
- [10] Kocks, U. F., & Mecking, H. (2003). Physics and phenomenology of strain hardening: the FCC case. Progress in materials science, 48(3), 171-273.
- [11] Bergström, Y. (1970). A dislocation model for the stress-strain behaviour of polycrystalline α -Fe with special emphasis on the variation of the densities of mobile and immobile dislocations. Materials Science and Engineering, 5(4), 193-200.
- [12] Vetter, R., & Van den Beukel, A. (1977). Dislocation production in cold worked copper. Scripta Metallurgica, 11(2), 143-146.
- [13] van Liempt, P. (1994). Workhardening and substructural geometry of metals. Journal of materials processing technology, 45(1-4), 459-464.
- [14] Taylor, G. I. (1934). The mechanism of plastic deformation of crystals. Part I. Theoretical. Proceedings of the Royal Society of London. Series A, Containing Papers of a Mathematical and Physical Character, 145(855), 362-387.

-
- [15] Ghosh, G., & Olson, G. B. (2002). The isotropic shear modulus of multicomponent Fe-base solid solutions. *Acta materialia*, 50(10), 2655-2675.
- [16] Scruby, C. B., & Moss, B. C. (1993). Non-contact ultrasonic measurements on steel at elevated temperatures. *NDT & E International*, 26(4), 177-188.
- [17] Frost, H. J., & Ashby, M. F. (1977). Deformation-mechanism maps for pure iron, two austenitic stainless steels, and a low-alloy ferritic steel. In *Fundamental aspects of structural alloy design* (pp. 27-65). Springer US.
- [18] Xiao, N., Tong, M., Lan, Y., Li, D., & Li, Y. (2006). Coupled simulation of the influence of austenite deformation on the subsequent isothermal austenite–ferrite transformation. *Acta materialia*, 54(5), 1265-1278.
- [19] Zurob, H. S., Hutchinson, C. R., Brechet, Y., & Purdy, G. (2002). Modeling recrystallization of microalloyed austenite: effect of coupling recovery, precipitation and recrystallization. *Acta materialia*, 50(12), 3077-3094.
- [20] De Vaucorbeil, A., Poole, W. J., & Sinclair, C. W. (2013). The superposition of strengthening contributions in engineering alloys. *Materials Science and Engineering: A*, 582, 147-154.
- [21] Zener, C., & Hollomon, J. H. (1946). Problems in Non-Elastic Deformation of Metals. *Journal of Applied Physics*, 17(2), 69-82.
- [22] Zener, C. (1948). *Elasticity and anelasticity of metals*. University of Chicago press.
- [23] Schoeck, G. (1956). Dislocation theory of plasticity of metals. *Advances in applied mechanics*, 4, 229-279.
- [24] (this thesis)
- [25] van Liempt, P., Bos, C., & Sietsma, J. (2016). A physically based yield criterion II. Incorporation of Hall Petch effect and resistance due to thermally activated dislocation glide. *Materials Science and Engineering: A*, 652, 7-13.
- [26] Tiryakioğlu, M., & Alexopoulos, N. D. (2008). The Effect of Artificial Aging on Tensile Work Hardening Characteristics of a Cast Al-7 Pct Si-0.55 Pct Mg (A357) Alloy. *Metallurgical and Materials Transactions A*, 39(11), 2772-2780.
- [27] Brown, N., & Lukens, K. F. (1961). Microstrain in polycrystalline metals. *Acta metallurgica*, 9(2), 106-111.
- [28] Brown, N. E. K. V. A., & Ekvall, R. A. (1962). Temperature dependence of the yield points in iron. *Acta metallurgica*, 10(11), 1101-1107.
- [29] Caillard, D., & Martin, J. L. (Eds.). (2003). *Thermally activated mechanisms in crystal plasticity* (Vol. 8). Elsevier.
- [30] Brown, S., & Anand, L. (1988). An internal variable constitutive model for the large deformation of metals at high temperatures. Defence Technical Information Center, OAI-PMH Repository (United States).
- [31] Mecking, H. (1975). Description of hardening curves of fcc single- and polycrystals (No. CONF-751164-3). Argonne National Lab., Ill.(USA).

A Appendix. Extension of Schoeck's model of anelasticity for stresses up to the yield stress

In Figure 5-2 an originally straight dislocation segment is shown that bows out under the action of a shear stress. In this Appendix an expression is derived on the basis of the line tension of the dislocation, offering resistance against its movement, as a function of the applied stress in the pre-yield regime.

The area A , sheared by the movement of the dislocation segment of length L between its initial state and its new equilibrium position, is given by:

$$A = \frac{1}{2}r^2(\phi - \sin(\phi)), \quad (\text{A1})$$

where r is the radius of curvature of the bowing segment, and ϕ its subtended angle. Schoeck [23] approximated eq. (A1) for small strain by using $\phi = L/r$, which leads to

$$A = \frac{L^3}{12r}. \quad (\text{A2})$$

The shear strain produced by the dislocation during bowing out from its initial position to the new equilibrium position is given by

$$\gamma = NbA, \quad (\text{A3})$$

where N is the number of dislocation segments of length L per unit volume, and b the magnitude of the Burgers vector. The radius of curvature r of the dislocation segment as a function of applied shear stress τ is

$$r = \frac{Gb}{2\tau}, \quad (\text{A4})$$

with G the shear modulus.

Combining eqs. (A2), (A3), (A4) with the relation $\rho = NL$, the anelastic shear modulus $\Theta_\gamma^{AE} = \frac{d\tau}{d\gamma}$ resulting from this dislocation movement is expressed as

$$\Theta_\gamma^{AE} = \frac{6G}{\rho L^2}. \quad (\text{A5})$$

This is the approximation made by Schoeck [23], which is valid only for very small stress. For the presently proposed model, eq. (A1) is not approximated, but combined with

$$\phi = 2 \arcsin\left(\frac{L}{2r}\right) \quad (\text{A6})$$

which yields an exact expression for the shear strain as a function of the shear stress, given by

$$\gamma = Nb \frac{G^2 b^2 \arcsin\left(\frac{\tau L}{Gb}\right) - GbL\tau \sqrt{1 - \left(\frac{\tau L}{Gb}\right)^2}}{4\tau^2}. \quad (\text{A7})$$

From eq. (A7), the exact expression for the anelastic shear modulus Θ_γ^a can be derived, again with $\rho = NL$:

$$\Theta_\gamma^{AE} = \frac{2\tau^3 \sqrt{1 - \left(\frac{\tau L}{Gb}\right)^2}}{Gb^2 \frac{\rho}{L} \left(\tau L - Gb \arcsin\left(\frac{\tau L}{Gb}\right) \sqrt{1 - \left(\frac{\tau L}{Gb}\right)^2} \right)}. \quad (\text{A8})$$

The limit of Θ_γ^a for $\tau = 0$ that follows from eq. (A8) is equal to Schoeck's approximation (eq. (A5)).

The dislocation line tension that is the basis of eq. (A4) is valid only for $r < \frac{1}{2}L$. At the critical value $r = \frac{1}{2}L$, the dislocation segments will start to emit dislocation loops corresponding to the Frank-Read mechanism. This happens at the critical shear stress $\tau_c = \frac{Gb}{L}$, and eq. (A8) is therefore valid for $0 < \tau < \tau_c$.

Eq. (A8) can be expressed in terms of a dimensionless stress parameter s defined as

$$s = \frac{\tau}{\tau_c} = \frac{\tau L}{Gb} \quad (\text{A9})$$

Eq. (A8) is then valid in the pre-yield regime $0 < s < 1$, and is expressed as

$$\Theta_\gamma^{AE} = \frac{2Gs^3 \sqrt{1 - s^2}}{\rho L^2 (s - \arcsin(s) \sqrt{1 - s^2})} \quad (\text{A10})$$

These equations have been derived for the case of single slip caused by dislocation glide as a function of the resolved shear stress τ on the segment. In order to render them of practical use in the analysis of experimental stress-strain curves, which are obtained from mechanical tests of polycrystalline materials, they must be rewritten in terms of equivalent stress σ and strain ε rather than shear stress and shear strain.

The Taylor factor M is the ratio between the macroscopic uniaxial tension (or equivalent stress) σ and the resolved shear stress τ , according to:

$$\sigma = \bar{M}\tau \quad (\text{A11})$$

This relation implies that the stress parameter s (eq. (A9)) is also representing the equivalent stress, with σ_c the critical stress for the activation of Frank-Read sources:

$$s = \frac{\sigma}{\sigma_c} \quad (\text{A12})$$

And, since the virtual-work principle $\tau d\gamma = \sigma d\varepsilon$ [1], [2] applies,

$$\Theta^{AE} = \bar{M}^2 \Theta_\gamma^{AE}. \quad (\text{A13})$$

Finally, introducing Young's modulus E (related to the shear modulus by $E = 2G(1+\nu)$, with ν Poisson's ratio) the expression for the anelastic contribution to the slope of the stress-strain curve in the pre-yield regime, *i.e.* $\sigma < \sigma_c$, becomes

$$\Theta^{AE} = \frac{\bar{M}^2 E s^3 \sqrt{1-s^2}}{\rho L^2 (1+\nu) (s - \arcsin(s) \sqrt{1-s^2})}, \quad (\text{A14})$$

which is eq. (5.9) of this paper.

References

- [1] Bishop, J. F. W., & Hill, R. (1951). XLVI. A theory of the plastic distortion of a polycrystalline aggregate under combined stresses. *The London, Edinburgh, and Dublin Philosophical Magazine and Journal of Science*, 42(327), 414-427.
- [2] Przybyla, C. P., Adams, B. L., & Miles, M. P. (2007). Methodology for determining the variance of the Taylor factor: application in Fe-3% Si. *Journal of Engineering Materials and Technology*, 129(1), 82-93.

Chapter 6. A physically based yield criterion II.¹

Incorporation of Hall Petch effect and resistance due to thermally activated dislocation glide.

Inventa omnium quae unquam inveni felicissima.

Christiaan Huygens

Abstract

The anelastic model developed in part I of this paper [1] is extended to incorporate the Hall-Petch effect and the thermally activated pre yield phenomena that were revealed in the stress cycling experiments. The yield criterion developed in [1] is tested by application to Hall-Petch experiments and measurements of the yield stress as a function of strain rate and temperature. The results of the strain rate/ temperature experiments support the conclusion that reversible dislocation glide occurs before yield and massive dislocation multiplication. The model is substantiated by analysis of parameters pertaining to the initial dislocation structure viz. the average initial dislocation segment length and density computed from experimental data by application of the model equations.

6.1 Introduction

In the accompanying paper [1], the elastic and anelastic behaviour of metals at stresses lower than the yield stress was analysed in relation to dislocation behaviour. This has led to a physically based definition of the yield stress, as being the stress at which dislocation segments become activated as Frank-Read sources. This accounts for the pinning of dislocations by solute atoms, precipitates and other dislocations, which determines the segment length of the Frank-Read sources. The effect of grain size was however not considered, whereas it is common knowledge that the presence of grain boundaries also has an effect on the yield stress, quantified in the Hall-Petch relation. Although the validity of the Hall-Petch relation is universally accepted, its physical basis is still an issue of discussion [2], [3], [4], [5], [6]. It should be borne in mind that

¹ Published as: van Liempt, P., Bos, C., & Sietsma, J. (2016). A physically based yield criterion II. Incorporation of Hall Petch effect and resistance due to thermally activated dislocation glide. *Materials Science and Engineering: A*, 652, 7-13.

the Hall-Petch relation describes the effect of grain size on the yield stress, and its physical basis should therefore be in the material's behaviour in the pre-yield range, rather than in terms of dislocation pile-ups [2], [7], or other aspects of post-yield plastic behaviour. The central issue addressed in the present paper is the question how the yield stress is determined by both the initially present dislocation structure and the grain size. In the analysis also the thermally activated propagation of dislocations will be taken into account. The analysis leads to a quantitative expression for the yield stress as a function of dislocation structure and grain size, which is consistent with the empirical Hall-Petch relation. A comprehensive set of experimental data over a range of grain sizes, temperature and strain rates will be presented to validate the model.

6.2 Grain boundary strain incompatibility

Below the yield stress, the deformation is the sum of the elastic deformation of the crystal lattice and reversible dislocation glide (dislocation anelasticity). When a polycrystal is subjected to a homogeneous stress below the yield stress, the elastic and anelastic part of the strain tensors of a grain will be different from its neighbouring grains. Therefore, strain incompatibilities will develop at the grain boundaries. The elastic contribution is a direct consequence of the individual orientations of the grains combined with the anisotropy of the elastic stiffness tensor. Meyers and Ashworth [8], [9] and Hirth [10] recognised the elastic incompatibilities, and proposed that the grain size dependence of the yield stress is due to stresses caused by the elastic strain incompatibility of deformation on both sides of the grain boundary. However, they considered incompatibilities in elastic strain only. In the field of crystal plasticity modelling it is recognized that also incompatibilities in plastic strain at the boundaries occur [11], [12]. The same kind of incompatibilities will occur due to pre-yield anelastic strain, which is associated with reversible dislocation glide. The anelastic contribution is a consequence of different – reversible- slip activities on the shear planes of the initially present dislocation segments, like in bulk plastic anisotropy. A model of anelastic strain as a function of stress has been developed in part I of this paper [1].

In order to quantify the grain boundary strain incompatibilities, consider two neighbouring grains a and b that have a certain misorientation, as depicted in Figure 6-1.

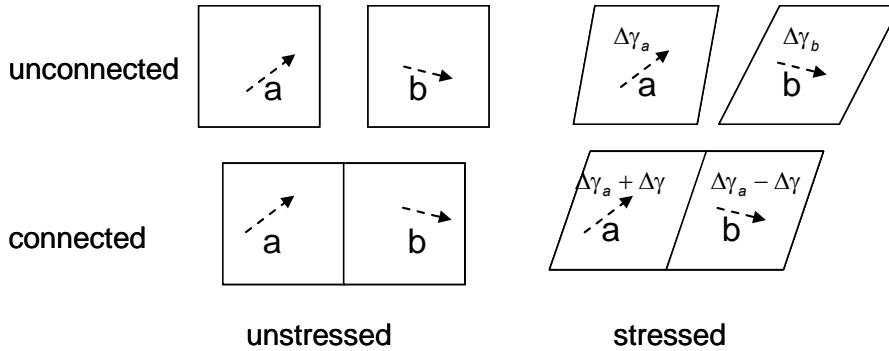


Figure 6-1. Strain incompatibility between differently oriented grains. The arrows indicate the grain orientation.

When subjected to an external shear stress, their local shear strains will be different, and geometrically necessary dislocations (GND's) will be formed at the grain boundary to restore continuity, which will be called grain boundary dislocations (GBD's). The strain incompatibility $\Delta\gamma$ between grains a and b is $\Delta\gamma = \gamma_b - \gamma_a$, where γ_a and γ_b are the shears that grain a and b would have if they were unconnected.

The incompatibility strain is the sum of the contributions due to elastic and anelastic contributions $\Delta\gamma_E$ and $\Delta\gamma_{AE}$ according to

$$\Delta\gamma = \Delta\gamma_E + \Delta\gamma_{AE} \quad (6.1)$$

Ashby et al. [13] have shown that the stress to generate dislocations at a grain boundary is a function of its dimensions. For boundaries larger than $5 \mu\text{m}$ this stress is less than $4 \cdot 10^{-4}G$, which is less than 20% of the yield stress. For the grain structures that are subject in this study, formation of Grain-Boundary Dislocations is therefore possible. The density of GBD's will be given by ρ_{GB} . Due to the strain incompatibility at the grain boundary, the GBD's form a low angle grain boundary, which is superposed on the existing grain boundary.

The strain incompatibilities between grains are seen to be associated with the crystallographic texture of the material. More specific, they relate to the misorientation between adjacent grains.

6.2.1 The grain boundary stress

The presence of the GBD's causes an additional resistance to the movement of the initially present potential Frank-Read sources of length L and density ρ_0 , which are assumed to be randomly distributed in the grain interior. We will

refer to this resistance as the grain boundary stress in the remainder of this study. The critical Frank-Read stress at which the potential sources become active, and which is the yield stress, is therefore dependent on the grain boundary stress. In this section the relation between the grain boundary stress and the grain size will be derived. This derivation leads to a Hall-Petch relation for the grain boundary stress.

Consider a grain with edge length D , where n dislocations of length $l_{GB} = D$ have formed at a grain boundary. n is given by

$$n = \frac{D}{\delta}, \quad (6.2)$$

where δ , which is dependent on the incompatibility strain $\Delta\gamma$, is the distance between the dislocations. The common relation for a low angle grain boundary is given by

$$\delta = \frac{b}{\Delta\gamma}, \quad (6.3)$$

where b is the magnitude of the Burgers vector. The N_g boundaries of the grain are shared with N_g neighbouring grains. From (6.2) and (6.3), introducing a shape factor z_v to express the grain volume by $V = \frac{D^3}{z_v}$, the grain boundary

dislocation density is now

$$\rho_{GB} = \frac{1}{2} N_g \frac{nD}{V} = \frac{N_g z_v}{2\delta D} = \frac{\xi \Delta\gamma}{bD}, \quad (6.4)$$

where $\xi = \frac{N_g z_v}{2}$ is a dimensionless parameter that characterizes the grain

structure. For cubic grains, $\xi = 3$. In order to arrive at an expression for the resistive stress originating from the grain boundaries to the motion of dislocations inside the grains the Taylor relationship can be applied. The Taylor relationship is not very sensitive to the spatial distribution of dislocations according to some authors [14], and is indeed universally successfully applied to situations that differ greatly from the regular distribution of dislocations that was Taylor's starting point [15]. We therefore treat ρ_{GB} like a conventional dislocation density. Substituting (6.4) in the Taylor equation, the equivalent grain boundary stress as felt by the initially present dislocation segments is given by

$$\sigma_{GB} = \alpha c \bar{M} G b \sqrt{\rho_{GB}} = \alpha c \bar{M} G b^{1/2} \sqrt{\frac{\xi \Delta\gamma}{D}}, \quad (6.5)$$

where b is the Magnitude of the Burgers vector, G the elastic shear modulus, $\bar{M}=3.06$ the Taylor factor of the polycrystal, $\alpha=0.15$ a crystallographic

constant [1] and c a stress concentration factor, which is introduced because the dislocation structures at the grain boundaries constitute low angle grain boundaries and thus are highly ordered compared to the dislocation cell boundary structures normally treated by this relation.

Note that eq. (6.5) seems to show the $D^{-1/2}$ dependence of the classical Hall-Petch relation, but it must be remembered that $\Delta\gamma$ is dependent on the applied stress σ , which affects the relation between σ_{GB} and D .

The tilt angle ϕ of the low angle grain boundary that is superposed on the original grain boundary is given by

$$\phi = \Delta\gamma \quad (6.6)$$

Let $\Delta\gamma_E^{ab}$ be the difference in elastic shear between neighbouring grains a and b (see Figure 6-1) :

$$\Delta\gamma_E^{ab} = \left| \gamma_E^a - \gamma_E^b \right| = \left| \frac{\tau}{G_a} - \frac{\tau}{G_b} \right| = \frac{\tau}{G} \left| \chi_a - \chi_b \right|, \quad (6.7)$$

where γ_E^a and γ_E^b are the local elastic shears of the neighbouring grains, G_a and G_b their resolved shear moduli and $\chi_{g=a,b}$ is the ratio between the isotropic shear modulus G and the shear modulus resolved in the loading direction of grain $g = a, b$. $|\chi_a - \chi_b|$ pertains to the misorientation between grain a and b . τ is the applied shear stress. The expectation value of $\Delta\gamma_E$ reads:

$$\Delta\gamma_E = \frac{\tau}{G} \langle |\chi_a - \chi_b| \rangle = \frac{\tau}{G} H = \frac{1}{3} \sqrt{3} \frac{\sigma}{G} H \quad (6.8)$$

The material constant H^2 is the average value of $|\chi_a - \chi_b|$ for the polycrystal.

In eq. (6.8) the shear stress τ is converted to the more practical equivalent stress σ [16].

In analogy to the elastic contribution, the anelastic contribution to the grain boundary strain incompatibility is proportional to the difference in anelastic shear of two neighbouring crystallites according to

$$\Delta\gamma_{AE} = \left| \gamma_{AE}^b - \gamma_{AE}^a \right| = S\gamma_{AE}, \quad (6.9)$$

² After Hirth, who was the first to recognize the relevance of elastic grain boundary incompatibility strains [10]

where γ_{AE} is the average anelastic strain incompatibility and S is a material constant³ that pertains to the average misorientation between neighbouring grains and the distribution of slip systems and the values of their critical resolved shear stress. Substituting eq. (6.8) and eq. (6.9) into eq. (6.5) using (6.3) and eq. (6.1) yields

$$\sigma_{GB} = \alpha c \bar{M} G b \sqrt{\frac{\zeta \left(\frac{H}{\sqrt{3}} \frac{\sigma}{G} + S \gamma_{AE} \right)}{b}} \sqrt{\frac{1}{D}}. \quad (6.10)$$

Note that the grain boundary stress is a function of the applied stress and the anelastic strain (which also depends on the applied stress). The parameters H and S that characterize the contributions of elastic and anelastic deformation to the grain boundary strain incompatibility and grain boundary stress should lie in the range $0 \leq (H, S) \leq 1$, since the absolute difference in strain between crystallites cannot be larger than their individual strain.

6.2.2 The Hall-Petch relation

In order to arrive at an expression for the yield stress, eq. (6.10) must be converted into an expression for the stress equilibrium of the initially present dislocation segments and solved for $\sigma = \sigma_y$, where σ_y is the yield stress. At an applied stress σ lower than the yield stress, it is in equilibrium with the sum of (i) the dislocation line stress σ_l due to the bowing out of the dislocation given by

$$\sigma_l = \frac{\bar{M} G b}{2r}, \quad (6.11)$$

where r is the radius of curvature of the stressed line segment, (ii) the resistance due to thermally activated dislocation glide⁴ (σ^* , which depends on strain rate $\dot{\epsilon}$ and temperature T) and (iii) the grain boundary stress. This results in

$$\sigma = \sigma_l + \sigma^* + \sigma_{GB}. \quad (6.12)$$

³ After Schoeck, who laid the groundwork for the anelastic strain model [31].

⁴ In [1] it was expected that thermally activated dislocation glide contributes to the yield stress. A preliminary analysis of our data has shown, that this contribution is not negligible. This stress contribution will be discussed in detail in a subsequent section.

Substituting eq. (6.10) into eq. (12) yields the following expression for the pre-yield stress:

$$\sigma = \sigma_l + \sigma^* + \alpha c \bar{M} G b \sqrt{\frac{\zeta \left(\frac{H}{\sqrt{3}} \frac{\sigma}{G} + S \gamma_{AE} \right)}{b}} \sqrt{\frac{1}{D}}. \quad (6.13)$$

The anelastic shear strain is a function of the dislocation line stress $\tau_l = \frac{\sigma_l}{\bar{M}}$, and is given by [1]:

$$\gamma_{AE}(\tau_l) = \frac{\rho_0 b}{L} \frac{G^2 b^2 \arcsin\left(\frac{\tau_l L}{G b}\right) - G b L \tau_l \sqrt{1 - \left(\frac{\tau_l L}{G b}\right)^2}}{4 \tau_l^2}. \quad (6.14)$$

Since the line stress is dependent on the applied stress, eq. (6.13) is recursive. Furthermore eq. (6.14) for the anelastic strain is transcendental, so that no general analytic solution for σ as a function of strain can be formulated. For the yield stress σ_y however, an exact solution can be found as follows.

At the yield stress, the dislocation line stress is equal to the critical Frank Read stress, so that the equivalent dislocation line stress for $\sigma = \sigma_y$ reads

$$\sigma_l^c = \bar{M} \frac{G b}{L}. \quad (6.15)$$

From eq. (6.14) it follows that the anelastic shear at yield - that is in the limit where $\tau_l = \tau_l^c$ - is given by

$$\gamma_{AE}^y = \frac{\pi b \rho_0 l}{8}. \quad (6.16)$$

Substituting $\sigma = \sigma_y$, σ_l^c from eq. (6.15) and γ_{AE}^y from eq. (6.16) in (6.13) and solving for the yield stress σ_y yields the following general expression for the yield stress as a function of grain size, temperature and strain rate and misorientation parameters S and H :

$$\sigma_y = \sigma_o + \left\{ s + 2h\sigma_o + \frac{h^2}{D} \right\}^{\frac{1}{2}} \sqrt{\frac{1}{D} + \frac{h}{D}}, \quad (6.17)$$

where the compound parameters σ_o , s and h are respectively

$$\sigma_0 = \sigma_i^c + \sigma^*(\dot{\epsilon}, T), \quad (6.18)$$

$$s = \left(\alpha c \bar{M} G b\right)^2 \xi S \frac{\pi \rho_0 L}{8} \quad \text{and} \quad (6.18b)$$

$$h = \frac{\left(\alpha c \bar{M}\right)^2}{2\sqrt{3}} G b \xi H. \quad (6.18c)$$

The effect of anisotropic anelastic behaviour of dislocations is given by the parameter s , that of anisotropic elasticity of the crystal lattice by h . Note that eq. (6.17) converges to the empirical Hall-Petch relation for large D and/or small values of h .

6.3 Experimental

In this section a series of tensile tests will be analysed by application of the model that is developed in the previous section.

All tensile tests were performed on a Gleeble 3800 system on a Fe-C-Mn alloy of composition 0.09 wt% C, 1.63 wt% Mn, 0.25 wt% Si and 0.55 wt% Cr, containing no precipitating elements. A tensile specimen of a special design to eliminate temperature gradients was employed [17], [18]. With this design, the gradients can be kept within 5°C along the specimen length, which suffices to ensure that yielding does occur homogeneously. The strain rates were 0.02, 0.2, 1.5, 5.5 and 20 s⁻¹. Temperatures ranged from 700 °C to 1200 °C in steps of 50 °C. All specimens were heated to the test temperature at 30 °C s⁻¹, and soaked at that temperature for 20 s before testing. The tests were performed at a vacuum pressure $p = 2.10^{-3}$ Torr obtained after flushing the vacuum chamber with Ar. The specimens that were tested below AC3 temperature were all austenitized at 910 °C, and then rapidly quenched to the test temperature to ensure that the material remained in a metastable austenitic state during the test. There were no indications of transformation (which would cause a sharp decrease in flow stress) during the tensile test for these cases.

As this procedure yields a different grain size at each temperature, the yield stresses must be corrected for grain size effects. Therefore, an additional series of Hall-Petch tests was executed. These consisted of an austenitization step at different temperatures to obtain different grain sizes, followed by tensile testing at a fixed temperature $T_{HP} = 910$ °C and strain rate $\dot{\epsilon}_{HP} = 0.2$ s⁻¹. After fitting eq. (6.17) to the Hall-Petch tests, this relation was used to correct the other tensile tests for grain size effects by subtraction of the second and third terms of eq. (6.17) from the yield stress. $\sigma_0 = \sigma_i^c + \sigma^*(\dot{\epsilon}, T)$.

From σ_i^c and the anelastic strain at the yield stress the length and density of the initially present dislocations can be computed.

All yield stresses were determined from a Kocks-Mecking plot of the stress strain data by the previously developed method [1]. This ensures that work hardening does not contribute to the experimentally determined yield stress values, and that any observed strain rate/temperature dependence is not due to plastic deformation. The Kocks-Mecking graphs were computed after filtering the data by a FFT- Chebychev filter. All stress data were corrected for temperature effects caused by the temperature dependence of the shear

modulus by scaling with $\frac{G(T)}{G(T_{ref})}$, with

$T_{ref} = 910 \text{ }^\circ\text{C}$. For $G(T)$ a polynomial published by Ghosh [19] was used.

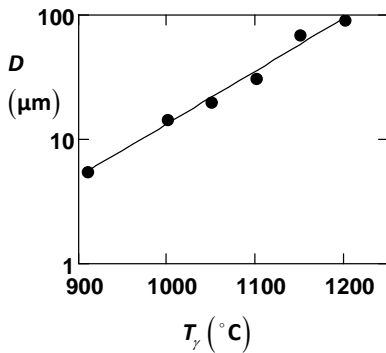
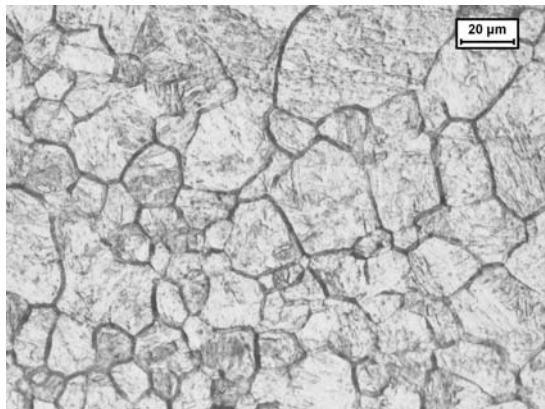


Figure 6-2. Austenite grain size vs. soaking temperature

6.3.1 Hall-Petch analysis

By application of identical heating and soaking cycles as in the tests at varying strain rate and temperature, samples having different grain sizes ranging from $D = 5.5$ to $90 \mu\text{m}$ were produced, as shown in Figure 6-2. These were immediately cooled to a fixed test temperature $T_{HP} = 910^\circ \text{C}$, from which the yield stresses were determined according to the

described method. All tensile tests in this series were executed at strain rate $\dot{\epsilon}_{HP} = 0.2 \text{ s}^{-1}$.



This ensures that the re- *Figure 6-3. Austenitic microstructure, made*
 sistance σ^* due to thermally *visible by transformation to martensite.*
 activated dislocation glide is
 constant in this dataset. Grain sizes were measured separately by reproducing
 the thermal cycles in a Bähr 1500 dilatometer, which can achieve sufficiently
 high cooling rates to transform the austenite microstructure to a fully
 martensitic structure, from which the original austenite microstructure can be
 characterized. An example of the micrographs obtained is shown in Figure 6-3.

In Figure 6-4 the fit of eq. (6.17) to this data is shown. The fitted parameters
 are listed in Table 1.

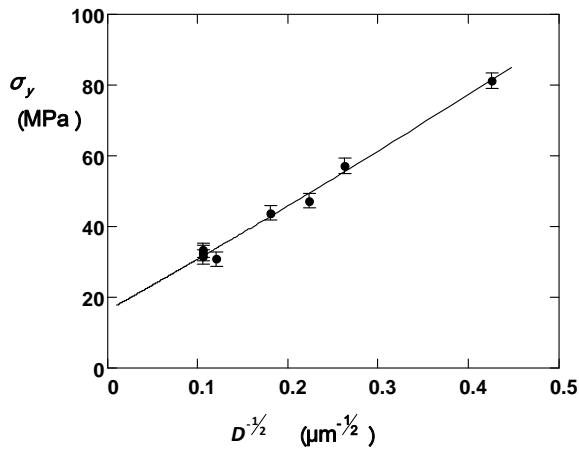


Figure 6-4. Yield stress σ_y vs. $\frac{1}{\sqrt{D}}$ of the Hall- Petch tests.

The maximal contribution of the last term in in eq. (6.17) to the yield stress varies from 1 to 5% for the experimental range of grain sizes so that it may be concluded that

σ_0	16.3 ± 0.6	MPa
s	$2.0 \cdot 10^4 \pm 0.1 \cdot 10^4$	$\text{MPa}^2 \cdot \mu\text{m}$
h	23 ± 10	$\text{MPa} \cdot \mu\text{m}$

the contribution of elastic incompatibility strains is insignificant in this case, which is consistent with the accepted validity of the empirical Hall Petch law.

6.3.2 The yield stress as a function of temperature and strain rate.

The correction for the grain size effect to obtain $\sigma_0 = \sigma_l^c + \sigma^*$ is done by application of eq. (6.17) using the values of Table 1. The result is shown in Figure 6-5.

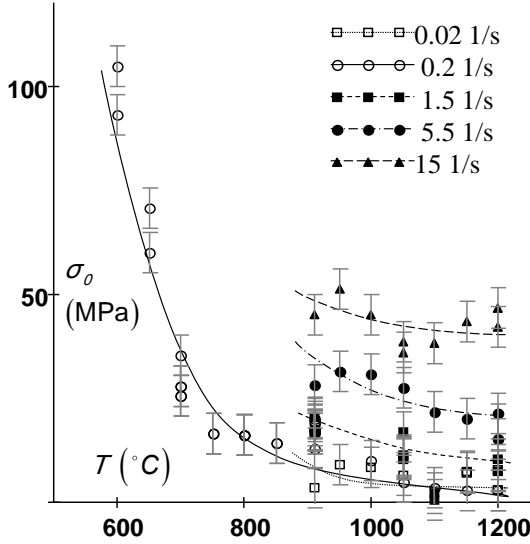


Figure 6-5. σ_0 as a function of temperature for all strain rates.

An important contribution to the yield stress at these temperatures is from the pronounced temperature and strain rate dependence seen to be a resistance due to thermally activated dislocation glide σ^* . This resistance is caused by the thermally activated bypassing of local obstacles by—in this case initially present—dislocations. It is a single valued function of the activation energy ΔG and can be described by a function proposed by Kocks et al. [20]:

$$\sigma^* = \sigma_0^* \left[1 - \left(\frac{\Delta G}{\Delta G_0} \right)^{1/q} \right]^{1/p} \quad (6.19)$$

In this equation, ΔG_0 is the maximal activation energy and σ_0^* the strength of the obstacles. The parameters p and q characterize the force- distance relation of the dislocation- obstacle interaction. ΔG is defined as

$$\Delta G(\dot{\epsilon}, T) = -k_b T \cdot \ln \left(\frac{\dot{\epsilon}}{\dot{\epsilon}_0} \right) \quad (6.20)$$

[21], [22], where k_b is Boltzmann's constant and $\dot{\epsilon}_0$ is a parameter that pertains to the initial dislocation structure and the distribution of local obstacles.⁵ $\dot{\epsilon}_0$ is given by [23]

$$\dot{\epsilon}_0 = \frac{bv_D \rho_0}{\lambda L} bA = \frac{b^2 v_D}{\alpha \bar{M}} \frac{\rho_0 \Delta x_0}{\lambda}, \quad (6.21)$$

where $\frac{bv_D}{\lambda}$ is the attempt frequency with v_D the Debye frequency and λ a phonon wavelength of the size of the obstacle [24], L the dislocation segment length and $A = L \Delta x_0$, with Δx_0 the distance between obstacles in the glide direction, is the area swept out by the dislocation between successive activation events, $\alpha = 0.15$ [1] and $\bar{M} = 3.06$ the Taylor factor.

Using eqs. (6.18),(6.19) and(6.20), σ_0 can be expressed as

$$\sigma_0 = \sigma_i^c + \sigma_0^* \left[1 + \left(\frac{k_b T \cdot \ln \left(\frac{\dot{\epsilon}}{\dot{\epsilon}_0} \right)}{\Delta G_0} \right)^{1/q} \right]^{1/p}. \quad (6.22)$$

Assuming $p=2$ and $q=1/2$ [25], the fit of this equation yields the parameter values listed in Table 2. The fitted data as a function of the activation energy are shown in 6-6.

σ_0^*	$3 \cdot 10^4 \pm 1 \cdot 10^4$	MPa
ΔG_0	2.0 ± 0.1	eV
$\dot{\epsilon}_0$	$9 \cdot 10^6 \pm 1 \cdot 10^6$	s ⁻¹
σ_i^c	10 ± 2	MPa

⁵ Note that $\dot{\epsilon}_0$ can be determined without knowledge of the functional form of σ^* , the only requirement being that the latter is a single valued function of ΔG .

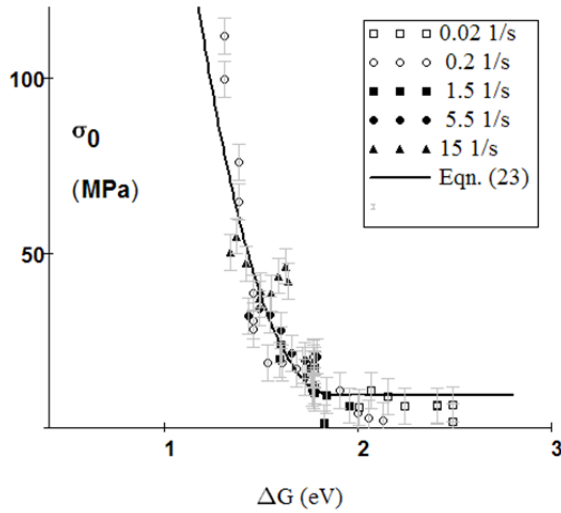


Figure 6-6. Fit of eq. (6.22)

The computed value of the athermal limit σ_l^c is quite small. The mean length of the dislocation segments L as computed from eq. (6.15) is $L = 4.3 \pm 0.4 \mu\text{m}$, which is smaller than all grain sizes albeit with a small margin for the material austenitized at 910°C .

From the value found for h (Table 1) using eq. (17c) and assuming $\xi = 3$, the product c^2H of the elastic incompatibility parameter and the stress concentration factor is $c^2H = 16 \pm 4$.

Next, from eq. (6.16) and the anelastic shear strain at yield γ_{AE}^y , the density of the initially present dislocations can be computed. γ_{AE}^y follows from the experimentally observed total strain at yield by

$$\gamma_y^{AE} = \bar{M} \varepsilon_y^{AE} = \bar{M} \left[\varepsilon_y - \frac{\sigma_y}{2G(1+\nu)} \right], \quad (6.23)$$

where ε_y^{AE} is the anelastic strain at yield and ε_y the total strain at yield. Within experimental error ε_y^{AE} is independent of grain size as expected. Its value is determined as $\varepsilon_y^{AE} = 2 \cdot 10^{-3} \pm 1 \cdot 10^{-3}$. This value is the average of the values derived from the strain at the yield stress, as determined from the extended Kocks Mecking plots and yields for the dislocation density: $\rho_0 = 8 \pm 4 \cdot 10^{12} \text{m}^{-2}$. From the maximum pre yield modulus determined in

part I of this paper [1], and the dislocation segment length $L = 4.3 \pm 0.4 \mu\text{m}$ computed above, the result is $\rho_0 = 5 \pm 2 \cdot 10^{12} \text{m}^{-2}$. This value agrees with that commonly used in models for hot deformation, e.g. [26], [27].

Assuming that the obstacles to dislocation glide are point defects, the characteristic phonon wavelength λ in eq. (6.21) can be taken as minimally $\lambda = b$. This is a conservative estimate. Depending on the nature of the interaction between dislocation and obstacle it may be several times larger. With $\dot{\epsilon}_0$ from Table 2, eq. (6.21) then yields $\Delta x_0 = 0.3 \dots 0.5 \pm 0.15 \text{nm}$, which is of the order of magnitude of the distance between solute C atoms $1.4 \pm 0.1 \text{nm}$, computed from the carbon content $x_C = 0.09 \text{wt\%}$ of the investigated alloy [1].

The anelastic incompatibility parameter S can now be computed from eq. (17b), and s from Table 1, which yields $c^2 S = 15 \pm 3$.

These results are summarized in Table 3.

Table 3. Structural parameters of the proposed Hall- Petch model			
L	4.3	± 0.4	μm
ρ_0	1.0	$\pm 0.5 \cdot 10^{12}$	m^{-2}
$c^2 H$	16	± 4	
$c^2 S$	15	± 3	

The stress concentration factor c can be computed from $c^2 H$ or $c^2 S$ if H or S are known.

Computation of S requires knowledge of the misorientation distribution and must be computed by crystal plasticity methods, which is outside the scope

of this article.

The elastic parameter H can be estimated from the elastic anisotropy of austenite. The maximal ratio of elastic shear moduli of the elastic stiffness tensor is characterized by the Zener anisotropy factor A_Z [28]:

$$A_Z = 2 \frac{C_{44}}{C_{11} - C_{12}} \quad (6.24)$$

which is the ratio between the shear modulus of an isotropic solid (polycrystal) and the maximal shear modulus of a single crystal. From experimental values reported for the elastic constants C_{ij} in [19] this ratio is $A_Z = 5.3 \pm 0.2$. For a random orientation distribution the average ratio is approximately

$$Z = \frac{1 + A_Z}{2} = 3.2, \text{ which is the average ratio between the shear strains in}$$

neighbouring crystallites:

$$Z = \frac{\gamma_E^a}{\gamma_E^b} = \frac{\gamma_E + \Delta\gamma_E}{\gamma_E - \Delta\gamma_E}. \quad (6.25)$$

Substituting for Z and solving for $\Delta\gamma_E$ using the relation $H = \frac{\Delta\gamma_E}{\gamma_E}$, which can be readily derived from eqs.(6.7) and (6.8), yields $H \approx 0.5$. The stress concentration factor c is then $c = 5.5$, and $S = 0.5$. Within experimental error, the contribution of elastic strain to the strain incompatibility at the grain boundaries is equal to that of the anelastic strain

6.4 Discussion.

In the past, a number of Hall Petch theories have been proposed, ranging from the classical pile-up theory to grain boundary dislocation source models of various complexity [2-6], [8], [9]. In the present paper, a physical model for the relation between grain size and yield stress is proposed that is a synthesis of a model of anelastic deformation due to reversible dislocation glide [1], the Frank-Read model and a model of strain incompatibilities that occur at the grain boundaries of a stressed polycrystal.

In part I of this paper [1], the theory of anelastic phenomena in the pre-yield strain region [29], [30], [31], [32] has been extended for stresses up to the yield point. In the present paper, the effects of thermally activated dislocation glide and grain boundary (Hall Petch) stress have been incorporated, the latter following Hirth's idea of strain incompatibilities due to anisotropy. Where Hirth considered elastic strain as the only contribution to the strain incompatibility at the grain boundary, in the present model reversible plastic strain (anelasticity) is also taken into account. Geometrically necessary dislocation (GND) layers have been proposed by e.g. Sinclair et al [3] and Delincé et al. [4], to model the Hall-Petch effect during plastic deformation. However, the yield stress occurs before plastic strain occurs, and the GND/GBD density is gradually built up during pre-yield strain. This is an important feature, and implies that the apparent pre-yield stiffness depends on the grain size. It does not preclude however, that further increase of the GBD density may occur beyond yield. According to the present theory, the Hall Petch coefficient is a function of the average misorientation, which is a property of the crystallographic texture.

The present model avoids theoretical constructions like pile-ups [2] or grain boundary dislocation sources [5], [8], [9] where it is tacitly assumed that some form of dislocation multiplication is the cause of the grain boundary stress. In our model, the dislocation sources are assumed to be an initially present microstructural feature. The yield process is explained by the Frank Read mechanism, which is influenced by the stresses generated by the grain boundaries, which accordingly are responsible for the grain size dependence of the yield stress. This interpretation is in agreement with the occurrence of anelasticity, and of the thermally activated glide resistance that is observed in

the pre-yield strain region. From elementary arguments it is shown that this theory leads to a grain size dependence of the yield stress. This in itself is a successful explanation of the yield stress being dependent on both the size of the initially present dislocation segments and on the grain size.

The yield stress eq. (6.17) is proportional to $D^{-1/2}$, albeit with some terms that are proportional to D^{-1} . A fit of the model to experiments with varying grain size shows that the D^{-1} terms are insignificant with respect to the experimental uncertainty, so that the final result complies with the experimentally well-established Hall Petch law. Since the D^{-1} terms are associated with the elastic contribution to the grain boundary strain incompatibilities, this suggests that $D^{-1/2}$ Hall-Petch behaviour is caused by the predominance of anelastic strain to the strain incompatibility. In other words, the empirically observed Hall-Petch law is mainly caused by the initially present dislocation segments. This can be explained by the fact that the anelastic contribution Θ^{ae} to the pre-yield stiffness Θ^{pre} , defined by $\Theta^{pre} = \left. \frac{d\sigma}{d\varepsilon} \right|_{\sigma \leq \sigma_y} = \frac{E\Theta^{AE}}{E + \Theta^{AE}}$ [1], approaches zero

when the stress approaches the yield stress. This implies that Θ^{pre} approaches Θ^{ae} and that the pre-yield behaviour is dominated by dislocation anelasticity at yield.

The Hall-Petch coefficient, computed from the fit of Figure 6-4 and which by neglecting h in eq. (6.17), is given by $K_y = \sqrt{s} = 141 \pm 3 \text{ MPa } \mu\text{m}^{1/2}$ is close to the value $K_y = 177 \text{ MPa } \mu\text{m}^{1/2}$ that can be computed from measurements published by Ouchi et. al⁶ [33]. Ouchi's results pertain to the flow stress at $\varepsilon = 0.1, 0.2$ and 0.3 rather than to the yield stress. This is probably because they used compression testing, in which the yield stress is difficult to observe. Their results show, that the Hall Petch effect is not dependent on strain. That is also the case for the Hall Petch effect at room temperature [34], [35].

The most satisfying feature of the model is the possibility to compute the density and size of the initially present dislocation segments from tensile data. The present theory will break down for grain sizes $D < L$, since the tacit

⁶ This is the only reference to Hall Petch analysis of low carbon steel in the austenitic temperature range that we could trace to date.

assumption of a grain size independent segment length is then no longer valid and the dislocation segment length then must become proportional to D .

From the values found for the initial dislocation density and length it may be concluded that the potential Frank Read sources are homogeneously distributed through the matrix, rather than residing in the grain boundaries. As the investigated alloy contains no precipitating elements that can provide pinning points for dislocation segments, we assume that these dislocation segments have the form of prismatic dislocation loops, which remain stationary under stress, while being able to bow out at the same time.

The initially present dislocations, however stationary, must be classified as mobile albeit within bounds, by virtue of the observed thermally activated glide. Storage of immobile dislocations in the sense of the Kocks-Mecking and Bergström theories of stage III work hardening only occurs after yielding. This provides for an additional and increasing resistance to the glide of mobile dislocations. Without this resistance the material would deform plastically under constant stress.

We may assume, that the observed resistance due to thermally activated glide will remain present during plastic deformation. This is an additional contribution to the strain rate and temperature dependence of the flow stress of austenitic Fe-C alloys, with respect to dynamic recovery. The glide resistance mechanism has not had as much attention in literature on Fe-C alloys as the strain rate and temperature dependence of work hardening caused by dynamic recovery. The two effects have respectively been identified with the mechanisms that cause strain rate sensitivity of the work hardening rate (indirect strain rate sensitivity or ISRS) and the strain rate sensitivity due to dislocation glide resistance (direct strain rate sensitivity or DSRS) by the present authors in a paper on the subject of dynamic strain ageing in the ferritic temperature range [36]. This is of importance in the field of modelling work hardening and stored energy and of the hot rolling process. The omission of thermally activated dislocation glide resistance may cause systematic errors in the results of hardening models that were fitted to hot rolling force data or other means of obtaining mean flow stresses, which is a widespread method in the industry [37], [38], [39].

6.5 Conclusions

- A model describing pre yield deformation and plastic yielding is presented. The model is essentially a synthesis of the extended Schoeck model of anelasticity [1] describing pre yield reversible dislocation glide, the Frank-Read mechanism and a Hall-Petch model. The Hall-Petch effect is explained by the formation of grain boundary dislocations (GBD's) that are necessary to maintain continuity at the grain boundaries as the load increases. The stress field associated with

the GBD structure constitutes an additional resistance to the bowing out of potential Frank Read sources. The Hall Petch coefficient is a function of the average misorientation that is associated with the crystallographic texture of the material. The $D^{-1/2}$ Hall-Petch law is explained by the fact that anelastic strain is the predominant factor, and is an indication of the presence of a density of potential Frank Read sources in the material sufficiently large for the model to be described by the empirical Hall Petch relation.

- Yield occurs when the critical Frank-Read stress for the longest segments of the initial dislocation structure is exceeded. The applied stress required (i.e., the macroscopic yield stress) is equal to the sum of the critical Frank Read stress, the Hall Petch grain boundary stress and the thermally activated glide resistance on the segments.

Acknowledgements

This research was carried out under project no. MC10.07297 in the framework of the Research Program of the Materials innovation institute (M2i) (www.m2i.nl). The support of M2i and Tata Steel Europe is gratefully acknowledged.

Reference

- [1] Liempt, P. van & Sietsma, J. (2015). A physically based yield criterion I. Determination of the yield stress based on analysis of pre-yield dislocation behaviour. To be published.
- [2] Li, J. C. M., & Chou, Y. T. (1970). The role of dislocations in the flow stress grain size relationships. *Metallurgical and Materials Transactions*, 1(5), 1145-1159.
- [3] Sinclair, C. W., Poole, W. J., & Bréchet, Y. (2006). A model for the grain size dependent work hardening of copper. *Scripta Materialia*, 55(8), 739-742.
- [4] Delincé, M., Bréchet, Y., Embury, J. D., Geers, M. G. D., Jacques, P. J., & Pardoën, T. (2007). Structure–property optimization of ultrafine-grained dual-phase steels using a microstructure-based strain hardening model. *Acta Materialia*, 55(7), 2337-2350.
- [5] Li, J. C. (1963). Petch relation and grain boundary sources. *Transactions of the Metallurgical Society of AIME*, 227(1), 239.
- [6] Bata, V., & Pereloma, E. V. (2004). An alternative physical explanation of the Hall–Petch relation. *Acta Materialia*, 52(3), 657-665.
- [7] Shimokawa, T., Kinari, T., & Shintaku, S. (2007, June). Dislocation-Grain Boundary Interactions by the Quasicontinuum Method. In *Key Engineering Materials* (Vol. 340, pp. 973-978).

-
- [8] Meyers, M. A., & Ashworth, E. (1982). A model for the effect of grain size on the yield stress of metals. *Philosophical Magazine A*, 46(5), 737-759.
- [9] Fu, H. H., Benson, D. J., & Meyers, M. A. (2001). Analytical and computational description of effect of grain size on yield stress of metals. *Acta Materialia*, 49(13), 2567-2582.
- [10] Hirth, J. P. (1972). The influence of grain boundaries on mechanical properties. *Metallurgical Transactions*, 3(12), 3047-3067.
- [11] Ashby, M. F. (1970). The deformation of plastically non-homogeneous materials. *Philosophical Magazine*, 21(170), 399-424.
- [12] Evers, L. P., Brekelmans, W. A. M., & Geers, M. G. D. (2004). Scale dependent crystal plasticity framework with dislocation density and grain boundary effects. *International Journal of solids and structures*, 41(1), 5209-5230.
- [13] Ashby, M. F., Gelles, S. H., & Tanner, L. E. (1969). The stress at which dislocations are generated at a particle-matrix interface. *Philosophical Magazine*, 19(160), 757-771.
- [14] Kocks, U. F., & Mecking, H. (2003). Physics and phenomenology of strain hardening: the FCC case. *Progress in materials science*, 48(3), 171-273.
- [15] Taylor, G. I. (1934). The mechanism of plastic deformation of crystals. Part I. Theoretical. *Proceedings of the Royal Society of London. Series A, Containing Papers of a Mathematical and Physical Character*, 362-387.
- [16] A. Mendelson. *Plasticity: theory and application*. Mac Millan Company, New York. 1968.
- [17] Abspoel, M., Neelis, B. M., & Liempt, P. van (2015). Constitutive behaviour under hot stamping conditions. *Journal of Materials Processing Technology*. IN PRESS
- [18] Liempt, P. van (2016), Ph.D. Thesis, Delft University of Technology
- [19] Ghosh, G., & Olson, G. B. (2002). The isotropic shear modulus of multicomponent Fe-base solid solutions. *Acta materialia*, 50(10), 2655-2675.
- [20] Kocks, U. F., Argon, A. S., & Ashby, M. F. *Thermodynamics and kinetics of slip*, 1975. *Progress in Materials Science*, 19.
- [21] Gibbs, G. B. (1965). The Thermodynamics of Thermally-Activated Dislocation Glide. *physica status solidi (b)*, 10(2), 507-512.
- [22] Schulze, V., & Vöhringer, O. (2000). Influence of alloying elements on the strain rate and temperature dependence of the flow stress of steels. *Metallurgical and Materials transactions A*, 31(3), 825-830.
- [23] Martin, J. L., & Kruml, T. (2004). Characterizing thermally activated dislocation mobility. *Journal of alloys and compounds*, 378(1), 2-12.
- [24] H.Suzuki in: *Rate Processes in Plastic Deformation of Materials*. J.C.M. Li and A. K. Mukherjee (eds.), ASM, Metals Park, OH (1975) 47.
- [25] Sarkar, S., & Militzer, M. (2009). Microstructure evolution model for hot strip rolling of Nb–Mo microalloyed complex phase steel. *Materials Science and Technology*, 25(9), 1134-1146.
- [26] Engberg, G., & Lissel, L. (2008). A physically based microstructure model for predicting the microstructural evolution of a C-Mn steel during and after hot deformation. *Steel Res Int*, 79(1), 47-58.

-
- [27] Domkin, K. (2005). Constitutive models based on dislocation density. Lulea University of Technology.
- [28] Paszkiewicz, T., & Wolski, S. (2008, March). Elastic properties of cubic crystals: Every's versus Blackman's diagram. In *Journal of Physics: Conference Series* (Vol. 104, No. 1, p. 012038). IOP Publishing.
- [29] Mott N. F., *Dislocation Theory of Plasticity of Metals*. 1952 a, *Phil. Mag.*, 43, 1151.
- [30] Friedel, J. (1953). XLVI. Anomaly in the rigidity modulus of copper alloys for small concentrations. *Philosophical Magazine*, 44(351), 444-448.
- [31] Schoeck, G. (1956). Dislocation theory of plasticity of metals. *Advances in applied mechanics*, 4, 229-279.
- [32] Ghosh, A. K. (1980). A physically-based constitutive model for metal deformation. *Acta Metallurgica*, 28(11), 1443-1465.
- [33] Ouchi, C., Okita, T., Ichihara, T., & Ueno, Y. (1980). Hot deformation strength of austenite during controlled rolling in a plate mill. *Trans. Iron Steel Inst. Jpn.*, 20(12), 833-841.
- [34] Armstrong, R. W. (1970). The influence of polycrystal grain size on several mechanical properties of materials. *Metallurgical and Materials Transactions*, 1(5), 1169-1176.
- [35] Butler, J. F. (1962). Lüders front propagation in low carbon steels. *Journal of the Mechanics and Physics of Solids*, 10(4), 313-318.
- [36] Liempt, P. van, & Sietsma, J. (2011). A revised criterion for the Portevin–Le Châtelier effect based on the strain-rate sensitivity of the work-hardening rate. *Metallurgical and Materials Transactions A*, 42(13), 4008-4014.
- [37] Jonas, J. J. (2000). The hot strip mill as an experimental tool. *ISIJ international*, 40(8), 731-738.
- [38] DeArdo, A. J. (1990). Modelling of deformation processing: wonderful tool or wishful thinking. *Mathematical Modelling of Hot Rolling of Steel*, 220-238.
- [39] Siciliano, Jr, F., Minami, K., Maccagno, T. M., & Jonas, J. J. (1996). Mathematical Modeling of the Mean Flow Stress, Fractional Softening and Grain Size during the Hot Strip Rolling of C-Mn Steels. *ISIJ international*, 36(12), 1500-1506.

Chapter 7. Work hardening

Blackadder: Baldrick, have you no idea what irony is?

Baldrick: Yes, it's like goldy and bronzy only it's made out of iron.

7.1 Introduction

In this chapter the work hardening behaviour will be studied, and a model fitted to the experimental data. The choice of an adequate work hardening model will be made by careful qualitative analysis of the work hardening behaviour. The aim of that analysis is to avoid incorporating redundant expressions -however plausible their inclusion physically may seem- into the model to be fitted, and conversely to provide for features of the hardening behaviour that are not (yet) considered in conventional theory. It is our conviction that assessing the raw data to guide the choice of an adequate model is crucial in formulating a physical model. A first step in this analysis has already been made in chapters 5 and 6 where the yield stress contribution to the flow stress has been isolated and fitted to a dedicated yield model.

In chapters 5 and 6 a not insignificant part of the yield stress has been shown to be due to the resistance associated with thermally activated dislocation glide (section 2.6). Dislocation glide resistance is the contribution to the flow stress that is necessary to propagate the mobile dislocations with the velocity that is required to maintain the macroscopically imposed strain rate. That implies that the dislocation glide resistance is a function of the density of mobile dislocations, as expressed by eqs. (6.19)... (6.22). Another implication is that dislocation glide resistance is present during post-yield plastic deformation as well as during pre-yield deformation, and one of the issues to be resolved is the question whether the post-yield glide resistance differs in magnitude from that at the yield instant or not. This question is equivalent to the problem of whether the density of mobile dislocations is constant during plastic deformation and if it is different from that in the pre-yield stress region. In this context it must be remarked that Bergström assumed that it is constant **[1]**. These issues will be addressed in section 7.3.

A second issue is whether dynamic strain ageing is occurring. Dynamic strain ageing is caused by pinning of stored dislocations by solute atoms. Characteristic features of dynamic strain ageing are

- a serrated appearance of the flow stress curve,
- an anomalously high hardening rate over a certain temperature range,
- a negative strain rate sensitivity of the work hardening rate in the low temperature part of that temperature range.

The occurrence of dynamic strain ageing can therefore be evaluated by inspection of the flow stress curves and/or of a plot of the hardening rate as a function of temperature. This will be addressed in section 7.3

From the yield theory developed in Chapter 6 it may be expected that the work hardening rate is dependent on grain size. This will be discussed in section 7.4.3, where the hardening rate of the tests dedicated to the Hall-Petch effect of the yield stress will be investigated with respect to grain size influences on the post-yield behaviour.

The next issue to be addressed is that of the initial work hardening rate. In the conventionally applied Kocks-Mecking and Bergström models it is assumed that the initial work hardening rate is an athermal (that is not associated with thermal activated mechanisms and therefore independent of strain rate and temperature) constant. The initial hardening rate can be evaluated by inspection of the Kocks-Mecking plot (hardening rate vs flow stress) of the flow stress behaviour. It must be evaluated at the yield stress, which is the level of stress where massive dislocation multiplication is initiated. This issue will be addressed in section 7.5.1, where it will be found that the assumption that the initial hardening rate is an athermal constant is not valid in general. An extension of the model to describe the observed behaviour is proposed in section 7.5.3

Fitting of the proposed work hardening model is described in section 7.6 after which the results are discussed. In section 7.7 a discussion of a more fundamental kind, namely the interpretation of the Taylor relation between work hardening and dislocation density will be presented. It will be found that an alternative interpretation of this relation, namely in terms of the Frank-Read critical stress for dislocation multiplication rather than as the stress to propagate dislocations through the dislocation substructure, is viable. That interpretation will be shown to lead to a consistent explanation of pre-yield anelastic deformation and post-yield plastic deformation.

7.2 Experimental

The alloy used for the experimental research is an Advanced High Strength steel grade with nominal composition $x_C = 0.09$ wt%, $x_{Mn} = 1.63$ wt%, $x_{Si} = 0.25$ wt%, $x_{Cr} = 0.55$, with x_i the mass fraction of element i . The computed transformation temperatures are $A3 = 850^\circ\text{C}$ and $A1 = 650^\circ\text{C}$. No precipitates are present in the microstructure. The steel is industrially hot rolled to a thickness of 2.0 mm. Tensile tests were conducted at temperatures in the stable austenite temperature range, and where feasible also at temperatures in the intercritical/metastable austenite temperature range. The latter temperature range was included since generally low temperatures cause high flow stress and

high hardening rates, and a low temperature has a similar effect as a high strain rate. Since the maximal feasible strain rate of the testing machine is an order of magnitude lower than that of the industrial rolling process -which is conducted in the stable austenite temperature range- this will improve the accuracy of extrapolation of the fitted model to the conditions of the target process.

The deformation tests that were performed fall into two categories:

1. Strain rate jump tensile tests. The strain rate jump test is also known as the constant structure test. This test is helpful in differentiating between direct and indirect strain rate sensitivities that are caused respectively by dislocation glide and dislocation multiplication. These tests therefore serve a qualitative diagnostic purpose, the results of which will be discussed in section 7.3.
2. Tensile tests at constant nominal strain rate and temperature, which respectively range between $0.02 \leq \dot{\epsilon} \leq 20 \text{ s}^{-1}$ and $700 \leq T \leq 1200 \text{ }^\circ\text{C}$. These are the tests that the flow stress model will be fitted to.

All tests were performed on a Gleeble 3800 testing machine. The tensile samples used are of the design that is described in Chapter 3. They are manufactured by Blok Velsen-Noord, The Netherlands by a CNC technique. All tests were routinely recorded by a standard HI resolution Sony handycam for the low strain rate tests ($\dot{\epsilon} \leq 0.2 \text{ s}^{-1}$) and a Phantom V5.0 high speed camera for the tests at strain rates $\dot{\epsilon} > 0.2 \text{ s}^{-1}$.

Table 4. Experimental strain rate and temperature range

Nominal strain rate	$\dot{\epsilon} = 0.02 \text{ s}^{-1}$	$\dot{\epsilon} = 0.2 \text{ s}^{-1}$	$\dot{\epsilon} = 1.5 \text{ s}^{-1}$	$\dot{\epsilon} = 5 \text{ s}^{-1}$	$\dot{\epsilon} = 15 \text{ s}^{-1}$
Temperature range [°C]			700	700	
	910	910			910
	1200	1200	1200	1200	1200

Note that a number of tests were conducted at temperatures below 850 °C, where the steel is in a metastable austenitic state. This was done to compensate for the fact that the maximum attainable strain rate is relatively low compared to that of the industrial hot rolling process. For the lower strain rates in that temperature range, transformation will set in during the test. At the highest rate the sensitivity of the high speed camera proved to be too low

for recording at the required frame rate (2100 fps). Therefore the temperature range for the two lowest and the highest strain rate tests has been restricted to the stable austenite temperature range, as shown in Table 4.

The samples were heated at a heating rate $\dot{T} = 20^\circ\text{Cs}^{-1}$ to the test temperature, after which they were annealed during 20 s to be fully transformed to austenite. This procedure was chosen to minimize the time of the testing procedure and avoid decarburisation during the test. A minor disadvantage is that at each test temperature the microstructure will have a different grain size D . The effect of grain size on work hardening -which is not very large- can however readily be incorporated into the hardening model along the lines laid out in Chapter 2, section 2.4 for the part that is attributable to dislocation mean free path effects, and a possible true Hall-Petch contribution as will be discussed in section 7.4.3. The relation between grain size and test temperature that has been determined in Chapter 6 will be employed.

The heating system was switched off at the start of deformation for the tests at strain rates $\dot{\epsilon} > 0.2\text{S}^{-1}$. This was done in order to avoid the interference with the electrical heating current. At $\dot{\epsilon} > 0.2\text{S}^{-1}$, the decrease of temperature during deformation was negligible. For the two lowest strain rates the heating was left on.

The recorded data have been pre-processed by the method outlined in Chapter 3. First, the interference due to the electrical heating was removed by a Chebychev filter in the Fourier domain. For analysis of the pre-yield strain regime, extended Kocks-Mecking graphs were calculated from the stress strain data recorded directly by the Gleeble system. From these, the yield stresses were calculated, and fitted to the yield stress model developed in Chapters 5-6. That model incorporates contributions of dislocation glide resistance, the Hall Petch stress and the critical Frank-Read stress associated with bowing out of initially present dislocations.

In order to obtain true stress-strain data for strains beyond the onset of necking, local strains were determined from the recorded video streams, after which local true strain and stress can be calculated. The strain values are based on the transverse strain, and the conversion to true strain was performed using $r_L=1$ for the Lankford r_L -value which denotes the ratio between transverse and longitudinal strain components. All stresses have been normalized for temperature variation of the elastic shear modulus of the crystal lattice by

multiplication of the stress values with $\frac{G(T_0)}{G(T)}$, where $T_0=910^\circ\text{C}$ is the

normalisation temperature, chosen as the minimum test temperature for which

the material remained in the austenitic state. The elastic shear modulus of austenite is given by the empirical relation [2]

$$G(T) = 92.648 \cdot \left[\begin{array}{l} 1 - 7.9921 \cdot 10^{-7} \text{K}^{-2} T^2 + \\ + 3.3171 \cdot 10^{-10} \text{K}^{-3} T^3 \end{array} \right] \text{GPa}, \quad (7.1)$$

with T in Kelvin. This equation is based on experimental values as well as on ab initio calculations and is therefore also valid for temperatures in the region where austenite is metastable.

Conventional Kocks-Mecking plots, i.e. the work hardening rate vs. the work hardening contribution σ_w , were calculated next by subtracting the yield stress σ_y from the flow stress σ_f , i.e. $\sigma_w = \sigma_f - \sigma_y$.

7.3 Analysis of strain rate jump tests

In general, the post-yield flow stress σ_f is the sum of the yield stress σ_y , a work hardening contribution σ_w and a dislocation glide resistance σ^* :

$$\sigma_f = \sigma_y + \sigma_w(\varepsilon, \dot{\varepsilon}, T) + \sigma^*(\dot{\varepsilon}, T) \quad (7.2)$$

Work hardening is associated with dislocation multiplication, while glide resistance is associated with thermally activated propagation of mobile dislocations, as explained in Chapter 2. Both are dependent on strain rate and temperature due to different thermally activated mechanisms. The flow resistance associated with thermally activated dislocation glide is often not taken into account in studies pertaining to flow stress at elevated temperature. In this chapter we will therefore examine which of these flow stress contributions should be present in the model to be fitted, and whether they can be fitted separately.

In chapters 5 and 6 it was found that there is already a considerable contribution to the yield stress caused by dislocation glide resistance associated with thermally activated glide. This conclusion was made on the basis of the newly proposed yield criterion. In contrast to the conventional 0.2 % offset plastic strain yield criterion ($R_{p0.2}$), the new criterion leaves no room for interpreting the observed strain rate/temperature dependence of the yield stress as to be due to thermal effects of the work hardening behaviour.

The dislocation glide resistance is dependent on the density of mobile dislocations (chapter 5, eq. 21) ρ_m which has been found to be virtually equal to the density of dislocations ρ_0 that are present before yielding occurs. While the success of fitting the glide resistance with a constant structure parameter $\dot{\epsilon}_0$ has shown that ρ_m is independent of the applied stress, it cannot be assumed a priori that it is not dependent on plastic strain.

As explained in Chapter 3, the strain rate jump test is a tool for distinguishing between the strain rate sensitivities due to dislocation glide, respectively due to dislocation multiplication (work hardening).

Two different types of jump test were made. The first type consists of a test where the strain rate is instantaneously increased and another in which it is decreased. The stress jump was executed at the same value of plastic strain, while the high and low strain rate values were equal for the two types of tests. The set of tests is completed by performing two tests at constant strain rate equal to the high, respectively low strain rate of the jump tests.

Care was taken to avoid that dynamic recrystallisation (DRX) interfered with work hardening in the jump tests, since DRX will cause yet another strain rate dependence than that of glide resistance and of work hardening. This was realized by choosing the plastic strain at which the strain rate jump was made to be well below the strain where the (true) flow stress is maximal. Any decreasing true flow stress at constant strain rate indicates that some stress relaxation process other than dynamic recovery occurs, most probably (dynamic) recrystallisation.

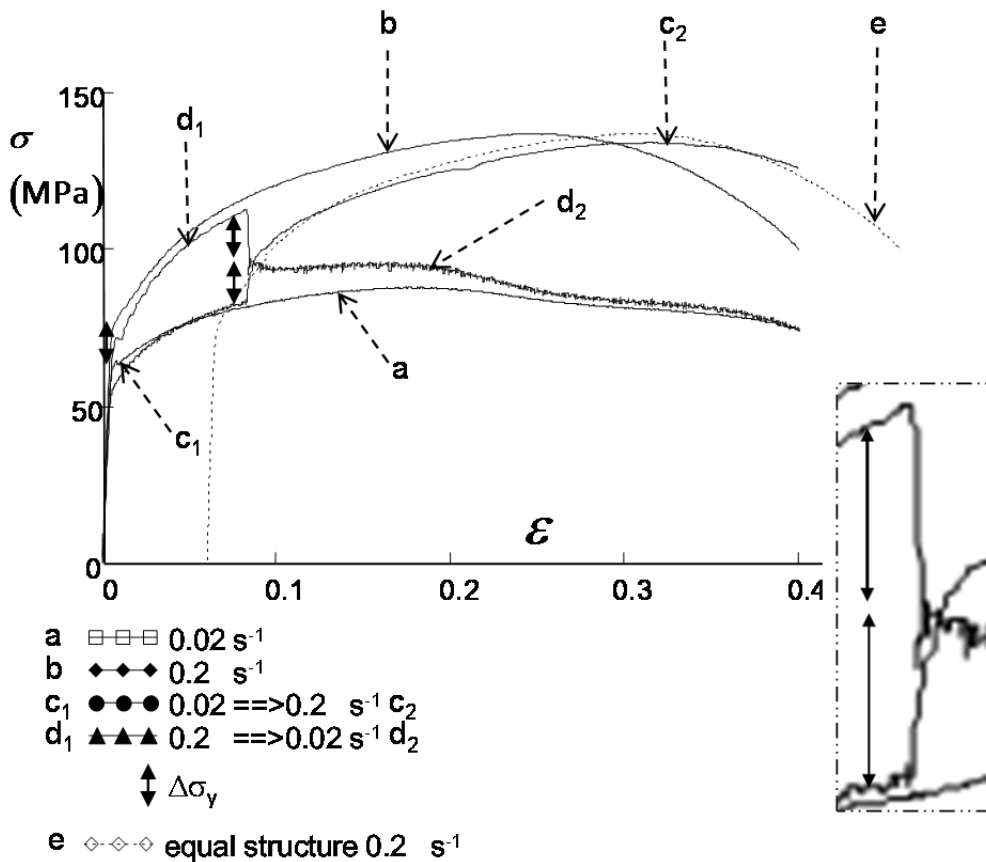


Figure 7-1. Constant strain rate and strain rate jump tests $T=910\text{ }^{\circ}\text{C}$. True stress vs true strain. Inset: detail at the strain rate jump instant.

In Figure 7.1 a typical result of the strain rate jump test sets is shown. All curves are of *local* true stress vs. local true strain, viz. they are corrected for necking. Two hardening curves at constant strain rates $\dot{\epsilon} = 0.02$ respectively 0.2 s^{-1} are plotted, and two curves where the strain rate was instantly increased at $\epsilon = 0.085$ from $\dot{\epsilon} = 0.02$ to 0.2 s^{-1} respectively decreased from $\dot{\epsilon} = 0.2$ to 0.02 s^{-1} .

The magnitude of the instantaneous stress changes of the jump test and the difference in yield stress between the two constant strain rate tests is indicated in that (dynamic) recrystallisation occurs at strains far beyond the jump event. Note that there is a distinct instantaneous change of the flow stress in both jump tests. This clearly indicates a significant contribution of flow resistance

associated with thermally activated dislocation glide. The stress increment respectively decrement at the jump instant is approximately equal to the difference in glide resistance for the two strain rates. The resistance associated with thermally activated dislocation glide is of the same order of magnitude as the degree of work hardening at moderate strain.

The yield stress of the constant rate hardening curves for $\dot{\epsilon} = 0.02$ respectively 0.2 s^{-1} is $\sigma_y(\dot{\epsilon} = 0.02 \text{ s}^{-1}) = 63 \pm 2 \text{ MPa}$ and $\sigma_y(\dot{\epsilon} = 0.2 \text{ s}^{-1}) = 77 \pm 2 \text{ MPa}$. The instantaneous stress increment respectively decrement at the strain rate jumps at $\epsilon = 0.085$ is within experimental error equal to the difference $\Delta\sigma_y = 14 \text{ MPa}$ between these two yield stresses. This indicates that the glide resistance during plastic deformation is equal to that at yield, at least for $0 < \epsilon < 0.085$.

7.3.1 Dislocation glide resistance as a function of strain

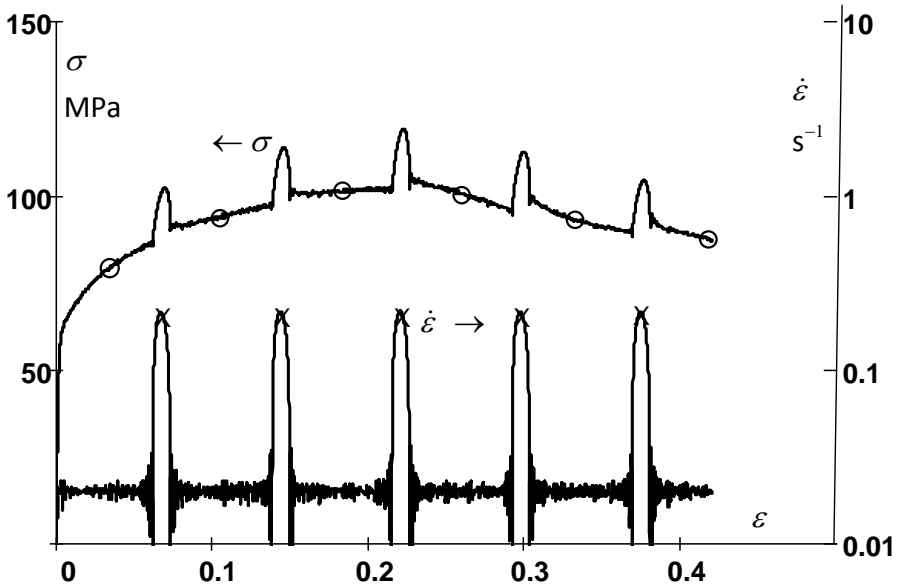


Figure 7-2. Multiple strain rate jump experiment $T=910 \text{ }^\circ \text{C}$. Strain rates $\dot{\epsilon} = 0.02\text{--}0.2 \text{ s}^{-1}$.

In order to see whether the glide resistance is dependent on strain for a larger strain range, a test with multiple strain rate jumps was performed, which is shown in Figure 7-2.

During deformation at $\dot{\epsilon} = 0.02 \text{ s}^{-1}$ a series of strain rate bursts of $\dot{\epsilon} = 0.2 \text{ s}^{-1}$ during a strain interval $\Delta\epsilon_{hi} = 0.012$ were performed. The bursts are separated by low strain rate intervals $\Delta\epsilon_{lo} \approx 0.075$. Note that the hardening rate during a strain rate burst is larger than that during the low strain rate intervals.

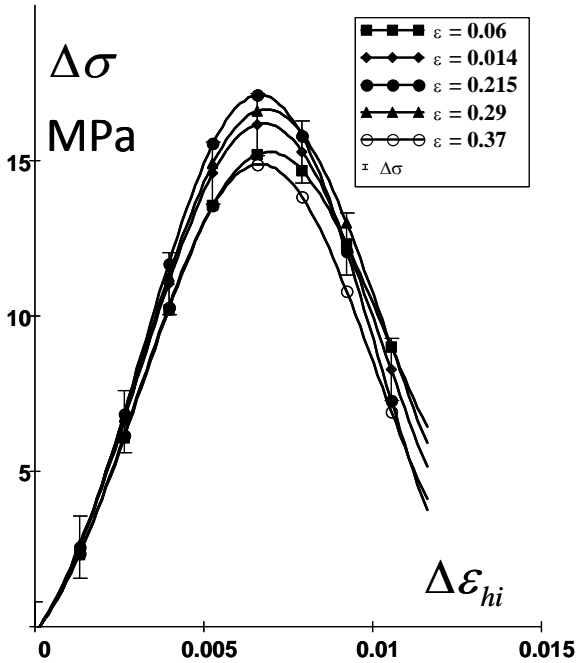


Figure 7-3. Stress bursts during the multiple strain rate jump test of Figure 7.2.

The stress bursts were separated from the stress-strain curve and plotted in Figure 7-3. All stress bursts are virtually equal within experimental error ($\delta\epsilon_{hi} \approx \pm 2 \text{ MPa}$).

The glide resistance appears to be approximately independent of strain, even after recrystallisation has set in at $\epsilon \approx 0.2$.

The conclusion is that the resistance associated with dislocation glide is constant in the post-yield strain range and equal to the glide resistance at yield to good approximation. This provides the advantage that the resistance associated with dislocation glide can be fitted independently from the flow stress.

7.3.2 State variable for work hardening

Another interesting observation that can be made from Figure 7.1 concerns the transient hardening just after the strain rate increment or decrement. In the case of a strain rate acceleration $\dot{\epsilon} = 0.02 \rightarrow 0.2 \text{ s}^{-1}$, the hardening rate becomes equal to that of the constant strain rate after a few percent of strain. This is demonstrated by the dotted line, which is the hardening curve at $\dot{\epsilon} = 0.2 \text{ s}^{-1}$, shifted by $\Delta\epsilon \approx 0.06$ in order to let the stress of the constant rate

and jump test coincide. The curves coincide quite satisfactorily over a strain range $\varepsilon = 0.1 \dots 0.3$. This indicates that the internal dislocation substructure -which defines the hardening rate of the jump curve- has become identical to that of the shifted constant strain rate curve. The state of the material after the strain rate jump at $\varepsilon \approx 0.085$ is apparently equal to the state of the material deformed at a constant high rate at $\varepsilon \approx 0.025$.

This comparison also demonstrates that the flow stress, and consequently since $\sigma = \sigma_y + \alpha Gb\sqrt{\rho}$, the dislocation density ρ is a valid state variable. This result indicates that a single state variable suffices to characterize work hardening. Consequently apparently no appreciable dynamic strain ageing takes place since, as explained in Chapter 2, DSA requires more than one state variable.

For the downward strain rate jump test, the situation is completely different. After strain deceleration it is obviously not possible to attain a similar state as in the material that was deformed at a constant low strain rate. The degree of work hardening in the initial high strain rate part of the downward jump test is now higher than that would have resulted from deformation at low strain rate. In other words, with respect to low strain rate deformation an excess dislocation density has been created during the high rate part of the test. After the jump, no relaxation to a lower stress appears to take place; the flow stress rather remains constant for a considerable range of strain $\varepsilon = 0.085 \dots 0.18$. This indicates that no appreciable dislocation annihilation occurs during that strain interval.

This is a convincing demonstration of the correctness of Bergström's interpretation of dynamic recovery as will now be shown. As pointed out in Chapter 2, the Kocks-Mecking and Bergström models of work hardening are mathematically identical, but differ in interpretation of the recovery term. In the literature on the Kocks Mecking model dynamic recovery is invariably interpreted as dislocation annihilation, although the authors of that theory have a more thoughtful point of view which recognizes the possibility of dislocation rearrangement as well [3]. From the annihilation interpretation, softening would be predicted in cases where with respect to the current deformation parameters, an excess density of dislocations is present. In the elementary equation for work hardening (eq. 2.17) the rate of increase of

dislocations becomes negative if $\rho > \left(\frac{U'}{\Omega}\right)^2$, where U' and Ω are respectively a dislocation storage and a dynamic recovery parameter, which are functions of strain rate and temperature.

If dynamic recovery is interpreted as remobilisation as in the Bergström school of thinking, no softening is expected, since dislocations obviously cannot be

removed from the system by remobilisation or some other type of dislocation rearrangement. This does not imply that dislocation annihilation does not occur at all, but rather that the annihilation rate is too low to cause appreciable

softening in the time interval $\Delta t = \frac{\Delta \varepsilon}{\dot{\varepsilon}} = \frac{0.1}{0.02 \text{ s}^{-1}} = 5 \text{ s}$ between the downward

strain rate jump at $\varepsilon = 0.085$ and the onset of recrystallisation at $\varepsilon = 0.18$.

The main conclusions of this section are:

- The work hardening contribution can be isolated by subtracting the yield stress from the flow stress. The glide resistance can be determined as a function of strain rate and temperature from the yield stress alone.
- Work hardening can be described by a single state variable, the dislocation density (or equivalently the stress).
- The mechanism of dynamic recovery is dislocation rearrangement (remobilisation), which leads to a decrease in dislocation multiplication and the associated hardening rate rather than a decrease in dislocation density.

7.4 Constant temperature / strain rate tests

Now that it has become clear that the dislocation glide resistance can be separated from the flow stress, the resulting work hardening can be analysed qualitatively to aid the selection of an appropriate work hardening model.

7.4.1 Occurrence of dynamic strain ageing behaviour

The subject of this section pertains to the question whether dynamic strain ageing occurs. For this purpose a plot of the flow stresses σ_f at strain $\varepsilon = 0.1$ vs. test temperature for all strain rates was made, which is shown Figure 7-4.

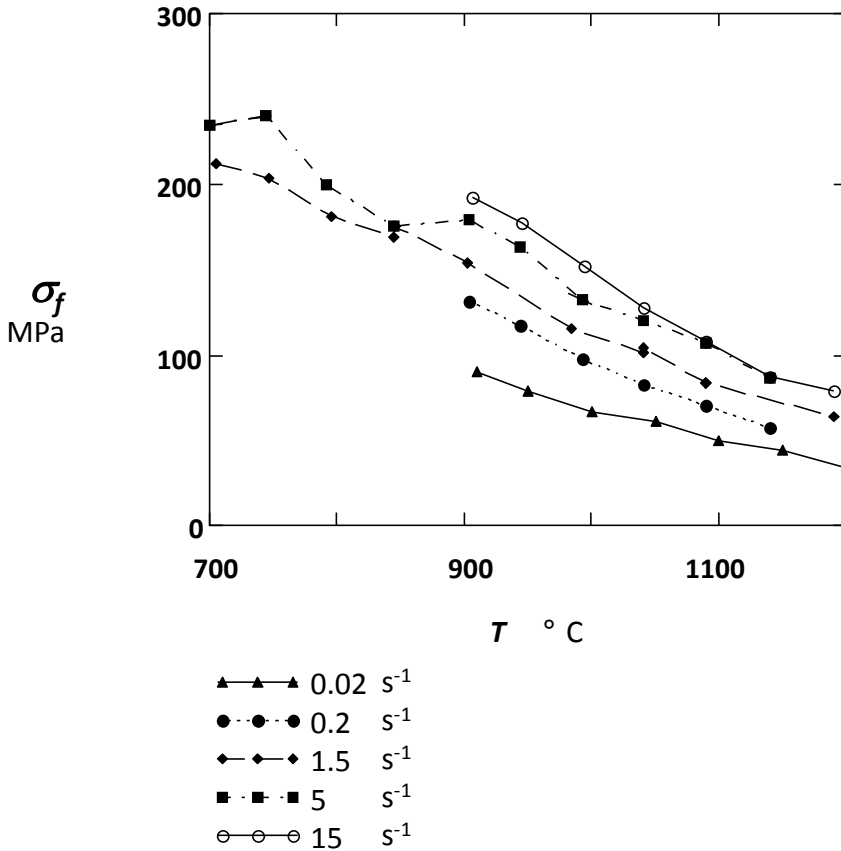


Figure 7-4. Flow stress at $\epsilon = 0.1$ as a function of temperature, for different strain rates.

If dynamic strain ageing would occur, an increased hardening rate and consequently an increased flow stress is expected in a finite temperature range, which depends on the kinetics of the dynamic strain ageing mechanism. This would show as a characteristic hump in the flow stress vs. temperature graph. For low strain rates a strong effect at low temperatures is expected, while for increasing strain rates the effect decreases and shifts to higher temperatures, as shown schematically in Figure 7-5.

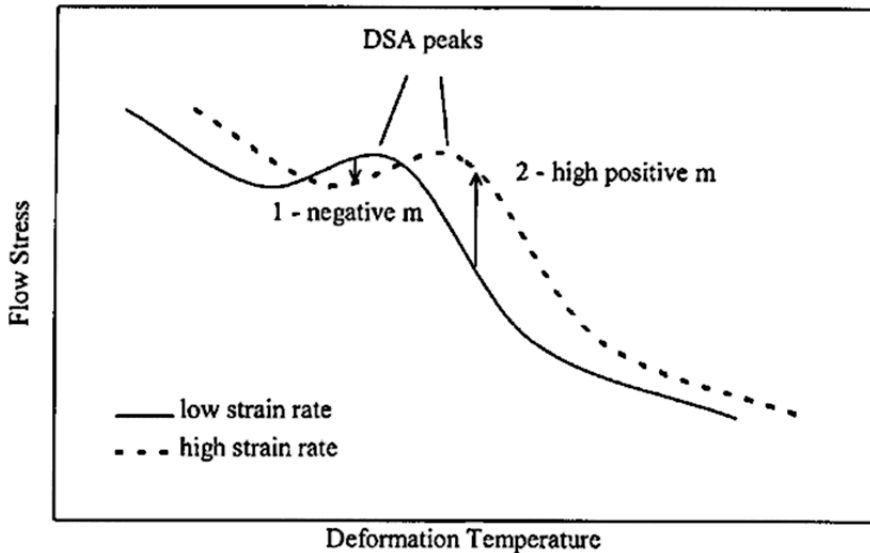


Figure 7-5. Schematic representation of anomalous hardening peaks due to dynamic strain ageing [4]. Compare to Figure 2-13.

None of the strain range series shows such a flow stress hump and we can conclude that no dynamic strain ageing occurs in the experimental strain rate/temperature range. An elementary variant of the Bergström type model is therefore adequate to describe the observed behaviour.

7.4.2 Dislocation storage and recovery rates

According to the conventional interpretation of the Bergström model (or for that matter the Kocks-Mecking model) (Chapter 2) the increase of dislocation density ρ as a function of strain is described as

$$\frac{d\rho}{d\varepsilon} = \frac{\bar{M}}{b\Lambda} U - \Omega\rho \quad (7.3)$$

where Λ is the dislocation mean free path, U a hardening parameter, Ω a dynamic recovery parameter (or probability of remobilisation in Bergström's interpretation), b the magnitude of the Burgers vector and \bar{M} the Taylor factor. This equation describes the increase of dislocation density with strain; the accepted explanation of the first term is that it pertains to the dislocation immobilisation or storage process. It is proportional to the inverse of the dislocation mean free path which is generally regarded as an athermal

parameter, i.e. it is not dependent on thermally activated processes and therefore not dependent on temperature and strain rate. The second term must, as discussed in section 7.3.2, be interpreted as due to remobilisation, and is interpreted in the literature as the only temperature/strain rate dependent parameter of the model.

Equation (7.4) is, by substitution of work hardening σ_w for ρ from the Taylor relation [5]

$$\sigma_w = \alpha \bar{M} G b \sqrt{\rho}, \quad (7.5)$$

seen to be equivalent to the following expression for the hardening rate Θ as a function of the work hardening contribution to the flow stress:

$$\Theta = \frac{\alpha^2 \bar{M}^3 G^2 b}{2 \sigma_w \Lambda} U - \frac{\Omega}{2} \sigma_w \quad (7.6)$$

An additional model describing the dislocation mean free path is now required. The dislocation mean free path is defined as the mean distance between obstacles that are impenetrable to propagating dislocations.

The accepted method [6], [7], which is equivalent to simply adding the hardening contributions due to obstacles of different kind [8], [9], is by taking Λ as the harmonic mean of the individual contributions λ_i :

$$\frac{1}{\Lambda} = \sum_i \frac{1}{\lambda_i}, \quad (7.7)$$

where i is an index denoting different types of obstacles. The form of eq. (7.7) ensures that the smallest inter-obstacle distance has precedence in the value of the overall mean free path Λ . Obvious impenetrable obstacles are grain boundaries, dislocation cell walls and precipitates. Some types of obstacles may only be impenetrable to some degree.

The corresponding contributions in eq. (7.7) are therefore the grain size $\lambda_1 = D$, the dislocation cell size $\lambda_2 = d_c$, the precipitation spacing $\lambda_3 = d_p$ and possibly the distance between solute atoms $\lambda_4 = d_s$.

Taking for the dislocation cell size the Staker-Holt relation $d_c = \frac{K_{SH}}{\sqrt{\rho}}$ (Chapter 2, eq. (2.28)), yields the following expression for the dislocation mean free path:

$$\frac{1}{A} = \frac{1}{D} + \frac{1}{d_p} + \frac{\sqrt{\rho}}{K_{SH}} + \frac{1}{d_s}. \quad (7.8)$$

Substituting for ρ from eq. (7.5), this yields with eq. (7.6) for the hardening rate:

$$\Theta = \frac{\alpha \bar{M}^2 G}{2} \left[\left(\frac{1}{D} + \frac{1}{d_p} + \frac{1}{d_s} \right) \frac{\alpha \bar{M} G b}{\sigma_w} + \frac{1}{K_{SH}} \right] U - \frac{\Omega}{2} \sigma_w. \quad (7.9)$$

7.4.3 Hall-Petch effect on post-yield behaviour

At this point, it must first be established if there are additional grain size influences -i.e. a true Hall-Petch effect in the classical sense- on work hardening in addition to the dislocation mean free path influence that is described by eq. (7.8). The grain size effect described by eq. (7.8) pertains to the freedom of movement that dislocations have within single grain of average size, whereas the Hall-Petch effect in the classical sense is the resistance due to strain incompatibilities at all grain boundaries of the polycrystal. Before proceeding with the analysis of dislocation multiplication we will turn our attention to the possible occurrence of a true Hall-Petch contribution to the post-yield flow stress.

In Chapter 6, the Hall-Petch effect is explained by the strain incompatibilities between neighbouring grains due to local misorientations. According to that theory, it may be expected that the strain incompatibilities between neighbouring grains continue to increase after the yield stress has been exceeded. This is in accord with the view taken by Ashby in his seminal paper on geometrically necessary dislocations [10]. The post-yield Hall-Petch effect is however less strong than its pre-yield counterpart, which can be shown by the following argument. If the increase of the strain incompatibilities as a function of post-yield strain proceeds at the same rate as in the pre-yield strain region, the resulting hardening rate would be much larger than is observed, as is discussed in the following paragraphs.

The anelastic strain at yield is $\varepsilon_y^{AE} = (2 \pm 1) 10^{-3}$, and the Hall-Petch stress varies between 30 and 80 MPa for material austenitized at $T = 1200$ to 910 °C (grain size from $D = 100$ μm to 8 to 10 μm). The rate of increase of the Hall-Petch stress with strain can be estimated as follows. According to eq. (6.5), the Hall-Petch stress varies as the square root of strain. Noting that eq. (6.5) leads to the conventional Hall-Petch equation, when rewritten in terms of true strain, it can be approximated by a first order polynomial around the yield point, according to

$$\sigma_y^{HP}(\varepsilon) = K_y^{pre} \frac{1}{\sqrt{D}} + \begin{cases} \frac{\Delta K_y^{pre}}{\varepsilon_y} \frac{1}{\sqrt{D}} (\varepsilon - \varepsilon_y) & \forall \varepsilon \leq \varepsilon_y \\ \frac{\Delta K_y^{post}}{\varepsilon_y} \frac{1}{\sqrt{D}} (\varepsilon - \varepsilon_y) & \forall \varepsilon > \varepsilon_y \end{cases}, \quad (7.10)$$

where the first term at the right hand side is the Hall-Petch contribution to the yield stress, and the second its change with strain around the yield point. ΔK_y^{pre} and ΔK_y^{post} are additional Hall-Petch contribution factors for strains that are not equal to the strain at the yield point.

From eq. (7.10) it follows that an additional grain size dependent contribution Θ_{HP} to the hardening rate given by eq. (7.8) will occur, which reads

$$\Theta_{HP} = \frac{\Delta K_y^{post}}{\varepsilon_y} \frac{1}{\sqrt{D}}. \quad (7.11)$$

If the pre-yield rate of increase of Hall-Petch stress would persist after yield, that is if $K_y^{post} = K_y^{pre}$, the post-yield (or initial stage III) hardening rate would be $\Theta_0 = 1.5 \dots 4.0 \times 10^4$ MPa. This is more than an order of magnitude larger than what is observed experimentally (see 7-6). Since the observed initial hardening rate must partly be explained by the initial dislocation multiplication rate, the conclusion is that the post-yield Hall-Petch effect is much smaller than the pre-yield effect. In the literature, the prevailing notion seems to be that the Hall-Petch effect pertains to the yield stress only [11], and consequently that post-yield Hall-Petch effects are non-existent.

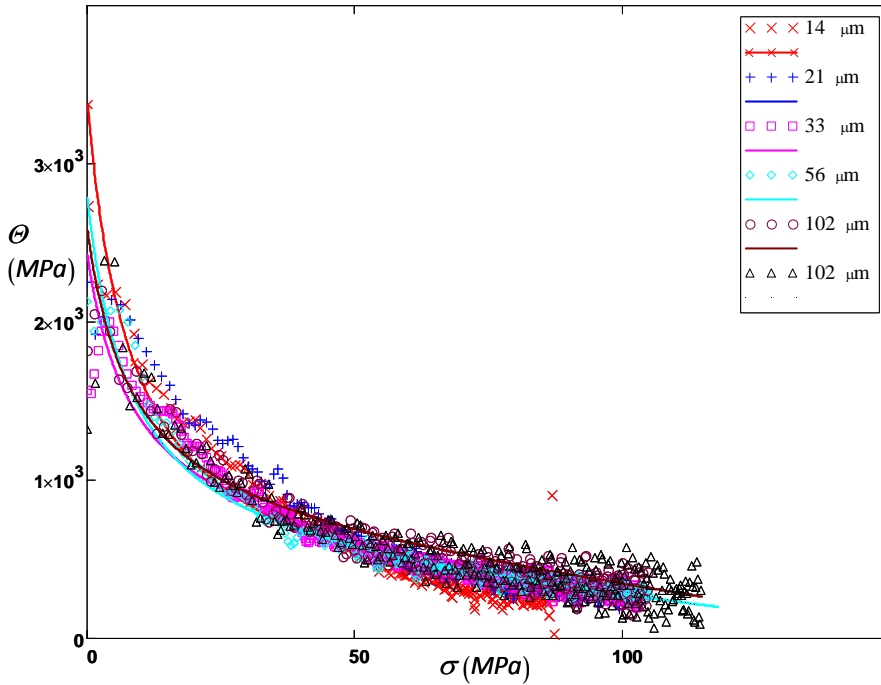


Figure 7-6. Experimental post-yield KM curves of the Hall-Petch experiments.

Since the temperature treatment prior to each tensile test of the experimental dataset is such that the material is austenitized at the temperature at which the tensile test itself is performed, the grain size of the sample for each test is dependent on the test temperature.

The post-yield KM plots of the Hall-Petch experiments shown in Figure 7-6. reveal no appreciable effect of the grain size on the hardening rate. The conclusion is that the influence of grain size on work hardening is weak or absent. There consequently is no reason to correct the flow stress data for a post-yield Hall-Petch effect, and the $\frac{1}{D}$ term pertaining to the effect of D on the dislocation mean free path in eq. (7.9) can also be abandoned.

Discussion

The question remains, why the Hall-Petch effect is so much weaker -or even absent- after the yield point has been exceeded, while at the same time its pre-yield counterpart is strong. The fact that the post-yield Hall-Petch effect is weak can be associated with the relative success of the Taylor hypothesis of crystal plasticity. The basic assumption of that hypothesis is that “the plastic strain of each grain [is] equal to the macroscopic plastic strain” [12]. This implies that

the strain incompatibility between neighbouring grains is zero, and according to the theory developed in Chapter 6 the Hall-Petch effect must then be absent. The physical reason for that behaviour may be that the stress caused by the Grain Boundary Dislocations (GBD's) that accommodate any existing incompatibility is neutralized by the abundance of dislocations that are generated during plastic flow¹. This is not dissimilar from Ashby's prediction that for plastically non homogeneous materials, the contribution of GND's to the flow stress is rapidly "swamped" by the Statistical Dislocations (SD's) during plastic deformation [10]. In the pre-yield stage however, no SD's are generated, and then the effect of GND's or GBD's is will not be attenuated.

7.5 Selection of sub-models

We now have established that a substantial temperature / strain rate dependent contribution to the flow stress is described adequately by that of the yield stress, and that all grain size effects on the work hardening rate may be neglected in the present case. The remaining issues are what temperature/ strain rate effects affect the hardening rate, and whether solute atoms contribute to the dislocation mean free path.

7.5.1 Thermally activated effects on the hardening rate

Since the investigated material contains no precipitating elements the d_p contribution to the dislocation mean free path can also be disregarded. Further, by neglecting the possible contribution of solute atoms to the dislocation mean

¹ For materials that cannot be successfully modelled by a crystal plasticity model based on Taylor's assumption with regard to texture development, it is however possible that there does exist a post-yield Hall-Petch effect. More sophisticated texture theories like the "Relaxed Constraints " [13] or the LAMEL [14] models do allow some degree of inter-grain strain incompatibility, and therefore materials that must so be modelled (with regard to texture) are expected to show a post-yield Hall-Petch effect. Note that in the Hall-Petch theory developed in Chapter 6, it is initially assumed that the stress in each grain is equal to the macroscopic stress. This is identical with Sachs' hypothesis [12], albeit that in our theory, the strain incompatibilities that result from that assumption [15] are resolved by the GBD's. The modern FEM Crystal Plasticity paradigm [15] does not rely on Sachs or Taylor like assumptions (or indeed any other relaxed conditions), but solve the problem of stress equilibrium and strain continuity across the grain boundaries simultaneously. Further discussion on this topic is the remit of Crystal plasticity, and is out of scope of the present study.

free path, this leads to a linear relation between the hardening rate and the work hardening contribution to the flow stress eq. (7.9), is given as:

$$\Theta = \frac{\alpha \bar{M}^2 G}{2} \frac{1}{K_{SH}} U - \frac{\Omega}{2} \sigma_w \quad (7.12)$$

This elementary expression for the work describes the so-called Stage III hardening rate according to the Kocks- Mecking [3], [17], [18], [19], respectively Bergström/Vetter [1], [16] theory. According eq. (7.12) the work hardening rate is a linear function of stress.

At elevated temperature, the work hardening rate is dependent on strain rate and temperature. This implies that either the dislocation storage rate and/or the remobilisation rate are influenced by some thermally activated process.

Kocks and Mecking [3], [17], [18], [19] concluded that the initial hardening rate $\Theta_0 = \Theta(\sigma_w = 0)$, which is the dislocation storage rate given by the first term of the right hand side of eq. (7.12), is an athermal quantity, i.e. independent of strain rate and temperature, and that the second term pertains to dynamic recovery, which is the cause of the strain-rate/temperature dependency of the

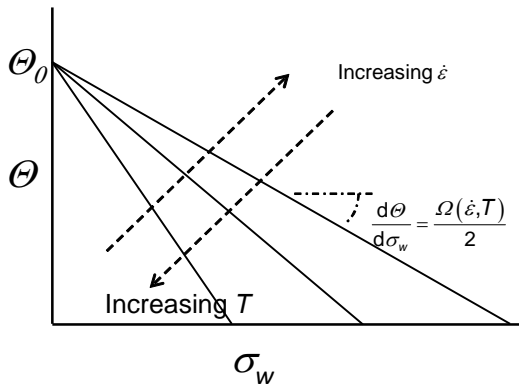


Figure 7-7. Schematic representation of the stage III hardening assuming an athermal storage rate.

work hardening rate. Bergström modelled dynamic recovery as remobilisation enhanced by thermally activated dislocation climb [30]. This leads to the behaviour that is schematically depicted in Figure 7-7, where all branches for different strain rate and temperatures have identical abscissa Θ_0 , and a negative slope that decreases for increasing temperature and decreasing strain rate. Kocks and Mecking's conclusions

were based on experimental observations of hardening of pure metals. In the literature on work hardening at elevated temperatures, the dislocation storage (or immobilisation) rate accordingly is generally treated as an athermal constant, e.g. [20], [[21], [22], with few exceptions [23], [24], so that the

remobilisation rate (or dynamic recovery) is the only thermally activated mechanism.

Kocks and Mecking's conclusion that Θ_0 is an athermal constant was drawn on the basis of experiments on pure Al [3] pure Cu [17], [18], [19] and Ag [19]. In the next section we will show by inspection of the data and an example from the literature, that alloys generally do not follow these elementary rules.

7.5.2 Immobilisation rate

The Kocks-Mecking plots of the complete data set are shown in Figure 7-8. Qualitatively, they show a radically different behaviour than that depicted in Figure 7-7. The initial hardening rate Θ_0 is strongly dependent on strain rate and temperature, see Figure 7-9. It varies between

$$\Theta_0 \left(\dot{\epsilon} = 0.02 \text{ s}^{-1}, T = 1200 \text{ }^\circ\text{C} \right) = 0.5 \text{ GPa} \text{ and}$$

$\Theta_0 \left(\dot{\epsilon} = 5 \text{ s}^{-1}, T = 700 \text{ }^\circ\text{C} \right) = 1.5 \text{ GPa}$. The slopes of the $\Theta(\sigma)$ lines on the other hand show only a weak dependence on strain rate and temperature, as shown in Figure 7-8.

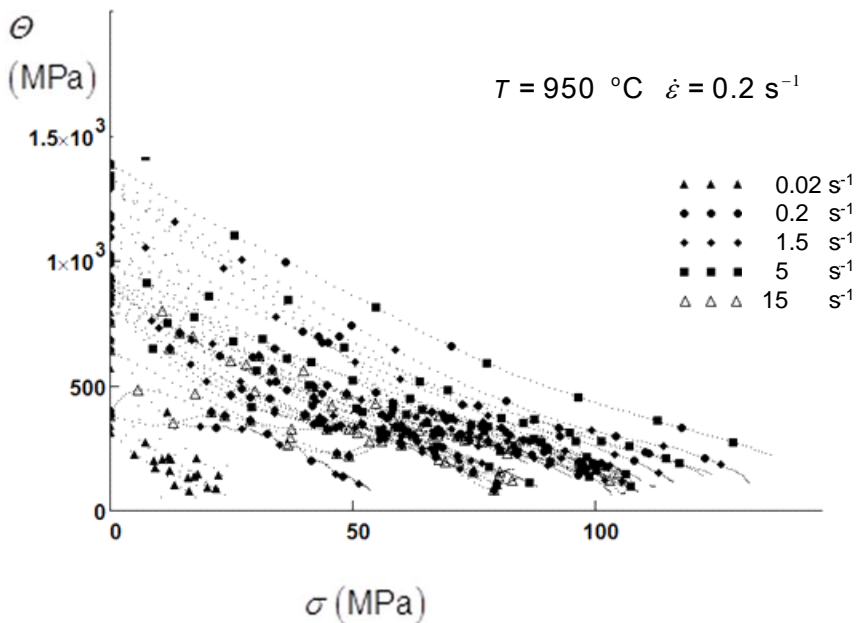


Figure 7-8. Experimental Kocks-Mecking graph of all tests, grouped by strain rate.

The obvious conclusion is that the hardening rate, and consequently the dislocation storage rate/mean free path are in general not athermal, and the hardening model must be modified to take that into account.

The non-athermal behaviour of the initial hardening rate has also been observed in a study of work hardening behaviour of a Fe-C-Mn-B steel grade developed for hot stamping and tested in the metastable austenite temperature range [24], as well as by other researchers for steel in the austenitic state [25], for austenitic steel [26] and indeed has been noticed by Kocks in his earlier work [3]. It is also observed for an Fe-Si steel grade, which remains in the ferritic state at high temperatures, as shown in Figure 7-10, which was calculated by subtracting the yield stress from Kocks-Mecking graphs published by Brown [27].

A reasonable assumption is therefore, that for *alloyed* metals the initial hardening rate, which is related to the -initial- dislocation mean free path, is influenced by interactions between dislocations and local obstacles, e.g. solute atoms or precipitates. This implies that a contribution to the dislocation mean free path that is proportional to some thermally activated interaction between dislocations and local obstacles must be included in the model.

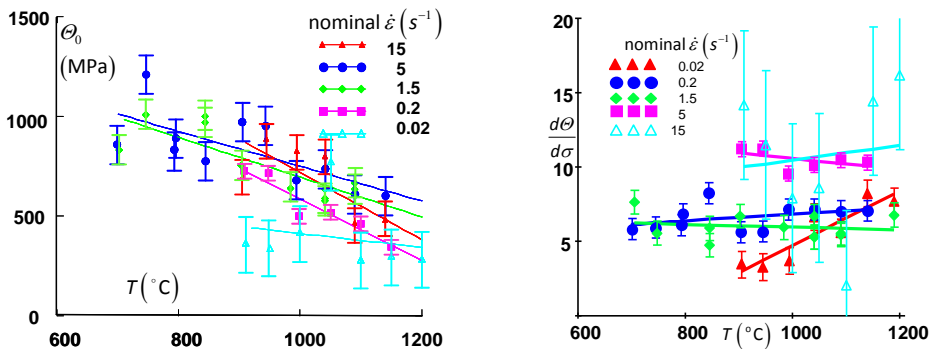


Figure 7-9. Initial hardening rates (left) and slopes of the KM curves (right).

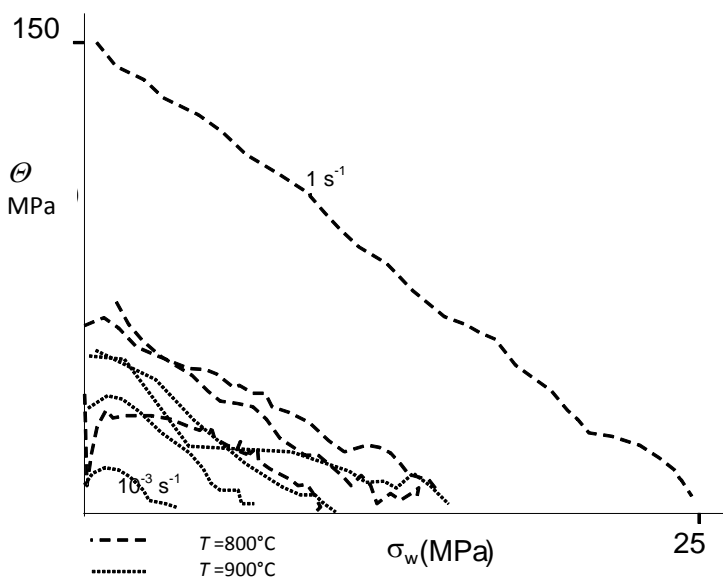


Figure 7-10. Kocks-Mecking plot for Fe2%Si. Strain rates $1 \cdot 10^{-3} \leq \dot{\epsilon} \leq 1 \text{ s}^{-1}$ Replotted from [27].

7.5.3 The sub-model for the dislocation mean free path

The contribution of precipitates in eq. (7.9) does not apply in the present case, since the investigated alloy does not contain precipitating elements. Since the initial hardening rate is observed to depend on strain rate and temperature, it is necessary to identify or include a contribution d_{th} due obstacles that can be passed by thermal activation. The obvious candidate is interstitial carbon, since that was found to be the probable cause of thermally activated dislocation glide in chapter 6. In this case d_{th} becomes identical to d_s : In itself that mechanism will not lead to immobilisation, since the obstacle can be passed by thermal activation. Other mobile dislocations may however arrive at the location of the obstacle during the waiting time of the first dislocation for thermally activated passing of the obstacle. We assume that the probability of an immobilisation event due to this interaction is finite. Another possibility is dislocation drag by jogs that have been created by interaction between edge and screw dislocations [28]. This mechanism involves capture or creation of vacancies. The activation energies involved are vacancy migration and vacancy formation, the activation energies of which are respectively $Q_m = 1.49 \text{ eV}$ and $Q_f = 1.54 \text{ eV}$ [29].

Qualitatively it is expected that d_{th} increases for increasing strain rate, since for high strain rates the waiting time will be small and consequently the probability of an immobilisation event will be small and the free path of this mechanism large. Since the waiting time follows Boltzmann statistics, we propose the following empirical relation:

$$d_{th} = d_{th0} \dot{\epsilon}^q \exp\left(\frac{-Q_\lambda}{k_b T}\right). \quad (7.13)$$

where d_{th0} is the limiting free path at absolute zero temperature, which in the case that the effect is caused by dislocation-solute interaction will be the average distance between solute atoms. Q_λ is the free energy of activation of this immobilisation process, and q an empirical parameter. The effect described by eq. (7.13) can be interpreted as a form of solution hardening that is associated with the work hardening rate rather than the common type of solution hardening which is a contribution to the dislocation glide resistance. The expression for the dislocation mean free path (eq. (7.8)) now becomes

$$\frac{1}{\Lambda} = \frac{1}{d_{th}} + \frac{\sqrt{\rho}}{K_{SH}}. \quad (7.14)$$

7.5.4 Dynamic recovery

Thermally activated dynamic recovery will be described in the model according to Bergström's theory of remobilisation assisted by dislocation climb [30] that is reviewed in Chapter 2.

The expression for the recovery factor is [30]

$$\Omega = \Omega_o + B \exp\left(-\frac{Q_v}{3k_b T}\right) \dot{\epsilon}^{-1/3} \quad (7.15)$$

where Ω_o is the athermal part of the remobilisation factor, i.e. the intrinsic probability of remobilisation due to reactions between mobile and immobile dislocations as shown in Chapter 2, fig 2.7.

Q_v is the activation energy of vacancy diffusion and B a compound parameter given by [30]

$$B = \left\{ kn_0 (2D_v)^{1/2} \right\}^{3/2}. \quad (7.16)$$

where D_v is the pre factor of vacancy diffusivity, n_v the vacancy density and k a proportionality constant.

The proposed model now reads

$$\Theta = \frac{\alpha \bar{M}^2 G}{2} \left[\frac{1}{d_{th0} \dot{\epsilon}^q \exp\left(\frac{-Q_d}{k_b T}\right)} \frac{\alpha \bar{M} G b}{\sigma_w} + \frac{1}{K_{SH}} \right] U - \frac{\Omega_0 + B \dot{\epsilon}^{-1/3} \exp\left(-\frac{Q_v}{k_b T}\right)}{2} \sigma_w. \quad (7.17)$$

This model predicts an infinite value for the initial hardening rate, which is not realistic, since no increase of $\Theta = \frac{d\sigma}{d\epsilon}$ from zero at yielding to infinity just after yielding is observed in practice.

This problem is due to a mathematical idiosyncrasy of this type of hardening theory, which is caused by the physically imperfect formulation of the mean free path as a harmonic mean of different contributions in eq. (7.7). The $\frac{1}{\sigma_w}$

factor in eq. (7.17) only occurs for dislocation free path contributions that are not proportional to $\frac{1}{\sqrt{\rho}}$, like the dislocation cell size term. For that

contribution it is cancelled by the Taylor relation in the reformulation of the dislocation density evolution in terms of stress, see eq. (7.4) to eq. (7.12). This problem is dealt with by assuming an initial dislocation density of the order $\rho_0 = 10^{12} \text{ m}^{-2}$, which is common practice in integration of models of the type of eq. (7.4) [1], [31], [32], [33]. This will show as an offset stress σ_0 in the hardening rate eq. (7.17), which then reads

$$\Theta = \frac{\alpha \bar{M}^2 G}{2} \left[\left(\frac{1}{d_{th0} \dot{\epsilon}^q \exp\left(\frac{-Q_d}{k_b T}\right)} \right) \frac{\alpha \bar{M} G b}{\sigma_w + \sigma_o} + \frac{1}{K_{SH}} \right] U + \frac{\Omega_0 + B \dot{\epsilon}^{-1/3} \exp\left(\frac{-Q_v}{k_b T}\right)}{2} (\sigma_w + \sigma_o) . \quad (7.18)$$

The choice $\rho_0 = 10^{12} \text{ m}^{-2}$ is equivalent to $\sigma_0 = 6.5 \text{ MPa}$ for austenite at $T = 910 \text{ }^\circ\text{C}$. In this case σ_0 must however not be interpreted as part of the initial flow stress (i.e. of the yield stress), but of a parameter pertaining to the hardening rate only. In section 7.7.2 we will show that it is already accounted for by the Frank-Read contribution to the yield stress.

7.6 Model Fit

It is customary to fit stress as a function of strain, with strain rate and temperature as fixed parameters. Most authors use a work hardening function that is derived by assuming that strain rate and temperature are constant during the test. Since we also use data obtained for the post-uniform strain range, the condition of constant strain rate cannot be met in our case. Another problem is that the model as formulated in eq. (7.18) cannot be integrated analytically to obtain an analytical work hardening function. This can however be put to advantage, since if the model is to be integrated numerically, the integration can be performed for strain rate and temperature that vary during the test.

Rather than fitting a numerical model in which eq. (7.18) is integrated numerically and work hardening computed by substituting the resulting dislocation density into the Taylor relation eq. (7.5) to the flow stress, we have chosen to fit eq. (7.18) directly to the hardening rates vs. work hardening stress that was computed from the experimental work hardening data.

The model was fitted to the hardening data by a Levenberg-Marquardt solving procedure implemented in Mathcad, version 14.0.0.163 [build 701291152].

The fitted parameters and their standard errors are listed in Table 5, and the fitted and measured Kocks-Mecking curves respectively measured and

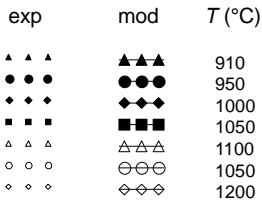
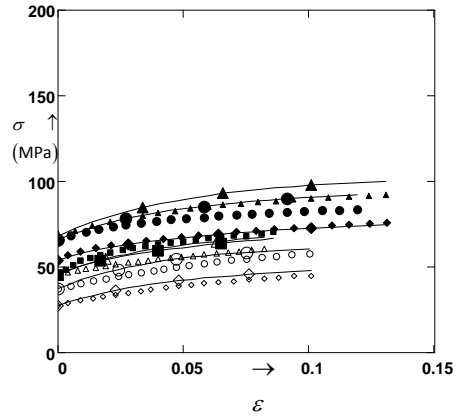
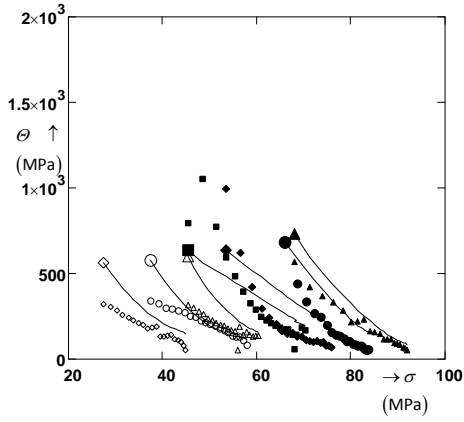
computed hardening curves for all strain rates and temperatures are shown in Figure 7-11.

The value of the activation energy of the thermally activated contribution due to local obstacles to the mean free path Q_λ is significantly lower than that of thermally activated passing of local obstacles (that were identified as solute C atoms) that was found in Chapter 6 ($\Delta G_0=2$ eV) as well as those of vacancy migration or vacancy formation ($Q_m= 1.49$ eV respectively $Q_f= 1.54$ eV). The sub model describing this effect is however empirical and further research into this effect is recommended.

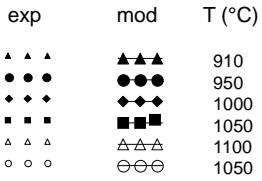
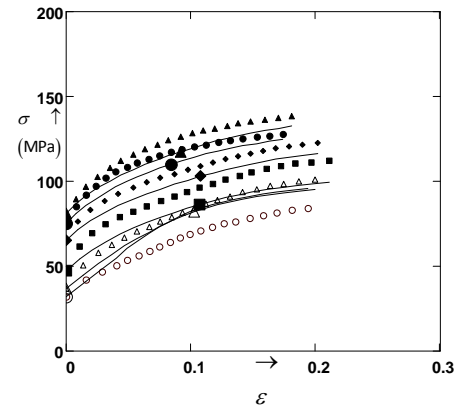
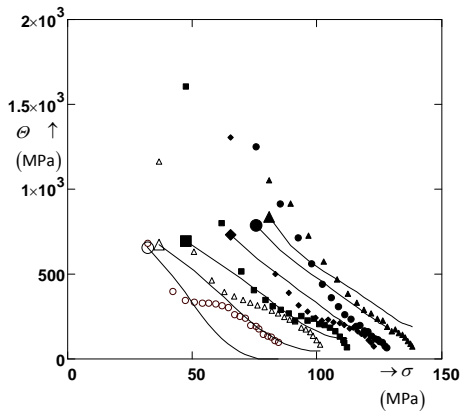
The activation energy Q_Ω of the remobilisation rate is smaller than that reported for vacancy migration $Q_{vm} = 1.49$ eV [29].

<i>Table 5. Parameter values for the fit shown in Figure 7-11.</i>			
parameter	value	St. err	dimension
d_{th0}	$3 \cdot 10^{-4}$	$3 \cdot 10^{-5}$	m^{-q}
q	0.13	0.02	
Q_λ	0.4	0.1	eV
U	0.16	0.01	
σ_0	14	2.	MPa
Ω_0	0.5	0.5	
D	21	5	s
Q_Ω	0.10	0.03	eV

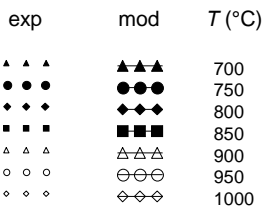
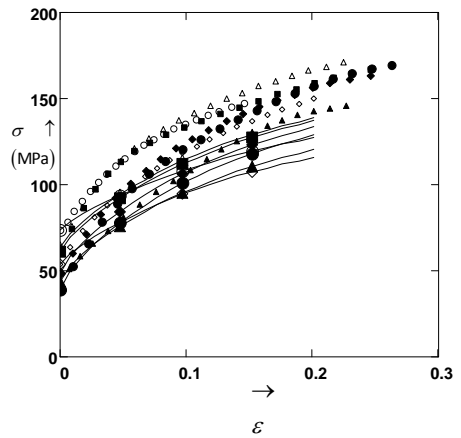
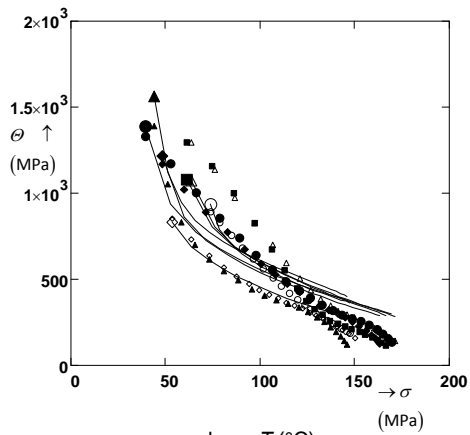
The value found for σ_0 is equivalent to an initial dislocation density $\rho_0 = 4 \times 10^{12} m^{-2}$. This is of the same order of magnitude as the value for the initial dislocation density found in Chapter 6.



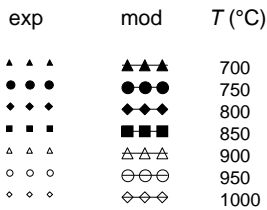
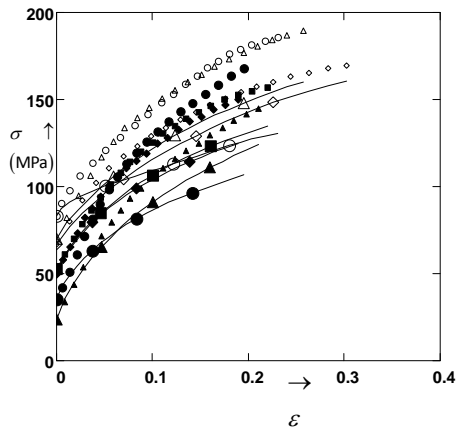
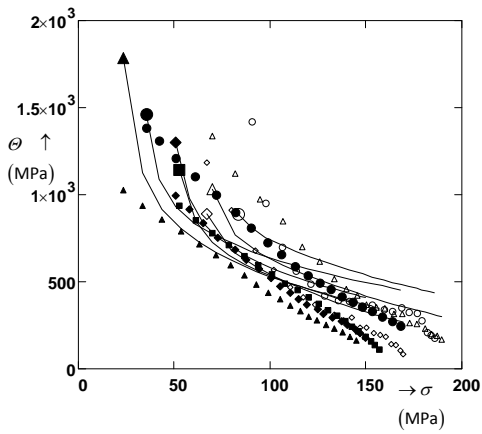
$$\dot{\epsilon} = 0.02 \text{ s}^{-1}$$



$$\dot{\epsilon} = 0.2 \text{ s}^{-1}$$



$$\dot{\epsilon} = 1.5 \text{ s}^{-1}$$



$$\dot{\epsilon} = 5 \text{ s}^{-1}$$

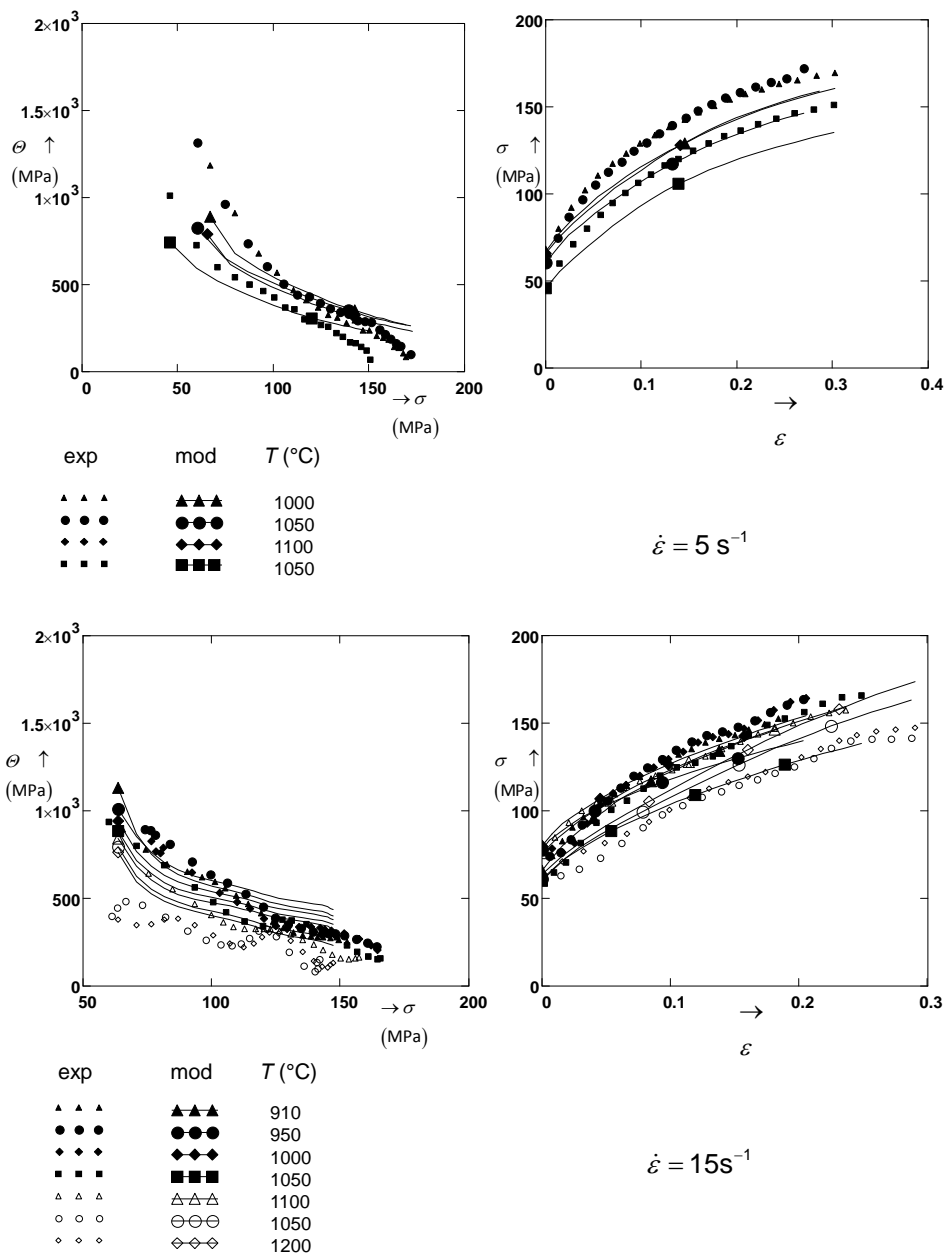


Figure 7-11. Work hardening rates vs. stress (left) resp. flow stress vs strain (right) grouped by nominal strain rate for different temperatures. Symbols: experimental values. Lines: fitted hardening rate respectively calculated flow stress.

7.6.1 Dislocation mean free path

The effect of obstacles that can be passed by thermal activation on the dislocation mean free path is appreciable, as shown in Figure 7-12, where the computed mean free path and the individual contributions due to grain size, obstacles that can be passed by thermal activation and dislocation cell size are plotted vs. strain. The actual mean free path is 50 to 10% smaller than the cell size in the case shown. The contribution of dislocation cell size is however the dominant effect, especially at larger strains. For deformation at the lowest temperatures and high strain rates, the thermally activated contribution becomes dominant, albeit for low

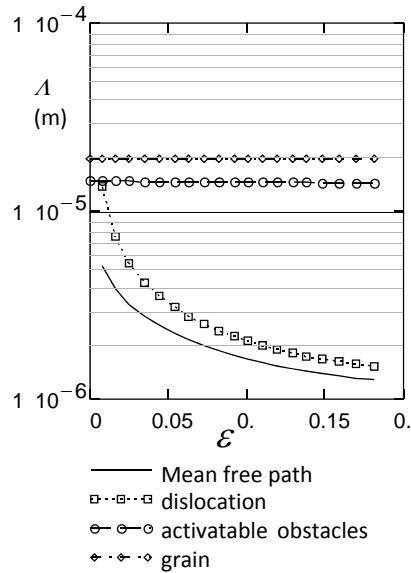


Figure 7-12. Computed dislocation mean free path and individual contributions.

$T = 910 \text{ }^\circ\text{C}$ $\dot{\epsilon} = 0.2 \text{ s}^{-1}$.

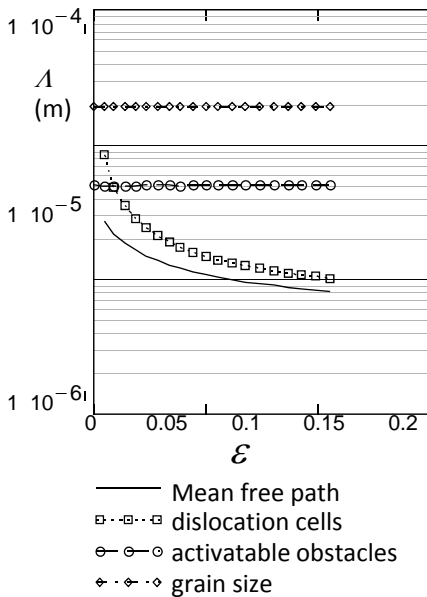


Figure 7-13. Computed dislocation mean free path and individual contributions.

$T = 700 \text{ }^\circ\text{C}$ $\dot{\epsilon} = 15 \text{ s}^{-1}$

strain values only, as is shown in Figure 7-13. The thermal contribution to the mean free path is seen to be several orders of magnitude larger than the distance between C atoms discussed in Chapter 2. This indicates that only a very small fraction (10^{-4}) of thermally activated passages of C atoms by dislocations leads to an immobilisation event. The effect on the work hardening rate is however substantial, as can be seen from the deviations from linear work hardening behaviour in the low strain part of the KM curves shown in Figure 7-11. We conclude that the proposed model functions satisfactory. In

the next section some theoretical issues pertaining to the consistency of the yield theory proposed in Chapter 6 and work hardening theory will be discussed

7.7 Discussion

7.7.1 Post-yield flow stress and yield stress

In this section, the basic principles pertaining to the quantification of yield and flow stress in terms of dislocation density and dislocation segment length will be reviewed. An attempt will be made to arrive at a consistent description of both pre and post-yield phenomena.

In Chapters 5 and 6, the yield stress is explained by the Frank-Read mechanism. The work hardening contribution to the post-yield flow stress on the other hand is commonly explained by the Taylor relation [5] between dislocation density and stress

$$\sigma_w = \alpha \bar{M} G b \sqrt{\rho}, \quad (7.19)$$

which is based on the principle that σ_w is a stress caused by the interaction between stored and mobile dislocations. It is “... often interpreted as the “passing stress” for a moving dislocation to glide through a forest of obstacles without being pinned” [34]. In other words, it is the stress that must be overcome for the dislocations to remain mobile. A crucial assumption in the derivation of the Taylor relation is that the dislocations are uniformly distributed. The empirical parameter α is introduced to correct for differences between the assumed and actual dislocation distribution, e.g. if there exists a cellular substructure rather than a uniform network. The experimental validity of the relation between dislocation density and work hardening expressed by eq. (7.19) with $\alpha \approx 0.15$ is very well documented [17], [35], [36] and widely accepted.

The condition that a fraction of the dislocation sub-structure must remain mobile is however not sufficient to explain the phenomenon of work hardening. That requires that dislocations must also be able to multiply, which may be assumed to be caused by the Frank-Read mechanism.

The Frank-Read mechanism describes yield stress as being due to the self-stress of a dislocation segment that bows out under the action of an applied stress, assuming that the material in the vicinity of that segment is free of internal stresses. The latter assumption -if true- guarantees that the dislocation loops

emitted by the Frank-Read segment are mobile, since the applied stress is larger than the self-stress of the loops.

It may be argued that the post-yield flow stress is the yield stress of deformed material. The question now arises how the interpretations of yield stress as proposed in Chapter 6 and of post-yield flow stress (i.e. work hardening) can be made consistent.

An alternative explanation of eq. (7.19) is given by the link length theory [37], which is based on the principle that the stored dislocation distribution is such that dislocation segments of sufficient size to be able to multiply at the value of the flow stress can be accommodated. It is assumed that these segments are straight, or equivalently that their environment is free of internal stresses.

To make dislocation multiplication during deformation possible, the length l_{FR} of dislocation segments that can operate at the flow stress as potential Frank-Read sources must according to eq. (5.A9) be equal to

$$l_{FR} = \frac{\bar{M}Gb}{\sigma_w}. \quad (7.20)$$

Note that the small contribution $\sigma_c^l = 10 \pm 2 \text{ MPa}$ of the Frank Read stress at yield is neglected as well as the post-yield Hall-Petch contribution to the flow stress which was found to be negligible in section 7.4.3. For a uniform dislocation network, this segment length is the link length l_u of such a network, which is given by

$$l_u = \frac{1}{\sqrt{\rho}} \quad (7.21)$$

From eqs. (7.19)..(7.21) follows $\alpha = 1$. This is more than 6 times larger than the accepted value $\alpha = 0.15$, and it is unlikely that there exist segments large enough to operate as Frank-Read sources during plastic deformation in such a network. Since the dislocations are however not uniformly distributed, but concentrated in the cell walls of the dislocation substructure, the discrepancy between the link length and the length of viable Frank-Read dislocation segments becomes even larger.

This problem can be resolved if it is assumed that the Frank-Read dislocation segments are situated inside the dislocation cells rather than in the cell walls. Let the length of these segments be some fraction $\phi < 1$ of the cell size, which is given by the Staker-Holt relation [38]

$$d_c = \frac{K_{SH}}{\sqrt{\rho}}. \quad (7.22)$$

The condition that the cell interior is free of stresses caused by the dislocations in the cell walls is most probably ensured by the fact that dislocations of opposite sign are arriving from opposite sides of the cell walls, thereby mutually screening their stress fields.

Substituting $l_{FR} = \phi \frac{K_{SH}}{\sqrt{\rho}}$, where l_{FR} is the length of the Frank-Read dislocation segments and ϕ the ratio of segment length to cell size, in eq. (7.20) yields

$$\sigma_w = \frac{\bar{M}Gb\sqrt{\rho}}{\phi K_{SH}}. \quad (7.23)$$

Since this must be identical with eq. (7.19), it follows that $\phi = \frac{1}{K_{SH}\alpha}$. With

$\alpha = 0.15$ and $K_{SH} = 15$, the estimated value of ϕ is $\phi = 0.4$, which is a not unreasonable result, since it is sufficient for free operation of the FR source. The empirical constant α can therefore be interpreted in terms of dislocation cell size and the size of the Frank-Read dislocation source size. The latter can in principle be determined from the flow stress after deformation according to the principles that pertain to the yield stress and which are laid down in chapter 5 and 6. Note that the value $\phi = 0.4$ implies that any stresses originating from the immobile dislocation sub structure must be small or negligible, since otherwise the Frank-read segments must be larger and ϕ closer to 1. This complies with the Low Energy Dislocation Structure (LEDS) theory [39].

The conclusion is that only the development of a dislocation substructure that has a cell size that relates to the dislocation density according to eq. (7.22) makes it possible to accommodate dislocation segments of sufficient length to be able to multiply at the observed flow stress. The main problem to be solved in the field of dislocation theory is therefore the question how the dislocations become arranged in a cell structure according to eq. (7.22).

This interpretation of the Taylor relation also offers an explanation for the phenomenon that the work hardening rate becomes zero after an abrupt change from high to low strain rate, as observed in Figure 7-1, curve d. At the instant of the strain rate jump, the flow stress is higher than it would have been if the sample had been deformed at the low rate (Figure 7-1, curve a).

Consequently the dislocation cell size at that instant is smaller than complies with the flow stress value for the strain rate just after the strain rate change. From eq. (7.20) follows that the Frank-Read sources are too short to be able to maintain the multiplication process at the lower flow stress, and that dislocation multiplication ceases.

It also resolves the question why the Taylor relation is not very sensitive to the spatial dislocation distribution (in the sense the classical interpretation). On the contrary it is, since it can be formulated as a related to a fundamental special distribution parameter of the substructure, namely the dislocation cell size. In the next sections the implications of this interpretation to the Hall-Petch theory proposed in Chapter 6 will be discussed.

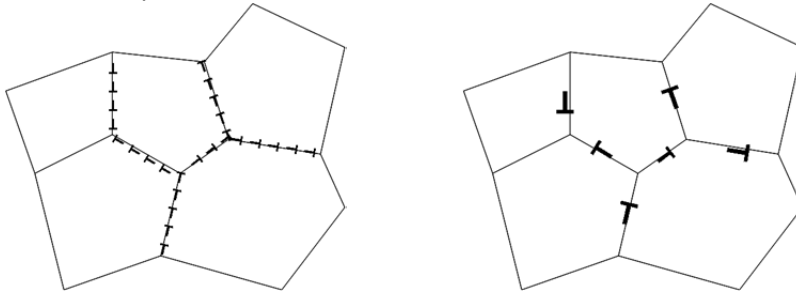


Figure 7-14. Schematic representation of grain boundary dislocations (left), combined in "hyper" dislocations (right).

7.7.2 The Taylor relation and the proposed yield stress theory

It can be argued as follows that this interpretation of the Taylor relation has no impact on its use in the formulation of the Hall-Petch/Frank-Read theory of the yield stress proposed in Chapter 6. There it is applied to a distribution of grain boundary dislocations. These grain boundary dislocations constitute a -strain dependent- additional low angle grain boundary at each existing grain boundary. These additional low angle grain boundaries can be interpreted as "hyper"-dislocations having a Burgers vector equal to the sum of the individual dislocations in the additional low angle grain boundary, and situated in the centre of the boundary, as depicted in Figure 7-14. These hyper-dislocations are uniformly distributed for a uniform grain structure, and can thus be treated according to the conventional interpretation of the Taylor relation, that is as a uniform distribution of -in this case hyper-dislocations.

Hall Petch treatment of dislocation cells

Some authors have proposed to take the cell size as an additional state variable and include the cell size hardening as a contribution to the flow stress like Mughrabi [40] and Nes [41] in their dual state variable models. They include a flow stress term proportional to $\frac{1}{d}$, or equivalently to $\sqrt{\rho}$, to include the flow stress due to geometrically necessary dislocations in the cell boundaries.

In relation to any misorientations that evolve between dislocation cells during deformation, the argument presented in the previous section may be reversed and applied to the dislocation cells.

If we treat the dislocation cells similar to grains, i.e. taking the cell boundary stresses due to inter-cell misorientation into account, the dislocation cell Hall-Petch contribution to the flow stress σ_c is given by:

$$\sigma_c = \frac{K_{HPc}}{\sqrt{d}}, \quad (7.24)$$

where K_{HPc} is the Hall Petch coefficient of the dislocation cell structure. Substituting for the cell size from eq. (7.22) yields

$$\sigma_c = \frac{K_{HPc}}{\sqrt{K_{SH}}} \rho^{\frac{1}{4}}. \quad (7.25)$$

The Hall-Petch contribution of dislocation cells to the flow stress is now seen to evolve at a lower rate than according to the dual state-variable model. According to the theory developed in chapter 6, K_{HPc} is proportional to the misorientation between neighbouring grains, in this case between neighbouring cells. The average misorientation between dislocation cells for moderate strains is only 1-2° [12], while the average misorientation between randomly oriented grains is 45° [42]. K_{HPc} is therefore 20-40 times smaller than the Hall Petch coefficient K_{HP} of the grain structure. With $K_{HP} = 141 \text{ MPa } \mu\text{m}^{1/2}$, this contribution to the flow stress constitutes only a fraction $f = 0.05$ to 0.1 , which was calculated from eq. (7.19) for moderate dislocation density, as shown in Figure 7-15.

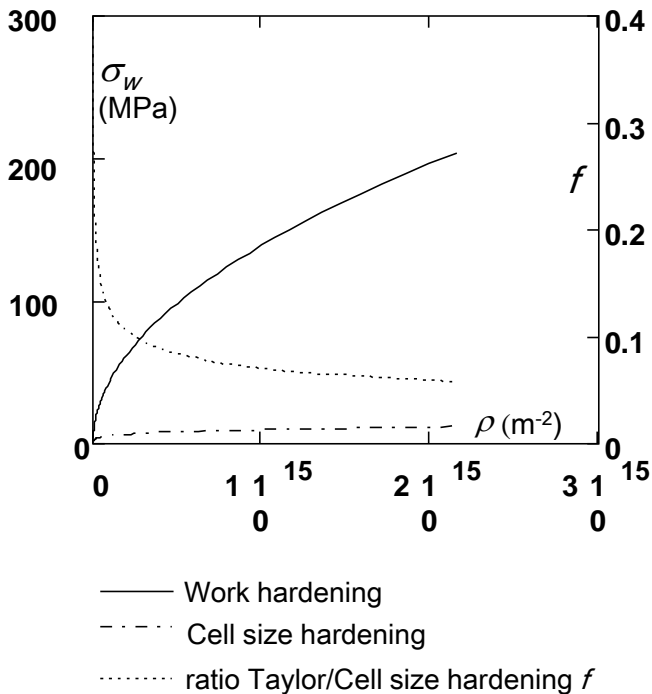


Figure 7-15. Actual work hardening and Hall-Petch hardening due to cell size.

As shown in this figure, the hardening contribution due to cell size according to the Hall-Petch theory is small compared to the actual work hardening and decreases rapidly in importance for increasing dislocation density/work hardening. Even if the dislocation cells develop into sub grains and the misorientation cell becomes large, this hardening contribution will remain relatively small due to the $\rho^{1/4}$ dependence of the cell misorientation hardening. In addition, sub grain formation probably does not occur during hot forming, due to the occurrence of dynamic recrystallisation, which prevents the development of large accumulated strains with which sub grain formation is associated.

The cell misorientation contribution to the flow stress can therefore safely be neglected. This is in agreement with our conclusion in section 7.3 of this chapter that work hardening is sufficiently characterized by a single state variable. It is now also clear, that the initial stress parameter σ_0 introduced in eq. (7.18) is identical to the Frank-Read contribution σ_i^c to the yield stress in eq. (6.22) in Chapter 6. The former is computed from the initially present dislocation structure by the Taylor relation, while the latter follows from the

Frank-Read model, which were shown to yield similar results in the treatment above. The yield and flow descriptions are thus rendered in a theoretically consistent manner.

Having arrived at a unified explanation of yield and flow stress, it can now be concluded that:

- The Taylor relation between work hardening and dislocation density can be interpreted as being due to the cell size which decreases proportional to $\sqrt{\rho}$ and which defines the segment length of active dislocation sources.
- The conventional explanation of the Taylor relation pertains only to situations where the dislocations (or clusters thereof) are homogeneously distributed, like the GND structures caused by misorientations at grain or dislocation cell walls.
- The work hardening effect due to cell wall GND's is relatively small.

7.8 Conclusions

By a careful breakdown of the experimentally observed hardening behaviour in the present and previous chapter, it was found that:

- A significant part of the effect of strain rate and temperature on the flow stress is due to resistance due to thermally activated dislocation glide.
- Thermally activated glide resistance is already fully operational at the yield point, and is not subject to change due to dislocation multiplication.
- In the present case, the resistance due to thermally activated dislocation glide is due to solution hardening.
- The yield stress is the sum of a Frank-Read contribution, a Hall-Petch contribution and the aforementioned resistance due to thermally activated dislocation glide.
- The -theoretically expected- Hall-Petch effect on the work hardening rate is insignificant in the present case.
- The common point of view that the initial hardening rate U is an athermal quantity is proven to be false.
- The temperature and strain rate influence of the work hardening rate is for a large part caused by a thermally activated mechanism of the initial hardening rate U .
- The latter mechanism can be interpreted as a form of precipitation hardening that pertains to the work hardening rate.

References

- [1] Bergström, Y. (1970). A dislocation model for the stress-strain behaviour of polycrystalline α -Fe with special emphasis on the variation of the densities of mobile and immobile dislocations. *Materials Science and Engineering*, 5(4), 193-200.
- [2] Ghosh, G., & Olson, G. B. (2002). The isotropic shear modulus of multicomponent Fe-base solid solutions. *Acta Materialia*, 50(10), 2655-2675.
- [3] Kocks, U. F. (1976). Laws for work-hardening and low-temperature creep. *Journal of engineering materials and technology*, 98(1), 76-85.
- [4] Barnett, M. R., & Jonas, J. J. (1997). Influence of ferrite rolling temperature on microstructure and texture in deformed low C and IF steels. *ISIJ international*, 37(7), 697-705.
- [5] Taylor, G. I. (1934). The mechanism of plastic deformation of crystals. Part I. Theoretical. *Proceedings of the Royal Society of London. Series A, Containing Papers of a Mathematical and Physical Character*, 362-387.
- [6] Engberg, G., & Lissel, L. (2008). A physically based microstructure model for predicting the microstructural evolution of a C-Mn steel during and after hot deformation. *Steel Res Int*, 79(1), 47-58.
- [7] Wang, X. T., Siwecki, T., & Engberg, G. (2003, July). A physical model for prediction of microstructure evolution during thermo mechanical processing. In *Materials Science Forum* (Vol. 426, pp. 3801-3806).
- [8] Estrin, Y., & Mecking, H. (1984). A unified phenomenological description of work hardening and creep based on one-parameter models. *Acta Metallurgica*, 32(1), 57-70.
- [9] Galindo-Nava, E. I., & Rivera-Díaz-del-Castillo, P. E. J. (2013). Thermostatistical modelling of hot deformation in FCC metals. *International Journal of Plasticity*, 47, 202-221.
- [10] Ashby, M. F. The deformation of plastically non-homogeneous materials. *Philosophical Magazine*, 1970, 21.170: 399-424.
- [11] Cahn, R., & Haasen, P. (1996). *Physical Metallurgy Vol.I..III*.
- [12] Sevillano, J. G., Van Houtte, P., and Aernoudt, E. (1980). Large strain work hardening and textures. *Progress in Materials Science*, 25(2), 69-134.
- [13] Van Houtte, P., Li, S., Seefeldt, M., & Delannay, L. (2005). Deformation texture prediction: from the Taylor model to the advanced Lamel model. *International Journal of Plasticity*, 21(3), 589-624.
- [14] Van Houtte, P., Li, S., Seefeldt, M., & Delannay, L. (2005). Deformation texture prediction: from the Taylor model to the advanced Lamel model. *International Journal of Plasticity*, 21(3), 589-624.
- [15] Roters, F., Eisenlohr, P., Bieler, T. R., & Raabe, D. (2011). *Crystal plasticity finite element methods: in materials science and engineering*. John Wiley & Sons.
- [16] Vetter, R., & Van Den Beukel, A. (1977). Dislocation production in cold worked copper. *Scripta Metallurgica*, 11(2), 143-146.

-
- [17] Kocks, U. F. (2001). Realistic constitutive relations for metal plasticity. *Materials Science and Engineering: A*, 317(1), 181-187.
- [18] Kocks, U. F., & Mecking, H. (2003). Physics and phenomenology of strain hardening: the FCC case. *Progress in materials science*, 48(3), 171-273.
- [19] Mecking, H., & Kocks, U. F. (1981). Kinetics of flow and strain-hardening. *Acta Metallurgica*, 29(11), 1865-1875.
- [20] Estrin, Y., & Mecking, H. (1984). A unified phenomenological description of work hardening and creep based on one-parameter models. *Acta Metallurgica*, 32(1), 57-70.
- [21] Domkin, K. (2005). Constitutive models based on dislocation density. Lulea University of Technology.
- [22] Lindgren, L. E., Domkin, K., & Hansson, S. (2008). Dislocations, vacancies and solute diffusion in physical based plasticity model for AISI 316L. *Mechanics of Materials*, 40(11), 907-919.
- [23] Galindo-Nava, E. I., & Rivera-Díaz-del-Castillo, P. E. J. (2013). Thermostatistical modelling of hot deformation in FCC metals. *International Journal of Plasticity*, 47, 202-221.
- [24] Abspoel, Michael, Bas M. Neelis, and Peter van Liempt. Constitutive behaviour under hot stamping conditions. *Journal of Materials Processing Technology* (2015).
- [25] Galindo Nava, E. I. (2013). Thermostatistical theory of plastic deformation in metals. TU Delft, Delft University of Technology.
- [26] Angella, G. (2012). Strain hardening analysis of an austenitic stainless steel at high temperatures based on the one-parameter model. *Materials Science and Engineering: A*, 532, 381-391.
- [27] Brown, S.B. An internal variable constitutive model for the hot working of metals. Thesis MIT 1987.
- [28] STRUNK, H.; FRYDMAN, R. Jog dragging in edge dislocations with application to plastic deformation and internal friction. *Materials Science and Engineering*, 1975, 18.1: 143-148.
- [29] Militzer, M., Sun, W. P., & Jonas, J. J. (1994). Modelling the effect of deformation-induced vacancies on segregation and precipitation. *Acta metallurgica et materialia*, 42(1), 133-141.
- [30] Bergström, Y., & Hallén, H. (1982). An improved dislocation model for the stress-strain behaviour of polycrystalline α -Fe. *Materials Science and Engineering*, 55(1), 49-61.
- [31] Domkin, K. (2005). Constitutive models based on dislocation density. Lulea University of Technology.
- [32] Bodin, A. (2002). Intercritical deformation of low-alloy steels. PhD thesis, Delft University of Technology.
- [33] Liempt, P. V., Onink, M., & Bodin, A. (2002). Modelling the influence of dynamic strain ageing on deformation behavior. *Adv. Eng. Mater*, 4, 225-232.
- [34] Gao, H. (2001). Strain gradient plasticity. In *Encyclopedia of Materials: Science and Technology* (pp. 8861-8865). Elsevier Science Ltd..

-
- [35] Dingley, D. J., & McLean, D. (1967). Components of the flow stress of iron. *Acta metallurgica*, 15(5), 885-901
- [36] François, D., Pineau, A., & Zaoui, A. (1998). *Mechanical behaviour of materials*. Dordrecht: Kluwer academic publishers
- [37] Kuhlmann-Wilsdorf, D., & Hansen, N. (1989). Theory of work-hardening applied to stages III and IV. *Metallurgical Transactions A*, 20(11), 2393-2397.
- [38] Staker, M. R., & Holt, D. L. (1972). The dislocation cell size and dislocation density in copper deformed at temperatures between 25 and 700 C. *Acta Metallurgica*, 20(4), 569-579.
- [39] Kuhlmann-Wilsdorf, D. (1999). The theory of dislocation-based crystal plasticity. *Philosophical Magazine A*, 79(4), 955-1008.
- [40] Mughrabi, H. (1987). A two-parameter description of heterogeneous dislocation distributions in deformed metal crystals. *Materials science and engineering*, 85, 15-31.
- [41] Nes, E. Recovery revisited. *Acta metallurgica et materialia* 43.6 (1995): 2189-2207.
- [42] Mackenzie, J. K. Second paper on statistics associated with the random disorientation of cubes. *Biometrika* 45.1-2 (1958): 229-240.

Summary

The literature pertaining to the dislocation theory of the flow stress of polycrystalline metals is reviewed. This is introduced by a qualitative overview of the formulation of constitutive equations, followed by a discussion on thermally activated dislocation glide and of work hardening. Of the latter the Bergström theory of work hardening is reviewed, contrasted with a review of the Kocks-Mecking work hardening model. In the last section the anomalous work hardening effect caused by dynamic strain ageing is discussed.

In Chapter 3 the experimental methods and techniques used in this study are discussed. The choice for executing tensile tests rather than compression testing is explained, and the advantages/disadvantages of the Gleeble thermomechanical testing system are discussed. These are respectively its versatility with respect to possible thermomechanical sequences and the occurrence of an awkwardly large temperature gradient in the standard tensile sample due to internal heating by an electric current combined with cooled grips. A specially designed sample that has been developed to minimise this temperature gradient is described, which makes use of a shunt resistance parallel to the gauge section of the sample. This ensures that the current density in the specimen shoulder section and the gauge section are equal, with consequently equal heating rates and final temperatures of both. This in turn prohibits heat flow from the gauge section to the grips, so that the temperature gradient in the gauge section is minimised. Next, a technique for non-contact measurement of strain and temperature is introduced as well as some special test techniques, namely deformation of metastable austenite (ausforming) at sub-critical test temperatures, the strain rate jump test and stress cycling are discussed. Non-contact strain measurement is a useful tool to compensate for the small useful uniform strain range of the tensile test. The ausforming technique is advantageous for extending the temperature window as a compensation for the relatively low (with respect to the hot rolling process) strain rate of the Gleeble system. The strain rate jump and is useful diagnostic tools with which the occurrence of thermally activated effects in the flow stress, namely whether they are caused by dislocation glide mechanisms, work hardening or both. The stress cycling test is a tool with which it can be determined whether deformation is reversible or plastic.

Finally Kocks-Mecking analysis of tensile data is discussed as an instrument to assess the yield stress, followed by a section pertaining to instrumental issues like machine stiffness corrections and suppression of disturbances in the measured signals by filtering in the frequency domain. It is shown that the disturbances caused by the heating system can be successfully suppressed by application of a Chebychev filter.

Chapter 4 is a theoretical exercise with which it is shown that dynamic strain ageing can be explained by a negative sensitivity of the work hardening rate due to segregation of solute atoms to the stored dislocations. This shows that the occurrence of dynamic strain rate effects can be judged by inspection of the flow stress as function of temperature at different strain rates, which will be done in Chapter 7.

In Chapter 5 the viability of using Kocks-Mecking analysis of the flow stress, which yields a physically based yield stress criterion is shown. An elementary model of anelastic pre-yield deformation is developed, based on the reversible dislocation glide mechanism. The yield stress is explained by the Frank-Read mechanism of dislocation multiplication. It is shown, that by this theory, the density and average length of pre-existing dislocation segments can –in principle- be determined from tensile test data¹⁴. This model is developed further in Chapter 6, where the additional effects of Hall-Petch hardening and thermally activated dislocation glide is incorporated. The Hall-Petch effect is explained by strain incompatibilities between neighbouring grains that are caused by anisotropy of the elastic stiffness tensor and of the dislocation glide process. It consequently is dependent on the grain misorientation distribution. The model is applied to the yield stress data of a comprehensive set of tensile tests. This quantitative analysis comprises two steps: firstly the hall Petch model is fitted to a subset of the data that is dedicated to grain size effects, after which the rest of the data is corrected for grain size influences and the model of thermally activated dislocation glide is fitted. The Hall-Petch analysis led to the conclusion that the effect of anisotropy of the elastic stiffness tensor to the yield stress is negligible. From the obtained parameter values of the dislocation glide model it is concluded that the density of pre-existing dislocations is of the same order of magnitude as is usually assumed as the initial value in fitting post-yield work hardening models. The thermally activated mechanism that causes dislocation glide resistance is probably associated with thermally activated passing of solute carbon by dislocations i.e. solute hardening.

In Chapter 7 the work hardening behaviour, obtained by subtraction of the yield stress from the flow stress data is first examined qualitatively. By analysis of the strain rate jump tests is found that the flow stress contribution associated with thermally activated dislocation glide is appreciable, that it is virtually equal to that of the yield stress and not appreciably dependent on

¹⁴ This theory has already contributed to several projects: a M2i project on degradation of the pre-yield modulus due to the accumulation of dislocations caused by plastic deformation and spring-back after deep drawing, and an internal project concerning sheet flatness defects due to temperature gradients on the runout table.

strain. The main consequence of this conclusion is that the (strain rate and temperature dependence of) the yield stress and of work hardening can be fitted separately. In addition it is shown that the Bergström interpretation of dynamic recovery is to preferred over that of the Kocks-Mecking school of thinking.

By examining the flow stress as function of strain rate and temperature during constant strain rate testing, is found that dynamic strain ageing does not occur. Next it is shown by examination of the Kocks-Mecking curves of the constant strain rate tests that grain size has no appreciable effect on the work hardening rate, and more importantly that the usual assumption of the dislocation immobilisation rate to be an athermal constant is not tenable in the case of alloyed metals. It is concluded that this behaviour is caused by a contribution to the dislocation mean free path that is associated with thermally activated passing of some kind of obstacle, possibly solutes, which can be interpreted as a form of "indirect" (in the sense of pertaining to the hardening rate rather than directly to the flow stress) solution hardening. These qualitative conclusions lead to the formulation of a work hardening expression in which an extra thermally activated effect on the dislocation immobilisation rate is included, and which is subsequently fitted to the work hardening data. It is shown that the proposed indirect thermally activated hardening contribution predominates in the low strain range.

The chapter is concluded with a discussion of theoretical character, where the position is taken that the alternative explanation of the Taylor relation between work hardening and dislocation density being due to dislocation cell size rather than resistive stresses due to dislocation density is to be preferred. It is then shown, that this leads to a consistent view on yield and flow stress.

In this thesis it is shown that resistance due to thermally activated glide is not negligible in deformation at elevated temperatures and that it does not vary appreciably as a function of strain. It is found that the Hall-petch effect is associated with plastic anisotropy, with little effect of elastic anisotropy. Furthermore, it is found that some kind of obstacles that can be passed by thermal activation is the cause of the strain rate/temperature dependence of the initial hardening rate.

Curriculum vitae

It takes twenty-one years to become a piper. Seven years learning, seven years practising and seven years playing¹⁵.
Séamus Ennis.

Peter van Liempt

Geboren op 31 maart 1951 te den Haag

1963-1967	MULO, Christelijke Streek MULO IJsselstein
1967-1973	Administratief employee KLM den Haag
1968-1972	Atheneum B, avondlyceum Noctua den Haag
1973-1980	Natuurkunde met Wiskunde en Astronomie. (kandidaatsexamenvakken) Afstudeerrichting Experimentele Natuurkunde. Bijvak Didactiek der Natuurkunde.
1980-2016	Wetenschappelijk medewerker bij Hoogovens b.v. IJmuiden (later Corus IJmuiden resp. TataSteel IJmuiden) tot 1990 bij de afdeling Walserijtechnologie, vanaf 1999 bij de afdeling Metaalkunde.
2008-2016	Promotie onderzoek "Flow and Yield stress at elevated temperatures" Uitgevoerd bij de afdeling Materials Science and Engineering, 3ME, Technische Universiteit Delft onder begeleiding van prof.dr.ir. J. Sietsma.
2016-....	Retired.

¹⁵ And possibly another seven years tuning (and seven years swearing...)

List of publications.

This thesis

van Liempt, P., & Sietsma, J. (2011). A revised criterion for the Portevin–Le Châtelier effect based on the strain-rate sensitivity of the work-hardening rate. *Metallurgical and Materials transactions A*, 42(13), 4008-4014.

van Liempt, P., & Sietsma, J. (2016). A physically based yield criterion I. Determination of the yield stress based on analysis of pre-yield dislocation behaviour. *Materials Science and Engineering: A*, 662, 80-87.

van Liempt, P., Bos, C., & Sietsma, J. (2016). A physically based yield criterion II. Incorporation of Hall Petch effect and resistance due to thermally activated dislocation glide. *Materials Science and Engineering: A*, 652, 7-13.

Other work

van Liempt, P. (1994). Workhardening and substructural geometry of metals. *Journal of materials processing technology*, 45(1-4), 459-464.

Rietman, A. D., Liempt, P., & Huetink, H. (1997). The modeling of compression tests with a physically based material model using finite elements.

van Liempt, P., Onink, M., & Bodin, A. (2002). Modelling the influence of dynamic strain ageing on deformation behaviour. *Advanced Engineering Materials*, 4(4), 225-232.

Wullink, J., van den Berg, F., van Liempt, P., & de Haas, M. (2008). Thermography applied to the evaluation of non-uniform deformation heat of metals. *Quantitative InfraRed Thermography Journal*, 5(1), 69-80.

Gautam, J., Miroux, A. G., Moerman, J., Barbatti, C., van Liempt, P., & Kestens, L. (2012). Determination of the Non-Recrystallisation Temperature (T_{nr}) of Austenite in High Strength C-Mn Steels. In *Materials Science Forum* (Vol. 706, pp. 2722-2727). Trans Tech Publications.

Moerman, J., Triguero, P. R., Tasan, C., & van Liempt, P. (2012). Evaluation of geometrically necessary dislocations density (GNDD) near phase boundaries in dual phase steels by means of EBSD. In *Materials Science Forum* (Vol. 702, pp. 485-488). Trans Tech Publications.

Vegter, H., Mulder, H., Liempt, P., & Heijne, J. (2014). Tailored work hardening descriptions in simulation of sheet metal forming. In AIP conference proceedings (Vol. 1567, pp. 474-481). AIP.

Vegter, H., Mulder, H., van Liempt, P., & Heijne, J. (2016). Work hardening descriptions in simulation of sheet metal forming tailored to material type and processing. *International journal of plasticity*, 80, 204-221.

Torkabadi, A., Van Liempt, P., Meinders, V. T., & Van den Boogaard, A. H. (2015). A constitutive model for the anelastic behavior of Advanced High Strength Steels. In *COMPLAS XIII: proceedings of the XIII International Conference on Computational Plasticity: fundamentals and applications* (pp. 378-385). CIMNE.

Abspoel, M., Neelis, B. M., & van Liempt, P. (2016). Constitutive behaviour under hot stamping conditions. *Journal of Materials Processing Technology*, 228, 34-42.

Arechabaleta, Z., van Liempt, P., & Sietsma, J. (2016). Quantification of dislocation structures from anelastic deformation behaviour. *Acta Materialia*, 115, 314-323.

Dankwoord

In dit onderzoek heb ik een lange reis door ons vakgebied gemaakt. Wat aanvankelijk een overzichtelijk project, met als doel het kwantificeren van de versterking van staal bij hoge temperaturen was, ontwikkelde zich gaandeweg tot een zoektocht door de literatuur en mijn denkhoofd aangaande de fundamentele mechanismen die de grondslag zijn van het plastische vervormingsgedrag in bredere zin. Met name op het gebied van dat wat zich afspeelt vóórdat staal een onomkeerbare vervorming ondergaat, heeft dit tot nieuwe inzichten geleid.

Ik wil hierbij allen die mij hierin hebben bijgestaan en begeleid bedanken. Allereerst mijn vrouw Conny, die mij al die tijd, waarin ik vaak meer een denkhoofd dan een aanspreekbare echtgenoot was, onvoorwaardelijk heeft gesteund, net zoals mijn kinderen Janneke en Guido. Daarnaast mijn promotor Jilt, zonder wiens aanhoudende vragen omtrent allerlei kwalitatieve verklaringen van het materiaalgedrag, de mooie kwantitatieve formules uit hoofdstuk vijf en zes misschien nooit zouden zijn geformuleerd. Mijn dank gaat ook uit naar Henk Vegter, die mij lang geleden op weg heeft geholpen in de metaalkunde, en die sindsdien mijn maatje in dit vak is gebleven. Zonder de steun van de Hoogovenaars Mark Maier, Jan Bottema, Rob Boom en René Duursma zou dit project niet van de grond zijn gekomen. In een andere rol verschaftte René me de argumenten om van de kwantitatieve uitdieping uit hoofdstuk vijf en zes werk te gaan maken. Ook Henk speelde een belangrijke rol bij het organiseren van een project in samenwerking met de Universiteiten in Twente en Delft waarin die theorie wordt toegepast en uitgediept. Dank aan mijn collega's Winfried Kranendonk, Kees Bos en Jos Mosk waarmee ik in het toepassingsproject "FIRM" zeer prettig heb samengewerkt. Dank ook aan Nick den Uijl, Marc Scholting, Marcel Lansbergen en Michael, Abspoel die de hier ontwikkelde experimentele en theoretische methoden hebben toegepast in hun Hot Forming project. Praktische toepassingen zijn altijd een belangrijke motor achter academisch onderzoek. Bij het experimentele werk heb ik waardevolle ondersteuning genoten van Hans Hofman, Nico Geerlofs en Frans Bosman, die de prototypes van het nieuwe Geeble sample heeft gemaakt. Van hem en van Jan Brussel heb ik ook waardevolle suggesties voor het ontwerp gekregen. Belangrijke gesprekspartners op theoretisch gebied waren Winfried, Henk, Jaap Moerman, Bernard Ennis en Hans Mulder. In het laboratorium heb ik met Heleen Schnitger (die de eerste grafiek produceerde waarin het pre-yield gedrag –hoofdstuk vijf en zes, alweer) zichtbaar was), Nick, Ron van Tol en Roy Engelen vele genoeglijke en productieve uren doorgemaakt. Tenslotte onze familie en vrienden, de trouwe supporters op de achtergrond. Bedankt, allemaal.

Propositions

to the thesis

Yield and flow stress of steel in the austenitic state

by Peter van Liempt

Gentlemen, you can't fight in here! This is the War Room!

President Merkin Muffley In: Dr. Strangelove, Stanley Kubrick

1. Portevin-le Châtelier instabilities are caused by a negative value of the strain rate sensitivity of the work hardening rate, not of that of the dislocation glide resistance. (Chapter 3&7)
2. The degradation of the pre-yield elastic modulus is caused by reversible glide of pre-existing dislocation segments (Chapter 5).
3. The Hall-Petch effect is caused by misorientations between neighbouring grains and hence is a textural effect(Chapter 6)
4. The initial work hardening rate is dependent on strain rate and temperature.
5. The relation between flow stress and dislocation density must be explained by the Frank-Read mechanism.
6. The lower yield stress is not a yield stress.
7. The upper yield stress and the proportional limit are physically identical.
8. In crystal plasticity, a distinction between yield locus and flow locus should be made.
9. Of all assumptions, the tacit one is the most dangerous (and maybe the most numerous).
10. It is pedantic for a PhD candidate to assume that propositions other than those pertaining to his/hers scientific field are worth proclaiming (the present one included).

These propositions are regarded to be opposable and defensible, and have been approved as such by the promotor prof. dr. ir. J. Sietsma.

Stellingen

bij het proefschrift

Yield and flow stress of steel in the austenitic state

door Peter van Liempt

Gentlemen, you can't fight in here! This is the War Room!

President Merkin Muffley In: Dr. Strangelove, Stanley Kubrick

1. Portevin-le Châtelier instabiliteiten worden veroorzaakt door negatieve waarde van de reksnelheidsgevoeligheid van de werkverstevingingssnelheid, niet door die van de dislocatiepropagatieweerstand. (Hoofdstuk 3&7)
2. De degradatie van de elastische stijfheid voorafgaand aan plastisch vloeien wordt veroorzaakt door reversibele propagatie van initieel aanwezige dislocaties (Hoofdstuk 5).
3. Het Hall-Petch effect wordt veroorzaakt door oriëntatieverschillen tussen aangrenzende korrels en is daarom een textuureffect (Hoofdstuk 6),
4. De beginwaarde van werkverstevingingssnelheid is afhankelijk van reksnelheid en temperatuur.
5. Het verband tussen de vervormingsweerstand en de dislocatiedichtheid moet worden verklaard door het Frank-Read mechanisme.
6. De onderste vloeigrens is geen vloeigrens.
7. De bovenste vloeigrens en de proportionaliteitsgrens zijn fysisch identiek.
8. In de kristalplasticiteitsleer zou onderscheid moeten worden gemaakt tussen de vloeigrenslocus en de deformatieweerstandslocus.
9. Van alle veronderstellingen is de stilzwijgende het gevaarlijkst (en misschien het meest talrijk).
10. Het is pedant voor een promovendus om te veronderstellen dat stellingen anders dan betrekking hebbende op zijn/haar vakgebied de moeite van het verkondigen waard zijn (de huidige meegerekend).

Deze stellingen worden geacht opponeerbaar en verdedigbaar te zijn ,en zijn als zodanig goedgekeurd door de promotor prof. dr. ir. J. Sietsma.